Uncovering Molecular Relaxation Processes with Nonlinear Spectroscopies in the Deep UV

Brantley Andrew West

A dissertation submitted to the faculty of the University of North Carolina at Chapel Hill in partial fulfillment of the requirements for the degree of Doctor of Philosophy in the Department of Physics.

Chapel Hill
2013

Approved by:

Dr. Laurie McNeil

Dr. Andrew Moran

Dr. Rene Lopez

Dr. Frank Tsui

Dr. Jack Ng

Abstract

BRANTLEY ANDREW WEST: Uncovering Molecular Relaxation Processes with Nonlinear Spectroscopies in the Deep UV
(Under the direction of Andrew Moran and Laurie McNeil)

Conical intersections mediate internal conversion dynamics that compete with even the fastest nuclear motions in molecular systems. Traditional kinetic models do not apply in this regime of commensurate electronic and nuclear motion because the surroundings do not maintain equilibrium throughout the relaxation process. This dissertation focuses on uncovering the physics associated with vibronic interactions at conical intersections. Of particular interest are coherent nuclear motions driven by steep excited state potential energy gradients. Technical advances have only recently made these dynamics accessible in many systems including DNA nucleobases and cyclic polyene molecules.

Optical analogues of multidimensional NMR spectroscopies have recently yielded transformative insight in relaxation processes ranging from energy transfer in photosynthesis to bond making and breaking in liquids. Prior to the start of this research, such experiments had only been conducted at infrared and visible wavelengths. Applications in the ultraviolet were motivated by studies of numerous biological systems (e.g., DNA, proteins), but had been challenged by technical issues. The work presented in this dissertation combines pulse generation techniques developed in the optical physics community with spectroscopic techniques largely pioneered by physical chemists to

implement two-dimensional ultraviolet spectroscopy (2DUV). This technique is applied at the shortest wavelengths and with the best signal-to-noise ratios reported to date.

Sub-picosecond excited state deactivation processes provide photo stability to the DNA double helix. Vibrational energy transfer from the solute to surrounding solvent enables relaxation of the highly non-equilibrium ground state produced by fast internal conversion. In this dissertation, nonlinear spectroscopies carried out at cryogenic temperatures are used to uncover the particular nuclear modes in the solvent that primarily accept vibrational energy from the solute. These measurements additionally expose a competition between internal conversion and vibrational energy transfer onto the DNA backbone.

Ring-opening reactions in cycloalkenes are one of the most fundamental reactions in organic chemistry. Traditional textbook understandings of these reactions conveniently hide the intricate physics that occurs prior to bond breaking. Sub-100-femtosecond internal conversion processes precede bond breaking in these systems. This dissertation directly monitors these dynamics in a derivative of cyclohexadiene, α-terpinene, and detects coherent wavepacket motions for the first time in solution.

To those I've loved along the way..

Acknowledgements

I would like to thank Dr. Andrew Moran for his advice and support over the last four years during the completion of my doctoral research. Never would I have been able to accomplish what has been done without his guidance. I would also like to express my gratitude to Dr. Laurie McNeil, her countless hours during my first year helping me revise and revise again my application for a National Science Foundation East Asia and Pacific Summer Institute fellowship allowed me to travel out of the country for the first time and spend the Summer of 2009 at Nanyang Technological University studying crystal growth techniques. This experience allowed me to take great leaps in my personal and professional life. Dr. Christian Kloc and Tan Ke Jie donated much time, energy, and effort to make this an enjoyable experience for me.

I would also like to thank the graduate students of the Moran Group; most importantly, Dr. Stephen Miller and Dr. Jordan Womick. Their guidance when I first joined the research group was priceless. I would also like to thank graduate students Paul Giokas and Brian Molesky for their help carrying out experimental investigations and providing insightful discussion. Anna Curtis, Nickolaus Montoni, and Andrew Ross also contributed to the investigations presented in this dissertation.

Prior to coming to graduate school at UNC, I attended Davidson College. Here my budding interest in physics was nurtured by several professors with whom I shared many hours in various laboratory and classroom settings. Without the help of Dr. John

Yukich, Dr. Wolfgang Christian, and Dr. Timothy Gfroerer I would not be where I am today. I would especially like to thank Dr. Gfroerer, my undergraduate advisor, for allowing me to bug him many times during office hours and to conduct a summer and two semesters of research in his semiconductor spectroscopy lab. I'd like to thank Mrs. Susan Owens, my high school physics teacher. Her class my senior year opened my eyes to the ways that physics was able to explain how things worked and move around me. It was Mrs. Owens that pointed me in the direction of physics, one which has been a trying, and sometimes overwhelming, but very rewarding journey. Lastly, I'd like to thank my parents for always stressing the importance of education and being a constant rock of support for as long as I can remember. Thank y'all!

Table of Contents

List of Tables

List of Figures

List of Abbreviations and Symbols

a,b	Electronic/Vibrational energy levels
I	Intensity
Γ	Linewidth
L	Length
θ	Angle
m,n	Electronic/vibrational energy levels
C(t,t')	Correlation function
Δ	Amplitude of fluctuation relaxation
□	Rate of fluctuation relaxation
□$^{-1}$	Timescale of fluctuation relxation
g(t)	Line broadening function
C(ω)	Spectral density
E_a	Energy level of state a
T	Pump probe delay, population time in Four Wave Mixing experiment
τ	Coherence time, time delay between Pulse 1 and 2 in Four Wave Mixing
t	Time, time between proble pulse and signal emission in Four Wave Mixing
χ	Molecular susceptibility
ω	Frequency
P	Polarizability, Electric field power

E	Electric Field
S	Optical response of system
k	Rate of physical process
ps	Picosecond
fs	Femtosecond
cm^{-1}	Wavenumber, a measure of frequency
K	Kelvin
λ	Wavelength, reorganization energy
nm	Nanometer
μm	Micrometer
CaF_2	Calcium fluoride
FS	Fused silica
TG	Transient grating
TRF	Time resolved flourescense
2D	Two dimensional
A	Adenine
T	Thymine
CHD	Cyclohexadiene
α-TP	Alpha-terpinine
HT	Hexatriene

7HA	7-methyl adenine
9HA	9-methyl adenine
UV	Ultraviolet
UD	Underdamped
OD	Overdamped
GSB	Ground State Bleach
ESE	Excited state emission
ESA	Excited state absorption
LO	Local oscillator
SHG	Second harmonic generation
OPA	Optical parametric amplifier
NOPA	Nonlinear optical parametric amplifier
FWM	Four wave mixing
Ti:S	Titanium doped sapphire crystal
BBO	Beta Barium Borate nonlinear optical crystal
GDD	Group Delay Dispersion
GVD	Group Velocity Dispersion
2DUV	Two dimensional ultraviolet experimental measurement
FROG	Frequency resolved optical gating

Chapter 1 . Introduction

1.1. Science at the Interface between Optical and Chemical Physics

Recent decades have seen tremendous growth in interdisciplinary research. Scientists with backgrounds in physics, chemistry, mathematics, biology, computer science, and medicine have begun to collaborate with common goals and research interests. The resulting cross-pollination of ideas has paved the way for many technological advances. Technology such as magnetic resonance imaging (MRI) resulted from the efforts of physicians, mathematicians, and physicists and mapping the human genome applied traditional chemistry techniques with basic biochemistry to advance scientific understanding. The fields of biophysics, materials science, and nanotechnology are examples of emerging interdisciplinary research areas, which require expertise from more than one traditional field. In a similar spirit, this dissertation forges new connections between the disciplines of optical physics and physical chemistry. Optical techniques pioneered in the field of attosecond laser science are merged with experimental techniques largely developed by physical chemists to investigate molecular relaxation processes initiated by deep UV laser light with unprecedented time resolution.

Femtosecond laser spectroscopies have long been central to fundamental understanding of molecular relaxation processes in condensed phases (i.e. solution, interfaces, solids, etc).[1] The two-dimensional (2D) spectroscopies employed in this

dissertation were first developed as optical analogues of NMR experiments (e.g., spin echo).[2-5] 2D spectroscopies can be thought of as a special case of a pump-probe experiment in which the waveforms associated with light absorption and emission are both resolved. 2D spectroscopy differs from a traditional (1D) pump-probe measurement where only the emission waveform is detected. As in NMR, the 2D representation exposes correlations between excitation and detection frequencies, thereby eliminating ambiguities of traditional 1D techniques. Detailed discussions of 2D spectroscopy can be found in Section 1.3 and 2.6.

2D experiments were first demonstrated in the infrared wavelength range in 1999-2000.[6-8] Experimental innovations made the extension of 2D spectroscopies to the visible spectral range possible in 2004.[9,10] Over the past decade, infrared (vibrational) and visible (electronic) femtosecond 2D spectroscopies have yielded transformative insight in processes ranging from chemical exchange equilibrium in liquids to energy transfer in photosynthesis.[11-16] At the time that the work presented in this thesis was initiated, the implementation of 2D spectroscopies in the deep UV was widely recognized as the next frontier in the march from "from NMR to X-rays".[17] Such extensions to the deep UV are challenged by laser pulse generation and management, interferometric phase stability, and (undesired) ionization of the sample medium. The work presented in this thesis successfully applies 2D spectroscopy in the deep UV with data quality that is comparable to that of the best experiments reported at longer wavelengths. The most recent work has even pushed the technology to the lower wavelength limit for aqueous solutions at 200nm.

Concomitant to this push toward the X-ray regime is an effort to observe and understand the fastest quantum dynamics in molecular systems. The understanding of sub-picosecond molecular relaxation mechanisms has progressed hand-in-hand with the development of shorter laser pulses. Research, most published within the last year, combining ultraviolet pump pulses (400nm, 266nm, and 200nm), photo-electron detection techniques, and theoretical models is transforming understanding of sub-100fs internal conversion transitions through conical intersections in gas phase cycloalkenes (i.e., textbook reactions in organic chemistry).[18-26] Similar techniques are also being used to understand ultrafast relaxation in DNA nucleobases and their derivatives.[27-29]

The work presented in this dissertation has extended 2D spectroscopies to the deep UV and established several new insights into sub-picosecond molecular relaxation processes in condensed phases. The research presented here has been featured as 2011 Editors Choice in the *Journal of Chemical Physics* and led to an invited perspective article on the present state of 2DUV spectroscopy in the *Journal of Physical Chemistry Letters*.[30,31] A second invited review for the journal *Chemical Physics* is in preparation.

The key contributions are summarized as follows:

- Optical analogues of NMR spectroscopies have been conducted in the deep UV spectral range (near 270nm) with unprecedented laser bandwidth and time resolution
- The influence of excited state energy barriers on DNA photoprotection mechanisms was examined in the first studies of DNA components at cryogenic temperatures

- Transitions between excited electronic states that precede ring-opening reactions in cycloalkenes were resolved for the first time in solution.
- Femtosecond laser experiments were carried out in solution with unprecedented time-resolution at 200nm (i.e., the lower wavelength limit for aqueous solutions) using laser filamentation techniques developed by the attosecond physics community.

1.2. Uncovering Ultrafast Molecular Relaxation Processes in Condensed Phases

Chemical reactions and other non-radiative relaxation processes that occur on the sub-picosecond timescale compete with even the fastest nuclear motions. Such a coincidence in time scales holds special meaning in condensed phases because standard rate theories, which assume that an equilibrated environment surrounds the system, cannot be applied.[32] This non-Markovian regime is understood by first considering that rate theories are often formulated using a reduced quantum mechanical description in solutions near ambient temperatures. Reduced descriptions typically follow the evolution of a few (quantum) degrees of freedom referred to as the "system", while relegating the remaining degrees of freedom to the "bath". Thus, widely employed Markovian kinetic models, which originate in a stochastic form of Fermi's golden rule, make the fundamental assumption that the bath maintains equilibrium throughout the relaxation process in the system (i.e. bath does not evolve). A large body of recent work has incorporated a non-equilibrium bath into models for exciton transport in photosynthetic complexes focusing on intermolecular degrees of freedom.[33-37] In contrast, the understanding of non-Markovian intramolecular excited state dynamics is a largely open area and is garnering particular interest because of the ubiquity of conical intersections in

molecules of biological and chemical significance[32], including DNA nucleobases where conical intersections provide photoprotection to the double helix.[38]

The systems to be discussed in this dissertation return to their electronic ground states at or near conical intersections (CIs).[30] A CI occurs when adiabatic electronic states obtained under the Born-Oppenheimer approximation become degenerate at a particular nuclear geometry. Transitions between electronic states where a wavepacket moves towards, passes though, and moves away from a conical intersection can take place on the sub-100 fs time scale. Here motion refers to changes in the nuclear coordinates of a molecule as the wavepacket moves on the excited state potential energy surfaces. The passage through the conical intersections can itself be much more rapid, calculations predict that passage through a CI can take place in as little time as several femtoseconds.[39] The time scale of relaxation through a conical intersection depends on the curvatures of the potential energy surfaces, which describe the dependence of energy on the nuclear geometry, and the non-adiabatic coupling between the different states. Ultrafast relaxation through CIs is promoted by divergence in the non-adiabatic coupling near the point of degeneracy.[39]

Conical intersections exist in a multi-dimensional space known as the branching space; each dimension of the branching space plays a unique role in tuning the characteristics of the CI and is spanned by a nuclear coordinate. For a CI to exist the branching space must be at least two dimensional, i.e. spanned by two nuclear coordinates. The first is known as the ‘g’ coordinate, which tunes the energy gap between electronic states, and the second as the h-coordinate, which tunes the coupling between states. While CI’s are ubiquitous in polyatomic molecules (3N-6 normal modes;

N>2) diatomic molecules are incapable of possessing them due to an insufficient number of nuclear coordinates and symmetry restrictions. Instead diatomic molecules possess avoided crossings. Figure 1 shows a polyatomic molecule guaranteed to have a CI by its large number of nuclear coordinates and the symmetry at its equilibrium (D_{4h}) geometry.[32]

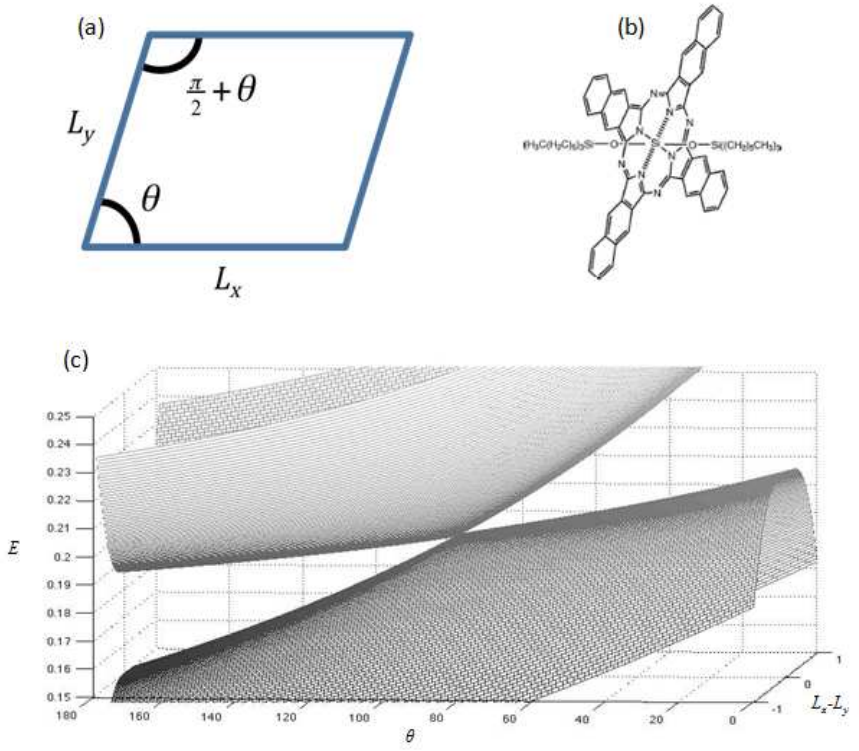

Figure 1.1. (a) Simple diagrammatic representation of the model system, a 2D potential well. L_x and L_y are the lengths of the box in the x-dimension and y-dimension respectively. θ is one angle between L_x and L_y. (b) Example of molecule where 2D particle in a box model applies from Ref. [32]. (c) A plot of the model system's potential energy surfaces. The two surfaces form a conical intersection when $L_x - L_y = 0$ and $\theta = 90°$.

The 2D particle in a box can be used to illustrate essential aspects of a CI if a "diamond distortion" coordinate is added (see Figure 1a). This is done by revising the canonical Hamiltonian with the addition of a new term that couples the direct product basis states. The Hamiltonian is written as

$$H = \begin{pmatrix} \frac{h^2}{8m}\left(\frac{4}{L_x^2}+\frac{1}{L_y^2}\right) & V_{12}(\theta) \\ V_{21}(\theta) & \frac{h^2}{8m}\left(\frac{1}{L_x^2}+\frac{4}{L_y^2}\right) \end{pmatrix} \tag{1.1}$$

where

$$V_{12}(\theta) = V_{21}(\theta) = V\left(\theta - \frac{\pi}{2}\right)^2 \tag{1.2}$$

Note that the coupling is a function of the angle between the x and y sides of the well as depicted in Figure 1; the angle, θ, is the h coordinate. The difference in the segment lengths, L_x - L_y, tunes the energy gap between the states and thus, is the g coordinate. The remaining coordinate, L_x + L_y, is referred to as a seam. It is intuitive that when the angle is 90° and the sides of the box are equal, the two states are degenerate; this is the nuclear geometry of the CI. The new Hamiltonian is diagonalized and eigenenergies of the coupled x/y system are produced. The eigenenergies of this model system are plotted in Figure 1c. The conical intersection forms at L_x=L_y and $\theta = 90°$, as expected. Degeneracy is lifted as the system is displaced along the g and h coordinates as shown. This model system has been introduced to aid in understanding the basic concepts of a CI. Potential energy surfaces can intersect at specific nuclear geometries and the shape of these surfaces near degeneracy points partly governs the rate of relaxation through these CIs. Such phenomena drive the ultrafast relaxation processes studied in this work for which 2D spectroscopy is ideally suited to examine.

1.3. Ultrafast Optical Spectroscopies: Past, Present, and Future

Femtosecond transient grating and two dimensional spectroscopies are ideally suited for studies of these ultrafast processes because of their superior time and spectral

resolution. However, femtosecond laser pulse generation was not possible in "turnkey", tabletop laser amplifier systems until the 1990's when solid state Ti:sapphire-based setups became commercially available[40]. These instruments utilized the advent of Kerr Lens mode locking techniques (KLML) to produce broad bandwidth laser pulses[41] and chirped pulse amplification (CPA) techniques to amplify these pulses to the milli-joule through multi-joule levels[42]. Prior to 1990, femtosecond pulses could be produced using laser dyes as a gain medium, however tunability of femtosecond pulse spectra was limited by the optical properties of the corresponding laser dyes and this tunability necessitated time-consuming optimization.[43]

Coincident with these advances in laser technology was the discovery of nonlinear optical crystals such as β-barium borate (BBO) which possessed large nonlinear optical coefficients, broad transparency ranges, low group velocity dispersion, and high damage thresholds.[44] Utilizing the optical parametric generation technique wherein a high frequency, high intensity 'pump' laser pulse amplifies a lower frequency, lower intensity 'signal' pulse in a nonlinear crystal; the narrow tuning range of the Ti:Sapphire lasers was overcome.[45] Technology had advanced where researchers were able to generate femtosecond laser pulses across the visible and infrared spectral ranges opening up a variety of molecular systems and relaxation phenomena to experimental investigation.

The femtosecond, nonlinear spectroscopies discussed in this dissertation are transient grating (TG) and two-dimensional (2D) spectroscopies. TG spectroscopy carries dynamic information similar to that of pump-probe spectroscopy where a pump pulse excites a fraction of molecules in a system to an excited state then a probe pulse

monitors the change in absorption induced by the excited molecules. By comparing pump-on and pump-off regimes one can measure the dynamic absorption spectrum of the excited state. In TG and 2D, a four-beam geometry is used for experimentation; three beams induce a nonlinear signal and the fourth beam is used as a reference field for interferometric detection. This implementation offers several key advantages. Interferometric detection and background-free signal collection allow for high signal-to-noise ratios and low fluence.[46,47] The non-collinear geometry also allows for polarization control of each beam which can be used to enhance or suppress certain signal components.

2D spectroscopy is unique because it allows for two-dimensional spectra to be obtained where change in absorbance is plotted versus excitation and detection frequency. This experiment can be thought of as a pump-probe spectroscopy experiment with dispersed excitation and detection as shown in Figure 1.2. For molecular systems possessing overlapping absorption bands, strong intermolecular couplings, or ultrafast relaxation mechanisms, 2D offers a distinct capability over traditional pump-probe measurements. In order to selectively excite a particular resonance, a narrow-band pump laser pulse is needed. This allows the dynamics of a single state to be probed but comes at the cost of time resolution because laser pulses are subject to a Fourier transform limit; a short pulse necessarily has a broad spectrum. This narrow-bandwidth (i.e. 'narrowband') pumping technique has been shown to be useful for selective excitation[48,49] but probing the fastest dynamics in complex systems is a challenge for pump-probe spectroscopy. In contrast, 2D spectroscopy is not subject to this limitation, broad-bandwidth pump pulses can be used to excite multiple resonances and resolve

relaxation and transitions among all states. The time resolution in 2D spectroscopy is limited only by the absorption line-widths of the system's resonances.

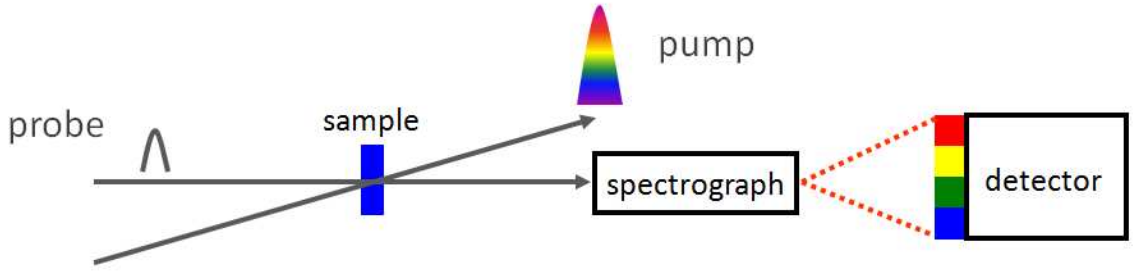

Figure 1.2. Transient grating and transient absorption spectroscopies can be wavelength resolved in the probe dimension (i.e. insensitive to pump wavelength). However, 2D spectroscopy is able to produce spectra which are resolved in both the pump and probe dimensions. This is the origin of the two-dimensional nature of the technique.

The most challenging issue facing implementation of 2D spectroscopies is obtaining interferometric precision on an order that allows for experimental results to accurately portray the physics probed, the necessary precision is ~λ/100. This requires timing errors of less than 0.17fs for a 5μm laser pulse and 0.017fs for a 500nm laser pulse, as well as a stable mechanical setup because fluctuations in optical path lengths can induce changes of 0.1fs over a 20 minute period.[4] Because of this challenge, 2D spectroscopy developed most rapidly in the infrared spectral range[6-8]. Technical advancements then allowed researchers to extend the technique to visible wavelengths.[9,10] Progress towards the UV is just beginning to be made and the work in this dissertation focuses on the development and application of UV-TG and -2D spectroscopy.

The ability to disperse an absorption signal into pumped and probed dimensions is the key functionality of 2D spectroscopy; any conformational change in a molecule which induces a modified absorption spectrum can be monitored. Figure 1.3 presents a basic schematic. When states m and n are populated by the pump laser pulse, mixing

processes can cause the population to transfer between the two states. The probe pulse interrogates the system after a certain time and records where the population is. If the probe pulse indicates that excitations are present at state m, then 2D spectroscopy is able to discern their origin, whether it is from state m itself or has transferred from state n.

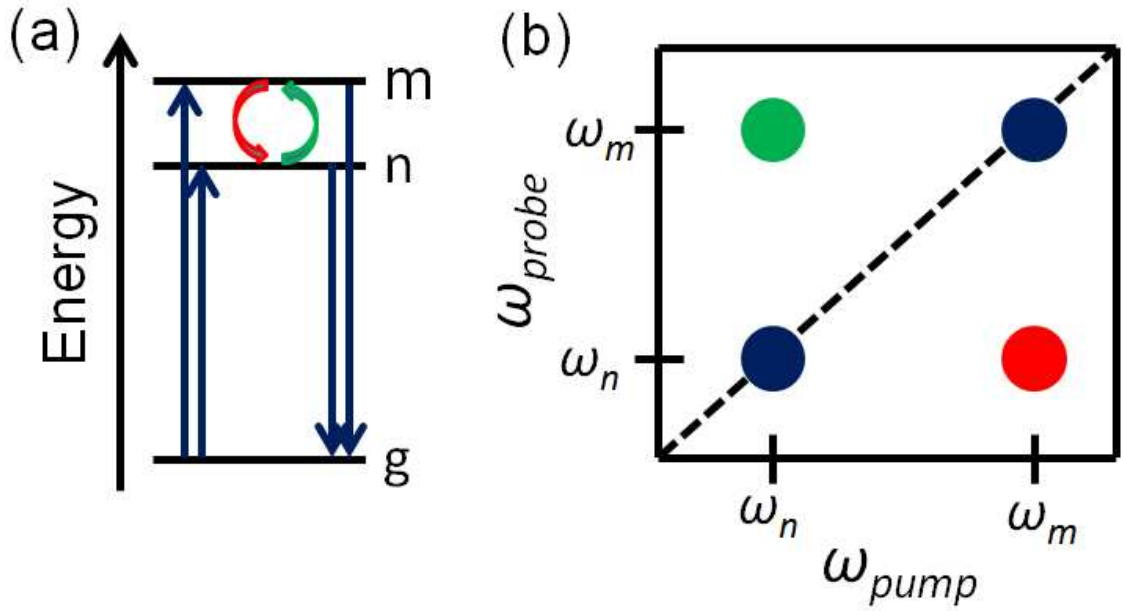

Figure 1.3. 2D spectroscopy is able to follow dynamics which involve molecular absorption at $\omega_{m(\omega_n)}$, followed by probe pulse interaction at $\omega_{n(\omega_m)}$. States m and n can represent anything from vibrational resonances for different isomers of a particular molecule to pigment excitations in a photosynthetic complex (i.e. Frenkel exciton states). (a) Transitions (red and green arrows) such as energy transfer, isomerization, or protein folding that happens in the pump-probe delay will show up as cross peaks in (b) the 2D spectrum (red and green cross peaks).

In Figure 1.3, states m and n can represent a variety of energy states such as vibrational modes of a molecule that undergoes structural change, different sites in a molecular crystal, or excitons in a protein pigment structure. 2D spectroscopy developed most rapidly in the IR (2D-IR) and has been used to understand a wide variety of systems where conformational changes are occurring on a fast time scale.[14] 2D-IR was the first two-dimensional optical technique to develop and was used to study processes including

dynamics of chemical exchange equilibrium, isomerization, and protein folding. [6,7,11,14,50-52]

The implementation of 2D spectroscopy at visible wavelengths (2D-VIS) required experimental apparatus utilizing diffractive optics in order to achieve the necessary phase stability for interferometric detection and data collection.[9,10] This technical advancement followed shortly after the implementation of 2D-IR and allowed new physics to be explored. One of the most compelling examples of 2D-VIS is in application to studying photosynthesis. In photosynthesis, light-driven reactions convert CO_2 into biomass. The most important step in this process is the capture and funneling of light to the reaction center where it is stored as electrical charge or chemical bonds.[13,16] The absorption spectra of these light-capturing complexes possess strongly overlapping resonances due to the presence of multiple pigment types. This, coupled with strong intermolecular interactions and fast relaxation processes makes these systems a prime candidate for investigation with 2D-VIS.[15]

The pathways followed by an excitation as it travels through the photosynthetic complex to a reaction center is fundamentally interesting because this process occurs with nearly unity quantum efficiency.[15] It is of fundamental interest to understand how Nature designed such efficient light collecting systems.[13,16] 2D-VIS can identify the character of delocalization between different sites and the origins of excitations as they move toward the reaction center, thereby identifying the specific spatial pathways that excitations follow.[15] Extensive research utilizing 2D-VIS in the Moran laboratory has identified the importance of vibronic (electron-phonon) coupling of the excited state in enhancing delocalization in hetero-molecular pigment sites.[53] Much like in 2D-IR, the capability of

2D-VIS to disperse absorption information in the pumped frequency has yielded transformative insights in these naturally-inspired systems and many others.

In progressing 'from NMR to X-rays'[17] the next step is implementation of these femtosecond TG and 2D techniques in the UV. In a book chapter published in 2009 Ogilvie and Kubarych stated that "Although the visible frequency regime currently represents the high-frequency limit at which 2D spectroscopy has been experimentally realized, it is unlikely to remain that way for long". [54] Implementation at 265nm is a natural next step because pulses with ample bandwidth and energy can more readily be produced at harmonics of Ti:Sapphire output (800nm). Obtaining the necessary intensity and bandwidth was achieved with non-collinear optical parametric amplification in the infrared and visible; however, similar techniques are not as effective in the UV due to properties of the non-linear medium used to generate the pulses. Alternative methods are necessary to produce UV laser pulses suitable for experimentation.

Development and implementation of these spectroscopies at 265nm and above is motivated by the study of many biological molecules whose lowest-energy resonances lie in the UV. Fundamental relaxation mechanisms in DNA photoprotection and elementary chemical reaction dynamics such as the ring opening of cycloalkenes are specific examples of what can be investigated.[55] 2D-UV is also complementary to current structural characterization methods such as UV circular dichroism. The two-dimensional nature of the technique enhances features that allow researchers to distinguish between different types of biological samples. Recent theoretical work has identified 2D-UV as an effective probe of structure in various biological samples, including helical proteins (hemoglobin) and sheet-containing proteins (monellin).[56] Similar to studies in the visible

and IR, 2D-UV provides a sensitive measure of structure due to interactions of the UV-resonant, highly-localized, carbonyl transitions.

To date, only a small amount of 2D-UV work has been published[57-61], however recent advances in optical physics that allow for generation of broad-band, high-intensity laser pulses tunable across the UV spectrum[62] bode well for numerous future studies to be undertaken. Preliminary research focused on technical challenges such as interferometric phase stability, characterization of undesired nonlinearities which contribute to measured signals, and ensuring that broad bandwidth pulses at 265nm are suitable for experimental use.[55] While these spectroscopies are reaching maturity in the UV researchers are also keeping an eye to future advancement.

Early application of femtosecond spectroscopy in the 1980's allowed researchers to produce 100fs pulses that could coherently excite vibrational wave packets and observe their oscillatory motion in real time.[63] Since the ultimate limitation in time resolution of a laser pulse comes from the period of the optical cycle, X-rays hold the possibility of allowing researchers to observe coherent valence electron motion in atoms. Such motion occurs on the attosecond time scale and it is theoretically possible to produce pulses with durations shorter than this motion.[17] Although the field is in preliminary stages of development, researchers have implemented time-resolved X-ray absorption spectroscopy experiments to observe nuclear dynamics and transition species in photo chemical reactions.[64] Similar to issues encountered in the UV, obtaining laser pulses with broad bandwidths and enough luminosity to be experimentally useful has proved challenging. Researchers have been able to produce attosecond pulses by utilizing high harmonic generation (HHG)[65,66] and high-intensity pulses with fourth-

generation synchrotron sources. Future work will combine the two methods to realize the full potential of attosecond X-ray science.[17]

Theoretical work has indicated that X-ray spectroscopies can be tuned to excite and probe specific atoms in molecules; this is due to the spread of binding energies (60-150eV) of 1s electrons in the atoms in the first row of the periodic table. Two-dimensional X-ray absorption spectroscopy (2D-XAS) can differentiate molecular species much like 2D measurements at longer wavelengths,[67] as well as provide information on interatomic couplings complementary to X-ray absorption spectroscopy.[17] Much like previous work, extending 2D spectroscopies into the UV and beyond to the X-ray regime will undoubtedly push technological limits, provide fundamental understanding of convoluted processes in molecular and atomic dynamics, and introduce new fundamental questions to be addressed by future research.

1.4. Excited State Deactivation in DNA Components

The solar spectrum contains a significant amount of harmful UV radiation (λ<400nm). One of the greatest carcinogenic threats to life is as old as life itself. Absorption of UV radiation from sunlight can initiate a chain of photochemical reactions that culminate in photodamage and impair functionality of DNA strands. This photodamage is known as photocarcinogenesis and is an ever-increasing threat to the world's human population.[68,69] It is no surprise that billions of years of evolutionary pressure have molded modern human DNA to be resilient to such damage. The nucleic acids that form the basis of RNA and DNA efficiently funnel energy from UV photon absorption into molecular vibrations on an ultrafast (sub-1ps) time scale. Only recently with the advent of ultrafast laser technology have researchers been able to study the

relaxation mechanisms which provide DNA is superior photostability. The lifetimes are so short that early literature even deemed the molecules as non-fluorescent.[70] Studies of isolated bases are interesting; however, investigating how dynamics change as molecules are bonded to replicate the double helix provides further fundamental insight into DNA photoprotection.

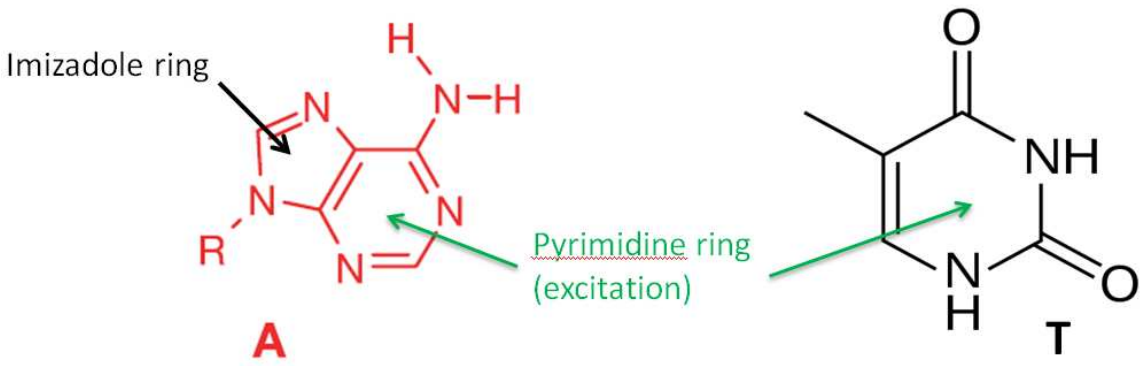

Figure 1.4. Shown is the structure of purine molecules and pyrimidine molecules represented by Adenine (A) and Thymine (T), respectively. The purine molecules have an imizadole ring in addition to the pyrimidine ring.

There are two classes of nucleic acids which form the DNA double helix; purines, which the adenine and guanine nucleobases belong to; and pyrimidines, which the thymine and cytosine nucleobases belong to. Purines are made up of an imizadole ring and a pyrimidine ring, while pyrimidines are composed solely of a pyrimidine ring. It is this pyrimidine ring which absorbs in the 230nm-280nm wavelength range. These two classes of molecules are shown in Figure 1.4. In the double helix, pryimidines and purines hydrogen bond to form base pairs; adenine bonds with thymine forming the A-T base pair and guanine bonds with cytosine to form the G-C base pair. Previous research has found that this base pairing does not negatively influence the ultrafast internal conversion process that provides DNA photostability. In fact, Schwalb and Temps showed that the relaxation time constant for an isolated G-C base pair in solution was

half that observed for the isolated guanine and cytosine nucleobases (i.e. without Watson-Crick base pairing).[71] This relaxation mechanism is proposed to be caused by a charge transfer state forming along the base pair which leads to a conical intersection back to the ground state.[72]

The other trait of the double helix is the stacking of nucleobases to form base strands. Two of these strands which are simultaneously base paired wrap around one another to form the double helix. The sequence of bases in the DNA strands is what encodes the genetic information that produces inter- and intra-special variation. This stacking however is also where photo damage can occur. The most common damage to DNA is the photo-induced reactions leading to a thymine-thymine (cyclobutane) dimer. This process can occur when thymine nucleobases are stacked adjacently along the strand. When a UV photon is absorbed by one of the adjacent thymine molecules photochemical reactions take place forming lesions within 1ps after absorption. However, it is agreed upon that the fast reaction rate and low quantum yield of this process indicate that there is a strong link between conformation prior to absorption and photodamage; only a small subset of possible conformations tends to lead to cyclobutane dimers. [73] Kohler *et al.* identified two major parameters that produce conformations leading to photodamage: the intermolecular distance and the torsion angle between adjacent thymine nucleobases. Certain configurations of these parameters lead to a dimerizable conformation where the lesion-forming photoreaction is likely to occur.[74]

Cyclobutane dimer formation disrupts normal cellular processing of DNA. Research has shown that in homogenous strands of nucleic acids, a large portion of initial excitations result in long-lived excited states. These states are delocalized over multiple

molecules in the strand and suppress the ultrafast internal conversion process pivotal to DNA photoprotection. Base stacking rather than base pairing dominates the relaxation mechanisms in the double helix and produces long-lived states making DNA susceptible to photodamage.[74] Most of the previous discussion has centered on nucleobases and monomolecular strands of base-stacked molecules. However; this homogenous case, while a good starting point for understanding dynamics, is never replicated in natural DNA systems. In light of this, researchers have also studied heteromolecular strands which contain realistic base stacking patterns and have found that a significant fraction of excitations undergo ultrafast IC dynamics that are virtually indistinguishable to the isolated nucleobase.[75]

Seeing that monomeric relaxation is indeed prevalent in double helices containing realistic base stacking sequences, further investigation of how molecules which possess localized excitations are affected by bonding to adjacent nucleobases is a natural direction. Work to be discussed in Chapter 5 and 6 will investigate the solute-solvent and intramolecular interactions that allow the >5eV of vibrational quanta localized on the molecules following internal conversion to flow into the solvent (heat bath), permitting the DNA nucleobases to return to an equilibrium state. This work will compare relaxation in the thymine nucleobase, nucleoside, and dinucleotide. As seen in Figure 1.5, this progression to larger molecular size constitutes an increase in the vibrational degrees of freedom. This is expected to enhance the transfer of vibrational energy (i.e. heat) in inter and intra molecular degrees of freedom. Investigations of the solute-solvent and intramolecular interactions are well motivated because previous research has shown that changing the high frequency (>300cm-1) spectrum of solvent vibrational resonances

has a significant impact on vibrational cooling kinetics. Prior to this work it was commonplace to assume higher frequency resonances had little impact on vibrational energy transfer dynamics.[76]

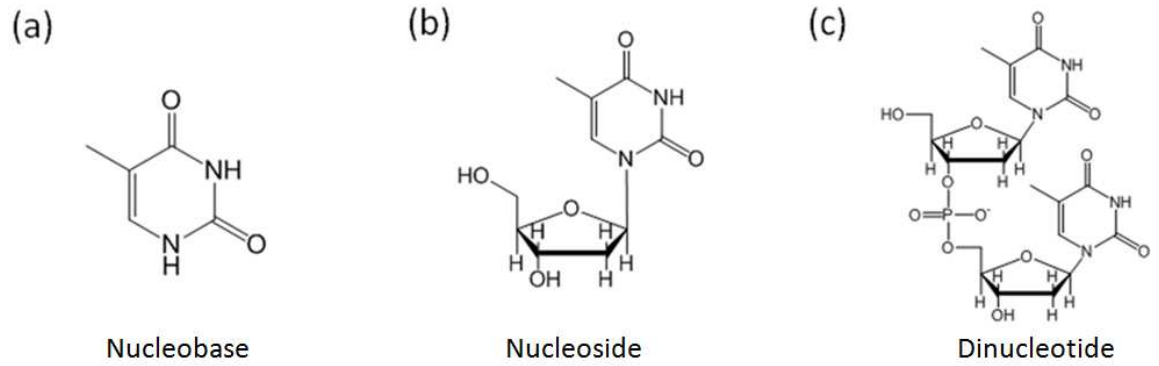

Figure 1.5. Shown are the Thymine nucleobase, nucleoside, and dinucleotide. Progression from left to right shows increasing molecular size and therefore increasing vibrational degrees of freedom. The impact on vibrational energy transfer (i.e. heat flow) due to these additional degrees of freedom will be examined.

1.5. Photoinduced Ring-Opening in Cycloalkenes

The photoinduced ring opening reaction which transforms cycloalkenes into conjugated polyenes is one of the most elementary chemical reaction processes in organic chemistry.[77,78] A cycloalkene is a closed ring of 3-8 carbon atoms possessing alternating double and single bonds for some distance around the ring. In a fully conjugated cycloalkene this pattern extends fully around the ring. For a partially conjugated cycloalkene the pattern may extend over a shorter distance. Photoinduced reactions break the bonds and distort the ring resulting in an open chain of conjugated carbon atoms. This process is illustrated in Figure 1.6. On the left in each column are the conjugated cycloalkenes, cyclohexadiene (CHD) in (a) and alpha-terpinine (α-TP) in (b). When a UV photon is absorbed by a cycloalkene, it initiates a series of sub-100fs relaxation processes which break the bonds and transform the molecule into its corresponding polyene photoproduct. This photoproduct can take on a variety of

molecular configurations, know as isomers, but the configuration which is most energetically accessible to the cycloalkene is shown. Further relaxation and thermalization after ring opening has taken place can produce alternative photoproducts; these dynamics take place on the 10-100ps time scale.[79-81]

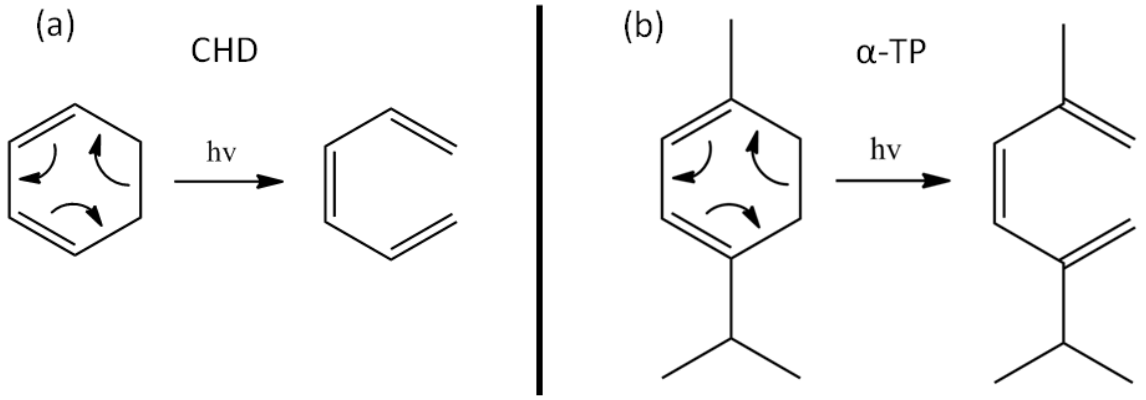

Figure 1.6. Photoinduced ring opening reaction of CHD and α-TP. These reaction schemes show only one of the possible isomers generated through ring opening. UV photon absorption by CHD (a) or α-TP (b) induces a chemical reaction which transforms the cycloalkene into a polyene photoproduct.

The Woodward-Hoffman rules use knowledge of nodes in the pi molecular orbitals to predict the type of motion involved in photoinduced ring opening processes.[82,83] Atomic orbitals can move in a conrotarty or disrotary direction in order to facilitate ring opening. The direction of motion produces a configuration which results in constructive orbital overlap. Figure 1.6(b) shows α-TP and its corresponding photoproduct. The sigma (single) bonds in α-TP in the far right carbon atoms rotate out of plane (out of the molecular plane), producing conjugation and an open ring in the resulting photoproduct. The Woodward-Hoffman rules are very powerful but also conveniently hide many of the intricacies of the physics behind these reactions.[84] The time scales and energetic paths of the photo-induced wavepacket across various potential energy surfaces prior to initiating ring opening are hidden.

In this dissertation, studies of two cycloalkenes possessing similar photoinduced reaction mechanisms will be presented, α-TP and CHD. α-TP possesses a structure very similar to CHD, as shown in Figure 1.6; however, it has additional aliphatic side groups. Similar relaxation processes should be expected in both molecules because the aliphatic substituents on α-TP weakly perturb the conjugated pi molecular orbitals of CHD and therefore have minor impact on the potential energy surfaces which drive the photo-induced reaction.[85,86] A large body of research conducted in the gas phase has found that sub-100fs internal conversion processes proceed through CIs and leave the system at a symmetry-breaking point where either the vibrationally-populated ground state of the cycloalkene or the polyene photoproduct can be reached. [24,79-81,84,85,87-93] As shown in Figure 1.7, the initial photoexcited wavepacket resides on the 1B state of CHD. Steep potential energy gradients drive this wavepacket directly towards the CI with the optically forbidden dark state 2A, this proceeds with a time constant of 55fs. The wavepacket then relaxes in the 2A potential well and encounters another CI with the 1A state, the ground state of CHD. It is at this point where the reaction can proceed to produce either CHD or hexatriene (HT), the photoproduct.

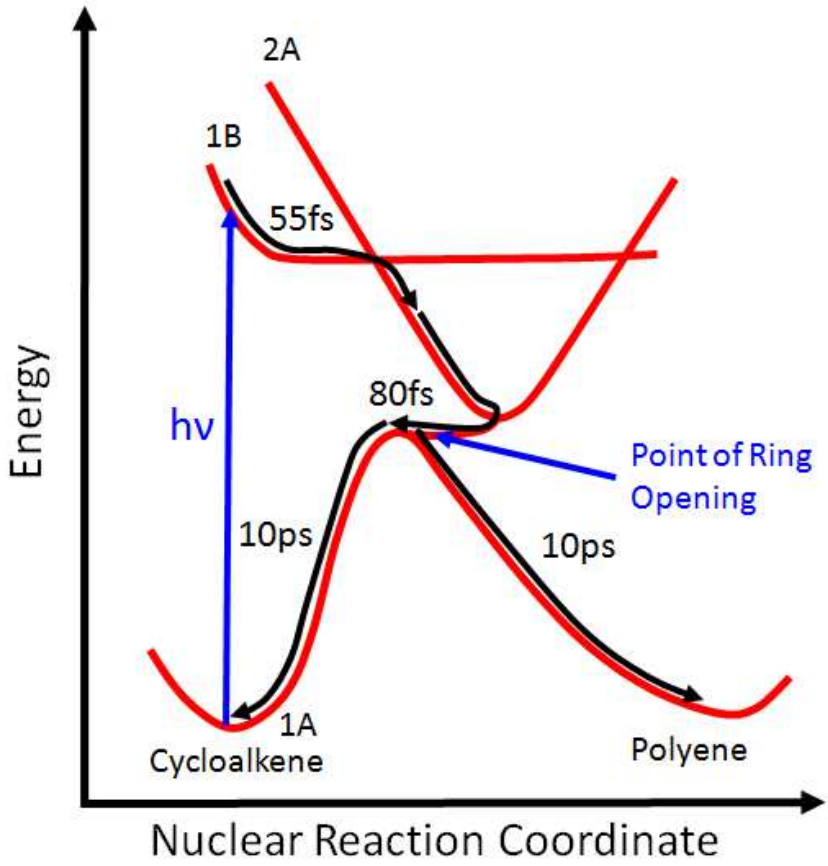

Figure 1.7. The relaxation scheme for cyclohexadiene (CHD) is shown. Photoexcitation into the 1B state initiates wavepacket motion towards a conical intersection with state 2A. State 2A then transfers population to the ground state, usually denoted 1A, within 80fs. Approximately 40% of the photoexcitations produce hexatriene (HT) in solution, whereas the yield is near 100% in the gas phase. Dynamics in α-TP are thought to follow a similar energetic scheme. Electronic states in α-TP are referred to in the same manner to facilitate comparison.

The photoinduced reaction to form HT proceeds with 100% efficiency in the gas phase[94]; however, in the condensed phase, only 40% of the photoexcited CHD molecules undergo ring opening[89,95]. Presently, the origin of this discrepancy in reaction yields between the gas phase and condensed phase is unknown.[87] Transient grating and 2DUV spectroscopies will be implemented at 265nm in effort to better understand these relaxation dynamics in solution. Previous condensed phase measurements have utilized pump-probe techniques to study the dynamics with time resolution of 100s of

femtoseconds. These studies focused on how different solvents affect the vibrational cooling and isomerization processes following the point of symmetry breaking and production of photoproducts.[79,80,91,96] Applying 2D-UV and transient grating techniques with 20fs time resolution will allow for sensitive probing of the sub-100fs internal conversion dynamics that precede ring opening in the cycloalkenes.

Relaxation processes that occur on a time scale less than 100fs hold a special place in condensed-phase studies. After absorption of a photon, the molecule and surrounding solvent reorganize to the new distribution of electron density induced by the excitation. However, this process takes time and generally occurs within 100fs of the excitation.[97,98] Traditional kinetic theories do not apply in this regime because the environment surrounding the solute has not equilibrated[99]; one outcome of commensurate electronic and nuclear relaxation in non-exponential decay dynamics. In fact, earlier experimental work demonstrated through analysis of resonance Raman excitation profiles that non-exponential dynamics exist in these systems.[92]

Controlling chemical reactions is an age-old idea and classical techniques vary the temperature, pressure, and concentration of various reactants to yield a desired outcome but offer no control of the quantum-mechanical degrees of freedom. The advent of femtosecond laser technologies and the control of pulse phase and polarization allows the possibility to control the quantum-mechanical reaction pathway of a photoinduced reaction.[100,101] Demonstration of these techniques involved genetic algorithms in which adaptive changes were made to the laser pulse properties using feedback from the experimental pathways so that the desired reaction is achieved.[102,103] These ideas have also been applied to the UV spectrum where researchers have demonstrated the ability to

control the characteristics of femtosecond UV laser pulses[104] and used computer analysis techniques to show that with properly varied fields, reaction yields of a ring opening reaction like that presented in this section can be enhanced by a factor of two[105]. However, the genetic algorithms that find the optimal pulse shapes in such experiments provide only indirect information on the underlying physics.

In order to draw physical insights from quantum control data, researchers must understand precisely how the reaction evolves and what molecular properties are linked to this evolution. The retention of wavepacket coherence during a non-radiative transition between electronic states is central to understanding such non-Markovian processes. Quantum control could potentially leverage this knowledge to 'steer' wavepackets towards specific product structures, thereby influencing the yield of products. 2D spectroscopy is important because it can distinguish relaxation-induced vibrational coherences (which mean that momentum is partially retained during the internal conversion transition) from vibrational coherences initiated by stimulated Raman processes. Coherences initiated by stimulated Raman processes possess no implication for control of quantum reaction pathways.[106] This makes 2D spectroscopy ideally suited to uncover the intricacies of the physics that drive these photochemical reactions.

This dissertation implements 2D-UV to investigate the impact of commensurate electronic and nuclear dynamics on the relaxation mechanisms of these cycloalkene-to-polyene photo-induced reactions. Comprehensive studies of one molecule have been undertaken and results published.[107] This work is presented in Chapter 7. The Moran group is now in the process of analyzing 2D spectra to uncover the interplay of electronic

and nuclear relaxation. An invited review article in *Chemical Physics* in is preparation for submission in the summer of 2013.

1.6. Structure of Dissertation

A brief overview of the material to be discussed in this dissertation will now be presented to aid readers in navigating areas of interest. This introductory chapter has provided context and background for the work to be presented in later sections. In Chapter 2, the theory behind the models and methods used in this dissertation will be discussed, including response function formalism, the reduced description of quantum mechanics, vibrational energy transfer, internal conversion and the nonlinear techniques. Chapter 3 will highlight the implementation and development of the laser pulses and spectroscopies used for the studies presented here. Especially interesting in this chapter is the discussion of a novel generation method used to produce ultrafast laser pulses at 267nm. This method follows a setup by Bradforth and coworkers[62] which was developed and used in all the experiments presented henceforth at 267nm.

From there, the dissertation will move into the studies of DNA nucleobases, Chapter 4 will present studies on the adenine nucleobase, the preliminary results from the new 2D-UV setup. The work will discuss the effect of different tautomers on the 2DUV lineshapes as well as present the delicacies of performing femtosecond spectroscopies in the UV. In Chapter 5, formalism and experimental work for studying vibrational energy transfer will be presented. Following internal conversion of the thymine excited state, >5eV of vibrational quanta exists on the ground state potential surface. This is a highly non-equilibrium state and possible explanations for temperature-independent dynamics are presented. In Chapter 6, previous methods and results are used to carefully study how

bonding to the DNA backbone and adjacent nucleobases impacts the ultrafast internal conversion dynamics. Research found that an increase in the number of vibrational degrees of freedom enhances heat transfer and tends to trap the nucleobases in their excited state while enhancing vibrational cooling in the ground state.

Chapter 7 will move into studies of electrocyclic ring opening reactions of cycloalkenes. These reactions are some of the most fundamental in organic chemistry but only recently has technology advanced to where 2D-UV can interrogate the physics behind the sub-100fs processes preceding ring opening. Along with the push to implement 2D-UV at 267nm and study a variety of systems at this wavelength, consistent work has been undertaken in the Moran laboratory to develop short laser pulses suitable for transient grating and 2D-UV spectroscopies at 200nm. Chapter 8 will present preliminary work describing the setup to produce and implement 200nm in these multidimensional spectroscopies. Finally, Chapter 9 presents concluding remarks on the accomplishments of this dissertation and the central themes of ultrafast relaxation processes driven by conical intersections and the nonlinear spectroscopies used to investigate them. Future directions in the field of research are also discussed.

1.7. References

(1) Fleming, G. R. *Chemical Applications of Ultrafast Spectroscopy*; Oxford University Press: New York, 1986.

(2) Cho, M. *Chem. Rev.* **2008**, *108*, 1331-1418.

(3) Hamm, P.; Zanni, M. T. *Concepts and Methods of 2D Infrared Spectroscopy*; Cambridge University Press: Cambridge, 2011.

(4) Jonas, D. M. *Annu. Rev. Phys. Chem.* **2003**, *54*, 425-463.

(5) Mukamel, S. *Annu. Rev. Phys. Chem.* **2000**, *51*, 691-729.

(6) Asplund, M. C.; Zanni, M. T.; Hochstrasser, R. M. *Proc. Natl. Acad. Sci.* **2000**, *97*, 8219-8224.

(7) Golonzka, O.; Khalil, M.; Demirdöven, N.; Tokmakoff, A. *Phys. Rev. Lett.* **2000**, *86*, 2154-2157.

(8) Hybl, J. D.; Albrecht, A. W.; Gallagher Faeder, S. M.; Jonas, D. M. *Chem. Phys. Lett.* **1998**, *297*, 307-313.

(9) Brixner, T.; Mancal, T.; Stiopkin, I. V.; Fleming, G. R. *J. Chem. Phys.* **2004**, *121*, 4221-4236.

(10) Cowan, M. L.; Ogilvie, J. P.; Miller, R. J. D. *Chem. Phys. Lett.* **2004**, *386*, 184-189.

(11) Anna, J. M.; Ross, M. R.; Kubarych, K. J. *J. Phys. Chem. A* **2009**, *113*, 6544-6547.

(12) Brixner, T.; Stenger, J.; Vaswani, H. M.; Cho, M.; Blankenship, R. E.; Fleming, G. R. *Nature* **2005**, *434*, 625-628.

(13) Collini, E.; Wong, C. Y.; Wilk, K. E.; Curmi, P. M. G.; Brumer, P.; Scholes, G. D. *Nature* **2010**, *463*, 644-647.

(14) Fayer, M. D. *Annu. Rev. Phys. Chem.* **2009**, *60*, 21-38.

(15) Lewis, K. L. M.; Ogilvie, J. P. *J. Phys. Chem. Lett.* **2012**, *3*, 503-510.

(16) Panitchayangkoon, G.; Hayes, D.; Fransted, K. A.; Caram, J. R.; Harel, E.; Wen, J.; Blankenship, R. E.; Engel, G. S. *Proc. Natl. Acad. Sci.* **2010**, *107*, 12766-12770.

(17) Mukamel, S.; Abramavicius, D.; Yang, L.; Zhuang, W.; Schweigert, I. V.; Voronine, D. V. *Acc. Chem. Res.* **2009**, *42*, 553-562.

(18) Bertrand, J. B.; Fabre, B.; Higuet, J.; Ruf, H. *Science (New York, N.Y.)* **2011**, *334*, 208-212.

(19) Evans, N. L.; Yu, H.; Roberts, G. M.; Stavros, V. G.; Ullrich, S. *Physical Chemistry Chemical Physics* **2012**, *14*, 10401-10409.

(20) Krause, P.; Matsika, S.; Kotur, M.; Weinacht, T. *The Journal of Chemical Physics* **2012**, *137*, 22A537-9.

(21) Schalk, O.; Boguslavskiy, A. E.; Stolow, A.; Schuurman, M. S. *Journal of the American Chemical Society* **2011**, *133*, 16451-16458.

(22) White, J. L.; Kim, J.; Petrovic, V. S.; Bucksbaum, P. H. *The Journal of Chemical Physics* **2012**, *136*, 054303-8.

(23) Wu, G.; Boguslavskiy, A. E.; Schalk, O.; Schuurman, M. S.; Stolow, A. *The Journal of Chemical Physics* **2011**, *135*, 164309-10.

(24) Kim, J.; Tao, H.; White, J. L.; Petrovic, V. S.; Martinez, T. J.; Bucksbaum, P. H. *J. Phys. Chem. A* **2012**, *116*, 2758-2763.

(25) PetroviÄ‡, V. S.; Siano, M.; White, J. L.; Berrah, N.; Bostedt, C.; Bozek, J. D.; Broege, D.; Chalfin, M.; Coffee, R. N.; Cryan, J.; Fang, L.; Farrell, J. P.; Frasinski, L. J.; Glownia, J. M.; GÃ¼hr, M.; Hoener, M.; Holland, D. M. P.; Kim, J.; Marangos, J. P.; Martinez, T.; McFarland, B. K.; Minns, R. S.; Miyabe, S.; Schorb, S.; Sension, R. J.; Spector, L. S.; Squibb, R.; Tao, H.; Underwood, J. G.; Bucksbaum, P. H. *Physical Review Letters* **2012**, *108*, 253006.

(26) Worner, H. J.; Bertrand, J. B.; Corkum, P. B.; Villeneuve, D. M. *Physical Review Letters* **2010**, *105*, 103002.

(27) Roberts, G. M.; Williams, C. A.; Young, J. D.; Ullrich, S.; Paterson, M. J.; Stavros, V. G. *Journal of the American Chemical Society* **2012**, *134*, 12578-12589.

(28) Williams, C. A.; Roberts, G. M.; Yu, H.; Evans, N. L.; Ullrich, S.; Stavros, V. G. *The Journal of Physical Chemistry A* **2012**, *116*, 2600-2609.

(29) Yu, H.; Evans, N. L.; Stavros, V. G.; Ullrich, S. *Physical Chemistry Chemical Physics* **2012**, *14*, 6266-6272.

(30) West, B. A.; Moran, A. M. *J. Phys. Chem. Lett.* **2012**, *3*, 2575-2581.

(31) West, B. A.; Womick, J. M.; Moran, A. M. *J. Chem. Phys.* **2011**, *135*, 114505.

(32) Farrow, D. A.; Qian, W.; Smith, E. R.; Ferro, A. A.; Jonas, D. M. *J. Chem. Phys.* **2008**, *128*, 144510.

(33) Lott, G. A.; Perdomo-Ortiz, A.; Utterback, J. K.; Widom, J. R.; Aspuru-Guzik, A.; Marcus, A. H. *Proc. Natl. Acad. Sci.* **2011**, *108*, 16521-16526.

(34) Rebentrost, P.; Aspuru-Guzik, A. *The Journal of Chemical Physics*, *134*, 101103-4.

(35) Ritschel, G.; Roden, J.; Strunz, W. T.; Aspuru-Guzik, A. n.; Eisfeld, A. *The Journal of Physical Chemistry Letters*, *2*, 2912-2917.

(36) Nalbach, P. I., A; GR Fleming; Thorward, M *New Journal of Physics* **2011**, *13*.

(37) Kubo, R. *Journal of Physical Society of Japan* **1957**, *12*, 570.

(38) Sobolewski, A. L.; Domcke, W. *Eur. Phys. J. D* **2002**, *20*, 369-374.

(39) Worth, G. A.; Cederbaum, L. S. *Annu. Rev. Phys. Chem.* **2004**, *55*, 127-158.

(40) Sterling, B.; Charles, G. D., III; Margaret, M. M.; Henry, C. K.; AIP: 1998; Vol. 69, p 1207-1223.

(41) Spence, D. E.; Kean, P. N.; Sibbett, W. *Opt. Lett.* **1991**, *16*, 42-44.

(42) Strickland, D.; Mourou, G. *Optics Communications* **1985**, *56*, 219-221.

(43) Fork, R. L.; Greene, B. I.; Shank, C. V.; AIP: 1981; Vol. 38, p 671-672.

(44) Eimerl, D.; Davis, L.; Velsko, S.; Graham, E. K.; Zalkin, A. *Journal of Applied Physics* **1987**, *62*, 1968-1983.

(45) Riedle, E.; Beutter, M.; Lochbrunner, S.; Piel, J.; Schenkl, S.; Spörlein, S.; Zinth, W. *Applied Physics B: Lasers and Optics* **2000**, *71*, 457-465.

(46) Goodno, G. D.; Dadusc, G.; Miller, R. J. D. *J. Opt. Soc. Am. B* **1998**, *15*, 1791-1794.

(47) Maznev, A. A.; Nelson, K. A.; Rogers, J. A. *Opt. Lett.* **1998**, *23*, 1319-1321.

(48) Pollard, W. T.; Dexheimer, S. L.; Wang, Q.; Peteanu, L. A.; Shank, C. V.; Mathies, R. A. *The Journal of Physical Chemistry* **1992**, *96*, 6147-6158.

(49) Arnett, D. C.; Moser, C. C.; Dutton, P. L.; Scherer, N. F. *The Journal of Physical Chemistry B* **1999**, *103*, 2014-2032.

(50) Ishikawa, H.; Kwak, K.; Chung, J. K.; Kim, S.; Fayer, M. D. *Proceedings of the National Academy of Sciences* **2008**, *105*, 8619-8624.

(51) Zheng J, K. K., Xie J, Fayer MD *Science* **2006**, *313*, 1951-1955.

(52) Junrong Zheng, K. K., John Asbury*, Xin Chen, Ivan R. Piletic, M. D. Fayer *Science* **2005**, *309*,1338-1343.

(53) Womick, J. M.; Moran, A. M. *The Journal of Physical Chemistry B*, *115*, 1347-1356.

(54) Jennifer P. Ogilvie, K. J. K. In *Advances in Atomic, Molecular, and Optical Physics*; Elsevier: 2009, p 249-321.

(55) West, B. A.; Moran, A. M. *The Journal of Physical Chemistry Letters*, *3*, 2575-2581.

(56) Abramavicius, D.; Jiang, J.; Bulheller, B. M.; Hirst, J. D.; Mukamel, S. *J. Am. Chem. Soc.* **2010**, *132*, 7769-7775.

(57) Selig, U.; Schleussner, C.-F.; Foerster, M.; Langhojer, F.; Nuernberger, P.; Brixner, T. *Opt. Lett.* **2010**, *35*, 4178-4180.

(58) Tseng, C.-H.; Matsika, S.; Weinacht, T. C. *Opt. Express* **2009**, *17*, 18788-18793.

(59) Tseng, C.-H.; Sándor, P.; Kotur, M.; Weinacht, T. C.; Matsika, S. *J. Phys. Chem. A* **2012**, *116*, 2654-2661.

(60) West, B. A.; Womick, J. M.; Moran, A. M. *J. Chem. Phys.* **2011**, *135*, 114505:1-114505:9.

(61) West, B. A.; Womick, J. M.; Moran, A. M. *J. Phys. Chem. A* **2011**, *115*, 8630-8637.

(62) Jailaubekov, A. E.; Bradforth, S. E. *Appl. Phys. Lett.* **2005**, *87*, 021107:1-021107:3.

(63) Rosker, M. J.; Dantus, M.; Zewail, A. H. *Science* **1988**, *241*, 1200-1202.

(64) Pfeifer, T. S., C.; Gerber,G. *Reports on Progress in Physics* **2006**, *69*, 443-505.

(65) Corkum, P. B. K., F. *Nature Physics* **2007**, *3*, 381-387.

(66) Kapteyn, H.; Cohen, O.; Christov, I.; Murnane, M. *Science* **2007**, *317*, 775-778.

(67) Schweigert, I. V.; Mukamel, S. *The Journal of Chemical Physics* **2008**, *128*, 184307-11.

(68) Miller, D. L.; Weinstock, M. A. *Journal of the American Academy of Dermatology* **1994**, *30*, 774-778.

(69) Kraemer, K. H. *Proceedings of the National Academy of Sciences* **1997**, *94*, 11-14.

(70) Crespo-HernÃ¡ndez, C. E.; Cohen, B.; Hare, P. M.; Kohler, B. *Chemical Reviews* **2004**, *104*, 1977-2020.

(71) Schwalb N.K., T. F. *Journal of American Chemical Society* **2007**, *129*, 9272-73.

(72) Sobolewski, A. L.; Domcke, W. *Physical Chemistry Chemical Physics* **2004**, *6*, 2763-2771.

(73) Schrader, T. E.; Koller, F. O.; Gilch, P.; Crespo-Hernandez, C. E. *Science (New York, N.Y.)* **2007**, *315*, 625-629.

(74) Middleton, C. T.; de La Harpe, K.; Su, C.; Law, Y. K.; Crespo-Hernández, C. E.; Kohler, B. *Annu. Rev. Phys. Chem.* **2009**, *60*, 217-239.

(75) de La Harpe, K.; Kohler, B. *The Journal of Physical Chemistry Letters* **2011**, *2*, 133-138.

(76) Middleton, C. T.; Cohen, B.; Kohler, B. *The Journal of Physical Chemistry A* **2007**, *111*, 10460-10467.

(77) Nenov, A.; Kölle, P.; Robb, M. A.; de Vivie-Riedle, R. *J. Org. Chem.* **2010**, *75*, 123-129.

(78) Turro, N. J. *Modern Molecular Photochemistry*; University Science Books: Sausalito, 1991.

(79) Anderson, N. A.; Pullen, S. H.; Walker, L. A.; Shiang, J. J.; Sension, R. J. *J. Phys. Chem. A* **1998**, *102*, 10588-10598.

(80) Lochbrunner, S.; Fuss, W.; Schmid, W. E.; Kompa, K. L. *J. Phys. Chem. A* **1998**, *102*, 9334-9344.

(81) Pullen, S. H.; Anderson, N. A.; Walker, L. A.; Sension, R. J. *J. Chem. Phys.* **1998**, *108*, 556-563.

(82) Van der Lugt, W. T. A. M.; Oosterhoff, L. J. *J. Am. Chem. Soc.* **1969**, *91*, 6042-6049.

(83) Woodward, R. B.; Hoffmann, R. *Angew. Chem. Int. Ed. Engl.* **1969**, *8*, 781-853.

(84) Reid, P. J.; Lawless, M. K.; Wickham, S. D.; Mathies, R. A. *J. Phys. Chem.* **1994**, *98*, 5597-5606.

(85) Garavelli, M.; Page, C. S.; Celani, P.; Olivucci, M.; Schmid, W. E.; Trushin, S. A.; Fuss, W. *J. Phys. Chem. A* **2001**, *105*, 4458-4469.

(86) Kosma, K.; Trushin, S. A.; FuB, W.; Schmid, W. E. *Phys. Chem. Chem. Phys.* **2009**, *11*, 172-181.

(87) Deb, S.; Weber, P. M. *Annu. Rev. Phys. Chem.* **2011**, *62*, 19-39.

(88) Fuß, W.; Schikarski, T.; Schmid, W. E.; Trushin, S.; Kompa, K. L. *Chem. Phys. Lett.* **1996**, *262*, 675-682.

(89) Kosma, K.; Trushin, S. A.; Fuß, W.; Schmid, W. E. *Phys. Chem. Chem. Phys.* **2009**, *11*, 172-181.

(90) Kuthirummal, N.; Rudakov, F. M.; Evans, C. L.; Weber, P. M. *J. Chem. Phys.* **2006**, *125*, 133307.

(91) Pullen, S. H.; Walker, L. A.; Donovan, B.; Sension, R. J. *Chem. Phys. Lett.* **1995**, *242*, 415-420.

(92) Trulson, M. O.; Dollinger, G. D.; Mathies, R. A. *J. Chem. Phys.* **1989**, *90*, 4274-4281.

(93) Njoya, O.; Matsika, S.; Weinacht, T. *ChemPhysChem*, n/a-n/a.

(94) Rudakov, F.; Weber, P. M. *Chem. Phys. Lett.* **2009**, *470*, 187-190.

(95) Minaard, N. G.; Havinga, E. *Recl. Trav.Chim. Pays. Bas.* **1973**, *92*, 1315-1320.

(96) Pullen, S. H.; Anderson, N. A.; Walker, L. A.; Sension, R. J. *J. Chem. Phys.* **1998**, *108*, 556.

(97) Mukamel, S. *Principles of Nonlinear Optical Spectroscopy*; Oxford University Press: New York, 1995.

(98) Nitzan, A. *Chemical Dynamics in Condensed Phases*; Oxford University Press: Oxford, 2006.

(99) Chandler, D. *Introduction to Modern Statistical Mechanics*; Oxford University Press: New York, 1987.

(100) Dantus, M.; Lozovoy, V. V. *Chemical Reviews* **2004**, *104*, 1813-1860.

(101) Gerber, G. *Chemphyschem* **2003**, *4*, 418-438.

(102) Baumert, T.; Bergt, M.; Brixner, T.; Kiefer, B. *Science (New York, N.Y.)* **1998**, *282*, 919-922.

(103) Brixner, T.; Damraurer, N. H.; Niklaus, P.; Gerber, G. *Nature* **2001**, *414*, 57-60.

(104) Pearson, B. J.; Weinacht, T. C. *Opt. Express* **2007**, *15*, 4385-4388.

(105) Carroll, E. C.; White, J. L.; Florean, A. C.; Bucksbaum, P. H.; Sension, R. J. *The Journal of Physical Chemistry A* **2008**, *112*, 6811-6822.

(106) Peters, W. K.; Jonas, D. M. *Proceedings of the National Academy of Sciences - PNAS*, *110*, 1203-1208.

(107) West, B. A.; Molesky, B. P.; Montoni, N. P.; Moran, A. M. *New Journal of Physics*, *15*, 025007.

Chapter 2 . Merging Condensed Phase Dynamics and Nonlinear Optical Spectroscopy

2.1. From Fermi's Golden Rule to Quantum Time Correlation Functions

Quantum relaxation processes in condensed phases generally originate in collective effects associated with an extremely large number of degrees of freedom. Statistical approaches in which the Hamiltonian is partitioned into a system and bath are often employed because the explicit treatment of all electronic and nuclear coordinates is impractical. Such reduced descriptions follow the dynamics in a handful of "interesting" system degrees of freedom, which undergo fluctuations imposed by thermally driven motions in the bath. These fluctuations induce bandwidth into macroscopic observables, such as the absorption line shapes and non-radiative transition rates, by coupling to the electronic states of the molecule. With each molecule in a solution experiencing a unique environment, one can envision that each member of the ensemble has slightly different electronic properties. It is now natural to question if following the properties, such as the ground to excited state transition frequency, of a single molecule in time would produce a probability distribution that resembles the snapshot of all molecular transition frequencies at one instant in time. In other words, is the time average of a molecular transition frequency equal to the ensemble average at a single point in time? A system with this property is said to be ergodic.[1]

One of the most common tools of time dependent quantum mechanics are time correlation functions (TCFs). They are commonly used to describe quasi-random

(stochastic) motions and irreversible processes in condensed phase dynamics. This chapter will introduce the fundamentals of TCFs and how they are related to spectroscopic observables of the systems being studied. One key advantage of TCFs is that they are able to represent a large number of degrees of freedom in the surroundings (i.e. the bath) with only a small number of variables through a probabilistic treatment. These variables represent the characteristics of the bath in the condensed phase.

The following section introduces Fermi's Golden rule by calculating the transition rate between initial state $|m\rangle$ and final state $|n\rangle$ due to a sinusoidal perturbation, which simulates an applied electromagnetic field with angular frequency $\omega = 2\pi\nu$. This rule will then be recast in the form of a TCF to aid the reader in understanding their origin and application. The derivation of Fermi's Golden Rule can be found in Reference [2] and time correlation functions in Reference [3]. The first order coefficient to basis state $|n\rangle$ due to the applied perturbation at t=0 assuming initial population in state $|m\rangle$ is given by:

$$c_n^{(1)} = -\frac{i}{\hbar}\int_0^t \hat{V}_{nm}(t')e^{i\omega_{nm}t'}dt' \tag{2.1}$$

where ω_{nm} is proportional to the energy gap between states $|m\rangle$ and $|n\rangle$. The time dependent perturbation is defined as

$$\hat{V}_{nm}(t') = 2V_{nm}\cos(\omega t') = V_{nm}(e^{i\omega t'} + e^{-i\omega t'}) \tag{2.2}$$

for $t \geq 0$. If this expression is inserted into Equation 2.1, first order coefficients are calculated as

$$c_n^{(1)}(t) = -\frac{i}{\hbar}V_{nm}\int_0^t (e^{i\omega t'} + e^{-i\omega t'})e^{(i\omega_{nm}t')}dt' = \frac{-iV_{nm}}{\hbar}\left[\frac{e^{i(\omega_{nm}+\omega)t}-1}{i(\omega_{nm}+\omega)} + \frac{e^{i(\omega_{nm}-\omega)t}-1}{i(\omega_{nm}-\omega)}\right] \tag{2.3}$$

Assuming that states $|m\rangle$ and $|n\rangle$ are separate molecular electronic energy levels and the perturbative radiation is in the ultraviolet region of the electromagnetic spectrum, the period of the waveform will be on the order of 1 fs. When the applied field is on or near resonance with the energy gap, ω_{nm} (i.e., $\omega \cong \omega_{nm}$), the right term in Equation 2.3 will dominate the first order coefficient for state $|n\rangle$. The probability of finding the system in state $|n\rangle$ at time "*t*" if initially in state $|m\rangle$ at $t = 0$, is given by square of the first order coefficient.

$$P_n(t) = \left|c_n^{(1)}(t)\right|^2 = \left|\frac{-iV_{nm}}{\hbar}\left[\frac{e^{i(\omega_{nm}-\omega)t}-1}{i(\omega_{nm}-\omega)}\right]\right|^2 = \frac{4\left|V_{nm}\right|^2}{\hbar^2(\omega_{nm}-\omega)^2}\sin^2\left[(\omega_{nm}-\omega)t/2\right] \qquad (2.4)$$

Euler's formula was used in the simplification. A plot of $P_n(t)$ versus $\omega_{nm} - \omega$ at various values of "*t*" shown in Figure 2.1 demonstrates the intuitive results from Equation 2.4. The probability of finding the system in state $|n\rangle$ increases with time as long as the applied field is on or near on resonance with the energy gap between states $|m\rangle$ and $|n\rangle$.

This result can also be interpreted by considering that at short times the electromagnetic field has gone through a small number of optical cycles. This causes uncertainty in the center wavelength of the applied field and therefore increases the bandwidth of the perturbation, the frequency range over which a transition can be initiated. After the perturbation has been 'turned on' for a longer period of time, it possesses a more well-defined center wavelength and a smaller bandwidth, which in turn reduces the probability of an off-resonant transition.

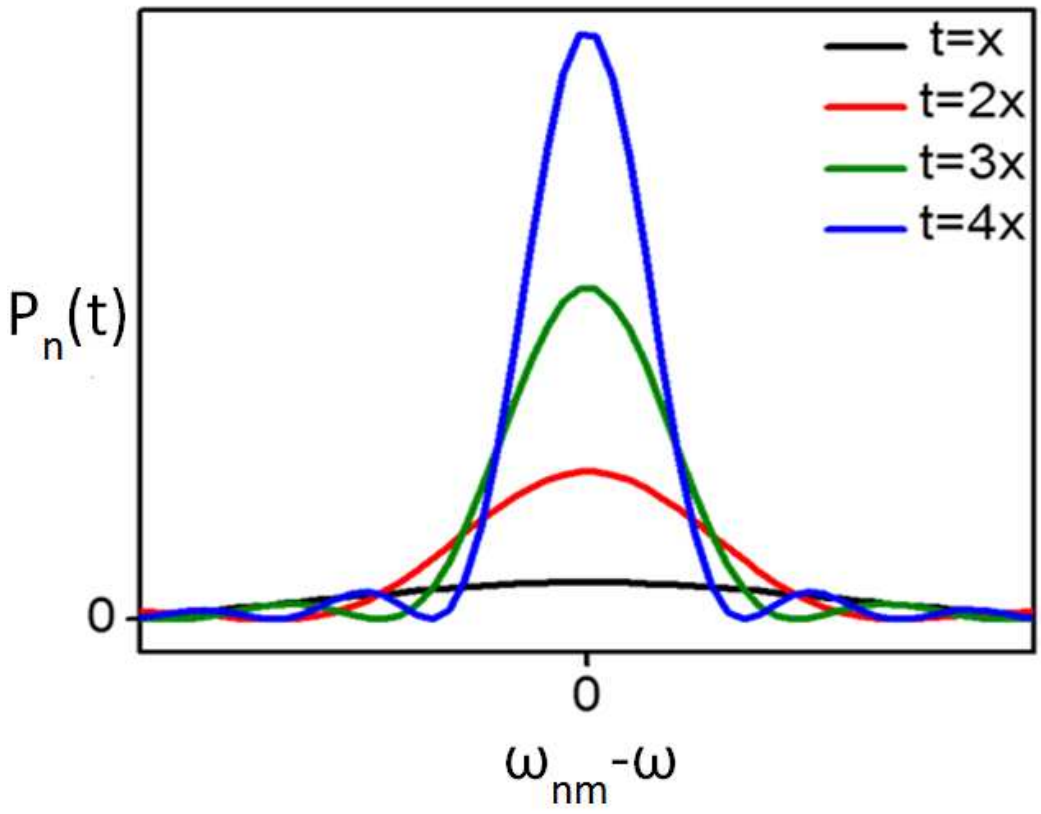

Figure 2.1. The probability of finding the system in state $|n\rangle$ at time "*t*" if initially residing in state $|m\rangle$ at $t=0$ as calculated by Equation 2.4. As "*t*" increases, the probability of being found in state $|n\rangle$ increases as long as the perturbative radiation is near resonance with ω_{nm}.

To obtain a 'steady state' solution that describes the behavior of the system for times long after the perturbation is turned on, the limit of Equation 2.4 as time approaches infinity is given by

$$\lim_{t\to\infty} P_n(t\to\infty) = \lim_{t\to\infty} \frac{4|V_{nm}|^2 \sin^2[(\omega_{nm}-\omega)t/2]}{\hbar^2(\omega_{nm}-\omega)^2} = \frac{2\pi t|V_{nm}|^2}{\hbar^2}\delta(\omega_{nm}-\omega) \qquad (2.5)$$

Equation 2.5 states that in the limit of long time a transition from state $|m\rangle$ to $|n\rangle$ can only be initiated if the frequency of the driving electromagnetic field exactly matches that

of the energy gap, ω_{nm}, between the two states. Taking the derivative of Equation 2.5 yields the steady state transition rate $k_{nm}(\omega)$ due to the perturbation.

$$k_{nm}(\omega) = \frac{\partial}{\partial t} P_n(t \to \infty) = \frac{2\pi |V_{nm}|^2}{\hbar^2} \delta(\omega_{nm} - \omega) \tag{2.6}$$

For this rate formula to be applied to condensed phases, transitions from a number of thermally populated initial states to a continuum of final states must be simulated. Summing rates from all initial states m to all final states n gives the total transition rate for such a system.

$$k_{Total}(\omega) = \sum_m \sum_n P_m k_{nm} \tag{2.7}$$

The probability of initially residing in state m at equilibrium is given by

$$P_m = \frac{e^{-\omega_m / k_B T}}{\sum_m e^{-\omega_m / k_B T}} \tag{2.8}$$

By substituting Equation 2.6 and 2.8 into 2.7 one obtains the expression for the total transition rate.

$$k_{Total}(\omega) = \frac{2\pi}{\hbar^2} \sum_m \sum_n P_m |V_{nm}|^2 \delta(\omega_{nm} - \omega) \tag{2.9}$$

Equation 2.9 is Fermi's Golden Rule, while this formula has been derived in the context of an applied electromagnetic perturbation to an interacting system, it is generally applicable to any process in which a term in the Hamiltonian is treated perturbatively (e.g. internal conversion, energy transfer, and electron transfer). The perturbation, $\hat{H}'$, couples the eigenstates of a reference Hamiltonian, m and n and the rate formula is more generally written as

$$k_{Total} = \frac{2\pi}{\hbar^2} \sum_m \sum_n P_m \left| H'_{nm} \right|^2 \delta(\omega_{nm}) \tag{2.10}$$

Equation 2.10 expresses Fermi's Golden Rule as a sum over states. Such an analytic treatment is possible in a system with a small number of degrees of freedom; however, in condensed phases, it is not always practical to carry out a sum over all quantum states. A reduced description is required. For ergodic systems, this same rate equation can be written as a time correlation function instead of an ensemble average.[3]

In condensed phase systems, the energy gap between states m and n fluctuates because of system-bath interactions. Thermal motion of the surrounding environment perturbs the system and creates inhomogeneity throughout the ensemble. Quantifying these fluctuations utilizing quantum time correlation functions allows for recasting of Equation 2.10 into a form that treats the system bath interactions with a small number of variables as opposed to an ensemble summation. To begin, Fermi's Golden Rule (Equation 2.10) is rewritten as

$$k_{Total} = \frac{2\pi}{\hbar^2} \sum_{mn} P_m \left| H'_{nm} \right|^2 \delta(\omega_{mn}) \tag{2.11}$$

where H' represents the perturbative part of the Hamiltonian that couples initial states and final states, m and n. These are eigenstates of the reference Hamiltonian H_0. Using the following definition of the delta function

$$\delta(\omega) = \frac{1}{2\pi} \int_{-\infty}^{\infty} dt \exp(i\omega t) \tag{2.12}$$

the rate equation can be written as

$$k = \frac{1}{\hbar^2}\sum_{mn} P_m \left|H'_{nm}\right|^2 \int_{-\infty}^{\infty} dt \exp\left(i\omega_{mn}t\right) \tag{2.13}$$

Equation 2.13 can be rewritten by expanding the coupling coefficient of the perturbing Hamiltonian, giving

$$k_{mn} = \frac{1}{\hbar^2}\sum_{mn} p_m \int_{-\infty}^{\infty} dt \left\langle m\middle|\hat{H}'\middle|n\right\rangle\left\langle n\middle|\hat{H}'\middle|m\right\rangle \exp\left(i\omega_{mn}t\right) \tag{2.14}$$

This can be further rewritten as

$$k_{mn} = \frac{1}{\hbar^2}\sum_{mn} p_m \int_{-\infty}^{\infty} dt \left\langle m\middle|\hat{H}'\middle|n\right\rangle\left\langle n\middle|\exp\left(i\omega_n t\right)\hat{H}'\exp\left(-i\omega_m t\right)\middle|m\right\rangle \tag{2.15}$$

Propagators in the interaction picture are given by

$$\left\langle m\middle|\exp\left(i\omega_m t\right) = \left\langle m\middle|\exp\left(i\hat{H}_0 t/\hbar\right)\right.\right. \tag{2.16}$$

$$\left\langle n\middle|\exp\left(i\omega_n t\right) = \left\langle n\middle|\exp\left(i\hat{H}_0 t/\hbar\right)\right.\right. \tag{2.17}$$

Equation 2.15 then takes the following form

$$k_{mn} = \frac{1}{\hbar^2}\sum_{mn} p_m \int_{-\infty}^{\infty} dt \left\langle m\middle|\hat{H}'\middle|n\right\rangle\left\langle n\middle|\exp\left(i\hat{H}_0 t/\hbar\right)\hat{H}'\exp\left(-i\hat{H}_0 t/\hbar\right)\middle|m\right\rangle \tag{2.18}$$

Using the definition of the time evolution operator, the following expression for the total transition rate is obtained, cast in terms of a quantum time correlation function.

$$k = \frac{1}{\hbar^2}\sum_{m} p_m \int_{-\infty}^{\infty} dt \left\langle m\middle|\hat{H}'\hat{H}'(t)\middle|m\right\rangle = \frac{1}{\hbar^2}\int_{-\infty}^{\infty} dt \left\langle \hat{H}'(t)\hat{H}'(0)\right\rangle \tag{2.19}$$

Note that the summation over initially populated states is inherent in the final expression, whereas the sum over final states has been eliminated.

2.2. Properties of Correlation Functions

Correlation functions are powerful tools for describing the steady state fluctuation dynamics of a system. They provide a measure of correlation between system observables at different points in time. Stochastic motions wash out this correlation over time; the time scale and amplitude of these fluctuations are contained in the parameters of the correlation function. The following section will present properties and physical interpretation of TCFs, this information can be found in References[3-6]. The most fundamental representation of a correlation function is given by

$$C_{AA}(t,t') = \left\langle A(t)\,A(t')\right\rangle \tag{2.20}$$

where A represents any arbitrary Hermitian operator defined in the space of the system. This function is technically an autocorrelation since it correlates the same observable value at different points in time. Classically, this function can be represented as a distribution in position and momentum space,

$$C_{AA}(t,t') = \int d\mathbf{p}\int d\mathbf{q} A(\mathbf{p},\mathbf{q};t)\,A(\mathbf{p},\mathbf{q};t')\rho(\mathbf{p},\mathbf{q}) \tag{2.21}$$

where $\rho(\mathbf{p},\mathbf{q})$ represents the canonical probability distribution and is given by

$$\rho = \frac{e^{\beta H}}{Z} \tag{2.22}$$

The probability distribution describes the thermal occupation of position and momentum space based off of the system Hamiltonian that sets the potential energy landscape. Equation 2.21 can be compared to the quantum correlation function which is a sum over a set of thermally populated states instead of a continuous distribution of position and momentum.

The quantum time correlation function involves the equilibrium (thermal) average over a product of Hermitian operators evaluated at two times. The quantum correlation function is given by

$$C_{AA}(t,t') = \sum_n p_n \langle n | \hat{A}(t) \hat{A}(t') | n \rangle \tag{2.23}$$

where p_n is the thermal occupation of $|n\rangle$ given by

$$\rho_n = \frac{e^{-\beta E_n}}{Z} \tag{2.24}$$

and Z is the quantum partition function. As previously noted the thermal average is implicit and emphasized in writing a correlation function.

This dissertation makes exclusive use of the interaction picture of quantum mechanics, where the dynamics of the system are fully governed by the reference Hamiltonian between interactions with the perturbation. In the case of having a time independent Hamiltonian, the correlation function can be simplified as follows and this representation will be used in future derivations and sections.

$$\begin{aligned} C_{\hat{A}\hat{A}}(t,t') &= \sum_n p_n \langle n | U^{\dagger}(t) \hat{A} U(t-t') \hat{A} U(t') | n \rangle \\ &= \sum_n p_n \langle n | \hat{A} U(t-t') \hat{A} | n \rangle e^{-i\omega_n (t-t')} \\ &= \sum_{nm} p_n \langle n | \hat{A} | m \rangle \langle m | \hat{A} | n \rangle e^{-i\omega_{nm}(t-t')} \\ C_{\hat{A}\hat{A}}(\tau) &= \sum_{nm} p_n \left| \hat{A}_{nm} \right|^2 e^{-i\omega_{nm}(\tau)} \end{aligned} \tag{2.25}$$

The final expression says that memory of the value of the observable, A, is lost due to a sum over many oscillatory functions with incommensurate frequencies. In other words, irreversible relaxation is generally found in systems with many thermally populated states.

In Equation 2.23, when $t = t'$, the values are perfectly correlated and $C_{AA}(t = t') = \langle A^2 \rangle$. However, after ample time (i.e. $t >> t'$) has permitted the stochastic fluctuations to randomize the values of the observables, $C_{AA}(t,t) = \langle A \rangle^2$. The time scale of this decay reflects the persistence of "memory" in the system. A graphical representation of correlation function decay is shown in Figure 2.2. The initial value of the correlation function is independent of time.

Since correlation functions represent *equilibrium* dynamics of a system, they are independent of absolute time and only depend on the time interval between observation points, τ.

$$C_{AA}(t,t') = C_{AA}(t-t',0) = C_{AA}(\tau) \tag{2.26}$$

To show this, consider the correlation function written with the use of the quantum time evolution operator, recall this is in the interaction picture and observables propagate in time according to the time independent part of the Hamiltonian, H_0.

$$\langle A(t)\,A(t')\rangle = \sum_n p_n \langle n|U^\dagger(t)\,\hat{A}U(t-t')\,\hat{A}U(t')|n\rangle \tag{2.1}$$

Recalling that the trace of a product of matrices is invariant to cyclic permutation Equation 2.27 can be rewritten as

$$\langle A(t)\,A(t')\rangle = \sum_n p_n \langle n|U^\dagger(t-t')\,\hat{A}U(t-t')\,\hat{A}|n\rangle \tag{2.2}$$

or

$$\langle A(t)\,A(t')\rangle = \langle A(t-t')\,A(0)\rangle \tag{2.3}$$

Thus showing that the quantum time correlation function is only dependent on the time interval between observations of the system variable, denoted by operator A.

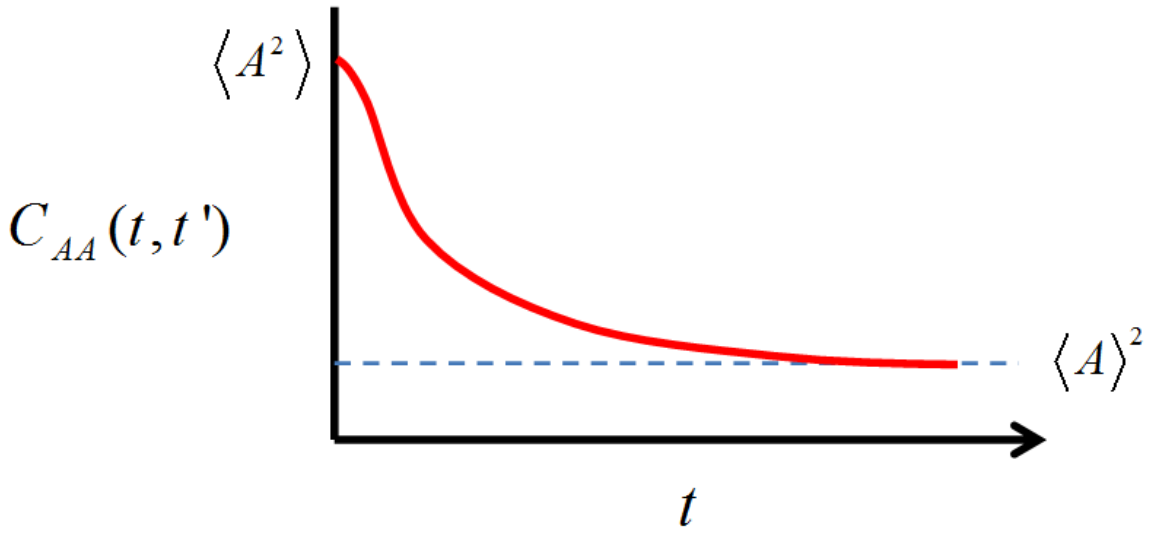

Figure 2.2. The correlation function $C_{AA}(t,t')$ is initially equal to the mean square value of the observable $\langle A^2 \rangle$. However, after sufficient time has allowed stochastic motions to dephase the correlation between the different time values, the correlation function decays to the square of the mean value of A. Spectroscopic line shapes and transition rates originate in the time scale and functional form of this decay. This plot is intentionally drawn to exhibit non-exponential behavior to underscore the point that the decays may assume a fairly complex functional form.

The spectral density can also be defined as the frequency domain correlation function. The spectral density is a direct representation of the thermal population of nuclear motions which influence spectroscopic observables and induce macroscopic dephasing.

$$C_{AA}(\omega) = \int_{-\infty}^{\infty} dt \exp(i\omega t) C_{AA}(t) \tag{2.4}$$

For a time independent Hamiltonian the spectral density can be directly calculated by rewriting the correlation function as follows,

$$
\begin{aligned}
C_{AA}(t) &= \left\langle A(t)\,A(0)\right\rangle = \sum_{n} p_n \left\langle n\left|U^{\dagger}(t)\,\hat{A}U(t)\,\hat{A}\right|n\right\rangle \\
&= \sum_{kmn} p_n \left\langle n|k\right\rangle\left\langle k\left|\hat{A}\right|m\right\rangle\left\langle m\left|\hat{A}\right|n\right\rangle \exp\left[i\left(E_k - E_m\right)t/\hbar\right] \\
&= \sum_{mn} p_n \left|\left\langle n\left|\hat{A}\right|m\right\rangle\right|^2 \exp\left[i\left(E_n - E_m\right)t/\hbar\right]
\end{aligned}
\tag{2.5}
$$

then taking the Fourier transform

$$
\begin{aligned}
C_{AA}(\omega) &= \sum_{mn} p_n \left|A_{nm}\right|^2 \int_{-\infty}^{\infty} dt \exp\left[i\left(\omega - \omega_{mn}\right)t\right] \\
&= 2\pi \sum_{mn} p_n \left|A_{nm}\right|^2 \delta\left(\omega - \omega_{mn}\right)
\end{aligned}
\tag{2.6}
$$

This expression looks very similar to that for Fermi's Golden Rule (Equation 2.10) obtained using first order perturbation theory. The Fourier transform of time correlation functions gives a rate of transition between thermally populated states. Physically, this can be interpreted as the spectrum of bath modes which can donate or receive quanta of vibrational energy to induce relaxation in the sample.

2.3. Cumulant Expansions in Spectroscopy and Dynamics

It is desirable to express the correlation function in a form that can be incorporated into expressions for simulating radiative and non-radiative processes as functions of experimentally accessible parameters. To obtain such a TCF, frequency fluctuations are considered in a general way. The argument applies to any system in which a frequency is subject to stochastic noise (e.g., harmonic oscillator, electronic states in a molecule, etc).[3] The following equation captures this phenomenon.

$$
\omega(t) = \omega_0 + \delta\omega(t) \tag{2.7}
$$

where ω_0 is the average transition frequency and $\delta\omega(t)$ is the fluctuation about that center frequency, thus simulating the noise. This process is qualitatively illustrated in

Figure 2.3. The advantage of using time correlation functions is that instead of summing over an entire ensemble of states to simulate relaxation phenomena, the fluctuations induced by these motions can be followed in time using only two parameters; Δ represents the amplitude of the fluctuations and Λ^{-1} represents their relaxation time scale. It will be shown that the relative values of these two parameters can have substantial impact on both spectroscopic line shapes and mechanisms of non-radiative transitions.

Kubo's cumulant expansion approach is a quantitative treatment of such fluctuation and can be motivated by first considering a physical process with oscillatory behavior for which the complex amplitude is written as $a(t) = |a| \exp(i\omega t)$.[7] The time derivative of the complex amplitude for such a system is trivial; however, the equation of motion becomes interesting when the frequency undergoes stochastic fluctuations

$$\frac{da(t)}{dt} = -i\omega(t)a(t) \tag{2.8}$$

In order to solve for $a(t)$ equation 2.34 is integrated to obtain

$$a(t) = a_0 \exp\left[-i\int_0^t dt'\omega(t')\right] \tag{2.1}$$

Now the correlation function for $a(t)$ is calculated as follows. This representation of the integral is a pivotal step in understanding how to mathematically incorporate a stochastic variable such as $\omega(t)$ in a time correlation function. The problem at hand is seen clearly by pulling the mean value of the frequency out of the time average.

$$\frac{\langle a^*(0)a(t)\rangle}{|a_0|^2} = \left\langle \exp\left[-i\int_0^t dt'\omega(t')\right]\right\rangle = \exp(-i\omega_0 t)\left\langle \exp\left[-i\int_0^t dt'\delta\omega(t')\right]\right\rangle \qquad (2.2)$$

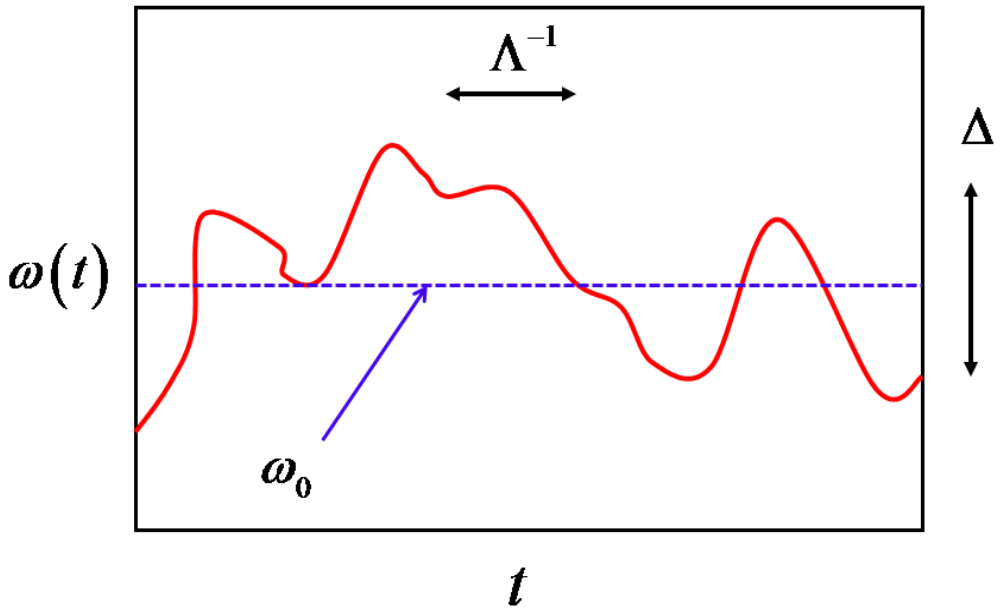

Figure 2.3. Fluctuations in a molecular energy gap are caused by random thermal motions of the surrounding environment. Two parameters, Δ and Λ^{-1}, are used to describe the fluctuation amplitude and the timescale of fluctuation relaxation, respectively.

The challenge is the evaluation of a time averaged exponential with a noisy argument. Evaluating the integral containing the stochastic variable $\delta\omega$ requires the cumulant expansion technique. Before evaluating equation 2.36, a brief introduction to the cumulant expansion is presented.

To obtain a statistical description of any random variable x, the moments of x: $\langle x \rangle, \langle x \rangle^2, \ldots$ must be characterized. The average of an exponential of x can then be expressed as

$$\left\langle e^{ikx} \right\rangle = \sum_{n=0}^{\infty} \frac{(ik)^n}{n!} \left\langle x^n \right\rangle \tag{2.3}$$

This expression can alternatively be expressed in cumulants, $c_n(x)$, as

$$\left\langle e^{ikx} \right\rangle = \exp\left(\sum_{n=1}^{\infty} \frac{(ik)^n}{n!} c_n(x) \right) \tag{2.4}$$

where the first several cumulants are: $c_1(x)$, mean; $c_2(x)$, variance, $c_3(x)$, skewness.

$$\begin{aligned} c_1(x) &= \langle x \rangle \\ c_2(x) &= \left\langle x^2 \right\rangle - \langle x \rangle^2 \\ c_3(x) &= \left\langle x^3 \right\rangle - 3\langle x \rangle \langle x \rangle^2 + 2\left\langle x^3 \right\rangle \end{aligned} \tag{2.5}$$

In Equation 2.37, the exponential expression is expanded and in Equation 2.38 the exponential argument is expanded, this is the key difference in the cumulant expansion compared with a Taylor expansion. Expansions in cumulants converge more rapidly than an expansion in moments. This becomes particularly important when considering that the random variable x may be a function of time, as in the case of the model in Equation 2.34. In fact, for a system that obeys Gaussian statistics, all cumulants with $n > 2$ vanish. This makes the cumulant expansion approach much more efficient in evaluating expansions of random variables. To obtain the above defined cumulants, coefficients of powers of x are compared in Equations 2.40 and 2.41. Assume that instead of expanding the exponential directly, the exponential argument can instead be expanded in terms of an operator or variable *H*.

$$F = \exp(c) = 1 + c + \frac{1}{2}c^2 + \ldots \tag{2.6}$$

$$c = c_1 H + \frac{1}{2}c_2 H^2 + \ldots \tag{2.7}$$

Inserting Equation 2.41 into 2.40 and collecting in powers of H gives

$$F = 1 + c_1 H + \frac{1}{2}(c_2 + c_1^2)H^2 + \ldots \tag{2.8}$$

Now, expanding the exponential in H and comparing to 2.42

$$F = \exp(fH) = 1 + f_1 H + \frac{1}{2} f_2 H^2 + \ldots \tag{2.9}$$

shows that,

$$\begin{aligned} c_1 &= f_1 \\ c_2 &= f_2 - f_1^2 \end{aligned} \tag{2.10}$$

Now expanding Equation 2.36 in cumulants brings an expression for the time correlation function normalized by maximum displacement.

$$\frac{\langle a^*(0)\, a(t)\rangle}{|a_0|^2} = \exp(-i\omega_0 t)\exp\left[-i\int_0^t d\tau_1 \langle \delta\omega(\tau_1)\rangle - \frac{1}{2}\int_0^t d\tau_1 \int_0^t d\tau_2 \langle \delta\omega(\tau_2)\,\delta\omega(\tau_1)\rangle + \cdots\right] \tag{2.11}$$

For a system with Gaussian statistics, the first term is zero because the average value of the displacement from the mean is zero (i.e. $\langle \delta\omega(\tau_1)\rangle$=0), and the second term is associated with the width of the distribution of frequencies. Furthermore, all higher-order terms vanish if the fluctuations are assumed to possess Gaussian statistics. Thus, the only integral left is the second order term and is denoted as $g(t)$.[7] This function damps the coherent oscillation due to the random perturbations from system-bath interactions. This process is shown in Figure 2.4.

The correlation function now expressed with $g(t)$ takes the following form.

$$\frac{\langle a^*(0)a(t)\rangle}{|a_0|^2} = \exp\left[-i\omega_0 t - g(t)\right] \tag{2.12}$$

$$g(t) = \exp(-i\omega_0 t)\exp\left[-\frac{1}{2}\int_0^t d\tau_1 \int_0^t d\tau_2 \langle \delta\omega(\tau_2 - \tau_1)\delta\omega(0)\rangle\right] \tag{2.13}$$

Equation 2.47 is usually rewritten using a change of variables where $T = \tau_1 - \tau_2$ leading to a final form for the line broadening function written in terms of the correlation function as

$$g(t) = \int_0^t dT(t-T)C(t) \tag{2.14}$$

where

$$C(T) = \langle \delta\omega(T)\delta\omega(0)\rangle \tag{2.15}$$

Equation 2.49 shows that the correlation function only depends on the time between points as discussed in the previous section.

The next step is to assume a functional form for $C(T)$ using the parameters presented in Figure 2.3. The correlation function representing bath dynamics will be cast in terms of the fluctuation amplitude, Δ, which describes the strength of the system bath coupling and Λ^{-1} which describes the correlation time or the time that it takes the bath to randomize any correlation from the previous evaluation of the observable quantity. The following functional form of the TCF is assumed.

$$C(T) = \Delta^2 \exp(-\Lambda T) \tag{2.1}$$

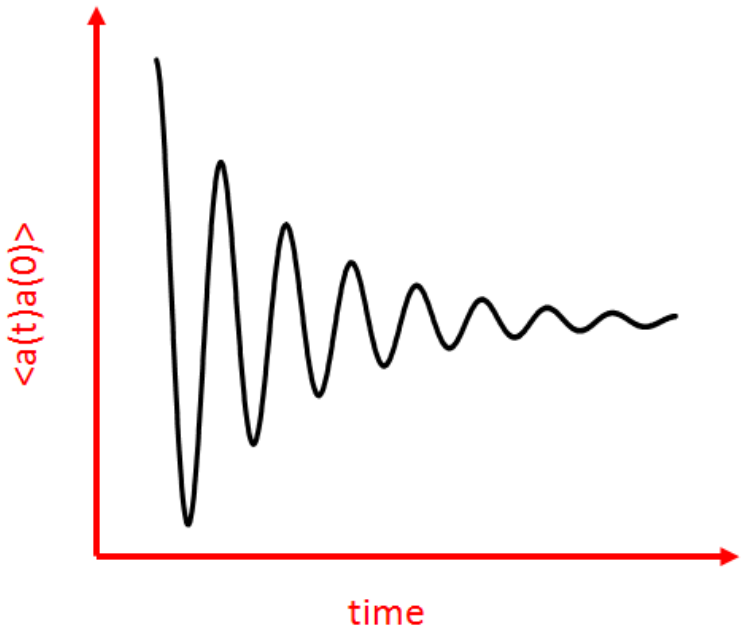

Figure 2.4. The $g(t)$ function damps oscillations in the correlation function. $g(t)$ represents dephasing due to random perturbation from the environment and eventually leads to motion that is uncorrelated with the initial conditions after a certain amount of time has passed.

With this form of the time correlation function, Kubo's $g(t)$ function is given by

$$g(t) = \Delta^2 \int_0^t dT\,(t-T)\exp(-\Lambda T) = \frac{\Delta^2}{\Lambda^2}\left[\exp(-\Lambda t) + \Lambda t - 1\right] \tag{2.2}$$

There are two interesting limits to this function which take on unique physical meaning and show special cases of how the line broadening function influences the system's optical lineshapes and kinetics such as vibrational cooling[8]. Section 2.4 will show how non-radiative relaxation mechanisms are also sensitive to these two regimes, particularly that shown in Equation 2.52. The first limit is that of inhomogeneous broadening, where

$$g(t) \approx \frac{1}{2}\Delta^2 t^2, \qquad \Lambda/\Delta << 1 \tag{2.3}$$

In this "slow modulation" limit, the fluctuation amplitude, Δ, is large compared to the rate at which memory is lost in the system, Λ. The opposite limit of the line broadening function is the homogenous or 'fast modulation' limit where

$$g(t) \approx \Delta^2 \Lambda t, \qquad \Lambda / \Delta >> 1 \tag{2.4}$$

Thus far, it has been shown how to incorporate thermally populated stochastic nuclear motions into the time correlation function approach to treat condensed phase dynamics. However, it is often advantageous to directly incorporate higher frequency nuclear modes into these expressions because of their strong coupling to molecular excitations. One such example is the strong coupling of the C=C stretch in aromatic molecules. These higher frequency modes are not thermally populated, but their strong coupling strength makes it necessary to have a framework that directly calculates their influence on spectroscopic lineshapes, such as absorbance and fluorescence. The following derivation incorporates high frequency (underdamped) nuclear coordinates into $g(t)$.[6]

To obtain the expression of the correlation function for underdamped oscillators the dimensionless harmonic oscillator Hamiltonian is introduced representing molecular ground and excited states. Note that there is displacement between the ground and excited states.

$$\begin{aligned} H_g &= \frac{1}{2}\sum_j \hbar\omega_j \left[P_j^2 + Q_j^2 \right] \\ H_e &= \hbar\omega_{eg}^0 + \frac{1}{2}\sum_j \hbar\omega_j \left[P_j^2 + \left(Q_j + D_j \right)^2 \right] \end{aligned} \tag{2.5}$$

It is assumed that the energy gap is linearly coupled to the position of the oscillator giving the following potential energy equation.

$$V = \hbar \sum_j \omega_j D_j Q_j \tag{2.6}$$

The correlation function for the high frequency underdamped oscillator then takes the following form.

$$C_{eg}(t) = \sum_n p_n \langle n | \delta\omega_{eg}(t) \delta\omega_{eg}(0) | n \rangle = \sum_n p_n \langle n | V(t) V(0) | n \rangle \tag{2.7}$$

By recasting the correlation function in terms of raising and lowering operators given by

$$C_{eg}(t) = \sum_j D_j^2 \omega_j^2 \sum_n p_n \langle n | \left[a_j^\dagger(t) + a_j(t) \right] \left[a_j^\dagger + a_j \right] | n \rangle \tag{2.8}$$

and incorporating the thermally averaged quantum number for an oscillator given by

$$\bar{n}_j = \sum_n p_n \langle n | a_j^\dagger a_j | n \rangle = \left[\exp\left(\hbar\omega_j / k_B T \right) - 1 \right]^{-1} \tag{2.9}$$

the following final expression for the correlation function is obtained.

$$C_{eg}(t) = \frac{1}{2} \sum_j D_j^2 \omega_j^2 \left[\coth\left(\frac{\hbar\omega_j}{2k_B T} \right) \cos\left(\omega_j t \right) - i \sin\left(\omega_j t \right) \right] \tag{2.10}$$

Now the framework has been laid for calculating spectroscopic observables in terms of TCFs. The total line broadening function $g(t)$ is given by summing the correlation function of low frequency thermally populated modes (overdamped) in Equation 2.51 and the discreet spectrum of underdamped modes in Equation 2.59

$$g(t) = g_{OD}(t) + g_{UD}(t)$$
$$g_{OD}(t) = \frac{\Delta^2}{\Lambda^2}\left[\exp(-\Lambda t) + \Lambda t - 1\right] - i\frac{\Delta^2}{2k_B T}[\exp(-\Lambda t) + \Lambda t - 1] \tag{2.11}$$
$$g_{UD}(t) = \frac{1}{2}\sum_j D_j^2\left[\coth\left(\frac{\hbar\omega_j}{2k_B T}\right)\left(1-\cos(\omega_j t)\right) + i\left(\sin(\omega_j t) - \omega_j t\right)\right]$$

The imaginary portion of the overdamped line broadening function g_{OD} was incorporated by Mukamel to account for solvent reorientation that led to red shifted fluorescence spectra (Stokes shift).[4]

Now, spectroscopic observables can be calculated using the time correlation function approach. The absorbance and fluorescence lineshapes are calculated by using Equations 2.61. The parameter λ is the reorganization energy, a measure of system bath coupling, and is given by $\lambda = \Delta^2/(2k_B T)$. Physically this means that larger reorganization energy stems from greater amplitude fluctuations in the transition frequency in Figure 2.3.

$$\sigma_{abs}(\omega) \propto \mathrm{Re}\left\{\int_0^\infty dt \exp\left[i\left(\omega - \omega_{eg}^0 - \lambda\right)t - g(t)\right]\right\}$$
$$\sigma_{fl}(\omega) \propto \mathrm{Re}\left\{\int_0^\infty dt \exp\left[i\left(\omega - \omega_{eg}^0 + \lambda\right)t - g^*(t)\right]\right\} \tag{2.12}$$

Figure 2.5 presents calculated absorbance spectra and correlation functions based on the presented formalism. The correlation function is calculated in the fast/slow modulation limit; however, the absorbance is calculated and shown in the inhomogeneous or slow modulation limit since this is the normal limit for line broadening in condensed phase systems. The absorbance is calculated assuming strong and weak system-bath coupling; this is further explained in the figure caption. Panel (a) shows how the bandwidth of the absorption resonance and blue shift of transition frequency increases with system-bath

coupling. Panel (b) shows that in the slow modulation limit the correlation function has a slow, almost Gaussian like decay, where the fast modulation limit has exponential decay.

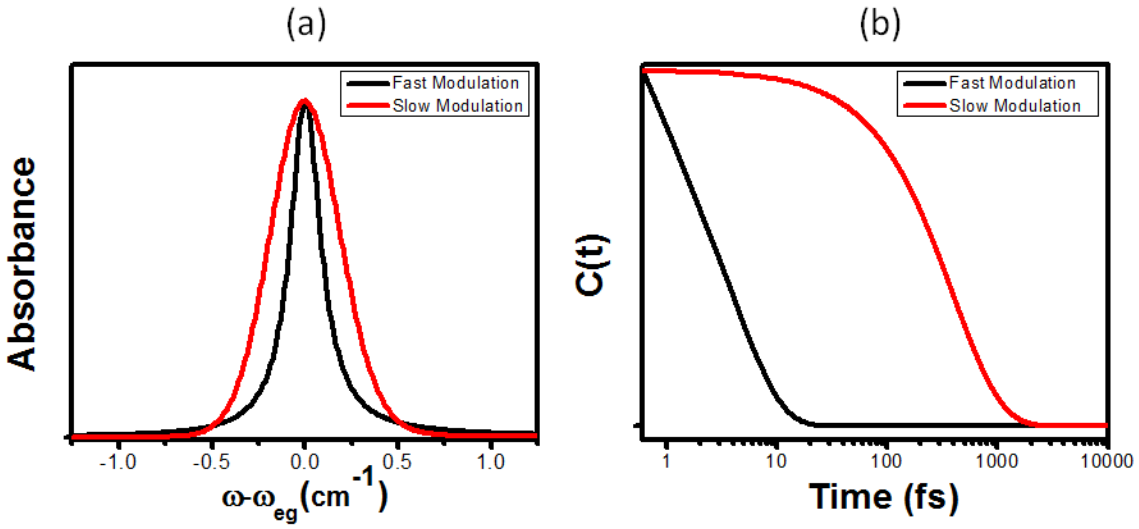

Figure 2.5. Correlation functions are shown for the two limits of line broadening in panel (b). Using Equation 2.61, the absorbance lineshapes are calculated in the strong and weak coupling regime in panel (a). The bath time scale is 100fs for this calculation. For strong:weak coupling Λ/Δ is equal to 0.1:1 respectively. Transition bandwidth and detuning from the transition frequency increases as system-bath coupling increases.

Many of the systems in this dissertation have a nonzero underdamped line broadening function $g_{UD}(t)$. In this case a progression of peaks is present in the absorption spectrum indicating that molecules in the excited state also possess vibrational quanta in the underdamped mode that modulates the line broadening function. This is known as a Franck-Condon progression. Figure 2.6 below shows (a) the potential energy surfaces representing the ground and excited states and (b) the corresponding absorption spectrum. Displacement along the nuclear coordinate between the ground and excited states causes the peak of the absorption spectrum to shift towards higher vibrational quanta in the excited state. In the limit of strong system-bath coupling in Figure 2.6 (b)

the transitions are less clear and this well approximates what a typical vibrational progression may look like in the condensed phase.

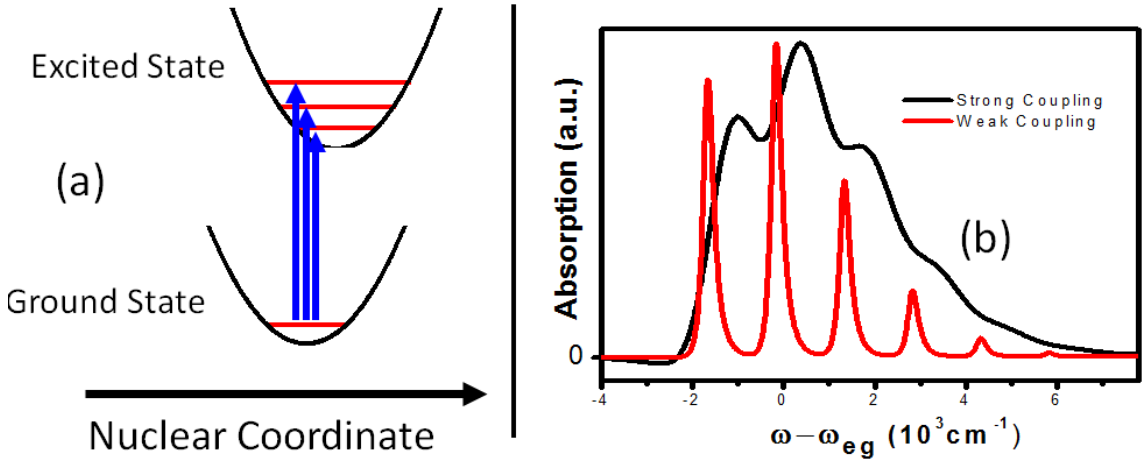

Figure 2.6. (a) Displacement of ground and excited potential energy surfaces with respect to the nuclear coordinate initiates photon absorption into a vibrational manifold in the excited state. (b) Absorption into this manifold peaks at a particular quanta in the excited state and is captured by a nonzero $g_{UD}(t)$. The bath time scale is 100fs for this calculation. For strong/weak coupling Λ/Δ is equal to 0.1/1 respectively.

Expressions can be obtained for the spectral density using Equation 2.32. Assuming an exponentially decaying correlation function like that expressed in Equation 2.51 the complex spectral density is obtained and separated into real and imaginary parts.

$$C_{OD}(\omega) = -\left(\frac{2\Lambda\Delta^2}{\omega^2 + \Lambda^2} + i\frac{2\omega\Delta^2}{\omega^2 + \Lambda^2} \right) \tag{2.13}$$

The imaginary (odd) part of the overdamped (OD) spectral density is independent of temperature and can be used as the basic quantity that describes the bath. Equation 2.62 is the expression for the spectral density that contains dephasing information of low frequency thermally populated modes. A similar expression can be obtained for the high frequency (underdamped) components of the spectral density from Equation 2.60 by carrying out the Fourier transform in Equation 2.32.

$$C_{UD}(\omega)=\frac{1}{2}\sum_j D_j^2\omega_j^2\int_{-\infty}^{\infty}dt\exp(i\omega t)\left[\coth\left(\frac{\hbar\omega_j}{2k_BT}\right)\cos(\omega_j t)-i\sin(\omega_j t)\right] \quad (2.14)$$

The odd part of this expression is given by

$$C''_{UD}(\omega)=\frac{1}{2}\sum_j D_j^2\omega_j^2\left[\delta(\omega-\omega_j)-\delta(\omega+\omega_j)\right] \quad (2.15)$$

The underdamped part of the correlation function yields modes in the spectral density at specific frequencies. Individual modes are given by j. The amplitudes of these modes are weighted by the product of their squared frequency, ω_j, and their squared displacement, D_j. The displacement represents the coupling, or degree of displacement, initiated in mode *j* by a perturbation, such as a molecular excitation. Larger displacement values yield larger amplitude in the spectral density indicating that more strongly displaced modes have a greater impact on observed dynamics.

2.4. Application of Time Correlation Function to Calculate System Dynamics: Vibrational Cooling and Internal Conversion Rates

Quantum time correlation functions capture the random thermal motion associated with stochastic motion in condensed phase systems. Knowledge of these fluctuations allows for calculation of many spectroscopic observables. Some of these include the Förster energy transfer rate, Marcus theory of electron transfer, and the absorbance lineshape as shown previously.[3-6] In the case of Marcus theory and Förster transfer, the rate can be rewritten as a time correlation function just like Fermi's golden rule was recast in Section 2.1. This section will briefly show how the correlation function is applied to calculate two rate formulas pivotal to the systems studied in this dissertation. The rate of vibrational energy transfer and the rate of internal conversion

will be cast in a time correlation function approach and the results of the rate formulas will be discussed.

Equation 2.19 is the most general form for obtaining a rate formula starting with any operator that induces transitions between system states. In the systems in this dissertation, ultrafast internal conversion processes leave greater than 5eV of energy from UV photon absorption as ground state vibrations of the solute. This is a highly non-equilibrium distribution of energy that relaxes through intra- and inter-molecular pathways passing to the solvent and eventually dissipating as low frequency solvent modes such as translations. Part of this research aims to understand the relaxation pathway and how vibrational energy redistribution affects the excited state deactivation mechanisms that are pivotal to function of DNA molecules and chemical reaction dynamics of cycloalkenes. A brief derivation of vibrational energy transfer follows, from Reference [8], and the complete derivation and application to experimental results is found in Chapter 5.

The rate formula in Equation 2.19 is cast in terms of the solute-solvent interaction operator $\hat{V}$.

$$K = \frac{1}{\hbar^2}\int_0^\infty dt \left\langle \hat{V}(t)\hat{V}(0)\right\rangle \tag{2.16}$$

The correlation function is then expanded in a complete set of harmonic oscillator eigenstates and similar to Equation 2.47 the cumulant expansion technique is used to simplify the expression to obtain

$$K = \frac{1}{\hbar^2}\sum_{mn} P_m \left|V_{mn}\right|^2 \Phi\left(\omega_{mn};T_{bath}\right) \tag{2.17}$$

where

$$\Phi\left(\omega_{mn};T_{bath}\right)=\mathrm{Re}\int_{0}^{\infty}dt\exp\left[i\omega_{mn}t-g\left(t;T_{bath}\right)\right] \tag{2.18}$$

In Equation 2.66 V_{mn} represents the coupling strength between vibrational modes m and n; and P_m is the thermal population of state m. T_{bath} is the temperature of the surrounding environment.

Two primary Brownian oscillator coordinates are needed to fully characterize the spectrum of solvent motions which couple to the vibrational modes in the solute (m). The effects of low frequency solvent motion on level m are incorporated using an overdamped coordinate much like that in Equation 2.62

$$C_L\left(\omega\right)=2\lambda\frac{\omega\Lambda}{\omega^2+\Lambda^2} \tag{2.19}$$

The second coordinate in the model represents the contribution from higher frequency (librational) modes using the spectral density

$$C_H\left(\omega\right)=\frac{S_{avg}\Omega_{avg}^2}{\delta\sqrt{2\pi}}\exp\left[\frac{-\left(\omega-\Omega_{avg}\right)^2}{2\delta^2}\right] \tag{2.20}$$

where S_{avg} and $S_{avg}\Omega_{avg}$ are respectively the average Huang-Rhys factor and total amount of reorganization energy associated with an inhomogeneous distribution of modes centered at Ω_{avg} with the width δ. Equation 2.69 gives a Gaussian lineshape to the delta function form of underdamped modes found in Equation 2.64. Figure 2.7 shows the mechanism of vibrational cooling where an excited harmonic oscillator is in the presence of a heat bath described by the spectral density

$$C_{Total}(\omega)=C_L\left(\omega\right)+C_H\left(\omega\right) \tag{2.21}$$

Now the two spectral densities are added together and used to generate the complete line broadening function $g(t;T_{bath})$.

$$g(t;T_{bath}) = \frac{1}{2\pi}\int_{-\infty}^{\infty} d\omega \frac{1-\cos(\omega t)}{\omega^2}\coth(\hbar\omega / 2k_B T_{bath})C(\omega) + \frac{i}{2\pi}\int_{-\infty}^{\infty} d\omega \frac{\sin(\omega t)-\omega t}{\omega^2}C(\omega) \qquad (2.22)$$

Most notable about Equation 2.71 is the dependence of $g(t)$ on the temperature of the solvent. The real part of $g(t;T_{bath})$ is primarily governed by the lower frequency, $\omega < k_B T_{bath}$, part of $C(\omega)$, which accounts for the exchange of energy between the solute and solvent. The imaginary part of $g(t;T_{bath})$ enables energetically downhill VC transitions starting in high frequency modes of the solute.

Chapter 5 of this dissertation applies this model to investigate how temperature influences the rate of thymine to solvent vibrational energy transfer. Experimental investigation found a temperature independent rate of vibrational relaxation in the thymine nucleobase at 300K and 100K. Application of this model identifies that the bath time scale and heating of the surrounding solvent contribute to the observed temperature independence. Figure 2.7(c) shows how the low frequency solvent motions of a fast bath peak at $\omega \approx k_B T$. Such a fast bath tends to wash out the contribution from the higher frequency modes in the spectral density as shown in Figure 5.6(a,b). This model was also applied to nucleotides and dinucleotides of the thymine family, reported in Chapter 6. This investigation found that vibrational energy transfer from solute to solvent actually causes an decrease in the excited state deactivation rate due to enhanced relaxation in the exited state potential well as the system size increases (nucleobase to dinucleotide), see Figure 6.1 for additional information.

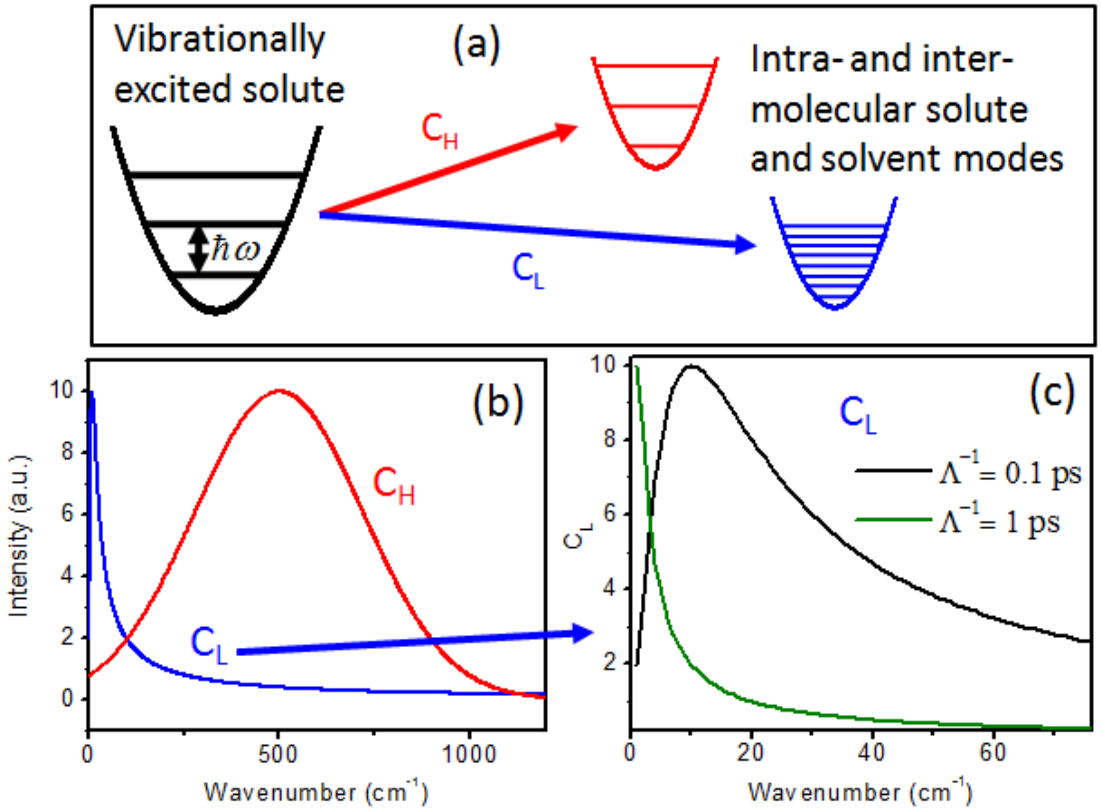

Figure 2.7. (a) Schematic of model vibrational cooling mechanism for an excited harmonic oscillator in the presence of a heat bath possessing two mechanisms of relaxation. C_L and C_H are respectively the low and high frequency components of the spectral density. C_L represents thermally populated stochastic motions of the heat bath(low frequency) and C_H represents temperature independent higher frequency part of heat bath. (b) A plot of the spectral densities obtained with the parameters utilized in Ch. 5. (c) The low frequency part of the spectral density as a function of the bath time scale, a 'fast' bath (0.1ps bath time scale) has a spectral density that peaks near 10 cm^{-1} whereas the slow bath (>1ps bath time scale) maximizes at much lower frequency.

The systems presented in this dissertation and numerous others possess excited electronic state configurations where one or more distinct electronic states can be accessed from the Franck-Condon geometry via nuclear relaxation. Interactions from either under-damped or over-damped inter- or intra-molecular modes can induce transitions between these excited states. In the case of having a high frequency intramolecular mode that strongly couples to the excitation, the two potential energy

surfaces possess a vibronic manifold of states and transitions can occur from the lowest energy vibrational level of the donor state a to the manifold of vibronic levels in state b. Figure 2.8 below shows the schematic of the relaxation process for which rate constants are being obtained. Population initially resides on electronic state a and makes a transition to electronic state b, partly enhanced by thermal fluctuations in the surrounding environment. In this model it is assumed that prior to the internal conversion process, population is at equilibrium in state a (i.e. residing in the m=0 state). This derivation is based off of class notes from Professor Andrew Moran.[6]

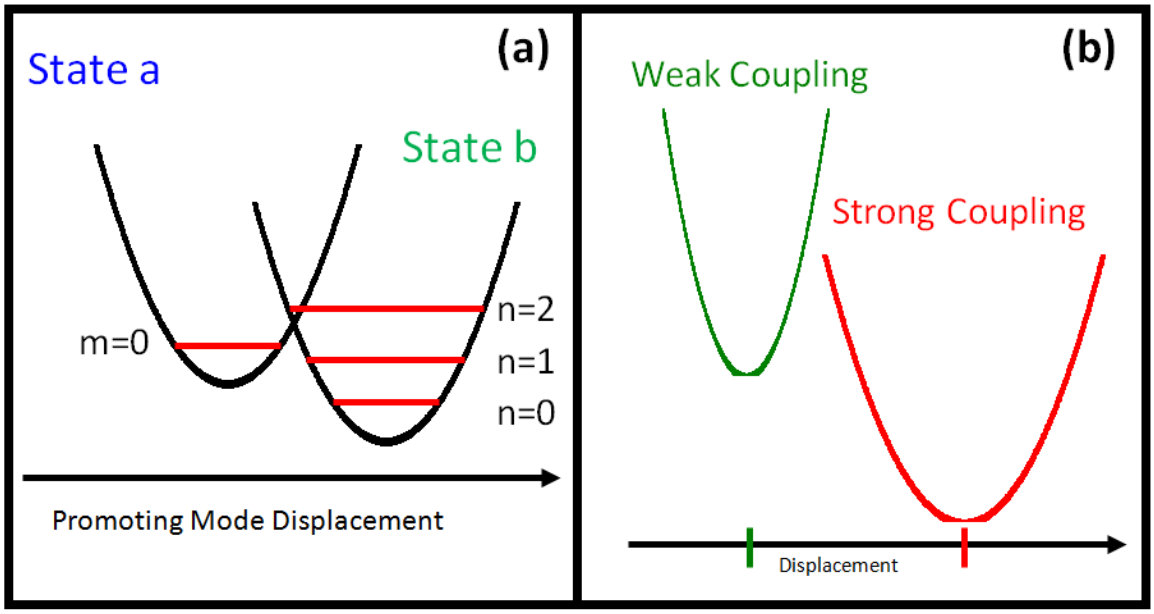

Figure 2.8. (a) Internal conversion sends electronic population from state a to state b. In this model it is assumed that the population starts in the lowest energy vibrational state in a and then makes a transition to any possible vibrational level in state b. (b) The bandwidths associated with each relaxation channel are directly related to the lineshapes of the potential energy surfaces. These are determined by the strength of the system bath coupling. System bath coupling varies the bandwidth and frequency of the transitions just like shown in Figure 2.5.

To calculate the rate formula for this transition process from state a to b, begin by tracking the time correlation function that couples states a and b and vibrational levels m and n.

$$K = \frac{1}{\hbar^2}\int_0^\infty dt \left\langle H'_{am,bn}(t) H'_{am,bn}(0) \right\rangle \tag{2.23}$$

The correlation function is then expanded in a complete set of harmonic oscillator eigenstates and similar to the derivation of the vibrational cooling rate the cumulant expansion technique is used to simplify the expression to obtain

$$k_{am,bn} = \frac{2\pi \left| H'_{am,bn} \right|^2}{\hbar^2} \delta\left(\omega_{am,bn}\right) \tag{2.24}$$

The matrix element $H'_{am,bn}$ controls the rate of non-radiative relaxation. Under the Born-Oppenheimer approximation, the matrix element can be rewritten as a product of two terms, one describing the electronic coupling between states a and b and the other the nuclear overlap integral. It is intuitive that transitions between different vibronic levels in the manifold will occur when the nuclear wave functions have the greatest degree of overlap. The matrix element can then be written as follows.

$$\left| H'_{am,bn} \right|^2 = \left| \left\langle \psi_a \chi_{a,m} \left| H' \right| \psi_b \chi_{b,n} \right\rangle \right|^2 = \left| H'^{el}_{ab}(R_0) \right|^2 \cdot \left| \left\langle \chi_{a,m} \middle| \chi_{b,n} \right\rangle \right|^2 \tag{2.25}$$

The first term in this expression $H'^{el}_{eg}(R_0)$ represents the coupling between the initial and final states in the transition. The fluctuations induced by the time correlation function can donate or accept quanta of energy allowing the two states to become degenerate and a transition to occur. The second term $\left\langle \chi_{a,m} \middle| \chi_{b,n} \right\rangle$ is the nuclear wavefunction overlap integral. By identifying the perturbation which initiates the

internal conversion process, this matrix element can be recast in a more usable form. The perturbation associated with internal conversion arises from the term in the Schrodinger equation involving the nuclear kinetic energy operator

$$T_N \psi(\mathbf{r};\mathbf{R})\chi(\mathbf{R}) = \frac{\hbar^2}{2m_\alpha}\left\{\chi(\mathbf{R})\frac{\partial^2\psi(\mathbf{r};\mathbf{R})}{\partial R_\alpha^2} + 2\frac{\partial\psi(\mathbf{r};\mathbf{R})}{\partial R_\alpha}\frac{\partial\chi(\mathbf{R})}{\partial R_\alpha} + \psi(\mathbf{r};\mathbf{R})\frac{\partial^2\chi(\mathbf{R})}{\partial R_\alpha^2}\right\} \quad (2.26)$$

where $\mathbf{R}$ is the nuclear coordinate, $\psi(\mathbf{r};\mathbf{R})$ is the electronic part of the wavefunction, T_N is the nuclear kinetic energy operator, $\chi(\mathbf{R})$ is the nuclear wavefunction, and α represents individual nuclear coordinates. The third term in Eq. 2.75 enters the differential equation used to obtain vibrational wavefunctions, and the first term is normally taken to be small compared to the first. Now the matrix element $H'_{am,bn}$ possessing separate electronic and nuclear wavefunctions can be written as

$$H'_{am,bn} = \frac{\hbar^2}{\mu_\alpha}\left\langle \psi_b^{el}\left|\frac{\partial}{\partial R_\alpha}\right|\psi_a^{el}\right\rangle\left\langle n_b\left|\frac{\partial}{\partial R_\alpha}\right|m_a\right\rangle \quad (2.27)$$

where ψ^{el} is the electronic wavefunction of state a or b, R_α is the coordinate associated with nuclear mode α, and $n_a(m_b)$ represent vibrational quanta in state $a(b)$. The second term here will be simplified because it encodes information on how the internal conversation rate will vary between the various vibronic levels of the donating and accepting states. By rewriting $\frac{\partial}{\partial R_\alpha}$ in terms of the creation $B^\dagger$ and annihilation B operators as

$$\frac{\hbar}{i}\frac{\partial}{\partial R_\alpha} = i\sqrt{\frac{\hbar\mu\omega}{2}}\left(B_\alpha^\dagger - B_\alpha\right) \quad (2.28)$$

and simplifying the resulting expression for the second term in Equation 2.76 assuming that the transitions occurs from the lowest energy vibronic level in state a the following is obtained

$$\left|\left\langle n_b\left|\frac{\partial}{\partial R_\alpha}\right|0_a\right\rangle\right|^2 = \frac{\mu_\alpha \omega_\alpha}{2\hbar}\left|\left\langle n_b\left|1_a\right\rangle\right|^2 \tag{2.29}$$

The rate equation incorporates overdamped $g_{OD}(t)$ and underdamped $g_{UD}(t)$ nuclear motions like described in the derivation of the line broadening functions. ω_{ba} is the free energy gap between states a and b and ω_{mn} is the energy difference between vibrational modes m and n. In general, the states a and b can have different equilibrium geometry with respect to low frequency nuclear motions. This is shown by a displacement along the nuclear coordinate in Figure 2.8.

$$K_{bn,am} = \sum_m \sum_n P_{am} \frac{\left|H'_{bn,am}\right|^2}{\hbar^2} \mathrm{Re}\left\{\int_0^\infty dt \exp\left[-i\left(\omega_{ab} + \omega_{mn}\right)t/\hbar - g_{OD}(t) - g_{UD}(t)\right]\right\} \tag{2.30}$$

As mentioned in the opening paragraph, it is assumed that the transition occurs from the lowest energy vibronic level in state a, so $m = 0$ and the vibronic levels are written explicitly from above equation 2.78 to obtain the final expression of the internal conversion rate.

$$K_{bn,a0} = \frac{\hbar\omega_\alpha}{2\mu_\alpha}\left|\left\langle \psi_b^{el}\left|\frac{\partial}{\partial R_\alpha}\right|\psi_a^{el}\right\rangle\right|^2 \sum_{n_b} \mathrm{Re}\int_0^\infty dt \left\langle 1_a\left|n_b\right\rangle\right\langle n_b\left|1_a\right\rangle \exp\left[i\omega_{ba}t + i\omega_n t - g_{OD}(t) - g_{UD}(t)\right]\right. \tag{2.31}$$

In equation 2.79 $\langle 1_a|n_b\rangle\langle n_b|1_a\rangle$ is specifically for the promoting mode. This mode possesses a large gradient in ψ with respect to the nuclear coordinate, all other displaced high frequency modes can be treated with $g_{UD}(t)$.

Now that the rate formula has been obtained, numerical calculation of the integrand gives insight into the physics driving these processes. Figure 2.9 highlights the unique properties of this internal conversion rate. The frequency of the promoting mode is set to be $1500\,\mathrm{cm}^{-1}$. Panel (a) shows how the rate in strong and weak coupling limits varies with the energy gap between states a and b. For this calculation the displacement d is set equal to zero so that internal conversion only occurs into the $\mathrm{n}=1$ vibrational level. Note how the bandwidth/center frequencies of the transition are dependent on bath properties. In a realistic condensed phase system given by the strong coupling limit the bandwidth of the transition is broad and the center frequency is shifted to a larger energy gap between states a and b due to reorganization energy associated with the surrounding solvent. Panel (b) sets the displacement to one. This is interesting because the rate has two points of maximum for the slow and fast modulation limit. This does not occur in the case of a Franck-Condon progression present in an absorption spectrum where there is a Poisson intensity distribution (as in Figure 2.6). This vibrational progression comes from the underdamped mode in $g_{UD}(t)$. Notice also how the bandwidth of the transition is broader in the strong coupling limit and the larger energy gap between states a and b.

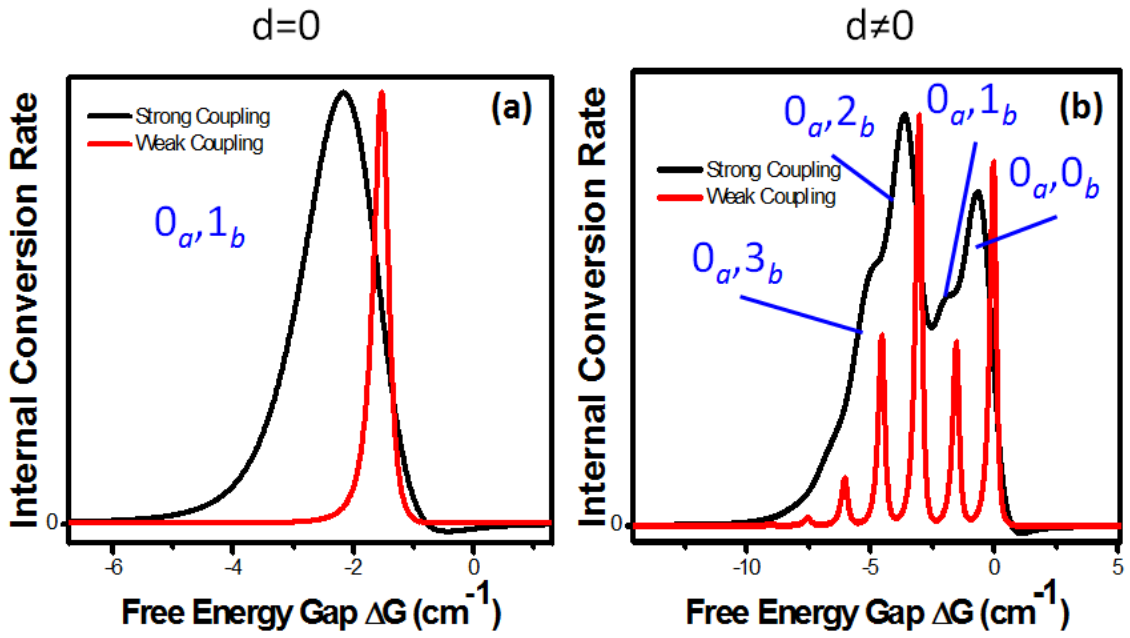

Figure 2.9. Blue text indicates the donating and accepting energy states respectively (donor, acceptor). (a) Internal conversion from state *a* to *b* with zero displacement along the nuclear coordinate is dominated by the transition to the singly excited vibrational quanta state of electronic state *b*. The transition bandwidth is much broader in the strong coupling limit. (b) In the case of non-zero displacement the transition can convert to any of the vibrational states in electronic state *b* resulting in multiple relaxation pathways. Note there are two local maxima; this is not the case for the vibrational progression in the absorption spectrum.

2.5. Connecting Time Correlation Functions and Nonlinear Spectroscopic Techniques

A formalism based on time correlation functions has been developed that treats the influence of stochastic motion in the solvent-solute system. The next step is to merge this theory with a description of the nonlinear experiments implemented in laboratory so that experimental results can be interpreted to understand the system response. This response convolutes the applied laser fields, molecular dynamics, and stochastic motions. The forthcoming section will provide a framework in which these mechanisms can be understood.[4,6]

When a laser field is incident upon an ensemble of molecules which interact with the applied field, a macroscopic polarization is produced in the sample. It is this

macroscopic polarization which emits radiation that is observed in experimentation and used to deduce processes occurring in the sample. There are a wide variety of processes which can take place in such an ensemble and depending on the physics driving each process; they can have unique dependence on the incident electric field. In order to account for the varying degrees of interaction strength, the macroscopic polarization of the sample is expanded in powers of the electric field.

$$P = \chi^{(1)}E + \chi^{(2)}E^2 + \chi^{(3)}E^3 + \cdots \tag{2.32}$$

where $\chi^{(N)}$ is the Nth-order susceptibility that contains information on the response of the material (e.g., energy transfer, resonant frequencies, dispersion, etc). The first order susceptibility contains information on the system's linear response to an applied electric field, such as the linear absorption spectrum. The second order susceptibility describes the system's response to second order processes such as sum frequency generation, difference frequency generation, and the optical Kerr effect. The third order susceptibility describes responses such as fluorescence, Raman, and pump-probe spectroscopy.

Time dependent perturbation theory is used to describe the microscopic origins of the polarization induced in the sample by the applied electric fields. A description of perturbation theory cast in the language of the density operator is more convenient for calculation of the system's response than the wavefunction approach. This is due to the fact that expectation values of observables are easily calculated in the density matrix formalism. The expectation value of operator, $\hat{A}$ with density matrix, $\hat{\rho}$, is obtained simply by taking the trace of the product of the two matrices.

$$\langle \mathrm{A} \rangle = \mathrm{Tr}\left(\hat{\rho} \cdot \hat{\mathrm{A}} \right) \tag{2.33}$$

In addition, the optical response decomposes into 'pathways' in which the order of field-matter interactions is naturally retained when using the density operator. Practitioners distinguish pathways using double-sided Feynman diagrams.

The time dependent wave function, $\psi(\vec{r},t)$, in a complete set of basis functions, ϕ_k, is given by

$$\psi(\vec{r},t) = \sum_k c_k \phi_k(\vec{r}) \exp(-i\omega_k t) \tag{2.34}$$

where ω_k is the frequency of state k and c_k is the coefficient describing the degree of contribution from state k to the overall wavefunction. The probability density is obtained by taking the square modulus of the wavefunction as

$$\left|\psi(\vec{r},t)\right|^2 = \sum_k \sum_m c_m c_k^* \phi_k^*(\vec{r}) \phi_m(\vec{r}) \exp(i\omega_{km} t) \tag{2.35}$$

Density matrix elements reflect the coefficients and time dependence of the wavefunction. The elements are given by

$$\rho_{mk}(t) = c_m c_k^* \exp(i\omega_{km} t) \tag{2.36}$$

Diagonal elements $(m = k)$ in the density matrix are known as populations and off diagonal matrix elements $(m \neq k)$ are known as coherences. In Dirac notation, the density matrix written in a set of basis vectors is given by

$$\hat{\rho}(t) = \sum_m \sum_k \rho_{mk}(t) |m\rangle\langle k| \tag{2.37}$$

Now that the density operator has been introduced the effect of perturbation on the quantum dynamics of the density matrix elements must be followed. In order to

accomplish this, it is necessary to solve the quantum Liouville equation. The quantum Liouville equation is given by

$$i\hbar\frac{\partial\rho}{\partial t}=\left[H,\rho\right] \tag{2.38}$$

The matrix representation of this equation is

$$i\hbar\frac{\partial\rho_{mk}}{\partial t}=\left\langle m\left|\left[H,\rho\right]\right|k\right\rangle \tag{2.39}$$

The Hamiltonian, H, of the system is divided into a time independent and time dependent part as

$$H=H^{(0)}+\lambda H^{(1)}\left(t\right) \tag{2.40}$$

with λ as a parameter which determines the strength of the perturbation. Elements of the density matrix are expanded with the same perturbation as follows

$$\rho_{mk}\left(t\right)=\sum_{N=0}\lambda^{N}\rho_{mk}^{(N)}\left(t\right)=\rho_{mk}^{(0)}\left(t\right)+\lambda\rho_{mk}^{(1)}\left(t\right)+\lambda^{2}\rho_{mk}^{(2)}\left(t\right)+\cdots \tag{2.41}$$

By inserting Equations 2.89 and 2.90 into the quantum Liouville equation (2.88) and grouping terms with similar dependence on the power of the perturbation, a series of equations which describe the time evolution of density matrix elements is obtained. Integrating this equation yields the value of the density matrix at order N

$$\rho_{mk}^{(N)}\left(t\right)=-\frac{i}{\hbar}\int_{0}^{\infty}\left\langle m\left|\left[H^{(1)}\left(t-t_{N}\right),\rho^{(N-1)}\left(t-t_{N}\right)\right]\right|k\right\rangle\exp\left(-i\omega_{mk}t_{N}\right)dt_{N} \tag{2.42}$$

In this equation, $\omega_{mk}=\left(E_{m}-E_{k}\right)/\hbar$ and t_{N} represents the time interval between interactions with the perturbation. Calculating the density matrix element at order N requires the evaluating of N nested commutators and 2^{N} terms. For example, to calculate

$\rho_{mk}^{(2)}$, it is first necessary to calculate $\rho_{mk}^{(1)}$ from $\rho_{mk}^{(0)}$ and then using $\rho_{mk}^{(1)}$ the expression for $\rho_{mk}^{(2)}$ can be obtained.

Equation 2.91 must be evaluated to determine the quantum dynamics of a system that interacts with a perturbation. In this case, the perturbation is an externally applied electric field $\vec{E}(t)$ that interacts with the material dipole, $\vec{V}$. The perturbing Hamiltonian representing the field-matter interaction is given by $H^{(1)}(t) = -\vec{V} \cdot \vec{E}(t)$. The general form of the material dipole which can be easily written in the density matrix formalism is $V = \sum_{a,b} \mu_{ab} |a\rangle\langle b|$ where μ_{ab} is the dipole matrix element for arbitrary states a and b, $\langle a|\mu|b\rangle$. This transition dipole 'moment' μ_{ab} represents the susceptibility of an interaction between states $|a\rangle$ and $|b\rangle$, induced by the electric field. The rate of absorption scales as the square of the transition dipole when evaluated at the level of Fermi's Golden rule (i.e., first-order perturbation theory). Maxwell's equations show that the nth-order electric field radiated by a sample is proportional to the respective component of the nonlinear polarization present in the sample. The following equation demonstrates.

$$E_s^{(n)}(t) = \frac{i2\pi\omega_s l}{n(\omega_s)c} P_s^{(n)}(t) \tag{2.43}$$

In Equation 2.92, $n(\omega_s)$ is the real part of the refractive index as a function of frequency and l is the path length of the emissive medium. Notably, the field radiated by the material is phase-shifted by 90° with response to the polarization. In a laboratory setting, the electric fields that are emitted by the sample are a direct measure of the polarization

induced by an applied electric field (the perturbation). The molecular properties and energy level structure dictate the response of the system and can be understood by using the density operator approach to describe the system-perturbation interaction. The polarization can be calculated by taking the trace over the density matrix and dipole operator product as in Equation 2.82.

$$P^{(N)}(t) = \mathrm{Tr}\left[V\rho^{(N)}(t)\right] \tag{2.44}$$

By substituting in Equation 2.91 in 2.93

$$\begin{aligned} P^{(N)}(t) = &\int_0^\infty dt_N \int_0^\infty dt_{N-1} \ldots \int_0^\infty dt_1 S^{(N)}(t_N, t_{N-1}, \ldots, t_1) \\ &\times E_N(t-t_N) E_{N-1}(t-t_N-t_{N-1}) \cdots E_1(t-t_N-t_{N-1}\cdots t_1) \end{aligned} \tag{2.45}$$

The N th order polarization is obtained where the N th order response function is

$$S^{(N)}(t_N, t_{N-1}, \ldots, t_1) = \left(\frac{i}{\hbar}\right)\mathrm{Tr}\left[\mathbf{VG}(t_N)\mathbf{VG}(t_{N-1})\ldots\mathbf{VG}(t_1)\mathbf{V}\rho^{(0)}(-\infty)\right] \tag{2.46}$$

In this equation, $\mathbf{V}$ and $\mathbf{G}$ are superoperators defined as

$$\mathbf{V}A = [V, A] \tag{2.47}$$

$$\mathbf{G}(t)A = \theta(t)\exp\left(\frac{-i}{\hbar}H^{(0)}t\right)A\exp\left(\frac{-i}{\hbar}H^{(0)}t\right) \tag{2.48}$$

where

$$\theta(t) = \begin{cases} 1, t \geq 0 \\ 0, t < 0 \end{cases} \tag{2.49}$$

At first glance, Equations 2.94-2.97 appear rather complicated; however, they allow for the product of response functions and electric fields (i.e. specific paths through the density matrix) to be computed and then integrated. To accomplish this, Equation 2.95 is read (right-to-left) starting with the equilibrium density matrix $\rho^{(0)}(-\infty)$. At time

$t - t_N - t_{N-1} \cdots - t_1$ this density matrix interacts with the dipole superoperator, $\mathbf{V}$, which induces a change of state in the density matrix. The Green function then evolves the system under the influence of the time independent Hamiltonian $H^{(0)}$ during time interval t_1. A specific form for these functions will be presented. This process continues until at time *t* a final transition occurs and the trace is taken. The Heaviside step function, shown in Equation 2.98, enforces causality (i.e., time evolution occurs after a transition to a new state caused by interaction with the electric field). From this, the polarization can be visualized as a process where radiation fields synchronize and select states while time evolution is controlled solely by the dynamics of the system itself in the time intervals between interactions with the field.

There are a large number of possible sequences of pathways through the density matrix and electric field interactions, depending on the nature of the sample and applied fields. In order to narrow down the possible number of pathways, the experimentalist relies on conservation of momentum to induce a radiated signal in a specific direction. In order to accomplish this, the wave vectors of the incident fields are controlled and the electric field in Equation 2.94 is treated classically as

$$\mathbf{E}_n(\mathbf{r},t) = \xi_n(t)\left(\exp\left[i\left(\mathbf{k_n}\mathbf{r} - \omega_n t\right)\right] + c.c.\right) \tag{2.50}$$

where $\xi_n(t)$ is a slowly-varying envelope function, $\mathbf{k_n}$ is the wave vector, and ω_n is the frequency. Classical treatment of the electric field is a good approximation because its wavelength is at least an order of magnitude larger than the systems of interest. In third order experiments, there are 3 applied electric fields which can act in any order yielding

6x6x6, or 216 possible combinations. Implementing conservation of momentum says that the signal wavevector must be a linear combination of applied fields given by

$$\mathbf{k}_{\mathbf{sig}} = \sum_{n} \pm \mathbf{k}_{\mathbf{n}} \tag{2.51}$$

The signals detected in the experiments presented in this dissertation are radiated in the phase matched direction $\mathbf{k_s = -k_1 + k_2 + k_3}$. This is the standard phase matching directions for third-order spectroscopies.[9,10] By combining the use of phase matching with control of the timing of the applied fields, the number of terms in Equation 2.94 drops significantly. There are six electric field and response function combinations which describe third order spectroscopic experiments (i.e. six components to Equation 2.94). The response function at third order contains eight terms and is given by

$$S^{(3)}(t) = \left(\frac{i}{\hbar}\right)^3 \theta(t_1)\theta(t_2)\theta(t_3) \times \sum_{\alpha=1}^{4} \left[R_\alpha(t_1,t_2,t_3) - R_\alpha^*(t_1,t_2,t_3) \right] \tag{2.52}$$

where R^* terms are the complex conjugates of R.

A more intuitive approach is achieved through the use of Feynman diagrams; these are a schematic representation of calculating the polarization in Equation 2.94. Feynman diagrams allow the path through the density operator to be tracked and the response function to be written by the specifics of the diagram. Feynman diagrams for the third order response are given in Figure 2.10 for the $k_s = -k_1 + k_2 + k_3$ wavevector. States of the system are represented by dummy indices with state a reserved for the ground state, state b represents the HOMO-LUMO electronic energy gap, and state c an energetically higher excited state. The levels lie energetically with respect to one another

such that $E_a < E_b < E_c$ so that the gaps between a and b and b and c are similar to the energy of a UV photon and a visible photon respectively. This energy level scheme is an accurate representation of the energetics of the DNA bases and ring opening systems present in this dissertation. The systems are in optical coherences in the t_1 and t_3 time intervals. Terms with a ground state population in t_2 are called ground state bleach (GSB) terms. Terms that have an excited state population in t_2 are called excited state emission (ESE) if the diagram terminates in the ground state and are called excited state absorption (ESA) if the diagram ends in an excited state. It is important to note that GSB and ESE have opposite sign to ESA terms. Physically GSB and ESE correspond to a decrease in absorption compared to the ground state and ESA corresponds to an increase in absorption because the molecule that absorbs the pump beam then absorbs the probe beam in the excited state.

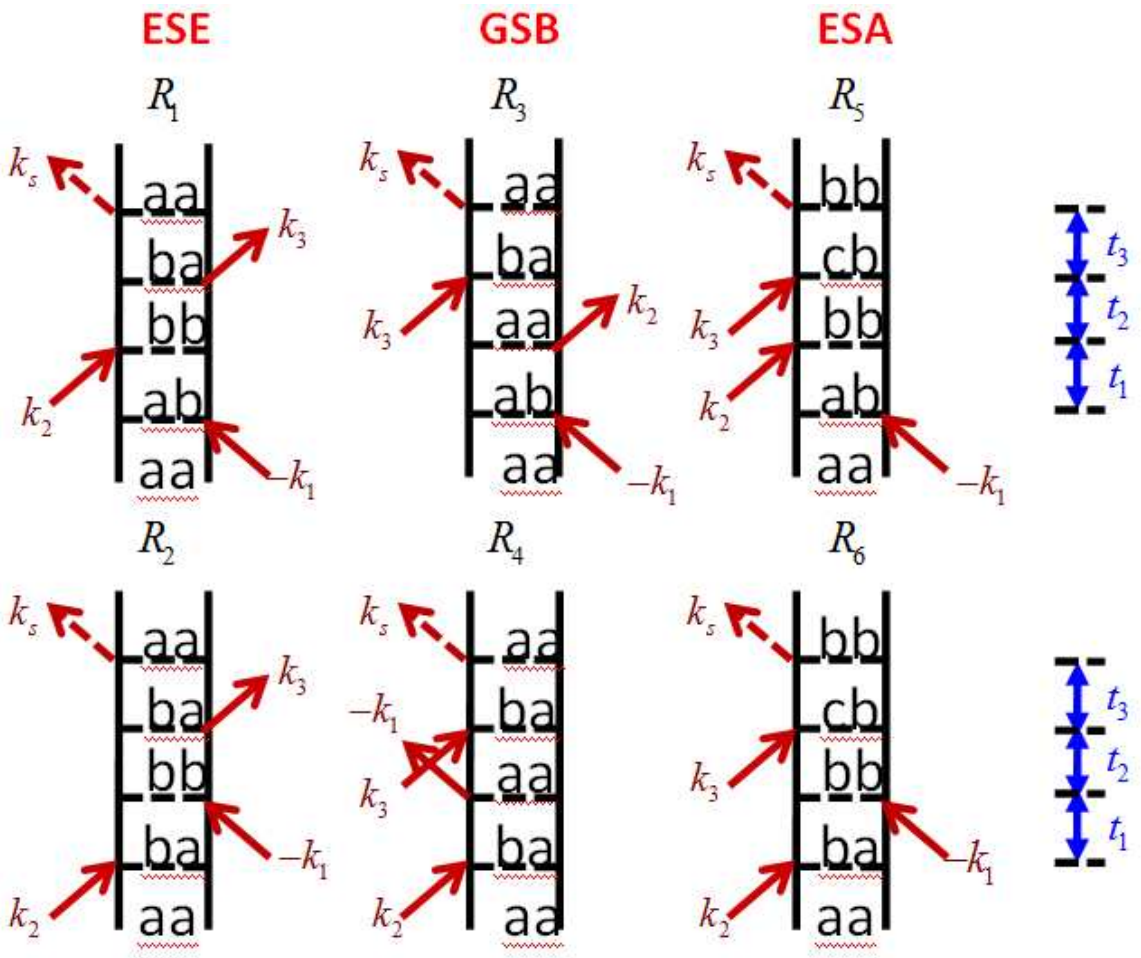

Figure 2.10. Feynman diagrams for a three level system where $E_a < E_b < E_c$. Time intervals t_1, t_2, and t_3 represent the time between interactions with the electric fields. The response function can be generated from each diagram and these can be summed and used to compute the polarization in the sample. Ground state bleach (GSB) and excited state emission (ESE) terms correspond to a decrease in absorption while excited state absorption terms show an increase in absorption (positive sign).

The calculated response functions for the three level system are adapted from Equation 2.101 and Figure 2.10. The six terms for a three level system are given by the following.

$$
\begin{aligned}
R_1(t_1,t_2,t_3) &= |\mu_{ab}|^4 \exp(-i\omega_{ba}t_1 - i\omega_{ba}t_3)\exp[-f_1(t_1,t_1+t_2,t_1+t_2+t_3,0)] \\
R_2(t_1,t_2,t_3) &= |\mu_{ab}|^4 \exp(i\omega_{ba}t_1 - i\omega_{ba}t_3)\exp[f_1(0,t_1+t_2,t_1+t_2+t_3,t_1)] \\
R_3(t_1,t_2,t_3) &= |\mu_{ab}|^4 \exp(i\omega_{ab}t_1 - i\omega_{ba}t_3)\exp[f_1(0,t_1,t_1+t_2+t_3,t_1+t_2)] \\
R_4(t_1,t_2,t_3) &= |\mu_{ab}|^4 \exp(-i\omega_{ba}t_1 - i\omega_{ba}t_3)\exp[-f_1(t_1+t_2+t_3,t_1+t_2,t_1,0)] \\
R_5(t_1,t_2,t_3) &= -|\mu_{ab}|^2|\mu_{bc}|^2 \exp(i\omega_{ab}t_1 - i\omega_{cb}t_3)\exp[f_2(t_1,t_1+t_2,t_1+t_2+t_3,0)] \\
R_6(t_1,t_2,t_3) &= -|\mu_{ab}|^2|\mu_{bc}|^2 \exp(-i\omega_{ba}t_1 - i\omega_{cb}t_3)\exp[-f_2(0,t_1+t_2,t_1+t_2+t_3,t_1)]
\end{aligned}
\tag{2.53}
$$

where

$$
\begin{aligned}
f_1(t_1,t_1+t_2,t_1+t_2+t_3,0) &= g_{bb}(t_1+t_2+t_3) + g^*_{bb}(t_2) + g^*_{bb}(t_3) + g_{bb}(t_1) \\
&\quad - g_{bb}(t_1+t_2) - g^*_{bb}(t_2+t_3) \\
f_1(0,t_1+t_2,t_1+t_2+t_3,t_1) &= g_{bb}(t_2+t_3) + g^*_{bb}(t_1+t_2) + g^*_{bb}(t_3) + g^*_{bb}(t_1) \\
&\quad - g_{bb}(t_2) - g^*_{bb}(t_1+t_2+t_3) \\
f_1(0,t_1,t_1+t_2+t_3,t_1+t_2) &= g_{bb}(t_3) + g^*_{bb}(t_1) + g^*_{bb}(t_2+t_3) + g^*_{bb}(t_1+t_2) \\
&\quad - g^*_{bb}(t_2) - g^*_{bb}(t_1+t_2+t_3) \\
f_1(t_1+t_2+t_3,t_1+t_2,t_1,0) &= g_{bb}(t_1) + g_{bb}(t_3) + g_{bb}(t_2) + g_{bb}(t_1+t_2+t_3) \\
&\quad - g_{bb}(t_1+t_2) - g_{bb}(t_2+t_3) \\
f_2(t_1,t_1+t_2,t_1+t_2+t_3,0) &= +g^*_{bb}(t_3) + g^*_{cc}(t_2) - g^*_{bb}(t_3) + g_{bb}(t_1+t_2) \\
&\quad + g_{bc}(t_1) - g^*_{bc}(t_1+t_2) - g^*_{bc}(t_2) \\
f_2(0,t_1+t_2,t_1+t_2+t_3,t_1) &= g_{bb}(t_3) + g^*_{cc}(t_1+t_2) - g^*_{bb}(t_3) + g_{bb}(t_2) \\
&\quad + g^*_{bc}(t_1) - g_{bc}(t_2) - g^*_{bc}(t_1+t_2)
\end{aligned}
\tag{2.54}
$$

The g-functions are from the correlation function approach to line broadening in Section 2.3.[4]

2.6. Transient Grating and Two Dimensional Spectroscopy

The response of the system to the applied electric fields has been treated. The specifics of the nonlinear spectroscopies will now be introduced. In Figure 2.11, the pulse timing configuration is shown for the experiments employed in this dissertation. This figure will be referenced upon several times in later chapters. Pulse 1 and 2 are

pump pulses and pulse 3 is the probe pulse. In Transient Grating spectroscopy the time delay between pump and probe, $T = t_2$, is scanned and the time delay between the pump pulses is held constant at zero, $\tau = t_1 = 0$. This experiment probes the dynamics of the excited state, such as energy transfer, internal conversion, and vibrational cooling. These mechanisms occur in the systems to be presented in later chapters. In two dimensional experiments, the time delay $t_1 = \tau$ is scanned; this scans the optical coherence between the ground and excited states in this three level system. The signal acquired as a function of time delay τ is then Fourier transformed into the frequency domain so that absorption signal is plotted as a function of pump and probe wavelength at a fixed time delay T, specifics of conducting an experimental two dimensional measurement are shown in Section 3.4.

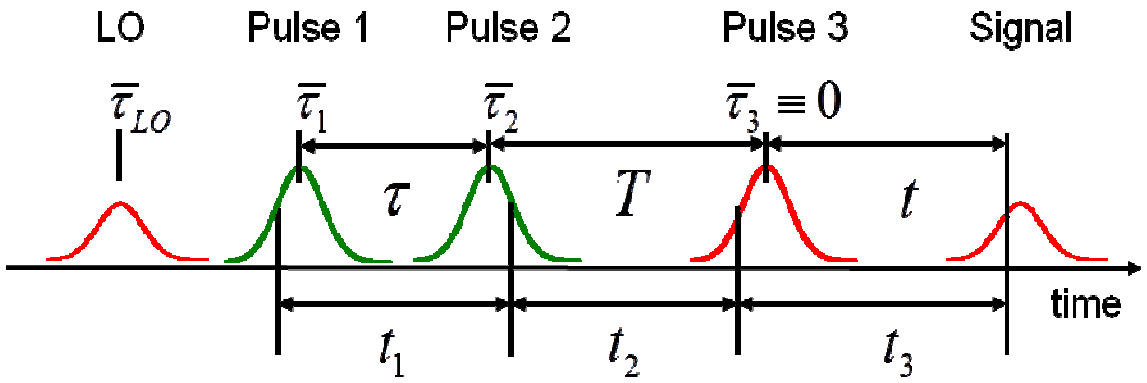

Figure 2.11. Timing scheme of laser pulses in the four wave mixing experiments implemented in this dissertation. For transient grating experiments, $\tau = 0$ and the time delay T is scanned until signal has fully decayed. In 2D experiments, T is held fixed and τ is scanned over a full range of positive and negative values to characterize the signal decay. The time delay t is a property of the solute and not experimentally controlled. LO is the local oscillator pulse used as the reference field for interferometric detection, this will be discussed further in Chapter 3, Section 4.

Two dimensional spectroscopy discerns the underlying mechanisms of line broadening in an ensemble, i.e. the degree of homogenous and inhomogeneous line

broadening. Homogeneous broadening is like being in the fast modulation limit for fluctuations and inhomogeneous broadening like the slow modulation limit. The ratio of diagonal, Γ_d and antidiagonal, Γ_{ad}, linewidths in a 2D spectrum characterize the type of broadening. In the inhomogeneous broadening limit for population times T that are small compared to the bath time scale, there is a large degree of correlation between the pumped and probed frequencies. In other words, dephasing has not yet randomized the correlation between pumped and probed frequencies. In this case $\Gamma_{ad}/\Gamma_d << 1$ and the two dimensional spectrum has an elliptical shape stretched along the diagonal line, $\omega_{t1} = \omega_{t3}$, as shown in Figure 2.12(a). For times much longer than the bath time scale, random thermal motions have washed out any correlation between the pumped and probed frequencies, i.e. each excited molecule has sampled the entire spectrum of possible energy gap values and $\Gamma_{ad}/\Gamma_d \approx 1$. This produces a circular 2D spectrum, as shown in Figure 2.12(b).

Two dimensional spectra are broken down into the six components shown in Figure 2.10. When two dimensional spectra being are being collected, time delays are scanned to probe the coherence between ground and excited states of the solute. Such coherence is a property of the ensemble and decays on the timescale of the inverse line-width of the electronic resonance in the absorption spectrum. To perform this experiment, the first time interval is scanned to measure the decay of the signal around $\tau = 0$. First, the delays are scanned when k_1 arrives to the sample before k_2, this is known as positive coherence time, or positive τ. This geometry is known as rephasing (RP) because the coherence is evolving with opposite sign in t_1 and t_3. The terms in the

top row of Figure 2.10 dominant this response. Signal must also be collected when k_2 arrives to the sample prior to k_1, or negative coherence time τ. This is known as the non-rephasing (NRP) geometry and the diagrams in the bottom row of Figure 2.10 dominate the response. The two components, RP and NRP, produce complex two dimensional spectra when Fourier transformed and the final absorptive two dimensional spectra is obtained by summing the real components of the RP and NRP measurements.

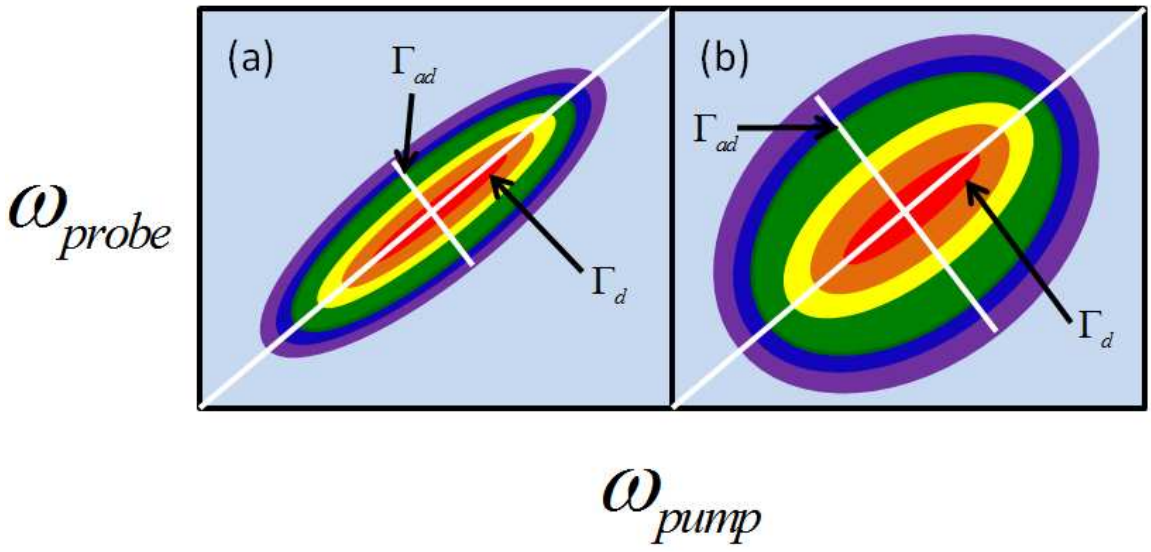

Figure 2.12. Cartoons representing the physics behind two dimensional spectra. (a) For times short compared to the relaxation timescale of the surroundings (decay time of correlation functions), Λ^{-1}, the pumped and probed dimensions are highly correlated and the ratio of antidiagonal to diagonal linewidth is very small ($\Gamma_{ad}/\Gamma_d \ll 1$). (b) System evolution in t_2 for periods longer than the bath timescale causes the spectrum to become circular and $\Gamma_{ad}/\Gamma_d \approx 1$.

The non-collinear geometry offered by the diffractive optics based experimental technique and detection in the $\mathbf{k_s = -k_1 + k_2 + k_3}$ phased matched direction affords the

ability to control the polarization of all three beams involved in the signal generation process as well as the polarization of the signal beam itself. This ability, unique to the four wave mixing geometries, allows for novel information to be gathered. As an example, a polarization condition known as 'magic angle' can be used in both four-wave mixing and standard two beam pump-probe techniques. In the magic angle configuration the pump and probe are polarized with a 54° angle between their polarizations. This allows for measurement of an isotropic response of the system, nuclear relaxation (such as rotational diffusion) does not contribute to the measured dynamics. When the pump and probe possess parallel polarizations, rotational diffusion creates decay in the observed signal with a time constant equal to that of molecular rotation, convoluting the decay dynamics with a process that is well understood and of little interest in present day research.

In a similar manner, the transient absorption anisotropy of the solute can be measured by comparing measurements of the system response when the pump and probe are parallel and when they are perpendicular. The anisotropy, $r(T)$, is computed as

$$r(T) = \frac{S_{ZZ}(T) - S_{XZ}(T)}{S_{ZZ}(T) + 2S_{XZ}(T)} \tag{2.55}$$

where S_{ZZ} is the system response with parallel pump and probe and S_{XZ} is the system response with perpendicularly polarized pump and probe. By comparing the parallel and perpendicular configurations, the anisotropy is sensitive only to relaxation processes that initiate a change in the transition dipole of the solute.[11-13] Transitions between electronic states possessing unique dipole orientation cause a decrease in the value of $r(T)$. Transition to another state causes S_{ZZ} to decrease, because the dipoles are no longer

aligned with the pump field, and causes S_{XZ} to increase because a transition to another electronic state resulting in a new dipole will interact more strongly with the probe beam that is perpendicular to the pump. Nuclear relaxation processes do not influence dynamics of the anisotropy in the Frank-Condon approximation making it an effective way to isolate electronic relaxation processes from nuclear solvation effects which sometimes occur on the same time scale. This chapter has laid from framework for understating the theoretical background of line broadening, relaxation mechanism, and introduction to the theory of the nonlinear spectroscopic techniques.

2.7. References

(1) Walter Greiner, L. N., Horst Stocker *Thermodynamics and Statistical Mechanics*; Springer-Verlag: New York, 1995.

(2) Sakurai, J. J. *Modern Quantum Mechanics* Addison Wesley Longman, 1994.

(3) Nitzan, A. *Chemical Dynamics in Condensed Phases*; Oxford Graduate Texts, 2006.

(4) Mukamel, S. *Principles of Nonlinear Optical Spectrscopy*; Oxford University Press, 1995.

(5) Tokmakoff, A.; Vol. 2013.

(6) Moran, A. M. 2008.

(7) Kubo, R. *Journal of the Physical Society of Japan* **1962**, *17*, 1100-1120.

(8) West, B. A.; Womick, J. M.; Moran, A. M. *J. Chem. Phys.* **2011**, *135*, 114505:1-114505:9.

(9) Lepetit, L.; Chériaux, G.; Joffre, M. *J. Opt. Soc. Am. B* **1995**, *12*, 2467-2474.

(10) Gallagher, S. M.; Albrecht, A. W.; Hybl, J. D.; Landin, B. L.; Rajaram, B.; Jonas, D. M. *J. Opt. Soc. Am. B* **1998**, *15*, 2338-2345.

(11) Qian, W.; Jonas, D. M. *The Journal of Chemical Physics* **2003**, *119*, 1611-1622.

(12) Fleming, G. R. *Chemical Applications of Ultrafast Spectroscopy*; University Press: New York, 1986.

(13) Farrow, D. A.; Smith, E. R.; Qian, W.; Jonas, D. M. *The Journal of Chemical Physics* **2008**, *129*, 174509-20.

Chapter 3 . Femtosecond Laser Pulse Generation, Characterization, and Experimentation in the Ultraviolet

Chapter 1 of this dissertation introduced the motivation and background for the science and systems that are to be studied. Investigating the ultrafast relaxation mechanisms of UV-absorbent molecules by implementing femtosecond two dimensional (2DUV) and Transient Grating spectroscopy at the shortest wavelengths and with the best time resolution of any lab in the world is the key accomplishment of this work. A theoretical foundation for understanding the relaxation processes and their signatures in experimental signals was presented in Chapter 2. Recall that a reduced description is implemented to treat the numerous degrees of freedom in the condensed phase with only a few variables in time correlation functions. This chapter will cover experimental issues including the amplification of femtosecond laser pulses, nonlinear optics, and the experimental methods used to study the systems of interest.

A foundational principle of laser pulse generation mechanisms is the nonlinear (parametric) interaction of photons is a polarizable medium. The polarization of a medium that an electromagnetic field is passing through can be expanded in powers of the electric field.

$$P = \chi^{(1)}E + \chi^{(2)}E^2 + \chi^{(3)}E^3 + \cdots \tag{3.1}$$

The second and third order polarizations will be defined as $P^{(2)} = \chi^{(2)}E^2$ and $P^{(3)} = \chi^{(3)}E^3$. Physical properties that occur as a result of $P^{(2)}$ tend to be distinct from

those associated with $P^{(3)}$. The second order polarization involves interaction of two photons which can produce laser light at frequencies equal to the sum or difference frequency value. [1] This process is illustrated in Figure 3.1.

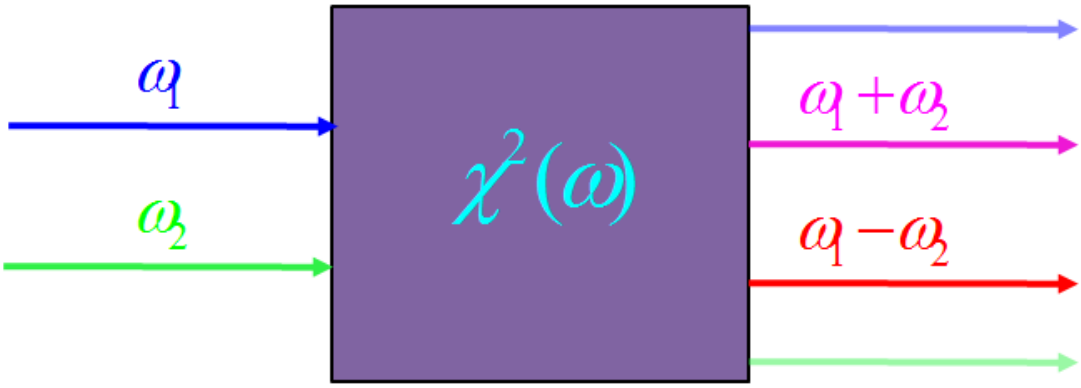

Figure 3.1. Second order parametric interactions can occur in a polarizable medium with a non-zero second order susceptibility, $\chi^2(\omega)$. This interaction occurs with high photon density typically accessible only by pulsed lasers. $P^{(2)} = \chi^{(2)}E^2$ describes the characteristics of this interaction, photons with the sum frequency and difference frequency are created. The photons ω_1 and ω_2 can come from the same or different laser pulses. In the special case when $\omega_1 = \omega_2$, the sum frequency generation process is known as second harmonic generation (SHG).

3.1. Chirped Pulse Amplification with Titanium Sapphire Gain Media

The parametric interaction of photons in nonlinear media allows access to a range of wavelength regimes from the far infrared to the X-ray.[2] However, in order for this process to occur, interacting photons must be in the same vicinity in time and space (i.e. high photon density). A robust gain medium and setup is needed to produce the laser pulses that drive nonlinear processes yielding pulses of tunable bandwidth and center wavelength. The amplified Ti:Sapphire (titanium doped sapphire) laser is ideally suited for generation of such pulses. The broad-bandwidth gain spectrum (700-1100nm), high thermal conductivity, and high energy storage density of Ti:Sapphire makes it an ideal

solid state laser material for use in pulsed lasers.[3] The demonstration of the self mode locked Ti:Sapphire laser was accomplished in 1990 by Sibbet and his group.[4] Amplified Ti:Sapphire lasers can reach terawatt output with pulses that are shorter than 20 fs.[3] The amplified Ti:Sapphire system in the Moran laboratory currently produces a 1.5W output (1.5mJ/pulse) with a pulse duration of 60fs. This power density is capable of driving nonlinear processes that produce 20fs, micro-joule pulses across the UV, visible, and infrared. This energy and bandwidth has been obtained in the UV by modifying the commercial laser system. A series of upgrades over the past two years has decreased the pulse duration from 180fs to 60fs. These upgrades are expanded on in Section 3.5.

The process of producing amplified Ti:Sapphire laser pulses starts with producing a 'seed' pulse. Such a pulse has desirable bandwidth, noise, and spatial quality. There are various ways to produce such pulses, including crystal and fiber based technologies. Typical seed pulses are generated by pumped Ti:Sapphire crystal-based lasers and produce 1-10nJ/pulse at a ~100MHz repetition rate. This pulse is then sent to the amplifier where the pulse energy is boosted by a factor of 10^6. However, a sub-100fs pulse at such high pulse energy is far beyond the damage threshold of the optics and the Ti:Sapphire crystals in an amplifier. To overcome this problem the pulse is first 'stretched'. The process of stretching involves sending the laser pulse through a series of bounces on gratings and focusing mirrors to force red wavelengths of the pulse to travel shorter distances than blue wavelengths. The pulse is now 'chirped' in time and its peak power density is much lower. Inside a typical amplifier pulses are 100s of picoseconds long making the power density manageable for the optics in the amplifier cavity.[3] This process of lowering the power density of a laser pulse by elongating it in time before

amplification is known as chirped pulse amplification and was originally implemented by Mourou and co-workers[5-7] utilizing optical compression techniques developed by Treacy and Martinez.[8-12]

Once the pulse has passed through the stretcher, it is ready for amplification. The first amplification step is the regenerative amplifier (regen). The regen is a cavity based, laser amplifier that relies on time-gated polarization optics to inject and eject the laser pulse. The low energy chirped seed pulse is injected into the cavity, makes approximately 20 round trips and is then ejected and sent to the next stage of amplification. The regenerative amplifier is typically used as the initial stage of amplification for a system that produces 50-100fs laser pulses with good spatial quality. Shot-to-shot intensity fluctuations are generally low in regenerative amplifiers because the gain of the seed pulse is readily saturated with facile control over the number of round trips in the cavity. However, the use of highly dispersive materials and gain narrowing in the regen makes recompression below 30fs almost impossible.[3] Typical gain values for regenerative amplifiers are $10^6 - 10^7$, resulting in up to 1-10mJ pulses after regenerative amplification. [13-21]

The next step in the amplification process is the multipass amplifier (MPA). In the MPA, the beam passes through the Ti:Sapphire gain medium multiple times without the use of a cavity; the geometry set by the optics determines the beam path and the number of passes. The particular geometry for utilizing a MPA varies between setups.[13,14,16,17] Multipass amplifiers are good for quickly boosting the pulse energies due to high gain without imparting as much dispersion as a typical regen. However, they are about half as efficient in terms of gain extraction (15% compared to 30% for the regen),

so a balance must be found between the tolerance of dispersion in the amplified pulses and how much pump laser power is required.[3] After amplification in these two stages the high energy laser pulse is then sent though a similar pattern of gratings and mirrors to compress the beam (i.e. synchronize arrival of all wavelengths within bandwidth). The result is a multi-joule femtosecond laser pulse that can be used to drive many nonlinear optical processes. Figure 3.2 shows the chirped pulse amplification process as described; values for repetition rate, power, and pulse duration correspond to the lab laser system.

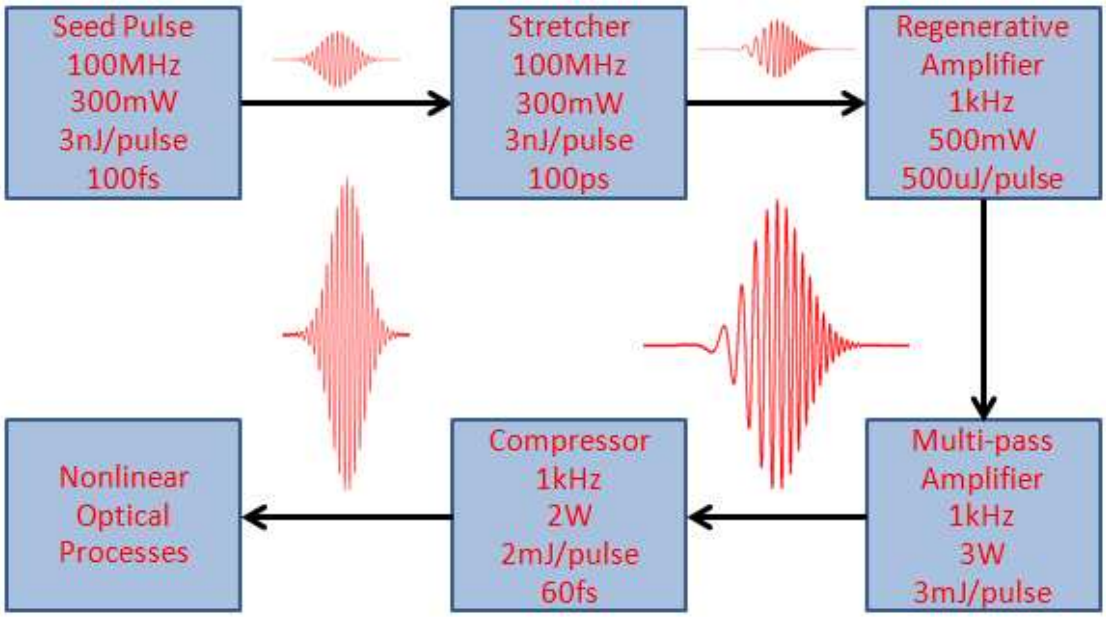

Figure 3.2. The process of generating an amplified, compressed, multi-joule laser pulse starts with the generation of a 'seed' pulse in a Ti:Sapphire oscillator. This pulse then goes through the stretcher, lengthening the pulse in time by a factor of 1,000. The pulse is then amplified in the regenerative amplifier and the multipass amplifier. After passing through the compressor, the laser pulse is 'short' and ready for use in experimentation. The values shown are from lab but are representative of typical amplifier values.[3]

3.2. Femtosecond Pulse Generation in the Ultraviolet: Fiber Capillaries and Filamentation

The previous section introduced the methods for creating a high-energy 'fundamental' laser pulse that forms the foundation for ultrafast spectroscopy

laboratories. These laser pulses are generally centered near 800nm and have a small tuning range.[3] In order to probe the physical properties of a variety of systems the ability to obtain short pulses across a large wavelength range is needed. Optical parametric amplifiers are commonly used to obtain femtosecond pulses across the visible and IR portion of the electromagnetic spectrum. Optical parametric amplifiers (OPAs) use a strong pump beam overlapped with a broadband 'seed' pulse to obtain the "signal" (seed meaning the desired femtosecond pulse, this seed pulse is distinct from that in Section 3.1, seed is a general term used to designate a beam to be amplified). By energy conservation, a third beam is created, the 'idler'. The name is derived from the fact that it is a product of amplification but not the pulse of interest. The equation for energy conservation is given as

$$\hbar\omega_p = \hbar\omega_s + \hbar\omega_i \tag{3.2}$$

Where $\hbar$ is Planks constant and ω_p, ω_s, and ω_i indicate the frequencies of the pump, signal, and idler beams respectively. For the interaction to be efficient all pulses must remain overlapped in time, this relationship is given by conservation of momentum (or phase matching) as

$$\hbar\mathbf{k}_p = \hbar\mathbf{k}_s + \hbar\mathbf{k}_i \tag{3.3}$$

The first step in this process of optical parametric amplification in the visible and infrared is the generation of the seed pulse, commonly known as 'continuum' generation. The process of continuum generation involves focusing a low energy pulse from the 800nm fundamental (~1μJ) into a transparent medium such as fused silica, calcium fluoride, or sapphire. Through the interaction of self-focusing and self-phase modulation, a large spectral broadening takes place.[22,23] Although the processes behind continuum

generation are not fully understood[24] the smooth spectrum, broad bandwidth, and low fluctuations of the broadened laser pulse are ideal for use as a seed in an OPA.

The next step in optical parametric amplification is combining the broadband seed pulse with a strong pump beam in a suitable nonlinear medium to produce the signal pulse. The nonlinear medium utilized depends on the desired properties of the amplified pulse as well as the desired tuning characteristics. Type I and Type II beta-barium borate crystals (BBOs) are suitable nonlinear media and can be used to obtain large bandwidths (Type I) or consistent bandwidth across a broad wavelength tuning range (Type II). The pump beam is typically either the fundamental wavelength (800nm) or the second harmonic of the fundamental (400nm). A 800nm pump is utilized for amplification of near- and mid-IR pulses while a 400nm pump beam is typically used to produce visible-wavelength signal pulses.[2]

When the pump and seed pulse possess the same wavevector when propagating through the nonlinear media, the aforementioned method is known as collinear optical parametric amplification. OPAs such as these can produce pulses from a few to dozens of μJs across the visible and infrared spectrum. The produced pulses have temporal widths generally no less than 30fs.[2] Considering the optical cycle is a few femtoseconds in the visible (lower limit to pulse duration), shorter pulses are desired to study the fastest relaxation processes and to push technological limits. Non-collinear optical parametric amplification (NOPA) is the process by which the seed and pump pulses are combined in the nonlinear medium with a slight angle between their wavevectors.[25] In this case, phase matching of the signal and idler pulses along the direction of propagation becomes

$$v_{gs} = v_{gi} \cos\beta \tag{3.4}$$

Where v_{gs} and v_{gi} are the group velocity of the signal and idler respectively and β is the phase matching angle. The angle β varies depending on the desired wavelength of the signal pulse but is typically on the order of a few degrees. Figure 3.3 shows how this phase matching angle maintains overlap of the pulses in the medium. Different group velocities of the signal and idler pulses limit the phase-matching bandwidth in a collinear geometry. The longer-wavelength idler pulse travels more rapidly than the shorter-wavelength signal; however, in a non-collinear geometry the small angle allows the pulse fronts to stay overlapped for a longer distance in the crystal medium. The shortest pulses generated by a NOPA setup obtained a pulse duration of 4.4fs.[26] In lab, NOPAs are utilized to produce sub-20fs pulses across the visible spectrum to study a variety of systems possessing ultrafast relaxation dynamics.[27-31]

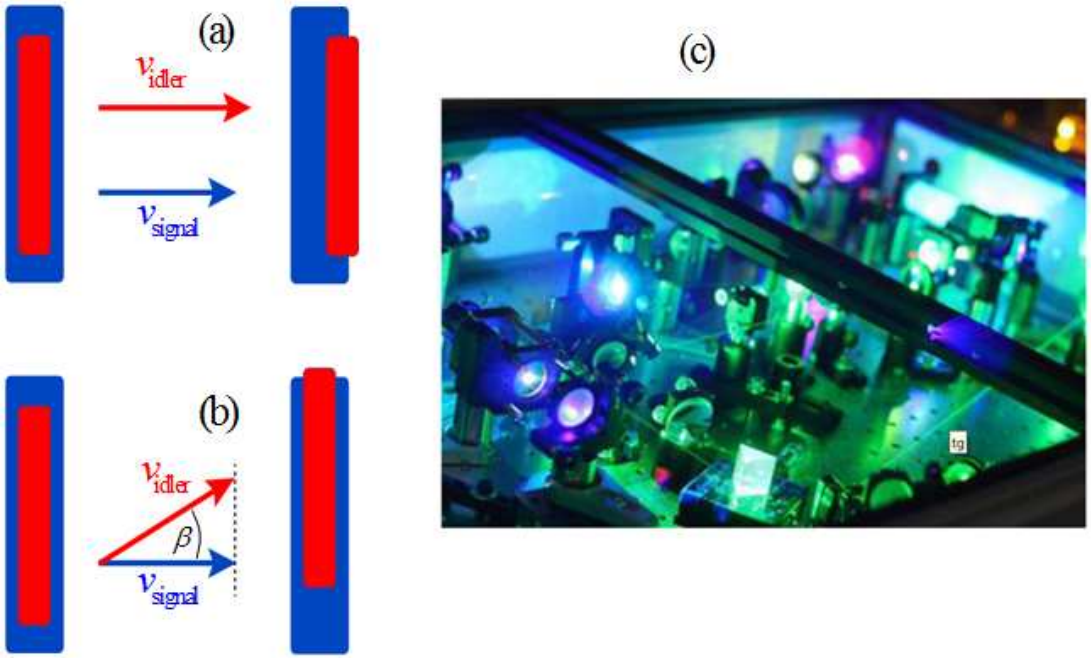

Figure 3.3. (a) In a collinear OPA the group velocity mismatch of the signal and idler pulse limit the bandwidth and energy that can be obtained in the amplification process. (b) In a NOPA, a slight angle β is geometrically introduced between the pump and seed pulse which allows the signal and idler pulses to remain overlapped for a longer distance in the crystal and broader bandwidths to be obtained. (c) NOPA in operation on optical table in Moran laboratory.

The desire to push optical parametric amplification techniques to higher wavelengths in the ultraviolet regime is thwarted by several factors. Many nonlinear crystals begin to absorb light in the UV spectral range and the group velocity mismatch between the signal and idler pulses becomes increasingly large, limiting bandwidth.[2] However, this did not stop researchers from extending visible and infrared OPA/NOPA techniques to the UV. Near ultraviolet pulses (NUV) created by sum frequency generation of the output from a NOPA with the amplified fundamental at 800nm made high energy, ~30fs pulses but only down to around 300nm.[32,33] The desire to produce pulses below 300nm led researchers to frequency double the visible output from a NOPA.[34] A special technique known as achromatic frequency doubling was able to overcome the narrow second-harmonic-generation bandwidth range that is physically inherent in BBO crystals by using prisms to generate a wavelength-dependent incidence angle on the BBO that created phase matching over a broad wavelength range. This method produced sub-10fs pulses tunable from 250nm-350nm but at the cost of low pulse energies and complicated setups.[35,36] It is desirable to have higher pulse energies with broad bandwidth to extend ultrafast spectroscopic techniques to the deep ultraviolet (DUV). Numerous experimental studies in photochemistry[37,38] and photobiology[39,40] would benefit from such technical advancement.

Preliminary work identified noble gases as an alternative nonlinear medium for generation of UV laser pulses to avoid the mismatch of group velocity between the interacting beams and absorption in the nonlinear medium.[41] The Kapteyn and Murnane group demonstrated the phase matched generation of UV pulses in argon-filled hollow core fibers.[42,43] Phase matching in the fibers is achieved by varying the pressure inside

the fiber. Pumping the hollow core fiber setup with 20fs pulses allows researchers to obtain 8fs 266nm output pulses.[44] Tunability in the DUV (214nm-244nm) was suggested by the same group through utilizing an OPA pulse in the parametric generation process,[45] and then demonstrated by Bradforth and co-workers utilizing 100+fs driving pulses.[46] These previously mentioned experiments all produced laser pulses at the third harmonic of Ti:Sapphire output and the work by Bradforth introduced tunability below 250nm for the first time. This body of work points towards the viability of combining hollow core fibers with existing nonlinear optical techniques to produce pulses useful for experimentation across a broad tuning range extending down to 200nm and below.[47]

In isotropic media such as air and noble gases, even ordered interactions such as second harmonic generation are forbidden and the lowest order nonlinear interaction is the third order interaction.[1] So called four-wave mixing (FWM) processes are responsible for parametric generation in such media (three input interactions and one signal beam). Difference frequency FWM to produce UV laser pulses is given by

$$\omega_{output} = \omega_f + \omega_f - \omega_{idler} \tag{3.5}$$

where ω_f is the fundamental frequency, ω_{idler} is the lower frequency pulse, and ω_{output} is the UV pulse. When $\omega_{idler} = \omega_f$, $\omega_{output} = 3\omega_f$ and the third harmonic is created at 266nm. Figure 3.4 shows the energetic interaction scheme and the output wavelength as a function of idler pulse wavelength, demonstrating the tunability shown in Reference [46].

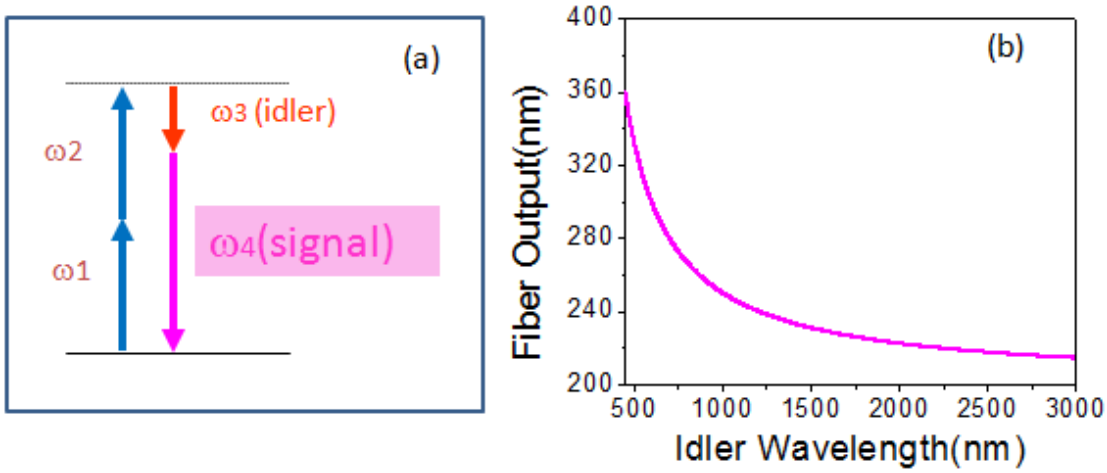

Figure 3.4. Four Wave Mixing (FWM) in isotropic media such as noble gases allows for third order interactions to occur. (a) The energy level scheme for the FWM interaction that can be utilized to produce UV laser pulses with broad bandwidth and high energy. (b) The output wavelength for a FWM process with a variable wavelength idler pulse according to the interaction given by Equation 3.5 is plotted. This plot shows how broad tunability can be introduced with the use of a NOPA pulse as the idler. **In this research, the idler wavelength is 800 nm and the third harmonic of Ti:Sapphire (267nm) output is the generated laser pulse.**

Given that high quality two dimensional and transient grating spectroscopies conducted with sub-50 fs pulses had not been implemented at UV wavelengths[48,49], this research aimed to study systems that had their lowest energy resonance near 267nm. In light of this and by following the design demonstrated by Jailaubekov *et al.* [46] a hollow core fiber was engineered and constructed to produce 20fs pulses at 267nm. Figure 3.5 shows the schematic of this setup.

A 90fs, 1mJ 800nm pulse is frequency doubled in a 0.25mm thick BBO crystal. These pulses are then chromatically separated and individually focused by 10" lenses into a 30cm long, 75μm diameter hollow core fiber (Polymicro TSP075375). The 10" lenses create a laser spot size at the entrance to the fiber that optimizes throughput through the fiber. The 800nm and 400nm pulses each have energy of 60μJ. A waveplate ("$\lambda/2$") is inserted in the path of the fundamental (800nm) beam to rotate its polarization parallel

with the second harmonic (400nm) pulse. A delay stage inserted in the path of the 400nm pulse allows for tuning of the path lengths so the pulses propagate through the fiber simultaneously. FWM inside the fiber creates approximately 1μJ of third harmonic (267nm) with a bandwidth of more than 1500 cm^{-1}. After the pulse is generated, it is separated from the other beams and sent through a combination of dispersion compensating mirrors (DCMs) and prisms to ensure the pulse is compressed at the sample position, ensuring the best possible time resolution. This setup is reported in published literature and reiterated in later chapters to show how the setup evolved.[50-52]

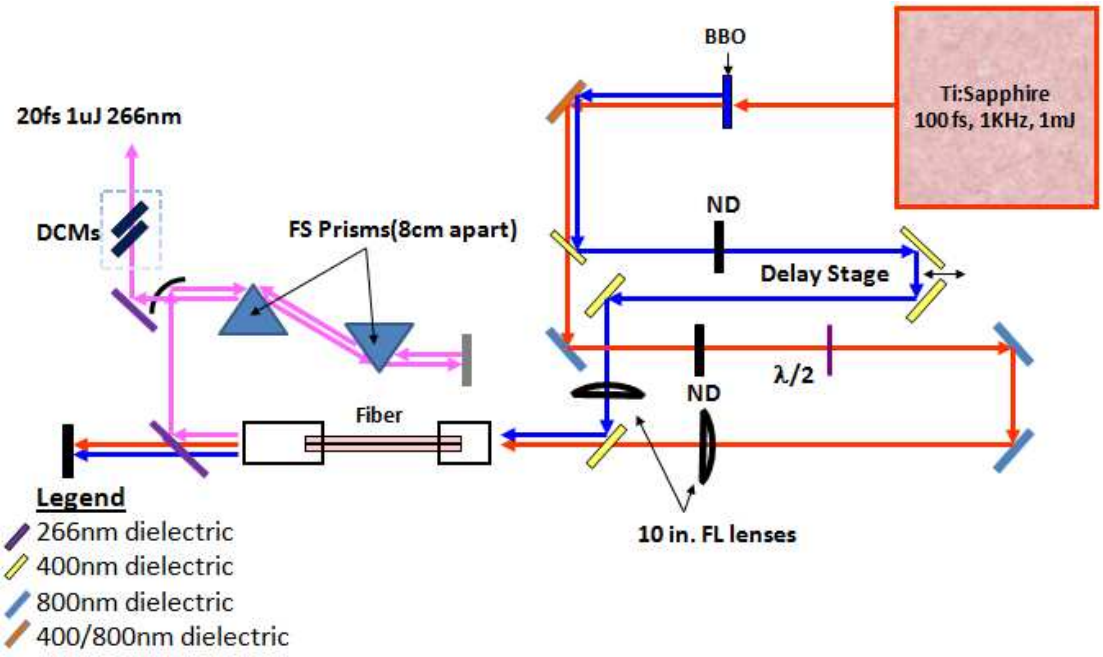

Figure 3.5. Schematic of third harmonic generation setup in the Moran laboratory. BBO is a beta-barium borate crystal used to generate 400nm from the 800nm fundamental pulse. ND indicates neutral density (wavelength independent) attenuators to control the energy of laser pulses entering the fiber. $\lambda/2$ is a waveplate used to control the polarization of the fundamental beam before it enters the fiber. PM is a parabolic mirror for collimating. Dispersion compensating mirrors (DCMs) and fused silica (FS) prisms are used to control the dispersion of the laser pulse.

Producing UV pulses with noble gases and hollow core fibers is highly advantageous to nonlinear optical crystals such as BBOs. Third harmonic pulses were

also produced by sum frequency generation in a BBO. Fundamental and second harmonic pulses were overlapped and the UV pulse energy and bandwidth was measured. While the UV pulse energy was very high (up to 60μJ), the duration was greater than 200fs. Figure 3.6(a) compares the pulse spectra obtained from parametric generation of 267nm in the hollow core fiber and sum frequency in a BBO crystal. It is obvious that the bandwidth from the hollow core fiber is much greater, thereby supporting shorter pulse durations. Figure 3.6(b) shows the hollow core fiber setup in operation.

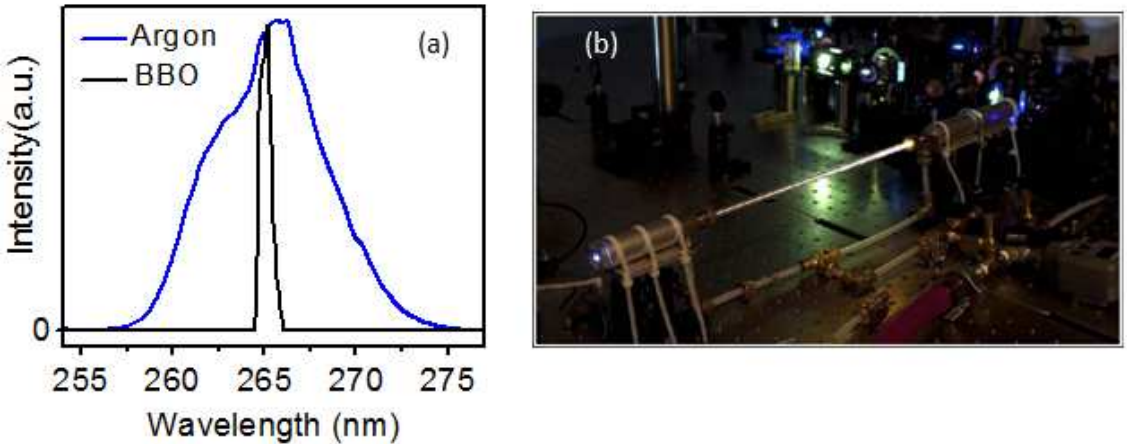

Figure 3.6. (a) Comparison of third harmonic laser pulses generated in 850Torr argon gas inside the hollow core fiber and those produced in BBO. The bandwidth of the hollow core fiber is much greater. (b) The home-built hollow core fiber setup in operation in the laboratory.

The spectrum shown for the third harmonic in Figure 3.6 (a) is taken with 850Torr of argon gas inside the fiber. Bradforth and coworkers published similarly broad third harmonic spectra with a 100fs fundamental pumping the setup and 250Torr of Argon.[46] Initial efforts involved pumping the third harmonic setup with substantially longer 180fs fundamental pulses. In order to obtain greater bandwidth, a higher pressure is used to achieve phase matching for the FWM process. Higher pressures are known to increase the self phase modulation (spectral broadening) of the input pulses which produces more bandwidth in the third harmonic pulse.[46] The ability to use this higher

pressure and still achieve phase matching is due to the multiple modes in which laser pulses can propagate through the fiber. The wavevector inside the fiber for light propagation is given by[53]

$$k(\lambda, P) = \frac{2\pi n(\lambda, P)}{\lambda}\left[1 - \frac{1}{2}\left(\frac{u_{nm}\lambda}{4\pi a}\right)^2\right] \tag{3.6}$$

where $n(\lambda, P)$ is the refractive index of argon (λ is the wavelength and P is the pressure), a is the fiber radius, and u_{nm} is the modal constant. Phase matched UV generation is achieved under the condition $\Delta k = 2k_{400} - k_{800} - k_{267}$ where the laser wavelengths are written as subscripts. Solving for $\Delta k = 0$ at 250Torr allows both the 800nm and the 400nm beam to be in the lowest order intra-fiber modes (EH_{11}). This is known as auto modal phase matching (AMP). However, solving for $\Delta k = 0$ at the higher pressure used in these experiments requires the 800nm and 400nm laser pulses to be in different higher order modes of propagation. This is known as cross modal phase matching (CMP).[54] Section 7.2.A contains a detailed study of CMP and AMP including solving the phase matching equation numerically, presenting output bandwidths, pulse energies, and images of the output laser pulses as a function of pressure. Also included is a comparison of hollow core fiber output bandwidth with the Quantronix Q-light seed laser (180fs duration for amplified pulse) and the Ti:Sapphire oscillator seed pulse (90fs duration for amplified pulse) which was implemented in the spring of 2012.

Cascaded third order processes have been shown to produce femtosecond laser pulses farther into the ultraviolet wavelength range at 200nm and 160nm.[47,54] Work by Misoguti and coworkers, briefly mentioned earlier, showed that focusing sub-30fs 800nm and 400nm beams inside a hollow core fiber produced output laser pulses at 200nm and

160nm via cascaded nonlinear interactions.[47] Third harmonic light is created via the interaction of 800nm and 400nm photons as $\omega_{266nm} = \omega_{400nm} + \omega_{400nm} - \omega_{800nm}$, the resulting 267nm light then interacts with 800nm and 400nm photons to produce 200nm light by $\omega_{200nm} = \omega_{266nm} + \omega_{400nm} - \omega_{800nm}$ or $\omega_{200nm} = \omega_{266nm} + \omega_{266nm} - \omega_{400nm}$. Further cascading can produce 160nm light, the fifth harmonic of Ti:Sapphire output, via several third order processes: 1) $\omega_{160nm} = \omega_{266nm} + \omega_{266nm} - \omega_{800nm}$; 2) $\omega_{160nm} = \omega_{200nm} + \omega_{400nm} - \omega_{800nm}$; and 3) $\omega_{160nm} = \omega_{200nm} + \omega_{266nm} - \omega_{400nm}$. Cascaded processes in hollow core fibers were tested using the setup described in Figure 3.5 and the resulting spectra obtained for the fourth harmonic are plotted in Figure 3.7. Broad spectra were obtained, despite the narrow bandwidth of the pump pulses (~90fs). The initial report by Misoguti on these cascaded processes commented on how they are efficient at producing broad bandwidths.[47] Although the spectra obtained had the necessary bandwidth for experimentation, the pulse energies and control over the spatial modes left much to be desired. Pulse energies less than 2nJ were obtained for the fourth harmonic generated in the hollow core fiber.

Filamentation is an alternative means of achieving high energy density in a nonlinear medium without restrictions on phase matching from mode propagation in fibers. Filamentation has been shown to be an effective way to leverage self phase modulation to spectrally broaden a strong 800nm fundamental pulse focused over a long distance.[55-57] Cascaded processes in filamentation that efficiently produce third and fourth harmonic pulses by pumping with the fundamental and second harmonic were demonstrated in 2009 by Fuji *et al.* [58,59] It should be noted that this was the only published research at the time producing 200nm laser light by filamentation. It should be noted that these researchers utilized a top of the line laser amplifier that produced 30fs

fundamental and second harmonic laser pulses. This allowed them to focus over long distances (>1m) to keep beam divergence low. Large beam divergence is known to degrade spatial quality after the filamentation process. This was attempted in the Moran laboratory with 90fs laser pulses and focusing over 10cm to achieve necessary power densities for filamentation formation.

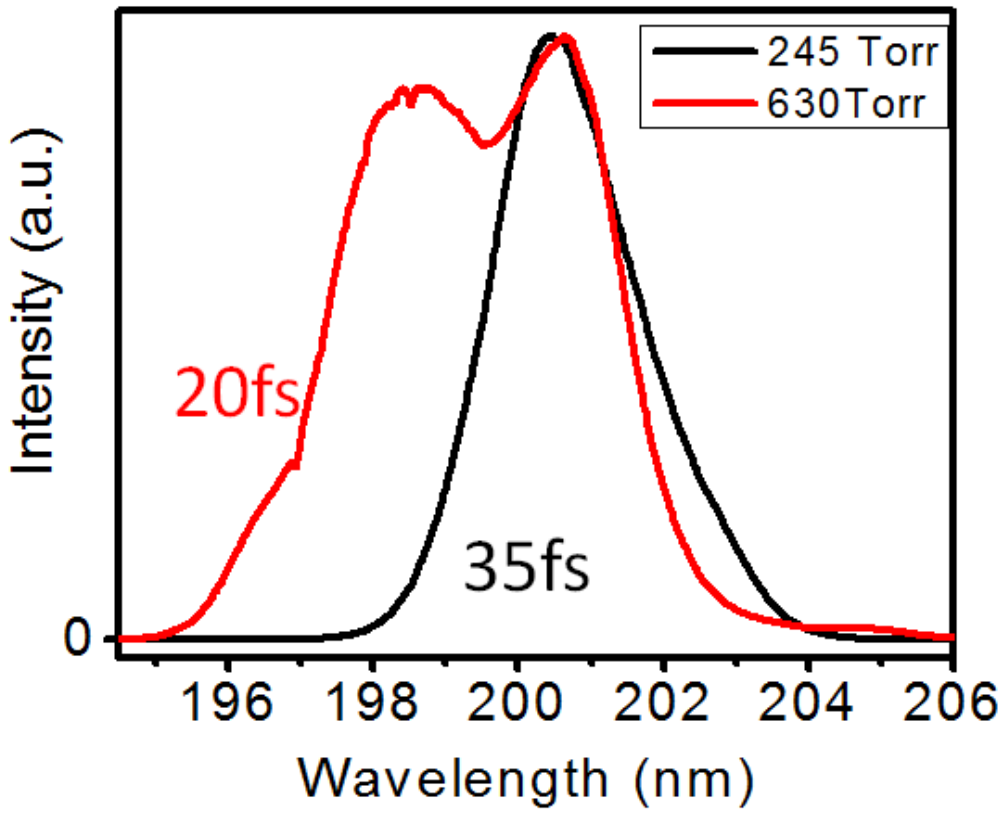

Figure 3.7. Fourth harmonic (200nm) pulses created via cascaded FWM processes in the hollow core fiber setup possessed desirable bandwidths but not enough pulse energy for experimentation.

A filamentation setup was constructed in which high energy fundamental and second harmonic pulses were overlapped temporally and spatially to produce a filament of both laser pulses. The setup, images of the filaments, and a spectrum of the fourth harmonic are shown in Figure 3.8. Pulses were generated at 200nm with 60fs durations and 300nJ pulse energies. A thorough presentation of the results from the filamentation

setup is presented in Section 9.2. This section examines the spatial profile of the output pulse and how the bandwidth and intensity characteristics of the 200nm pulse vary with pressure and nonlinear meduim (air vs. argon). It should be noted that the successful implementation of this techique with the described fundamental laser pulse characteristics is considered a breakthrough.

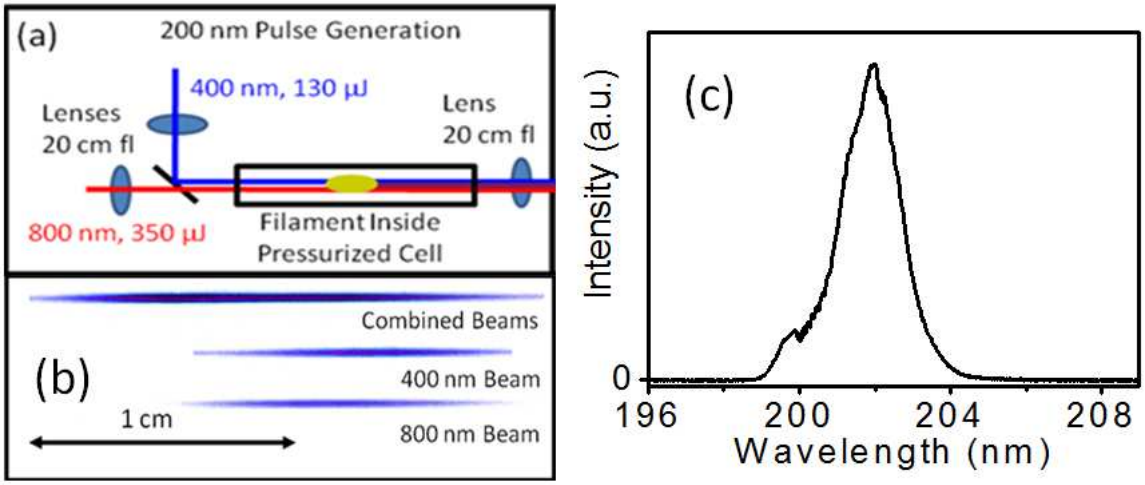

Figure 3.8. Results from filamentation setup for generating fourth harmonic pumped by the 800nm fundamental. (a) Setup for generation of 200nm pulse. 800nm and 400nm pulses are focused in air /argon to create filamentation and produce fourth harmonic. (b)The combined filament is twice as long as that for each individual beam. (c) The output spectrum for 200nm pulse.

3.3. Dispersion Management in the Ultraviolet

The process of parametric generation and propagation through lenses and other transmissive optics necessary to control laser pulses induces dispersion in the pulses. This is due to the wavelength-dependent refractive indices of all media involved (e.g., air, prisms, liquid solvents). It is well known that red wavelengths travel faster than blue wavelengths through transparent materials, thereby inducing a delay between the different colors of a laser pulse; this is called a “chirped” pulse. Positive (normal) chirp is defined as red wavelengths preceding blue; this is the common effect after propagation through transmissive media. Negative (anomalous) chirp occurs when the shorter

wavelengths within the laser pulse precede the longer wavelengths. In an experiment, it is desirable for all wavelengths of a laser pulse to arrive at the sample simultaneously, forming a 'compressed' pulse and maximizing time resolution. Therefore, it is imperative to be able to control how wavelengths are related to one another in time, in other words, the experimentalist must be able to control the spectral phase (also known as dispersion). This section will introduce the theory and methodology to compress femtosecond pulses for experimentation. This section is modeled after an intuitive discussion of this subject found in Reference [60].

In the time domain, the electric field for a Gaussian pulse with center frequency, ω_0, pulse duration, Δt, and phase, $\theta(t)$, is described by

$$E(t) = \sqrt{A_t(t)} \exp\left[-i(\omega_0 t + \theta(t))\right] + c.c. \tag{3.7}$$

where c.c. denotes the complex conjugate. In this time domain representation, $A_t(t)$ is the pulse envelope function, ω_0 determines the color, and $\theta(t)$ describes the temporal relationship among the different frequency components. The phase is responsible for the broadening effect in dispersive media and can be thought of as adding a complex width to the Gaussian envelope. While the time domain representation is intuitive for thinking about the pulse duration, calculating the effect of dispersive media on the pulse is problematic.[61] Due to properties of Fourier transformations, it is much easier to solve for the effects of dispersion in the frequency domain.[62] Performing a Fourier transformation on equation 3.7 yields the electric field expressed as a function of frequency, given by

$$E(\omega) = \sqrt{A_\omega(\omega)} e^{-i\varphi_{Pulse}(\omega-\omega_0)} \tag{3.8}$$

where negative field components have been neglected. In equation 3.8, ω represents angular frequency and $\varphi(\omega)$ describes the relation between the frequency components of the pulse. Angular frequency is converted to observable frequency v as $v = \frac{\omega}{2\pi}$. The uncertainty principle is given by $c_B = \Delta v \Delta t$. This describes the relationship between the bandwidth of a laser pulse and the shortest pulse duration which can be obtained. The coefficient c_B is known as a time bandwidth product and depends on the pulse profile. For Gaussian pulse envelopes, $c_B = 0.441$.

Now that the mathematical representation of an ultrafast laser pulse has been introduced, the effect of travelling through a dispersive medium needs to be quantified. The emerging pulse from a medium is given by

$$E_{out}(\omega) = E_{in}(\omega) R(\omega) e^{-i\varphi_{Mat}(\omega-\omega_0)} \tag{3.9}$$

Where $\varphi_{Mat}(\omega - \omega_0)$ is the spectral phase added by the material and $R(\omega)$ is an amplitude scaling factor which can typically be approximated by $R(\omega) \approx 1$ for transparent material.[61] It is common to express spectral phase as a Taylor expansion around the center frequency ω_0 as

$$\varphi(\omega-\omega_0) = \varphi_0 + \varphi_1 \cdot (\omega-\omega_0) + \varphi_2 \cdot \frac{(\omega-\omega_0)^2}{2} + \varphi_3 \cdot \frac{(\omega-\omega_0)^3}{6} + \ldots \tag{3.10}$$

In this expression for the spectral phase, φ_0 only adds a constant to the phase, the second term adds a delay to the pulse. The third and fourth terms are referred to as the group delay dispersion (GDD) and third order dispersion (TOD), respectively. It is these terms that alter the time duration (dispersion) of a laser pulse. Terms higher than the third order term will be neglected as they only play a role in highly dispersive materials or for

ultrabroad bandwidths, neither of which are used in the experiments presented in this dissertation. Using this Taylor expansion for the spectral phase and truncating at the third term allows equation 3.8 to be rewritten as

$$E(\omega) = \sqrt{A_{\omega}(\omega)}e^{-i(\varphi_{2,Pulse}+\varphi_{2,Mat})\frac{(\omega-\omega_0)^2}{2}} \tag{3.11}$$

showing that the phases in the frequency domain are simply additive. In this expression the term for TOD has been omitted, but these effects are additive in the same manner. In order to understand the effect that material dispersion has on the pulse duration Equation 3.11 must be Fourier transformed back into the time domain to yield $E_{out}(t)$.

$$E_{out}(t) = \sqrt{A_t^{'}}e^{\frac{4\ln 2 t^2}{2[\Delta t^2 + i4(\ln 2)\varphi_2]}} \tag{3.12}$$

By squaring equation 3.12 and comparing it to the general form for a Gaussian pulse envelope the equation for the output pulse duration as a function of un-chirped duration and GDD (φ_2) can be obtained as

$$\Delta t_{out} = \frac{\sqrt{\Delta t^4 + 16(\ln 2)^2 \varphi_2^{\,2}}}{\Delta t} \tag{3.13}$$

As a last step, Equation 3.13 is solved for GDD while replacing the transform limited pulse duration, Δt, with the bandwidth of the pulse giving an expression for the second order dispersion as a function of pulse bandwidth and duration

$$\varphi_2 = \frac{1}{4(\ln 2)}\sqrt{\left(\frac{c_B \Delta t_{out}}{\Delta v}\right)^2 - \left(\frac{c_B}{\Delta v}\right)^4} \tag{3.14}$$

where $\Delta\nu = c\Delta\lambda/\lambda^2$. Equation 3.13 provides a means to predict output pulse duration based on the Fourier transform limited pulse duration (or bandwidth) and the amount of GDD experienced by the pulse. Equation 3.14 computes the amount of GDD imposed on a laser pulse with bandwidth $\Delta\nu$ and output pulse duration Δt_{out}. Figure 3.9 uses equation 3.13 to investigate how GDD affects laser pulses of varying input duration (bandwidth). Panel (a) shows how, for a set amount of dispersion, shorter pulses have larger stretching factors ($\Delta t_{out}/\Delta t$) than longer pulses possessing less bandwidth. Panel (b) investigates how laser pulses in the UV are more sensitive to a set amount of GDD than are longer wavelength pulses. The Sellmeier equations below will enable calculation of the GDD associated with certain amounts of material so that one can predict the effect of passage through optics on the pulse duration.

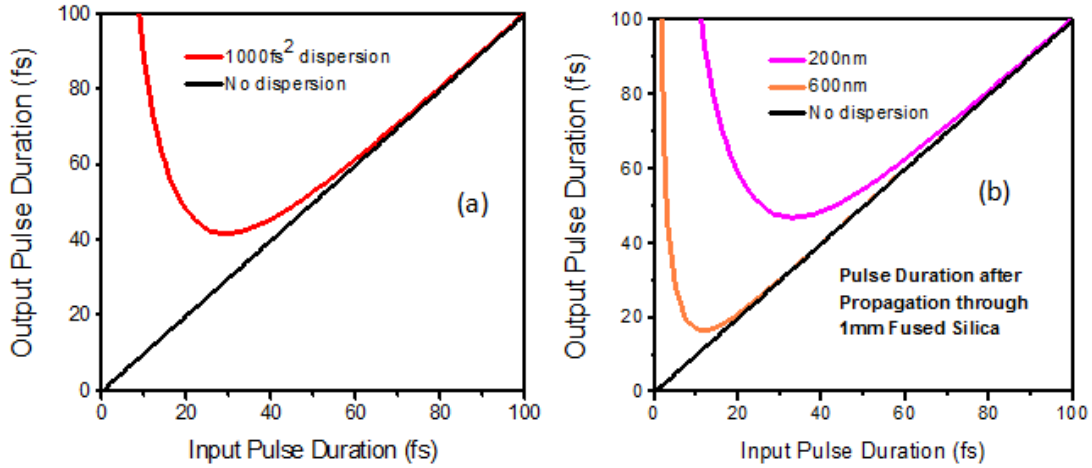

Figure 3.9. The effect of GDD is shown in panel (a). 1000fs^2 of dispersion has a significant impact on the pulse duration of pulses less than 40fs. A 20fs pulse is stretched by a factor of 2 due to this amount of dispersion, a 60fs pulse is barely affected. Panel (b) shows how pulses with shorter wavelengths are much more sensitive to a dispersive medium.

Now that the effect of GDD on laser pulse duration/dispersion can be calculated it is useful to be able to quantify and predict the amount of GDD a pulse will obtain after

propagation through a dispersive medium. The group velocity dispersion (GVD) is given by,

$$GVD = \frac{\lambda^3}{2\pi c^2}\left(\frac{d^2 n}{d\lambda^2}\right) \tag{3.15}$$

where $n(\lambda)$ is the wavelength dependent index of refraction. GDD is simply the product of GVD with the length of the material. The third order dispersion can similarly be calculated by

$$TOD = -\frac{\lambda^4}{4\pi^2 c^3}\left(3\frac{d^2 n}{d\lambda^2} + \frac{\lambda d^3 n}{d\lambda^3}\right) \tag{3.16}$$

where the total amount of accumulated dispersion is given by the product of TOD and the material length. The material index of refraction is needed to compute these quantities. The Sellmeier equation estimates refractive curves for materials. The equation is given by

$$n^2(\lambda) = 1 + \frac{B_1\lambda^2}{\lambda^2 - C_1} + \frac{B_2\lambda^2}{\lambda^2 - C_2} + \frac{B_3\lambda^2}{\lambda^2 - C_3} \tag{3.17}$$

where B_1, B_2, B_3, C_1, C_2, and C_3 are the Sellmeier coefficients. They are unique for each material and describe the characteristics of the refractive index curve.[63] By solving Equation 3.17 for any material such as fused silica (FS) or calcium fluoride (CaF_2) the effects on a laser pulse of known bandwidth, center wavelength, and pulse duration can be determined. FS and CaF_2 are common materials to use in the UV because of their high transmission rates and low dispersion properties. A table of Sellmeier coefficients for a large variety of materials can be found directly on CVI Melles Griot's website.[64]

The preceding section has introduced the methodology to quantify dispersion of a laser pulse due to propagation through a transmissive medium. The key point to take from this discussion is that the effects of dispersion are amplified as the bandwidth increases (pulse duration decreases) and as the center wavelength of the pulses gets shorter. Dispersion effects in the UV are half an order of magnitude greater than in the visible. The impact of third order dispersion (TOD) was bypassed in this section because a thorough discussion is given in Chapter 9 Section 2 which presents spectra showing the impact that varying amounts of TOD have on the spectral qualities of ultrafast laser pulses. The key point when considering TOD is to keep the amount of glass encountered by a laser pulse minimal. The next section will present the use of prisms to create a setup which has the opposite sign of GDD induced by transmission through optics. This allows the experimenter to cancel the effects of optics transmission and have a compressed pulse at the sample position.

Conventional methods of pulse compression involve the use of prisms and gratings.[61,65-67] Prisms impart a set amount of negative GVD and positive TOD per unit length of separation but cannot be used to compress pulses with very broad bandwidths (15-20fs is about the minimum) because the TOD imparted by the prism compressor setup is additive to transmission through optics (in contrast, prisms reverse effects of GDD from transmission through optics). Too-broad bandwidths or passage through too many optics will impart enough TOD to distort the pulse phase at the sample.[3] Grating compressors can tune the ratio of imparted GDD and TOD but have very low throughputs making them unusable for compression of low energy femtosecond laser pulses. Specially-coated dielectric mirrors known as dispersion-compensating mirrors impart

negative GDD and TOD with each bounce. DCMs are commonplace for compression of ultrabroadband laser pulses (bandwidth to support a <15fs pulse) in the visible regime and at the wavelength ouput of Ti:Sapphire amplifiers (near 800nm). These have also been demonstrated to be useful in the UV.[68] This research utilizes a setup that combines a fused silica prism compressor and DCMs to achieve optimal pulse compression, minimizing GDD and TOD.

The schematic showing how a prism compressor functions is shown in Figure 3.10. The incoming laser pulse has positive chirp meaning that red wavelengths precede blue wavelengths in time. This pulse hits the first prism, refracts and travels a distance d as the various wavelengths diverge from one another. At the second prism, the red wavelengths are forced to travel through a larger amount of glass, which delays them with respect to the blue wavelengths. After prism 2 the beam hits a flat mirror, M1, which reflects the beam back through the setup. Prism 2 causes the beams to converge back together at prism 1 and then exit the setup. M1 is slightly misaligned vertically so that the exiting pulse can travel either under or over M2. The output pulse actually possesses negative dispersion, blue wavelengths exiting first. Propagation through optics on the path to the sample will add positive dispersion which leaves the pulse compressed at the sample position.

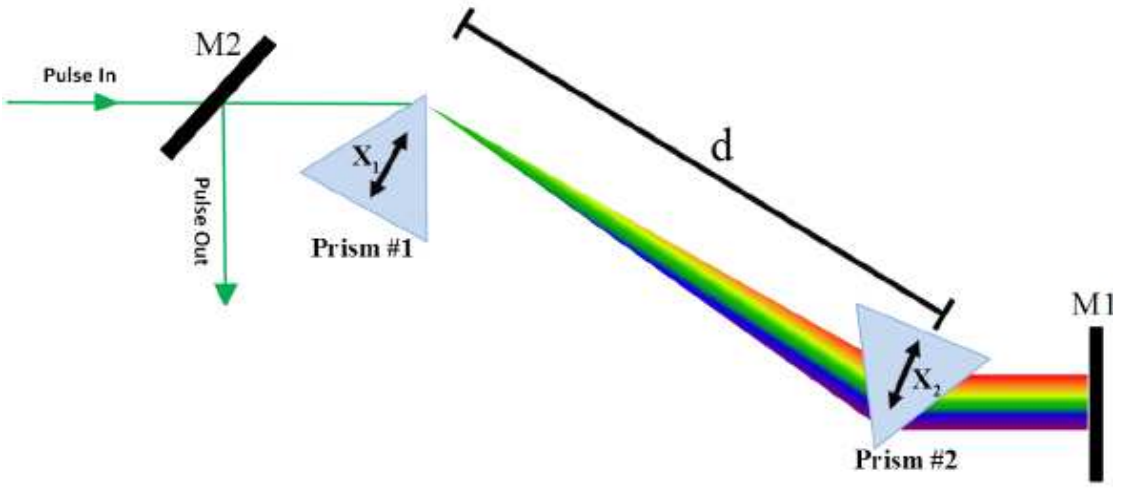

\

Figure 3.10. Prism compressor setup utilized in lab to impart negative GDD on femtosecond laser pulses. The input pulse is positively chirped and hits the first prism which refracts and causes the beam to diverge. Red wavelengths pass through more glass than do blue wavelengths in the second prism. M1 reflects the dispersed pulse back through the prism and M2 reflects it on towards the experiment.

The GDD imparted by a prism compressor is given by

$$GDD_{Prism} \approx \frac{\lambda^3}{2\pi c^2}\left[-8\mathrm{d}\left(\frac{dn}{d\lambda}\right)^2 + 4\left(\frac{d^2n}{d\lambda^2}\right)2D\right] \tag{3.18}$$

where λ is the wavelength of light, c is the speed of light, d is the tip-to-tip prism separation, D is the beam diameter, and n is the index of refraction of the prism material. In this expression, the first term is always negative and is proportional to the distance, d, between the two prisms. Thus, increasing the inter-prism distance increases the negative GDD accumulated by the prism compressor. The second term is always positive and is dependent on the path lengths through the prisms. This is easily controlled experimentally as one can simply move the prisms forwards and backwards in the beam (X_1 and X_2 in Figure 3.10). The net result is a setup with tunability in three dimensions: d, X_1, and X_2 which allow the experimenter to eliminate GDD and minimize TOD in the laser pulse. A given configuration of the prism compressor produces unique values of

GDD and TOD. Typically the experimenter minimizes GDD with the compressor setup. TOD can be reduced by minimizing the amount of optics encountered by the pulse.

3.4. Four Wave Mixing Interferometry: Transient Grating and Two Dimensional Spectroscopy

The previous sections have demonstrated how a femtosecond laser pulse is affected by the nonlinear parametric generation processes and transmission through dispersive media. Techniques used to reverse these effects and have all wavelengths arrive simultaneously at the sample were also introduced. This section will present the methods of four wave mixing interferometry which are used for pulse characterization and experimentation. First, the instrument used to undertake the two dimensional and transient grating spectroscopies in this dissertation will be presented since it is used for pulse characterization as well as experimentation on the samples. These experiments can be thought of as a more complicated version of pump-probe spectroscopy where a pump pulse excites a small fraction of molecules in an absorbing medium and then a probe pulse monitors the change in absorption induced by this excited state. The delay between pump and probe is scanned to observe how the system returns to equilibrium (steady state absorption). The key difference in these experiments is that the signal pulse is emitted in a background-free direction and there are two pump beams. A fourth beam (local oscillator, LO) is geometrically aligned (by the experiment) with the signal beam and allows for interferometric detection of emitted signal. A close-up picture of the view at the sample is shown in Figure 3.11

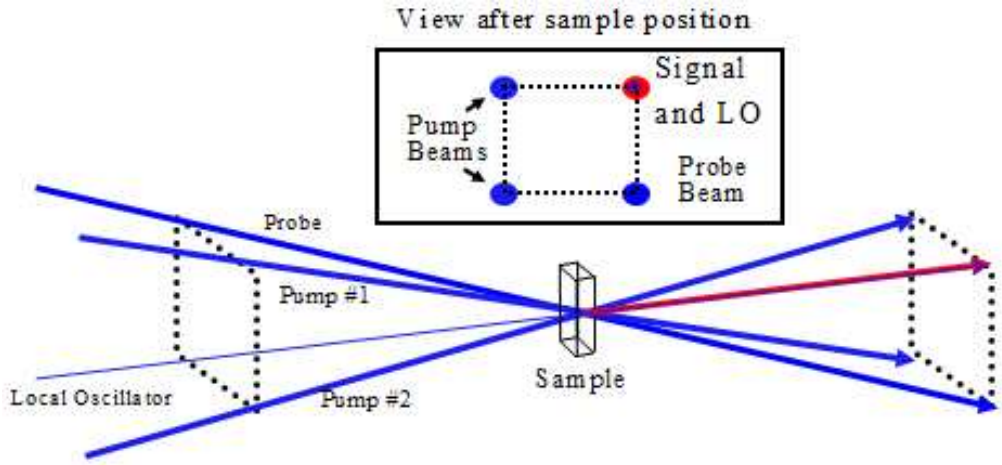

Figure 3.11. The view of the nonlinear experiments employed in lab to highlight the differences with traditional pump probe spectroscopy. In pump probe spectroscopy, only two beams are utilized, a pump pulse and a probe pulse. Key features of this setup are background-free and interferometric signal detection. Three laser pulses (2 pump, 1 probe) induce signal emission.

There are a few approaches to Fourier transform 2DUV techniques. The first is a two-beam geometry based on pulse-shaping technology and is very similar to that shown in Figure 1.2(similar to pump probe geometry).[49,69] The other is a passively-phase-stabilized diffractive-optic-based interferometer employing four pulses, where one pulse is used as a reference for interferometric signal detection.[52,70] The basic configuration of the diffractive optics based interferometer is shown in Figure 3.12.

The key to interferometric stability is to generate pairs of phase-related pulses at the sample.[71,72] Any instability in the reflections off of the spherical mirror cancel so the setup is immune to noise associated with vibrations and thermal motion that would otherwise randomize the relative phase of the signal field and the laser pulse used as a reference beam. This geometry is preferred because in transient grating mode the setup can scan to hundreds of picoseconds delay between pump and probe pulses. Figure 2.11 in chapter 2 shows the standard method of pulse timing and naming of the delays. **Transient grating mode scans the pump probe delay, T , whereas two dimensional**

spectroscopy scans the delay between pulses 1 and 2, τ. Non-radiative transitions occur in T, the pump is absorbed in τ, and signal is radiated in t. Scanning τ is accomplished by inserting or removing glass in the path of the laser pulses through the

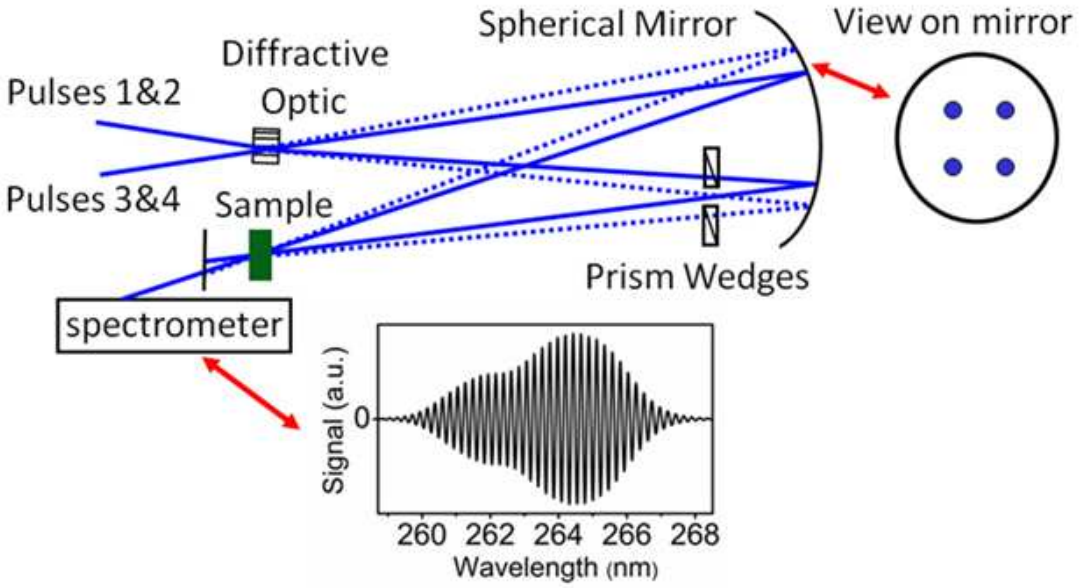

Figure 3.12. Basic schematic of the four wave mixing interferometer. Two pulses are sent into the setup with a mechanically controlled delay between them. The pulses are focused onto a diffractive optic to create the beam pattern shown on the mirror. The four beams are then sent to the sample (see Figure 3.11). Prism wedges are inserted into the paths of pulses 1 and 2 to control their relative delay. This delay is scanned in 2DUV experiments. All four beams are incident at the sample; pulses 1, 2, and 3 induce signal emission and pulse 4 is used as a reference field for interferometric detection of the signal. A typical interferogram is shown.

use of prism wedges as shown in Figure 3.12. The delay τ is typically scanned to $|\tau| < 100\ fs$, as the signal decays with a time constant of roughly 50fs.[52,70] The signal as a function of τ is then Fourier transformed at each detected pixel on the CCD detector to obtain the two dimensional spectra that are shown throughout this dissertation. 2D spectra can be taken at any pump-probe delay time T. Comparing the shape of 2D spectra (antidiagonal/diagonal line-width) as T varies reveals the timescale of solvent reorganization (solvation), vibrational cooling, and coherent vibrational motion.[51,52,73,74]

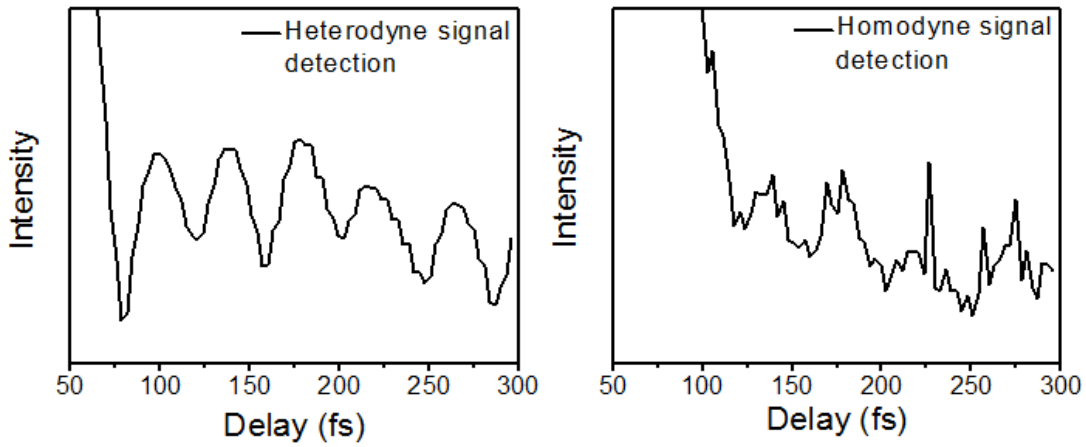

Figure 3.13. Measured transient grating signal profiles as a function of pump probe delay. The left figure is taken with interferometric detection and the right with homodyne detection (i.e. collected without the local oscillator). The amplification of the signal with heterodyne detection is obvious. The observed modulation in the signal is due to coherent oscillation of the 800 cm^{-1} Raman active mode in cyclohexane.

Considering that the signal is interferometrically detected, it is necessary to separate the contribution of the reference field from the detected field so that only the third-order signal of interest remains. This method of signal collection is known as optical heterodyne detection (OHD). The measured interferogram is given by

$$I = \left|E_{ref}\right|^2 + \left|E_S(t)\right|^2 + 2\left|E_{ref}E_S(t)\right|\cos(\phi_{ref} - \phi_S) \tag{3.19}$$

where E_{ref} is the reference field, $E_S(t)$ is the time dependent signal field, and ϕ_{ref} and ϕ_S are the phases of the reference and signal fields, respectively. [71,75] In the experiments discussed herein, the reference field term is numerically removed through a Fourier transform/apodization routine. This routine Fourier transforms the measured interferogram into the time domain, selects the signal via a Gaussian apodization function, then Fourier transforms this signal back into the frequency domain. In the limit of the reference field intensity being much greater than the signal intensity (i.e.,

$\left|E_{ref}\right|^2 \gg \left|E_S(t)\right|^2$) the term $\left|E_S(t)\right|^2$ can be neglected, this is a typical case in the laboratory,. This reduces the measured signal intensity to the following

$$I = 2\left|E_{ref} E_S(t)\right| \cos(\phi_{ref} - \phi_S) \tag{3.20}$$

Equation 3.20 shows that the measured interferogram is linear with respect to the signal field and the components of the phase of the reference field and signal are present. These components allow for full characterization of the signal field (i.e. separation into real and imaginary components). The real component of the measured signal is identical to the measured signals in pump-probe spectroscopy. Furthermore OHD amplifies the signal by a factor of $2\left|E_{ref} / E_S(t)\right|$ compared to the homodyne signal (signal collected without interferometric detection).[75] Figure 3.13 demonstrates this by plotting the acquired signal for cyclohexane as the pump-probe delay is scanned. The observed oscillations in time are due to coherent motion of the 800 cm^{-1} Raman active vibrational mode of cyclohexane. The only change made between the two measurements was the reference field was blocked for homodyne signal collection. It is quite obvious that the observed signal-to-noise ratio in the case of interferometric detection is much better. Being able to resolve this particular vibrational coherence with such deep modulation requires a laser pulse with a duration that is at most half of the vibration period. The period of oscillation for this mode in cyclohexane is 42fs which is a strong internal check to ensure that the laser pulses are on the order of 20fs.

Now that the experimental setup and signal detection have been introduced, samples are ready to be studied and new physics explored. However, before measuring signals that carry information on relaxation dynamics of UV absorbent materials, the

experimentalist must ensure that the laser pulse is properly compressed, well behaved, and ready for experimentation. The process of Frequency Resolved Optical Gating (FROG) allows the phase of the laser pulse to be determined by using the pump pulses as a 'gate' which induce signal generation in the four wave mixing experiment only when all three pulses are temporally overlapped in the sample.[66] This process simply involves placing a transparent medium at the sample position and scanning the pump-probe delay. When all pulses are overlapped in time and space in the sample, signal generation occurs. The signal profile as a function of delay is given by the spectrogram

$$I_{FROG}^{TG}(\omega,T)=\left|\int_{-\infty}^{\infty}E(t)\left|E(t-T)\right|^{2}\exp(-i\omega t)\,dt\right|^{2} \tag{3.21}$$

where the delay between pulses is given by T and it is assumed that all pulses are the same wavelength. Two pulses, $\left|E(t-T)\right|^{2}$, act as a gating function for the third field, the probe pulse in Figure 3.11. Since the spectrogram is resolved in frequency and time, the phase of the pulse can easily be observed. A chirped laser pulse will show tilt in the spectrogram where a compressed pulse shows all wavelengths arriving simultaneously at the sample position. Measuring a FROG spectrogram allows the experimenter to determine is the laser pulse is compressed. Figure 3.14(a) shows a spectrogram of the compressed third harmonic pulse. Panel (b) is another plot of the interferometrically detected oscillations from cyclohexane.

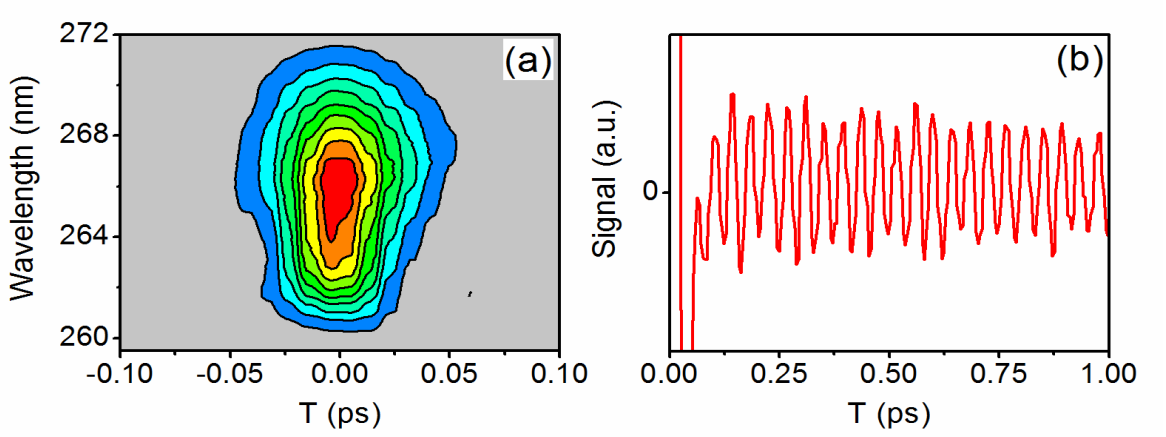

Figure 3.14. (a) Compressed third harmonic FROG spectrogram measured in the experimental setup with homodyne detection. All wavelengths arriving simultaneously (vertically aligned spectrogram) indicates proper pulse compression. (b) View of vibrational coherence of cyclohexane over a larger delay range than in Figure 3.13.

All of these studies utilize dynamic sample volumes to avoid damage from UV excitation. Studies on the DNA nucleobases presented in Chapter 4, 5, and 6 implement a low-noise rotating sample holder, modeled after that described in Reference[76]. The sample holder enables the use of small sample volumes and can be adapted to the cryostat, which is useful for measurements at cryogenic temperatures. The transient grating measurements shown in Figure 4.4 demonstrate that motion of the sample causes fairly little noise in the signal phase. For example, with a peak power of 1.4GW/cm^2, signal-to-noise ratios of 350:1 at T=0.5ps and 38:1 at T=100ps in the absorptive transient grating signal component are obtained (the absorptive signal component is sensitive to phase noise). A gravity fed jet is utilized in Chapters 7 and 8. Section 7.2B contains background on this setup.

3.5. Ongoing Technical Developments

In the Fall of 2009 when I first started work in the Moran lab, the laser fundamental was seeded by a fiber oscillator from Quantronix called the Q-light. This

seed laser, while very stable and requiring little maintenance, only produced enough bandwidth to make 150+fs amplified pulses. This bandwidth is non-tunable. In the spring of 2012, the Moran lab laser system was upgraded by building a Ti:Sapphire seed laser to provide the seed pulse to amplify in the commercial Quantronix system instead of amplifying the pulse from the Q-light. Figure 3.15 compares the output spectra from the fiber and Ti:Sapphier oscillators. Research conducted in Chapters 4, 5, and 6 were undertaken with 25fs, 267nm pulses driven by 150+fs fundamental pulses produced with the Q-light. Chapter 7 and 8 utilized the upgraded Ti:Sapphire seed laser to produce 20fs 267nm pulses and 60fs 200nm pulses.

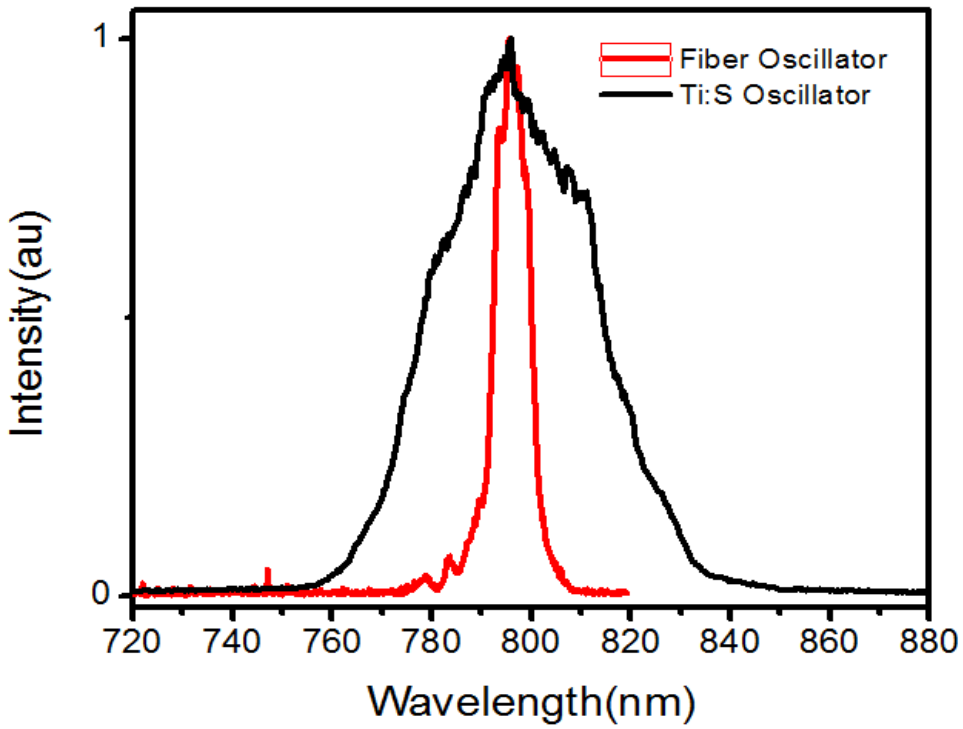

Figure 3.15. Comparison of original Q-light fiber oscillator spectrum with the Ti:Sapphire oscillator spectrum installed in the spring of 2012. The bandwidth of the Ti:Sapphire oscillator is more than four times that of the fiber oscillator (and this is a conservative spectrum for the new oscillator).

At this point the seed laser was no longer the limiting factor in amplifying a broader bandwidth fundamental. The stretcher and compressor from Quantronix were not engineered to handle the broad bandwidth from a Ti:Sapphire laser pulse. The laser

beam was clipped edge of mirrors when the beam was dispersed in the stretcher and compressor. Figure 3.16 shows the laser pulse at different stages in the amplification process. The skewed (non-Gaussian) shapes indicate that the stretcher and compressor cut off a significant part of the bandwidth. Still, this upgrade produced an amplified fundamental pulse that was approximately 90fs when fully optimized.

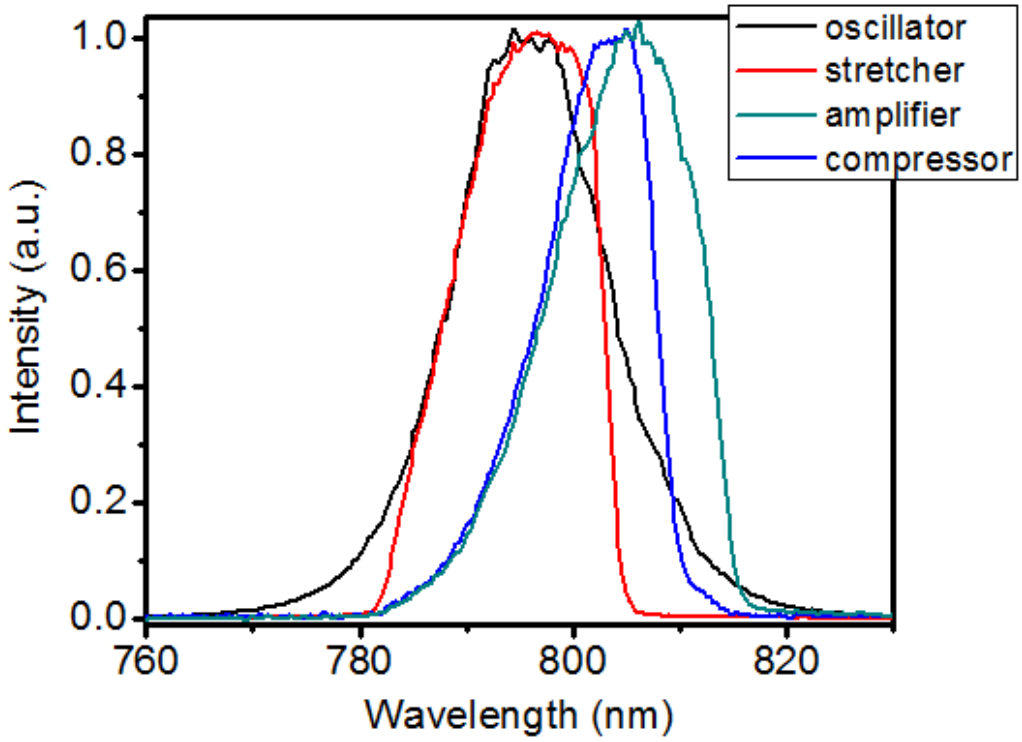

Figure 3.16. Spectra taken inside the Quantronix laser amplifier. The oscillator spectrum shows the Ti:Saphhire seed pulse from the laser that was installed in lab Spring 2012. The 'stretcher' pulse shows clipping on the red side of the spectrum. The 'amplifier' demonstrates the typical red shift observed between the amplified laser pulse and the seed pulse. This is due to the chirped pulse amplification technique. Red wavelengths precede blue wavelengths in the amplifer and are more strongly amplified. Comparing the 'compressor' pulse to the 'amplifier' pulse shows how bandwidth is further cut off by the optics in the compressor. After moving the stretcher and compressor outside the amplifier, this clipping was eliminated.

In the spring of 2013, the original stretcher and compressor were modified and rebuilt outside the commercial amplifier box and several optical elements purchased

which were able to handle the broader bandwidth. Recent experimentation has indicated that the compressed pulses from the Quantronix amplifier in lab are 60fs. This opens up new realms of possible nonlinear optical processes and bandwidth generation. Future research will most likely focus on enhancing the time resolution and experimental capabilities at 200nm, the beginning of the vacuum UV spectral range. The 200nm spectra presented above in Figure 3.8 were identical to those used to undertake investigations that are presented in Chapter 8. Figure 3.17 compares the pulses generated in the fall of 2012 with those recently generated in spring 2013 after the stretcher and compressor were rebuilt outside of the laser amplifier. It is clear that the bandwidth after the recent upgrade is superior and experimentation has measured the 200nm pulses to have a time duration of 30fs, one half the previous duration. Current research is attempting to spectrally broaden the 800nm pulse before 200nm generation to further increase bandwidth, thereby decreasing 200nm pulse duration.

At this point the foundations have been laid to understand the experimental investigations presented in the following chapters, all of which are publications in peer reviewed journals. The following chapters will present two dimensional and transient grating spectroscopies conducted at the third and fourth harmonic of Ti:Sapphire laser output with by far the greatest sensitivity and time resolution reported to date.[73] The experimental work reported herein presents first steps towards the UV in extending two dimensional spectroscopy 'from NMR to x-rays".[77]

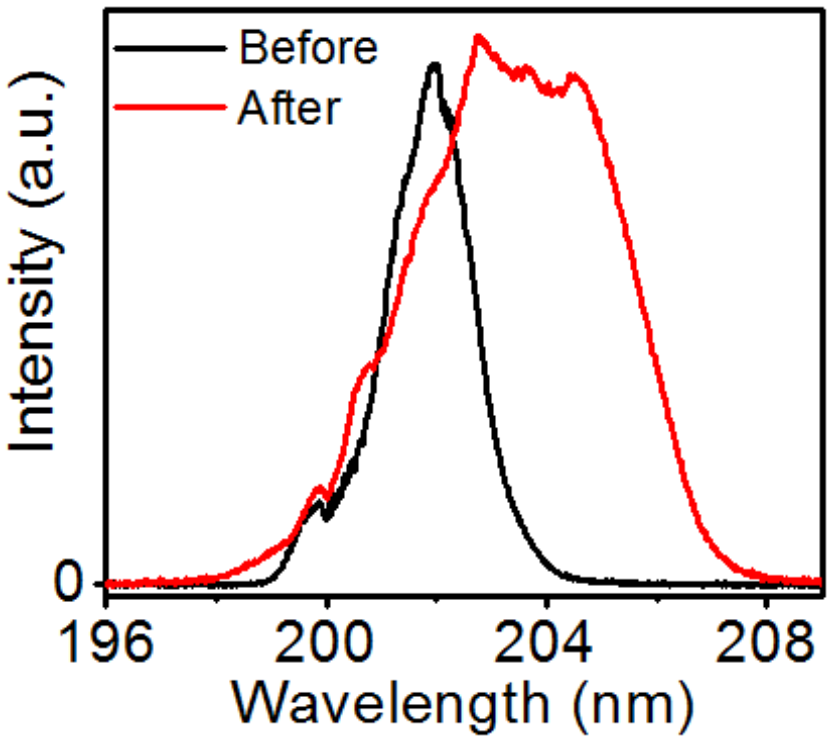

Figure 3.17. Shown are fourth harmonic spectra taken before and after the upgrade to the laser amplification system in spring 2013. Recent measurements have indicated that 200nm pulses possess a time duration of 30fs. Further work is being undertaken to push this lower and utilize these pulses for experimentation.

3.6. References

(1) Boyd, R. W. *Nonlinear Optics*; Third ed.; Academic Press: London, 2008.

(2) Cerullo, G.; De Silvestri, S. *Review of Scientific Instruments* **2003**, *74*, 1-18.

(3) Sterling, B.; Charles, G. D., III; Margaret, M. M.; Henry, C. K.; AIP: 1998; Vol. 69, p 1207-1223.

(4) Spence, D. E.; Kean, P. N.; Sibbett, W. *Opt. Lett.* **1991**, *16*, 42-44.

(5) Strickland, D.; Mourou, G. *Optics Communications* **1985**, *56*, 219-221.

(6) Maine, P.; Strickland, D.; Bado, P.; Pessot, M.; Mourou, G. *Quantum Electronics, IEEE Journal of* **1988**, *24*, 398-403.

(7) Pessot, M.; Maine, P.; Mourou, G. *Optics Communications* **1987**, *62*, 419-421.

(8) Martinez, O. E.; Gordon, J. P.; Fork, R. L. *Journal of the Optical Society of America. A, Optics, image science, and vision* **1984**, *1*, 1003-1006.

(9) Treacy, E. *Quantum Electronics, IEEE Journal of* **1969**, *5*, 454-458.

(10) Martinez, O. E. *J. Opt. Soc. Am. B* **1986**, *3*, 929-934.

(11) Martinez, O. *Quantum Electronics, IEEE Journal of* **1987**, *23*, 1385-1387.

(12) Martinez, O. *Quantum Electronics, IEEE Journal of* **1987**, *23*, 59-64.

(13) Zhou, J.; Huang, C.-P.; Shi, C.; Murnane, M. M.; Kapteyn, H. C. *Opt. Lett.* **1994**, *19*, 126-128.

(14) Backus, S.; Peatross, J.; Huang, C. P.; Murnane, M. M.; Kapteyn, H. C. *Opt. Lett.* **1995**, *20*, 2000-2002.

(15) Rudd, J. V.; Korn, G.; Kane, S.; Squier, J.; Mourou, G.; Bado, P. *Opt. Lett.* **1993**, *18*, 2044-2046.

(16) LeBlanc, C.; Grillon, G.; Chambaret, J. P.; Migus, A.; Antonetti, A. *Opt. Lett.* **1993**, *18*, 140-142.

(17) Lenzner, M.; Spielmann, C.; Wintner, E.; Krausz, F.; Schmidt, A. J. *Opt. Lett.* **1995**, *20*, 1397-1399.

(18) Salin, F.; Squier, J.; Mourou, G.; Vaillancourt, G. *Opt. Lett.* **1991**, *16*, 1964-1966.

(19) Squier, J.; Coe, S.; Clay, K.; Mourou, G. r.; Harter, D. *Optics Communications* **1992**, *92*, 73-78.

(20) Vaillancourt, G.; Norris, T. B.; Coe, J. S.; Bado, P.; Mourou, G. A. *Opt. Lett.* **1990**, *15*, 317-319.

(21) Wynne, K.; Reid, G. D.; Hochstrasser, R. M. *Opt. Lett.* **1994**, *19*, 895-897.

(22) Alfano, R. R. *The Supercontinuum Laser Source*; Springer: New York, 1989.

(23) Fork, R. L.; Shank, C. V.; Hirlimann, C.; Yen, R.; Tomlinson, W. J. *Opt. Lett.* **1983**, *8*, 1-3.

(24) Gaeta, A. L. *Physical Review Letters* **2000**, *84*, 3582-3585.

(25) Riedle, E.; Beutter, M.; Lochbrunner, S.; Piel, J.; Schenkl, S.; Spörlein, S.; Zinth, W. *Applied Physics B: Lasers and Optics* **2000**, *71*, 457-465.

(26) Shirakawa, A.; Sakane, I.; Takasaka, M.; Kobayashi, T. *Applied Physics Letters* **1999**, *74*, 2268-2270.

(27) Womick, J. M.; Moran, A. M. *The Journal of Physical Chemistry B*, *115*, 1347-1356.

(28) Miller, S. A.; Stuart, A. C.; Womick, J. M.; Zhou, H.; You, W.; Moran, A. M. *The Journal of Physical Chemistry C*, *115*, 2371-2380.

(29) West, B. A.; Womick, J. M.; McNeil, L. E.; Tan, K. J.; Moran, A. M. *The Journal of Physical Chemistry C*, *114*, 10580-10591.

(30) Miller, S. A.; Fields-Zinna, C. A.; Murray, R. W.; Moran, A. M. *The Journal of Physical Chemistry Letters*, *1*, 1383-1387.

(31) Womick, J. M.; Miller, S. A.; Moran, A. M. *The Journal of Physical Chemistry B* **2009**, *113*, 6630-6639.

(32) Kozma, I.; Baum, P.; Lochbrunner, S.; Riedle, E. *Opt. Express* **2003**, *11*, 3110-3115.

(33) Wittmann, M.; Tschirschwitz, F.; Korn, G.; Nibbering, E. T. J. *Applied physics. B, Lasers and optics* **2000**, *71*, 885-887.

(34) Ziegler, L. D.; Morais, J.; Zhou, Y.; Constantine, S.; Reed, M. K.; Steiner-Shepard, M. K.; Lommel, D. *Quantum Electronics, IEEE Journal of* **1998**, *34*, 1758-1764.

(35) Baum, P.; Lochbrunner, S.; Riedle, E. *Opt. Lett.* **2004**, *29*, 1686-1688.

(36) Lochbrunner, S.; Riedle, E. *Applied physics. B, Lasers and optics* **2004**, *79*, 1027-1032.

(37) Moskun, A. C.; Bradforth, S. E. *The Journal of Chemical Physics* **2003**, *119*, 4500-4515.

(38) Vilchiz, V. H.; Kloepfer, J. A.; Germaine, A. C.; Lenchenkov, V. A.; Bradforth, S. E. *The Journal of Physical Chemistry A* **2001**, *105*, 1711-1723.

(39) Ullrich, S.; Schultz, T.; Zgierski, M. Z.; Stolow, A. *Journal of the American Chemical Society* **2004**, *126*, 2262-2263.

(40) Pecourt, J.-M. L.; Peon, J.; Kohler, B. *Journal of the American Chemical Society* **2001**, *123*, 10370-10378.

(41) Backus, S.; Peatross, J.; Zeek, Z.; Rundquist, A.; Taft, G.; Murnane, M. M.; Kapteyn, H. C. *Opt. Lett.* **1996**, *21*, 665-667.

(42) Durfee III, C. G.; Backus, S.; Murnane, M. M.; Kapteyn, H. C. *Opt. Lett.* **1997**, *22*, 1565-1567.

(43) Durfee Iii, C. G.; Rundquist, A.; Backus, S.; Chang, Z.; Herne, C.; Kapteyn, H. C.; Murnane, M. M. *Journal of Nonlinear Optical Physics & Materials* **1999**, *08*, 211-234.

(44) Durfee Iii, C. G.; Backus, S.; Kapteyn, H. C.; Murnane, M. M. *Opt. Lett.* **1999**, *24*, 697-699.

(45) Misoguti, L.; Backus, S.; Durfee III, C. G.; Bartels, R.; Murnane, M. M.; Kapteyn, H. C. *Ultrafast Phenomena XII*; Springer: Berlin, 2001.

(46) Jailaubekov, A. E.; Bradforth, S. E. *Appl. Phys. Lett.* **2005**, *87*, 021107/1-021107/3.

(47) Misoguti, L.; Backus, S.; Durfee, C. G.; Bartels, R.; Murnane, M. M.; Kapteyn, H. C. *Physical Review Letters* **2001**, *87*, 013601.

(48) Selig, U.; Schleussner, C.-F.; Foerster, M.; Langhojer, F.; Nuernberger, P.; Brixner, T. *Opt. Lett.* **2010**, *35*, 4178-4180.

(49) Tseng, C.-H.; Matsika, S.; Weinacht, T. C. *Opt. Express* **2009**, *17*, 18788-18793.

(50) West, B. A.; Moran, A. M. *The Journal of Physical Chemistry Letters*, *3*, 2575-2581.

(51) West, B. A.; Womick, J. M.; Moran, A. M. *J. Chem. Phys.* **2011**, *135*, 114505:1-114505:9.

(52) West, B. A.; Womick, J. M.; Moran, A. M. *J. Phys. Chem. A* **2011**, *115*, 8630-8637.

(53) Schmeltzer, R. A. *The Bell System technical journal* **1964**, *43*, 1783-+.

(54) Durfee, C. G.; Misoguti, L.; Backus, S.; Kapteyn, H. C.; Murnane, M. M. *J. Opt. Soc. Am. B* **2002**, *19*, 822-831.

(55) Couairon, A.; Franco, M.; Mysyrowicz, A.; Biegert, J.; Keller, U. *Opt. Lett.* **2005**, *30*, 2657-2659.

(56) Stibenz, G.; Zhavoronkov, N.; Steinmeyer, G. *Opt. Lett.* **2006**, *31*, 274-276.

(57) Berge, L. *Physical review. E, Statistical physics, plasmas, fluids, and related interdisciplinary topics* **2003**, *68*.

(58) Fuji, T.; Horio, T.; Suzuki, T. *Opt. Lett.* **2007**, *32*, 2481-2483.

(59) Fuji, T.; Suzuki, T.; Serebryannikov, E. E.; Zheltikov, A. *Physical Review A* **2009**, *80*, 063822.

(60) Corporation, T. a. A. C. N. In *Newport Application Notes*.

(61) Diels, J.; Rudolf, W. *Ultrashort Laser Pulse Phenomena*; Second Edition ed.; Academic Press: Massachusetts, 2006.

(62) Brigham, E. O. *The Fast Fourier Transform: An Introduction to Theory and Application*; Prentice Hall: New Jersey, 1973.

(63) Sellmeier, W. *Annalen der Physik und Chemie* **1871**, *219*, 272-282.

(64) CVI Melles Griot.

(65) Sherriff, R. E. *J. Opt. Soc. Am. B* **1998**, *15*, 1224-1230.

(66) Trebino, R. *Frequency Resolved Optical Gating: The Measurement of Ultrashort Laser Pulses.*; Kluwer Academic Publishers: Boston, Dordrecht, London, 2000.

(67) Fork, R. L.; Martinez, O. E.; Gordon, J. P. *Opt. Lett.* **1984**, *9*, 150-152.
(68) Rivera, C. A.; Bradforth, S. E.; Tempea, G. *Optics Express* **2010**, *18*, 18615-18624.

(69) Tseng, C.-H.; Sándor, P.; Kotur, M.; Weinacht, T. C.; Matsika, S. *J. Phys. Chem. A* **2012**, *116*, 2654-2661.

(70) West, B. A.; Womick, J. M.; Moran, A. M. *J. Chem. Phys.* **2011**, *135*, 114505.

(71) Goodno, G. D.; Dadusc, G.; Miller, R. J. D. *J. Opt. Soc. Am. B* **1998**, *15*, 1791-1794.

(72) Maznev, A. A.; Nelson, K. A.; Rogers, J. A. *Opt. Lett.* **1998**, *23*, 1319-1321.

(73) West, B. A.; Moran, A. M. *J. Phys. Chem. Lett.* **2012**, *3*, 2575-2581.

(74) Brantley, A. W. a. B. P. M. a. N. P. M. a. A. M. M. *New Journal of Physics*, *15*, 025007.

(75) Brixner, T.; Mancal, T.; Stiopkin, I. V.; Fleming, G. R. *J. Chem. Phys.* **2004**, *121*, 4221-4236.

(76) Fanciulli, R.; Cerjak, I.; Herek, J. L. *Rev. Sci. Instrum.* **2007**, *78*, 053102/1-053102/5.

(77) Mukamel, S.; Abramavicius, D.; Yang, L.; Zhuang, W.; Schweigert, I. V.; Voronine, D. V. *Acc. Chem. Res.* **2009**, *42*, 553-562.

Chapter 4 . Probing Ultrafast Dynamics in Adenine With Mid-UV Four-Wave Mixing Spectroscopies

4.1. Introduction

Knowledge of the inner workings of electronic relaxation processes in DNA bases progresses steadily with technology and innovative experimentation.[1-9] Modern insights into these systems stem from the determination of <200fs internal conversion time scales in various DNA nucleosides and short oligomers using transient absorption measurements.[10] Fluorescence upconversion and photoelectron spectroscopies have since provided additional information on these dynamics.[2,3,7-9] In addition, theoretical models contribute descriptions of the potential energy surfaces and conical intersections enabling these extremely fast relaxation processes.[11-15] Despite a large body of work, consensus has not yet been reached on some basic issues. The nature (e.g., $n\pi^*$, $\pi\pi^*$) and energetic order of the lowest energy singly excited states in the solvated bases is difficult to discern based on earlier ultrafast spectroscopic studies because the excitation frequency (i.e., pump frequency) has seldom been systematically tuned across the broad mid-UV absorbance spectra of the bases. Moreover, because of the rapid relaxation rates found in these systems, tradeoffs between time and frequency resolution will ultimately challenge the interpretation of conventional "pump-probe" measurements utilizing such tunable pump pulses.[16] As stated in Chapter 1, the goal of this dissertation is to implement four wave mixing techniques in the UV to undertake two dimensional and

---

transient grating measurements. This chapter represents the first steps towards that goal. Among the principal advantages of two-dimensional photon echo (2DPE) spectroscopy is the attainment of time and frequency resolution limited only by the line widths of the system's resonances.[16-19]

The unique capabilities of 2DPE have been leveraged to obtain new insights into processes ranging from chemical exchange equilibrium in liquids to energy transfer in photosynthesis.[20-25] For technical reasons, 2DPE techniques were first applied and have matured most rapidly at infrared wavelengths,[16,26,27] although such experiments are now routinely conducted using visible laser pulses.[28-31] Further progress "from NMR to X-rays" [32] must contend with several challenges encountered in the mid-UV spectral range (200-300nm) including the attainment of adequate laser bandwidth, interferometric phase stability, and the suppression of undesired nonlinearities in the solvent medium (e.g., ionization of solute and solvent).[33-36] Solutions to these problems are motivated by the understanding of myriad biological systems whose lowest energy electronic transitions are found in the mid-UV (e.g., DNA bases, amino acids).

In this chapter, photoinduced relaxation processes are investigated in adenine using heterodyne-detected transient grating (TG) and 2DPE spectroscopies conducted in the mid-UV spectral range. These experiments are the first to combine a specialized method for generating 25fs mid-UV laser pulses and the passive phase stability afforded by diffractive optic based interferometry.[37-39] Adenine is an excellent model system with which to begin such TG and 2DPE studies because its dynamics are fairly well-defined when photoexcited and probed in the mid-UV.[40] Figure 4.1 overlays the spectrum of the laser pulses with the absorbance spectrum of adenine. Only a small portion of the

absorbance spectrum is covered despite the >800cm^{-1} laser bandwidth. In part, the broad line width of adenine represents contributions from several tautomers with different absorbance spectra.[40] Two $\pi\pi^*$ transitions also occur in this frequency range, although only one of these resonances has a significant oscillator strength.[9,15] Strong solute-solvent interactions (e.g., hydrogen bonding) also broaden the line width. These three line broadening mechanisms are carefully delineated in the present set of experiments.

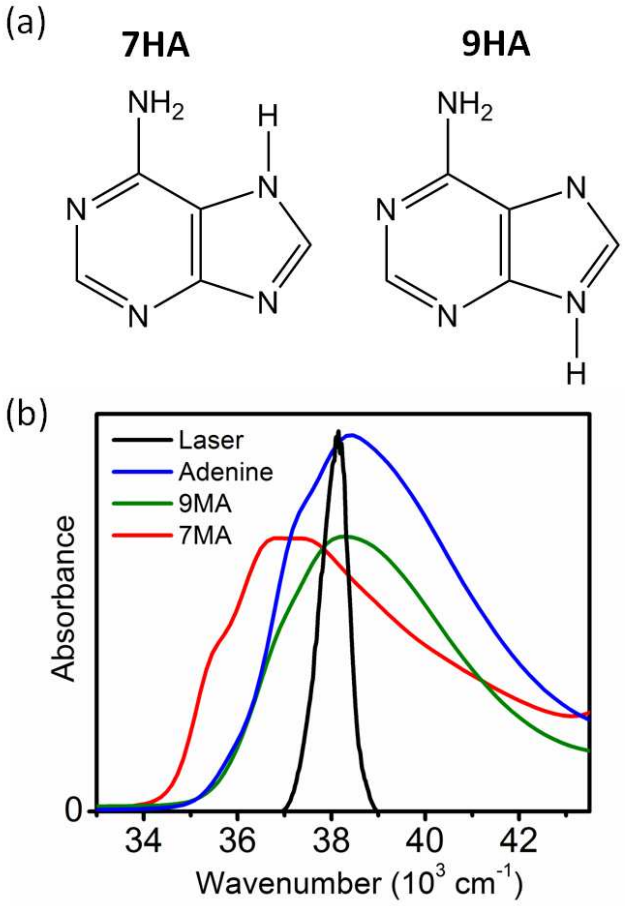

Figure 4.1. (a) Structures of the 7HA and 9HA tautomers of adenine. (b) Laser spectrum (black) overlaid on the linear absorbance spectra of adenine (blue), 9-methyladenine (green), and 7-methyladenine (red).

Tautomerization of adenine is an area where 2DPE is well-equipped to yield unique insights. Most relevant to the spectral range examined here are the 7HA and 9HA

tautomers, which are found at approximately 22% and 78% proportions in aqueous solution near pH=7.[40-42] The transition frequencies of the 7HA (37100cm^{-1} or 269.5nm) and 9HA (38400cm^{-1} or 260.4nm) tautomers have been estimated using the absorbance spectra of 7-methyladenine (7MA) and 9-methyladenine (9MA).[40] The 2DPE experiments presented below, which employ broadband laser pulses centered at 38000 cm^{-1} (263nm), therefore superpose signals associated with both 7HA and 9HA. The application of 2DPE to adenine is partially motivated by the prospect that signal components associated with 7HA and 9HA will give rise to correlations in the excitation and emission frequencies. Such correlations arise because, at equilibrium, 7HA absorbs and emits radiation at lower frequencies than 9HA. By contrast, resolution in these signal components is not readily achieved with one-dimensional techniques (e.g., transient absorption, TG), that yield only the emission spectra. In principle, 2DPE can also track interconversion in the 7HA and 9HA tautomers. However, such dynamics will be accessible only if the exchange of tautomers occurs before the nonlinear polarization decays due to ground state recovery (<2ps). Overall, while this initial demonstration of 2DPE in the mid-UV is fairly simple, it is useful for overcoming technical challenges and paves the way towards the study of more complex systems.

4.2. Experimental Methods

Generation of 25fs, 38000cm^{-1} laser pulses is achieved using argon gas as a nonlinear medium.[37,43] The setup resembles that developed by Bradforth and co-workers and performs similarly.[37] Briefly, 12660cm^{-1} (800nm) and 25320cm^{-1} (400nm) pulses with 40 μJ energies and 160cm^{-1} FWHM bandwidths are focused into a 75 micron diameter hollow-core fiber filled with 0.65atm argon gas. The 38000cm^{-1} pulses

generated inside the fiber have 1.0 μJ energies and FWHM bandwidths of 800-950cm^{-1}. A fused silica prism compressor with a tip-to-tip prism separation of 13cm fully compensates for dispersion accumulated in transmissive optics between the fiber and the sample. TG signals generated in a 1mm thick fused silica window have FWHM widths of 30fs, which corresponds to a <24.5fs pulse duration if Gaussian pulse envelopes are assumed.[44] This work was completed prior to the upgrade in spring of 2012 as discussed in Section 3.5 so the pulses driving the third harmonic generation setup were >150fs.

TG and 2DPE experiments utilize a diffractive optic-based interferometer similar to those described in earlier applications at visible wavelengths (cf., Supporting Information).[28-30,38,45] The optical layout is compact and the interferometer is enclosed in a box to suppress phase fluctuations caused by air currents. Significant differences in the interferometric phase stability achieved at mid-UV and visible wavelengths are not found, which is evidenced in the high signal-to-noise ratios of the absorptive four-wave mixing signal components presented below (i.e., the absorptive part of the signal is sensitive to noise in the phase). In this setup, the diffractive optic generates a boxcars laser beam geometry in which signals are collected under the phase matching condition, $\mathbf{k}_S = -\mathbf{k}_1 + \mathbf{k}_2 + \mathbf{k}_3$. Three of the laser pulses induce the nonlinear polarization, whereas the fourth (attenuated) pulse is used as a reference field for signal detection by spectral interferometry.[46,47] In all experiments, signals are detected using a back-illuminated CCD array (Princeton Instruments PIXIS 100B) mounted on a 0.3 meter spectrograph with a 3600 g/mm grating. Integration times range between 100-400 ms and are adjusted based on the signal intensity.

As shown in Figure 2.11, both TG and 2DPE experiments involves a sequence of three laser pulses. TG measurements use a motorized translation stage to scan T (with τ =0), which is the interval in which relaxation processes such as internal conversion and vibrational cooling occur. 2DPE scans τ from -100fs to +100fs (at various T) by moving fused silica prism wedges in the paths of pulses 1 and 2.[29] The delay, τ, is associated with absorption of the "pump" pulses (i.e., pulses 1 and 2) and is ultimately limited by the inverse linewidth of the ππ* transition. Fourier transformation in τ yields the excitation dimension of the 2DPE spectrum, ω_τ; the emission dimension, ω_t, is obtained by dispersing the signal pulse in the spectrometer. In both techniques, scans of the pulse delays are repeated 20-40 times and averaged as needed to optimize the signal-to-noise ratios.

Solutions of adenine, 9MA, and 7MA are prepared in an aqueous sodium phosphate buffer at pH=7. The solutions have optical densities of 0.5-0.75 at 265 nm in a 0.5mm path length. The optical densities are set at the minimum values for which acceptable signal-to-noise ratios are achieved in TG and 2DPE experiments. 2DPE spectra are corrected for propagation effects using established procedures (cf., Supporting Information).[48] Distortions in the line shapes exceeding 10% of the maximum amplitude are not observed at ODs less than 0.75; the shape of the laser spectrum (and signal) changes relatively little during propagation in the solution because the absorbance line width of adenine is broad compared to the laser bandwidth. Moreover, robust aspects of the 2DPE line shapes are focused upon for which the insights obtained are insensitive to the OD. Undesired effects associated with these relatively high ODs are also ruled out by comparing signals acquired for multiple solutes (i.e., adenine, 9MA, and 7MA).

Each of the three incoming laser pulses used in the TG and 2DPE experiments possesses a fluence of approximately 4.65×10^{13} photons/cm^2. It is estimated that 0.4% of the molecules are photoexcited using the sum of the fluences for pulses 1 and 2 (i.e., the "pump" pulses) and the extinction coefficient of adenine at 38000cm^{-1}.[49] Low fluences must be employed because high peak powers, which scale as the inverse of the pulse duration, induce (undesired) ionization of solute and solvent.[50] The relationship between the peak power of the laser pulses and the photoionization of adenine is examined in the following Section.

The electronic polarizability of the solvent dominates signal emission when all three pulses are overlapped in the sample.[51] This nonlinearity has been identified as a major challenge facing femtosecond spectroscopies conducted in the mid-UV spectral range.[33] The TG measurement presented in Figure 4.2 shows that the spike at T=0 is approximately 10 times larger than the signal radiated by adenine at T=1.0ps. Dynamics at T<0.15ps are impossible to study because of this undesired solvent response. Notably, the presence of this quasi-instantaneous nonlinearity requires temporal overlap of all three laser pulses in the solution. Therefore, provided that $T \geq 0.15$ps, this non-resonant response can be neglected when only pulses 1 and 2 are temporally overlapped (e.g., when τ is comparable to the 25fs pulse duration).

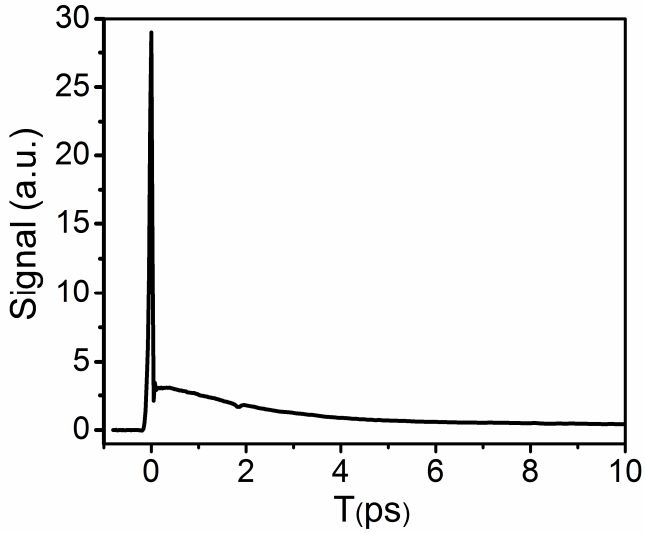

Figure 4.2. Absolute value of TG signal measured for a solution of adenine with an optical density of 0.75 in a 0.5mm path length. The spike at T=0, which is primarily caused by the electronic polarizability of the solvent, is 10 times larger than the signal radiated by adenine at T=1ps.

4.3. Results and Discussion

4.3. A. Probing Relaxation Processes with Transient Grating Spectroscopy

The TG experiments presented in this Section are motivated by two goals. These represent the first steps to establishing the viability of four wave mixing at this wavelength range by comparing to known results and ensuring that undesired contributions are not present in measured signals. First, it is shown that this particular "one-color" TG configuration is capable of reproducing the results of earlier transient absorption studies of adenine derivatives in which recovery of the ground state bleach (GSB) was observed on a time scale of 2ps.[40,52] Second, the relationship between the peak power of the laser pulses and the generation of undesired species (e.g., adenine cation) is examined. Previous investigations of adenosine in aqueous solution show that photoionization becomes problematic at peak powers as low as 2GW/cm^2.[50] It should therefore be anticipated that weak signal strengths will challenge measurements

employing short mid-UV laser pulses because the signal field amplitude is directly proportional to the concentration of photoexcited molecules. For example, with 25fs laser pulses, a peak power of 2GW/cm^2 corresponds to a fluence of approximately 6.8× 10^{13}, which results in the excitation of only 0.6% of the molecules in the sample (this calculation uses the sum of the fluences for pulses 1 and 2).

The absolute value of the TG signal field is plotted at both T=0.5ps and T =100ps in Figure 4.3a. The desired third-order signal scales as the peak power, P_{peak}, raised to 3/2 (i.e., $P_{peak}^{3/2}$). Figure 4.3a shows that the TG signals obtained at T=0.5ps maintain linearity over a wide range in $P_{peak}^{3/2}$, whereas the signals measured at T=100ps exhibit a significant amount of curvature with respect to $P_{peak}^{3/2}$. To make clear the origin of this behavior, Figure 4.3b overlays fits of the absorptive TG signal components obtained at various peak powers. As discussed in appendix A1, this absorptive representation of the TG signal provides information equivalent to that derived from a conventional transient absorption experiment; dispersive nonlinearities present in homodyned TG do not contribute to the signals in Figure 4.3b (e.g., thermal grating).[53,54] The signal amplitude measured at long delay times (i.e., A_0 parameter in Table 4.1) increases with peak power, whereas the τ_1 and τ_2 time constants change fairly little. Fortunately, there is a small window from 0.7-1.4 GW/cm^2 in which reasonable signal-to-noise ratios are achieved without major distortions in the decay profiles at T<5ps. The long-lived component, A_0, is assigned to ionization of the solute (not solvent) because similar behavior is not observed in the pure buffer solution (Figure 4.3c).

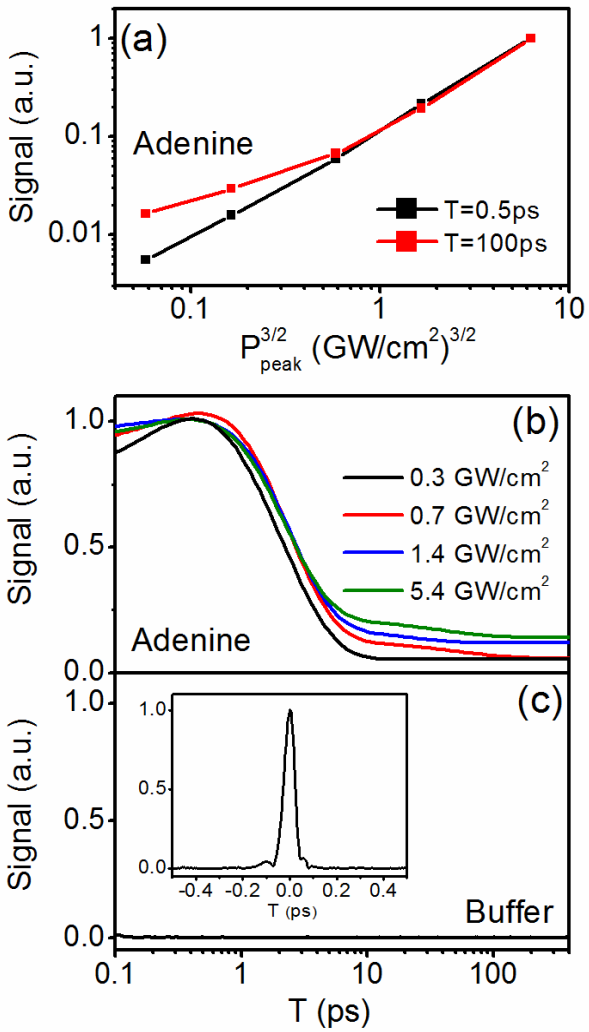

Figure 4.3. (a) Absolute value of TG signals obtained at T=0.5ps (black) and T=100ps (red). P_{peak} is the peak power associated with each of the three incoming laser pulses. The desired third-order signal varies linearly with respect to $P_{peak}^{3/2}$. (b) Fits of the absorptive components of TG signals acquired at various peak powers. The measured signals and fits are overlaid in the Supporting Information. (c) Absolute value of TG signal obtained for the pure buffer at a peak power of 1.4GW/cm^2. The inset shows the instantaneous response of the buffer when the pulses are overlapped in time.

TG signals acquired under the magic angle polarization condition sense recovery of the ground electronic state while excluding contributions from solute reorientation. The rise time of the TG signal, τ_1, is slightly slower than the time scale (<200fs) at which the $\pi\pi^*$ excited state is depopulated.[1,10] It is postulated that sensitivity to the internal

conversion process arises through excited state absorption (ESA) nonlinearities that contribute weakly at ω_t =38000cm^{-1}. The rate of bleach recovery is ultimately limited by vibrational cooling processes that take hold following internal conversion. The time constant, τ_2, is in good agreement with the vibrational cooling rates measured in closely related adenine derivatives.[52] The third time constant, τ_3, varies with the peak power and is most likely associated with photoionization.[34]

Table 4.1. Fitting parameters for transient grating signals shown in Figure 4.3

[a],[b]parameter	0.3 GW/cm^2	0.7 GW/cm^2	1.4 GW/cm^2	5.4 GW/cm^2
A_0	0.05±0.01	0.06±0.01	0.12±0.01	0.14±0.01
A_1	-0.69±0.28	-0.83±0.16	-0.87±0.19	-0.66±0.08
τ_1 (ps)	0.27± 0.22	0.51± 0.11	0.67± 0.09	0.48± 0.07
A_2	1.36±0.22	1.57±0.17	1.63±0.18	1.35±0.09
τ_2 (ps)	1.99± 0.30	1.89± 0.15	1.75± 0.12	1.76± 0.09
A_3	-------	0.07±0.01	0.07±0.01	0.08±0.01
τ_3 (ps)	-------	52.4±21.2	18.9±4.3	39.7±7.1

[a] Fit to Equation $S(T) = A_0 + \sum_{i=1}^{3} A_i \exp(-T/\tau_i)$.

[b] The error is defined as two standard deviations.

The transient absorption anisotropy shown in Figure 4.4 is useful for establishing signal generation mechanisms.[55,56] The real (absorptive) parts of the measured TG signals, $S_{ZZZZ}(T)$ and $S_{ZZXX}(T)$, enter the anisotropy as

$$r(T) = \frac{S_{ZZZZ}(T) - S_{ZZXX}(T)}{S_{ZZZZ}(T) + 2S_{ZZXX}(T)} \tag{4.1}$$

In this notation, the $S_{ZZZZ}(T)$ tensor element involves all-parallel electric field polarizations, whereas in $S_{ZZXX}(T)$ pulses 1 and 2 have polarizations orthogonal to pulse

3 and the signal. The anisotropy measured at T =0.1ps (r =0.37) is close to the value that would be found if the signal represented only the GSB of a single ππ* electronic resonance (r =0.4).[55,56] The deviation from 0.4 may reflect either minor contributions from ESA or the second ππ* transition, which is known to possess a relatively small oscillator strength.[9,15] Two relaxation mechanisms can be reliably identified at the level of noise present in the anisotropy. The 1.13 ps time constant is most likely associated with vibrational cooling. For example, it is possible that the relative contribution of ESA increases concomitant with vibrational cooling (i.e., reduction in GSB); the anisotropy would decay if the GSB and ESA nonlinearities involve different transition dipole orientations. The 18.5ps time constant is assigned to rotational diffusion. Using the viscosity of water (1cP), the Stokes-Einstein-Debye equation yields a rotational diffusion time of 18.5ps for a solute volume of 76Å^3, which is in reasonable agreement with the dimensions of adenine.[57]

4.3. B. Photon Echo Signatures of Tautomerism

The 2DPE experiments presented in this Section aim to distinguish signals radiated by the 7HA and 9HA tautomers of adenine. It has been demonstrated that photoexcitation near 38000cm^{-1} initiates dynamics in both species with roughly 22% (7HA) and 78% (9HA) proportions.[40-42] Moreover, as shown in Figure 4.1, the ππ* electronic resonances of the 9HA-like and 7HA-like model systems, 9MA and 7MA, are respectively found at frequencies higher (38400cm^{-1}) and lower (37100cm^{-1}) than the peak of the laser spectrum.[40] 2DPE can therefore leverage its resolution in the excitation frequency, ω_τ, to disentangle signals associated with 7HA and 9HA. The behaviors of the two tautomers must be distinct in T because 7HA possesses a longer ππ* excited

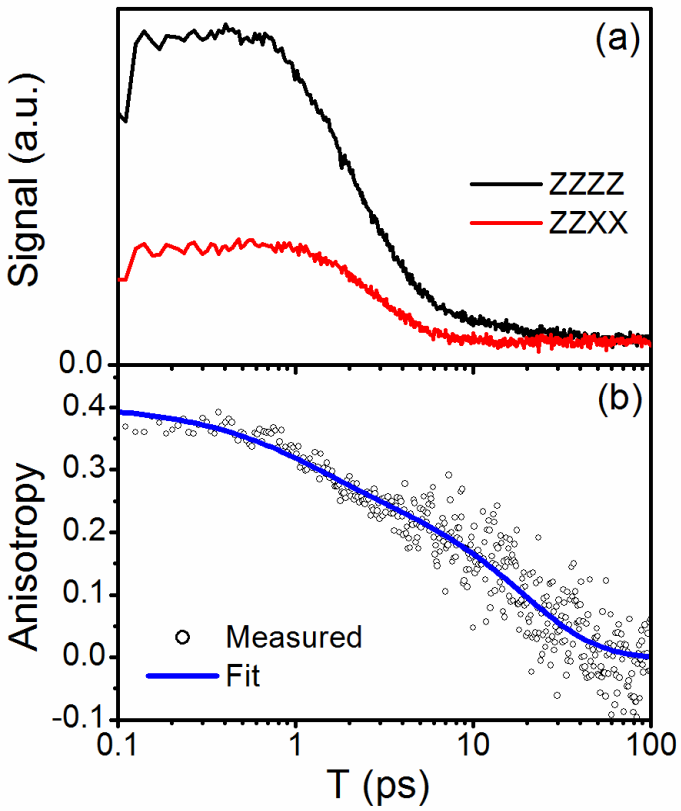

Figure 4.4. (a) Absorptive components of TG signals acquired under the $S_{ZZZZ}(T)$ and $S_{ZZXX}(T)$ polarization conditions. The sign of the signal corresponds to a "bleach". (b) Transient absorption anisotropy generated using the tensor elements shown in panel (a). The anisotropy is fit using $S(T) = \sum_{i=1}^{2} A_i \exp(-T/\tau_i)$, where A_1=0.12, τ_1=1.13ps, A_2 =0.28, and τ_2 =18.5ps.

state lifetime than 9HA.[40] In addition, the longer-lived ππ* excited state in 7HA may also influence the line shapes of the 2DPE spectra by way of ESA signal components.

The 2DPE spectra of adenine presented in Figure 4.5 undergo (subtle) changes with increasing T. Dynamics are characterized in the line shapes by comparing the FWHM line widths corresponding to diagonal, Γ_d, and anti-diagonal, Γ_{ad}, slices through the spectra; the diagonal ($\omega_t = \omega_\tau$) and anti-diagonal ($\omega_t = -\omega_\tau$ +75890cm^{-1}) lines connect opposite corners of the contour plots in Figure 4.5. In adenine, the ratio, Γ_{ad}/Γ_d

, is close to 0.95 at T =0.15ps and rapidly decreases within the first ps after excitation, reaching an asymptotic value near 0.85. Inhomogeneous line broadening gives rise to similar line shapes (i.e., Γ_{ad}/Γ_{d} <1.0), but is irrelevant here because solvation processes in aqueous solution are dominated by dynamics at T <0.1ps.[58] By contrast, the time scale alone does not rule out the influence of intramolecular modes on the 2DPE spectra. That is, the observation of different dynamics at high and low ω_{τ} may also reflect the photoexcitation of different ππ* vibronic levels within a particular tautomer. Indeed, such vibronic effects are known to govern the kinetics of adenine in the gas phase.[3,7,59]

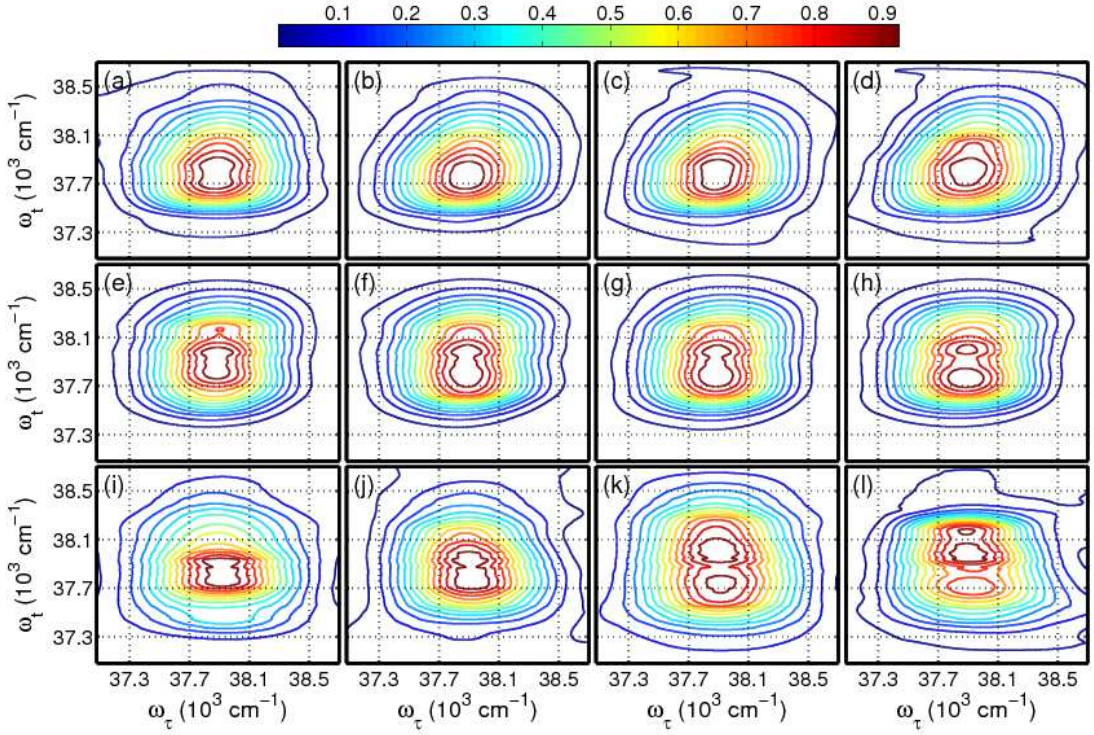

Figure 4.5. Absorptive part of 2DPE spectra acquired for aqueous solutions of (a)-(d) adenine; (e)-(h) 9-methyladenine; (i)-(l) 7-methyladenine. The delay times are organized as follows: T =0.15ps (first column); T =0.20ps (second column); T =0.60ps (third column); T =3.00ps (fourth column). The amplitude of each spectrum is normalized to 1. The quasi-instantaneous response of the solvent prevents the measurement of spectra at T <0.15ps.

To address the influence of nuclear relaxation on the 2DPE spectra of adenine, 2DPE spectra of 9MA and 7MA are presented in Figure 4.5. Here, with inspiration taken from earlier work,[3,40] 9MA and 7MA are regarded as a 9HA-like and 7HA-like model systems with similar Franck-Condon progressions.[60] Ratios in the 2DPE line widths, Γ_{ad}/Γ_{d}, found for these two derivatives are overlaid with those of adenine in Figure 4.6.

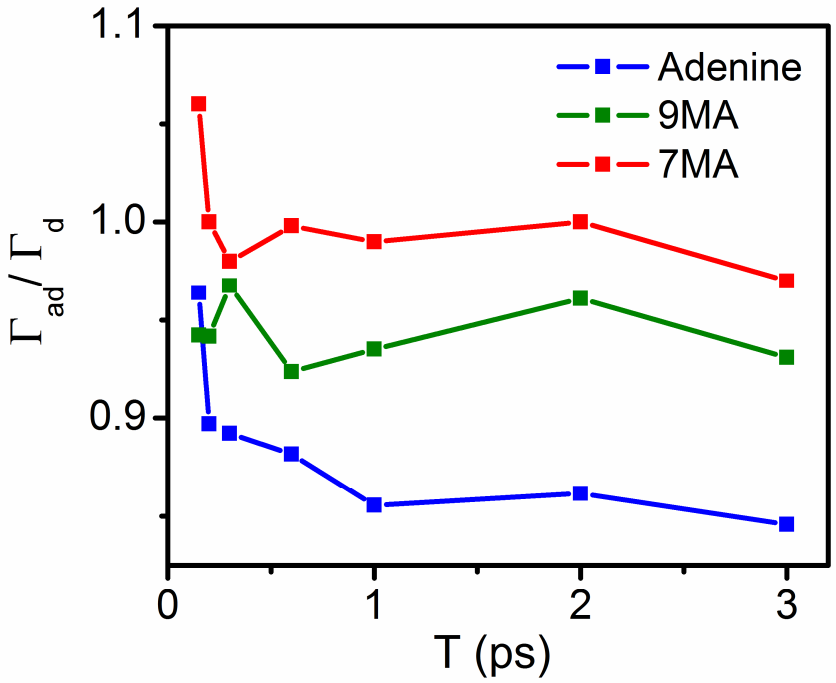

Figure 4.6. Ratio in the anti-diagonal, Γ_{ad}, and diagonal, Γ_{d}, 2DPE line widths obtained for adenine (blue), 9-methyladenine (green), and 7-methyladenine (red). These data suggest that solvation of the 7HA tautomer contributes to dynamics in the 2DPE line shape of adenine at $T \leq 0.3$ps.

Compared to adenine, the line shapes of 9MA and 7MA possess "rounder" shapes with Γ_{ad}/Γ_{d} ranging from approximately 0.95-1.05. The ratios, Γ_{ad}/Γ_{d}, obtained for 9MA are essentially independent of T, whereas those of 7MA decrease substantially between T=0.15ps and T=0.3ps. This initial decay in Γ_{ad}/Γ_{d} is similar to that found in adenine. However, unlike adenine, Γ_{ad}/Γ_{d} does not continue to decrease after T=0.3ps

in 7MA. On the basis of this comparison, it is suggested that nuclear relaxation involving the 7HA tautomer primarily contributes to evolution in the 2DPE line shape of adenine at T <0.3ps. The red-shifted linear absorbance spectrum of 7HA (compared to 9HA) underlies its influence on the 2DPE spectra of adenine at T <0.3ps. As illustrated in Figure 4.7, it is envisioned that equilibration of the "hole" wavepacket in the ground electronic state of 7HA causes the GSB signal component to shift towards smaller ω_t with increasing T. Because of the extremely fast time-scale (<0.3ps), it is suggested that these dynamics primarily reflect reorganization of the aqueous solvent.[58] Such nuclear relaxation results in an overall increase (decrease) in signal amplitude below (above) the 2DPE diagonal ($\omega_\tau = \omega_t$), thereby causing Γ_{ad}/Γ_d to decrease.

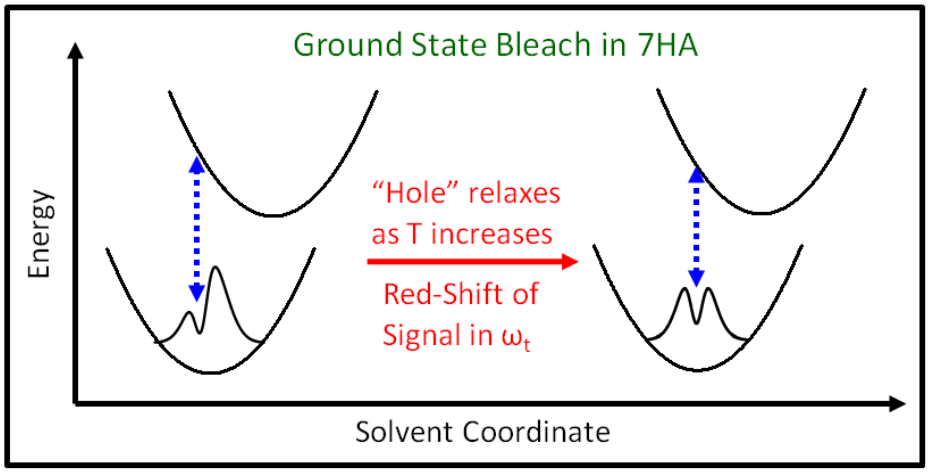

Figure 4.7. Schematic explaining the influence of solvation on the GSB signal component of 7HA. Photoexcitation at energies greater than the peak of the linear absorbance spectrum produces a "hole" wavepacket in the ground electronic state. Equilibration of the wavepacket causes a red-shift in the signal emission frequency, ω_t.[66] This solvation process causes amplitude in the 2DPE spectrum to concentrate below the diagonal ($\omega_\tau = \omega_t$) as T increases.

In addition to solvation of 7HA, it is likely that electronic relaxation processes also contribute to evolution in the 2DPE line shape of adenine. Additional relaxation

mechanisms must be invoked, for example, to explain why Γ_{ad}/Γ_d continues to decrease after T=0.3ps in adenine but not in 7MA. It is proposed that the dynamics at T>0.3ps can be fully understood by considering the interference between signals radiated by the 7HA and 9HA tautomers. The key to the mechanism proposed in Figure 4.8 is that internal conversion is much faster in 9HA (τ_{IC}^{9HA}<300fs) than it is in 7HA ($\tau_{IC}^{7HA} \approx$ 4.2ps).[8,40] This difference in kinetics allows ESA to influence the emission spectra of 7HA (primarily lower ω_τ) at T>0.3ps, where the response of 9HA (primarily higher ω_τ) is dominated by GSB. In this interpretation, the T-dependent emergence of a weak ESA signal component in 7HA (with opposite sign to GSB) suppresses the overall signal amplitude in the upper left quadrant of the 2DPE spectrum, thereby causing a decrease in Γ_{ad}/Γ_d. Based on the linear absorbance spectra of 9MA and 7MA, narrow features are not observed in Figure 4.5 because the line widths of 9HA and 7HA are quite broad (and overlapping). Contributions from stimulated emission (SE) are probably negligible at ω_t =38000cm^{-1} when T>0.15ps; for example, SE has been observed in adenosine near ω_t =32500cm^{-1} at T<0.1ps.[61] Simulations of the optical response will ultimately be needed to delineate all signal components but cannot yet be carried out with information provided by the present measurements. For example, it is also possible that "hot" ground state absorption, which has been detected at ω_t<37000cm^{-1} in adenosine,[50] has a significant influence on the 2DPE line shapes. Transient absorption experiments employing broadband dispersed probe pulses in the 30000-40000cm^{-1} range will be useful for refining the present interpretation.

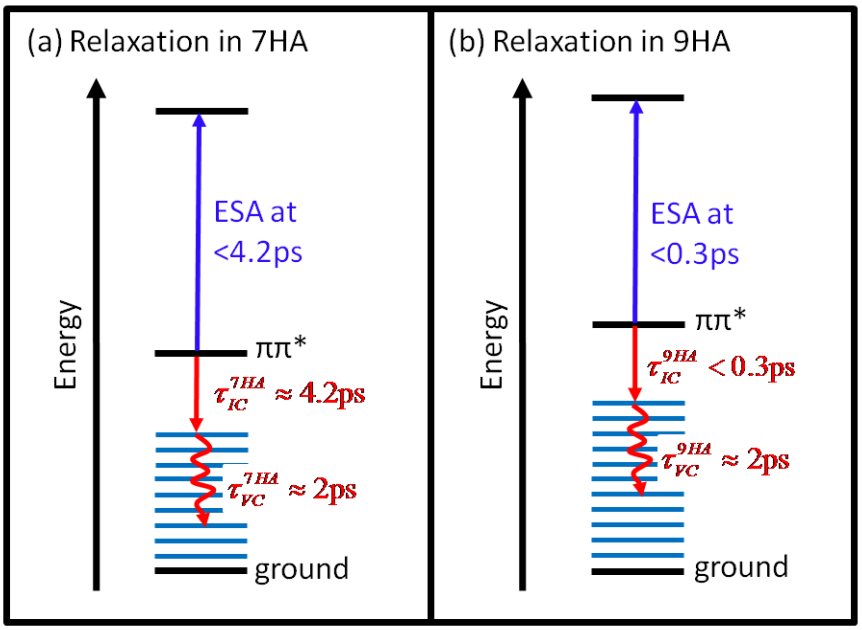

Figure 4.8. Summary of relaxation processes in the (a) 7HA and (b) 9HA tautomers of adenine. ESA influences the 2DPE line shapes of only 7HA at T>0.3ps because it possesses a longer ππ* excited state lifetime than 9HA. It is postulated that interference between GSB and ESA nonlinearities gives rise to the dynamics observed in the 2DPE line shapes of adenine at T>0.3ps.

4.4. Conclusion

In summary, heterodyne-detected TG and 2DPE spectroscopies have been extended to the mid-UV in this study of photoinduced relaxation processes in adenine. First, the power densities at which photoionization of the solute takes hold have carefully been characterized (cf., Figure 4.3). This work is the first to explore these processes in a transient grating geometry employing three short (25fs) mid-UV laser pulses with equal energies; this point is notable because all three pulses can induce solute ionization. It is found that a reasonable compromise between power density and signal strength is obtained at peak powers of 0.7-1.4 GW/cm^2 per pulse, which results in signal-to-noise ratios ranging from 35-350 at T=0.5ps. In addition, the line width limited time and frequency resolution of 2DPE has been leveraged to reveal a superposition in signals

associated with the 7HA and 9HA tautomers. It is postulated that: (i) solvation of the 7HA tautomer gives rise to dynamics in the 2DPE line shape of adenine at T <0.3ps; (ii) the long-lived ππ* excited state of 7HA influences dynamics in the 2DPE spectra at T >0.3ps by way of ESA nonlinearities. The process illustrated in Figure 4.7, which underlies mechanism (i), is fully consistent with the present set of experiments. However, a more complete understanding of mechanism (ii) (i.e., the role of electronic relaxation) will require further investigation. Overall, the present work demonstrates spectroscopic methods that will be valuable for the study of a variety of biomolecules whose lowest energy electronic resonances are found in the mid-UV, a principle goal which this dissertation sought out to achieve. The next steps are applying this technique to uncover new physics in DNA nucleobases, the subject of the next chapter. New theoretical models suggest that such experiments will be useful for probing both dynamics and structure in biological systems.[62,63]

This experience suggests that the major obstacle facing 2DPE experiments conducted in the mid-UV is the large off-resonant response of the solvent, which dominates at $T \leq 0.1$ps when 25fs pulses are utilized (cf., Figure 4.2). Newly developed 2D spectroscopies in which fluorescence is detected may be one solution to this problem.[64,65] Detection of incoherent emission makes these experiments immune to the undesired coherent response of the solvent. Future studies in the group will also explore relaxation dynamics in nucleobases at cryogenic temperatures where the time scale of solvation processes is much greater than the 25fs pulse duration. Correlations in ω_τ and ω_t, which are not found in the present room temperature 2DPE spectra, may then be preserved at $T > 0.15$ps.

4.5. References

(1) Kohler, B. *J. Phys. Chem. Lett.* **2010**, *1*, 2047.

(2) Markovitsi, D.; Gustavsson, T.; Talbot, F. *Photochem. Photobiol. Sci.* **2007**, *6*, 717.

(3) Satzger, H.; Townsend, D.; Zgierski, M. Z.; Patchkovskii, S.; Ullrich, S.; Stolow, A. *Proc. Natl. Acad. Sci.* **2006**, *103*, 10196.

(4) Buchvarov, I.; Wang, Q.; Raytchev, M.; Trifonov, A.; Fiebig, T. *Proc. Natl. Acad. Sci.* **2007**, *104*, 4794.

(5) Towrie, M.; Doorley, G. W.; George, M. W.; Parker, A. W.; Quinn, S. J.; Kelly, J. M. *Analyst* **2009**, *134*, 1265.

(6) Billinghurst, B. E.; Loppnow, G. R. *J. Phys. Chem. A* **2006**, *110*, 2353.

(7) Evans, N. L.; Ullrich, S. *J. Phys. Chem. A* **2010**, *114*, 11225.

(8) Pancur, T.; Schwalb, N. K.; Renth, F.; Temps, F. *Chem. Phys.* **2005**, *313*, 199.

(9) Kwok, W.-M.; Ma, C.; Phillips, D. L. *J. Am. Chem. Soc.* **2006**, *128*, 11894.

(10) Pecourt, J.-M.; Peon, J.; Kohler, B. *J. Am. Chem. Soc.* **2000**, *122*, 9348.

(11) Marian, C. M. *J. Chem. Phys.* **2005**, *122*, 104314/1.

(12) Sobolewski, A. L.; Domcke, W. *Eur. Phys. J. D* **2002**, *20*, 369.

(13) Broo, A. *J. Phys. Chem. A* **1998**, *102*, 526.

(14) Marian, C. M.; Kleinschmidt, M.; Tatchen, J. *Chem. Phys.* **2008**, *347*, 346.

(15) Perun, S.; Sobolewski, A. L.; Domcke, W. *J. Am. Chem. Soc.* **2005**, *127*, 6257.

(16) Jonas, D. M. *Annu. Rev. Phys. Chem.* **2003**, *54*, 425.

(17) Mukamel, S. *Annu. Rev. Phys. Chem.* **2000**, *51*, 691.

(18) Hybl, J. D.; Albrecht Ferro, A.; Jonas, D. M. *J. Chem. Phys.* **2001**, *115*, 6606.

(19) Ogilvie, J. P.; Kubarych, K. J. *Adv. At. Mol. Opt. Phys.* **2009**, *57*, 249.

(20) Fayer, M. D. *Annu. Rev. Phys. Chem.* **2009**, *60*, 21.

(21) Kim, Y. S.; Hochstrasser, R. M. *Proc. Natl. Acad. Sci.* **2005**, *102*, 11185.

(22) Ishizaki, A.; Calhoun, T. R.; Schlau-Cohen, G. S.; Fleming, G. R. *Phys. Chem. Chem. Phys.* **2010**, *12*, 7319.

(23) Collini, E.; Wong, C. Y.; Wilk, K. E.; Curmi, P. M. G.; Brumer, P.; Scholes, G. D. *Nature* **2010**, *463*, 644.

(24) Anna, J. M.; Ross, M. R.; Kubarych, K. J. *J. Phys. Chem. A* **2009**, *113*, 6544.

(25) Womick, J. M.; Moran, A. M. *J. Phys. Chem. B* **2009**, *113*, 15747.

(26) Asplund, M. C.; Zanni, M. T.; Hochstrasser, R. M. *Proc. Natl. Acad. Sci.* **2000**, *97*, 8219.

(27) Khalil, M.; Demirdöven, N.; Tokmakoff, A. *J. Phys. Chem. A* **2003**, *107*, 5258.

(28) Cowan, M. L.; Ogilvie, J. P.; Miller, R. J. D. *Chem. Phys. Lett.* **2004**, *386*, 184.

(29) Brixner, T.; Mancal, T.; Stiopkin, I. V.; Fleming, G. R. *J. Chem. Phys.* **2004**, *121*, 4221.

(30) Sperling, J.; Nemeth, A.; Hauer, J.; Abramavicius, D.; Mukamel, S.; Kauffmann, H. F.; Milota, F. *J. Phys. Chem. A* **2010**, *114*, 8179.

(31) Panitchayangkoon, G.; Hayes, D.; Fransted, K. A.; Caram, J. R.; Harel, E.; Wen, J.; Blankenship, R. E.; Engel, G. S. *Proc. Natl. Acad. Sci.* **2010**, *107*, 12766.

(32) Mukamel, S.; Abramavicius, D.; Yang, L.; Zhuang, W.; Schweigert, I. V.; Voronine, D. V. *Acc. Chem. Res.* **2009**, *42*, 553.

(33) Zimdars, D.; Francis, R. S.; Ferrante, C.; Fayer, M. D. *J. Chem. Phys.* **1997**, *106*, 7498.

(34) Reuther, A.; Iglev, H.; Laenen, R.; Laubereau, A. *Chem. Phys. Lett.* **2000**, *325*, 360.

(35) Selig, U.; Schleussner, C.-F.; Foerster, M.; Langhojer, F.; Nuernberger, P.; Brixner, T. *Opt. Lett.* **2010**, *35*, 4178.

(36) Tseng, C.-H.; Matsika, S.; Weinacht, T. C. *Opt. Express* **2009**, *17*, 18788.

(37) Jailaubekov, A. E.; Bradforth, S. E. *Appl. Phys. Lett.* **2005**, *87*, 021107/1.

(38) Goodno, G. D.; Dadusc, G.; Miller, R. J. D. *J. Opt. Soc. Am. B* **1998**, *15*, 1791.

(39) Maznev, A. A.; Nelson, K. A.; Rogers, J. A. *Opt. Lett.* **1998**, *23*, 1319.

(40) Cohen, B.; Hare, P. M.; Kohler, B. *J. Am. Chem. Soc.* **2003**, *125*, 13594.

(41) Gonnella, N. C.; Nakanishi, H.; Holtwick, J. B.; Horowitz, D. S.; Kanamori, K.; Leonard, N. J.; Roberts, J. D. *J. Am. Chem. Soc.* **1983**, *105*, 2050.

(42) Holmén, A. *J. Phys. Chem. A* **1997**, *101*, 4361.

(43) Durfee III, C. G.; Backus, S.; Murnane, M. M.; Kapteyn, H. C. *Opt. Lett.* **1997**, *22*, 1565.

(44) Trebino, R. *Frequency Resolved Optical Gating: The Measurement of Ultrashort Laser Pulses*; Kluwer Academic Publishers: Boston, Dordrecht, London, 2000.

(45) Moran, A. M.; Maddox, J. B.; Hong, J. W.; Kim, J.; Nome, R. A.; Bazan, G. C.; Mukamel, S.; Scherer, N. F. *J. Chem. Phys.* **2006**, *124*, 194904:1.

(46) Lepetit, L.; Chériaux, G.; Joffre, M. *J. Opt. Soc. Am. B* **1995**, *12*, 2467.

(47) Gallagher, S. M.; Albrecht, A. W.; Hybl, J. D.; Landin, B. L.; Rajaram, B.; Jonas, D. M. *J. Opt. Soc. Am. B* **1998**, *15*, 2338.

(48) Yetzbacher, M. K.; Belabas, N.; Kitney, K. A.; Jonas, D. M. *J. Chem. Phys.* **2007**, *126*, 044511/1.

(49) *Handbook of Biochemistry and Molecular Biology*; 3 ed.; Fasman, G., Ed.; CRC Press: Boca Raton, 1975; Vol. 1.

(50) Pecourt, J.-M.; Peon, J.; Kohler, B. *J. Am. Chem. Soc.* **2001**, *123*, 10370.

(51) Moran, A. M.; Nome, R. A.; Scherer, N. F. *J. Chem. Phys.* **2006**, *125*, 031101:1.

(52) Middleton, C. T.; Cohen, B.; Kohler, B. *J. Phys. Chem. A* **2007**, *111*, 10460.

(53) Vauthey, E.; Henseler, A. *J. Phys. Chem.* **1995**, *99*, 8652.

(54) Fourkas, J. T.; Fayer, M. D. *Acc. Chem. Res.* **1992**, *25*, 227.

(55) Fleming, G. R. *Chemical Applications of Ultrafast Spectroscopy*; University Press: New York, 1986.

(56) Qian, W.; Jonas, D. M. *J. Chem. Phys.* **2003**, *119*, 1611.

(57) Debye, P. *Polar Molecules*; The Chemical Catalog Company: New York, 1929.

(58) Jimenez, R.; Fleming, G. R.; Kumar, P. V.; Maroncelli, M. *Nature* **1994**, *369*, 471.

(59) Bisgaard, C. Z.; Satzger, H.; Ullrich, S.; Stolow, A. *Chem. Phys. Chem.* **2009**, *10*, 101.

(60) Oladepo, S. A.; Loppnow, G. R. *J. Phys. Chem. B* **2011**, *115*, 6149.

(61) Jailaubekov, A. E. Ultrafast Electronic Deactivation of DNA Bases in Aqueous Solution, PhD Thesis, University of Southern California, 2007.

(62) Jiang, J.; Mukamel, S. *Phys. Chem. Chem. Phys.* **2011**, *13*, 2394.

(63) Jiang, J.; Mukamel, S. *Angew. Chem. In. Ed.* **2010**, *49*, 9666.

(64) Tekavec, P. F.; Lott, G. A.; Marcus, A. H. *J. Chem. Phys.* **2007**, *127*, 214307/1.

(65) Tian, P.; Keusters, D.; Suzaki, Y.; Warren, W. S. *Science* **2003**, *300*, 1553.

(66) Mukamel, S. *Principles of Nonlinear Optical Spectroscopy*; Oxford University Press: New York, 1995.

(67) Cho, M. *Chem. Rev.* **2008**, *108*, 1331.

Chapter 5 . Influence of Temperature on Thymine-to-Solvent Vibrational Energy Transfer

5.1. Introduction

A myriad of biological processes are initiated by the exchange of energy between solute molecules and their environments.[1,2] General physical insight into these complex many-body dynamics is still coming into focus despite numerous investigations over many decades. Photoinduced relaxation processes in DNA is one area where solute-solvent interactions give rise to particularly intriguing fundamental physics.[3-15] Internal conversion (IC) rapidly (<300fs) deactivates electronic excited states in the DNA bases, thereby suppressing the formation of lesions (e.g., thymine dimers) known to inhibit cellular function.[16,17] At the instant following IC, the nucleobases are left in "hot" quantum states, wherein a subset of vibrational modes possesses a highly non-equilibrium distribution of excitation quanta (i.e., >4eV in excess energy).[18,19] While it is clear that equilibrium is re-established within approximately 5ps in most nucleobases, the mechanisms behind such "vibrational cooling" (VC) processes are not well-understood. Of particular interest in this work are the specific classes of nuclear motions involved in VC (e.g., translations, librations) and kinetic effects originating in the impact that VC has on the temperature of the solute's environment.

Previous experimental and theoretical studies provide a framework for discussing the influence of solute-solvent interactions on VC.[20-27] Two general VC mechanisms are

---

Reprinted with permission from *Journal of Chemical Physics*, **135,** 114505-1-9 (2011).

considered: (i) energy is transferred from an intramolecular mode of the solute to an intermolecular (or intramolecular) mode in the solvent with the same frequency; (ii) the solute transfers population between intramolecular modes with different frequencies with the solvent either donating or accepting the amount of energy associated with the frequency difference. A large body of work suggests that energy is most effectively accepted by the lowest frequency modes of the solvent because they are associated with the greatest "friction"; hereafter associate modes at frequencies $<300cm^{-1}$ with the most significant friction for the purpose of discussion. In this view, mechanism (i) should be dominated by modes of the solute and solvent with frequencies $<300cm^{-1}$. By contrast, under mechanism (ii) VC is well-described as a cascade in which the overall rate is governed by the ability of the solute to concentrate energy in its lowest frequency intramolecular vibrations.[25] This picture wherein the low frequency modes of the solvent are the primary energy acceptors is challenged by the observation of pronounced isotope effects (e.g., deuteration of water) on the rate of VC in hydrogen-bonding solvents.[19,28] The key point in these earlier studies is that isotopic substitution of the solvent is known to primarily influence the spectrum of solute-solvent friction at frequencies $>>300cm^{-1}$.[29] It has therefore been suggested that the observed isotope effects reflect relaxation channels in which the solvent accepts energy using intermolecular (librational) modes at frequencies $>700cm^{-1}$.[19]

In this paper, the influence of temperature on VC is examined in the thymine nucleobase at both 100K and 300K in a mixture of methanol and water. Thymine is well-suited for fundamental studies of VC because its relatively small size facilitates the interpretation of experiments and makes it amenable to high-level theoretical models. In

addition, the transfer of energy from thymine to the solvent is readily monitored with the femtosecond transient grating (TG) and two-dimensional photon echo (2DPE) spectroscopies available in the laboratory. The present experiments are particularly sensitive to VC because, as shown in Figure 5.1, all laser pulses are resonant with the lowest energy $\pi\pi^*$ electronic resonance of thymine near 38000cm^{-1}, similar to the systems investigated in Chapter 4. With respect to the physics underlying VC, reduction in the equilibrium temperature of the system shifts the spectrum of solute-solvent friction to lower frequencies in addition to narrowing the "bandwidths" of relaxation channels through which the solute and solvent exchange energy using modes with frequencies >300cm^{-1}. Here the relationship between these temperature effects and specific aspects of the solute-solvent interactions is explored (e.g., mode frequency, coupling strength, time scale of fluctuations) using experimental measurements and model calculations.

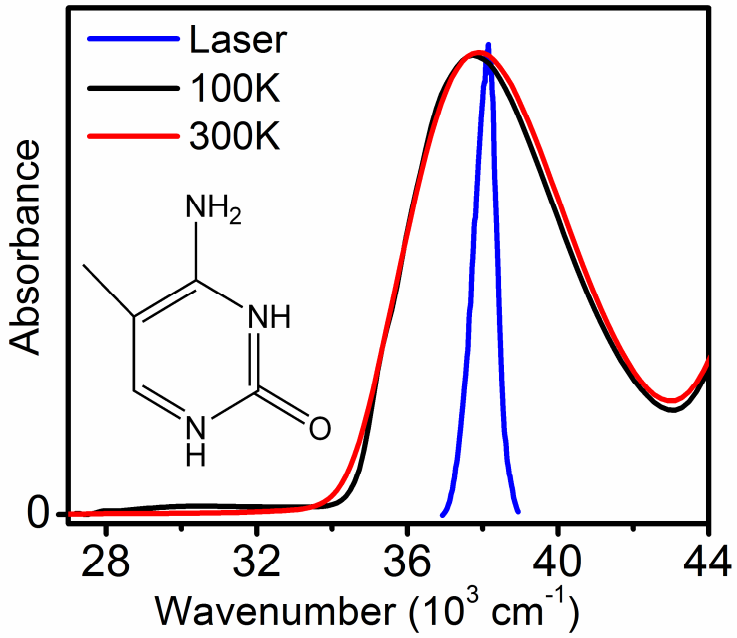

Figure 5.1. Absorbance spectra of thymine in an 85:15 mixture of methanol:water at 100K (black) and 300K (red). Also shown is the spectrum of the laser (blue) used in TG and 2DPE measurements. The structure of thymine is displayed in the inset.

Notably, this work is one of the first applications of 2DPE spectroscopy in the mid-UV spectral range. In the past decade, 2DPE spectroscopy has had a transformative impact on the understanding of processes ranging from chemical exchange equilibrium in liquids to energy transfer in photosynthesis.[30-38] Motivated by technical feasibility and particular scientific questions, 2DPE was first demonstrated and has developed most rapidly at infrared and visible wavelengths.[31,39-45] 2DPE has only recently been extended to the mid-UV spectral range (200-300nm)[46-48] and still must contend with several challenges including the attainment of adequate laser bandwidth and the suppression of undesired nonlinearities in the solvent medium (e.g., ionization of solute and solvent).[49,50] Solutions to these technical challenges will open the door to the study of numerous biological systems whose lowest energy electronic transitions are found in the mid-UV (e.g., DNA bases, amino acids).

5.2. Materials and Methods

Generation of 25fs, 38000cm^{-1} laser pulses is achieved using a 75 micron diameter hollow-core fiber filled with 0.65atm argon gas.[51,52] The setup resembles that developed by Bradforth and co-workers and performs similarly.[52] Briefly, 12660cm^{-1} and 25320cm^{-1} pulses with 40 μJ energies and 130fs durations (160cm^{-1} FWHM bandwidths) are focused into the fiber to generate 25fs, 38000cm^{-1} pulses with 1.0μJ energies (900cm^{-1} FWHM bandwidth). Two fused silica prisms separated by 13cm fully compensate for dispersion accumulated in transmissive optics between the fiber and the sample. The time-bandwidth product of these pulses (<0.5) is close to the Fourier transform limit for Gaussian pulse envelopes ($\approx$0.44).[53]

TG and 2DPE experiments utilize a diffractive optic-based interferometer similar to those described in earlier applications at visible wavelengths.[54-56] The diffractive optic generates a four-pulse laser beam geometry. Three of the laser pulses induce the nonlinear polarization and the fourth (attenuated) pulse is used as a reference field for signal detection by spectral interferometry.[57,58] As indicated in Figure 2.11, TG measurements use a motorized translation stage to scan T (with τ=0). Relaxation processes such as internal conversion and vibrational cooling occur in the delay, T. 2DPE scans τ from -100fs to +100fs (at various T) by moving fused silica prism wedges in the paths of pulses 1 and 2. Numerical Fourier transformation in τ yields the excitation dimension of the 2DPE spectrum, ω_τ; the emission dimension, ω_t, is obtained by dispersing the signal pulse in the spectrometer.[41] In all experiments, signals are detected using a back-illuminated CCD array (Princeton Instruments PIXIS 100B) mounted on a 0.3 meter spectrograph with a 3600 g/mm grating. Integration times range between 100-400 ms based on the signal intensity. In both the TG and 2DPE techniques, pulse delays are scanned 20-40 times as needed to optimize the signal-to-noise ratios.

Thymine (Fisher) is dissolved in an 85:15 mixture of methanol:water because this mixture produces a glass with high optical quality at cryogenic temperatures. Importantly, both components of the mixture form hydrogen bonds and therefore exhibit the VC dynamics of interest to this work. The solutions are contained in a 0.5mm thick fused silica cuvette mounted on a low-noise rotating sample holder inside a liquid nitrogen cooled cryostat (Oxford Instruments Optistat-DN).[59] The sample moves 25μm after each laser shot and the FWHM diameter of laser spot is 90 μm. Photobleaching is not observed at this rate of sample rotation. The measurements shown below, which have

signal-to-noise ratios exceeding 30:1 at 300K, demonstrate that motion of the sample causes little noise in the signal phase (the absorptive TG and 2DPE signal components are sensitive to noise in the signal phase). Each of the three incoming pulses possesses a fluence of 4.65×10^{13} photons/cm^2 and a peak power of 1.4GW/cm^2. By summing the fluences of pulses 1 and 2, it is estimated that 0.4% of the thymine molecules in the focal volume are photoexcited. Increasing the laser fluence generates larger signal strengths but must be avoided with the present 25fs pulses because photoionization of the solute and solvent becomes problematic at peak powers greater than 1.4GW/cm^2 as discussed in Section 4.3.A.[46,50]

5.3. Results

5.3. A. Effect of Temperature on Relaxation Kinetics

The TG experiments presented in this Section photoexcite the lowest energy $\pi\pi^*$ electronic resonance of thymine. Recovery of the equilibrium system is governed primarily by two relaxation processes. First, IC returns thymine to the ground electronic state where it initially possesses a large amount of excess vibrational energy. This excess vibrational energy is then transferred into the surrounding solvent. The absorptive representation of the TG signal (i.e., real part of the complex signal field) utilized here provides information equivalent to that obtained in a conventional transient absorption experiment.[60] Thus, relaxation of the system is directly monitored without the (undesired) contributions from thermal gratings found in homodyned TG signals.[61,62]

At both 100K and 300K, the signals have a sub-ps rise time (τ_1) which is assigned to IC based on the attainment of similar time constants in related work.[63-65] In this interpretation, the "bleach" in the signal increases (i.e., rises) because IC removes

destructive interference(s) associated with excited state absorption. Notably, a shorter IC time constant is found at 300K (250fs) than at 100K (340fs). The origin of this weak temperature dependence is not immediately clear. One interpretation is that the dynamics reflect the presence of a small excited state potential energy barrier.[66] However, it is also possible that deformation modes play a critical role in crossing through the conical intersection. For example, out-of-plane motions (e.g., rotation around NH_2) would be particularly sensitive to the rigidity of the solvent at 100K. This issue is still under investigation.

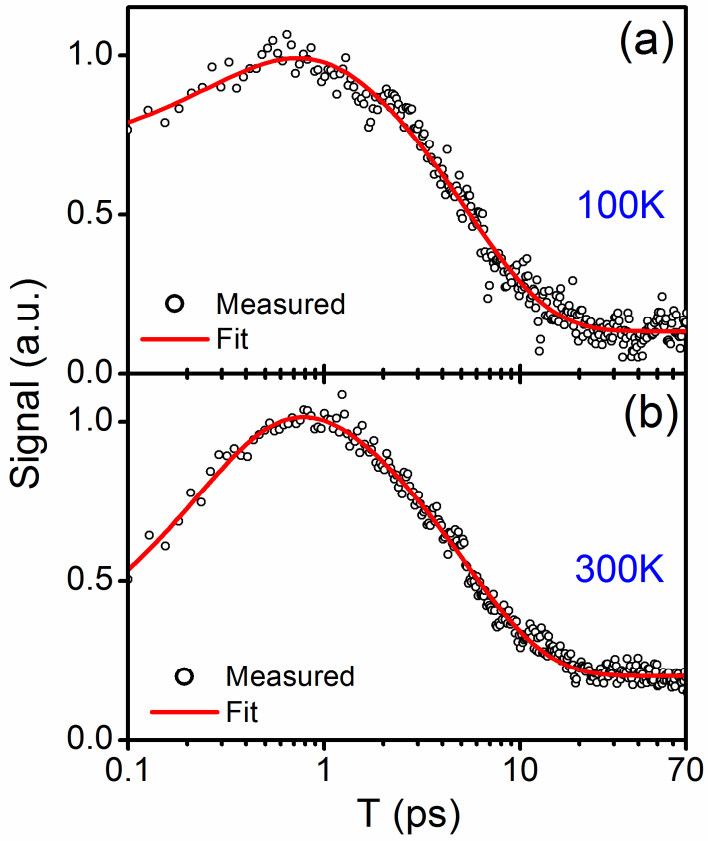

Figure 5.2. Absorptive part of TG signal field measured for thymine at (a) 100K and (b) 300K. The experiments are conducted with 25fs, 38000cm^{-1} laser pulses under the magic angle polarization condition. Fitting parameters are given in Table 5.1.

Remarkably, the time constants associated with VC, τ_2, cannot be distinguished within experimental error at 100K and 300K. This result is inconsistent with a physical picture wherein the lowest frequency modes of the solute constitute the dominant "gateway" for energy transfer into the solvent (in the equilibrium system). An alternative interpretation might invoke relaxation channels involving higher frequency (>300cm^{-1}) modes, which should be less sensitive to this temperature difference. However, it is important to recognize that the true dynamics are complicated by the impact of VC on the "effective" temperature of the environment. The mechanisms behind this insensitivity to temperature will be explored in detail with model calculations in Section IV. Although thymine is the subject of this chapter, it should be mentioned that a similar insensitivity of VC to temperature in both adenine and thymidine has been observed, which suggests that this behavior may generalize to a variety of other nucleobases (cf., Supporting Information).[67] Strong conclusions regarding the temperature dependence of the offset in the signal at long delay times, A_0, cannot presently be drawn.

Table 5.1. Fitting parameters for transient grating signals shown in Figure 5.2

[(a),(b)]parameter	100 K	300 K
A_0	0.13±0.01	0.20±0.01
A_1	-0.51±0.08	-0.96±0.08
τ_1 (ps)	0.34±0.09	0.25±0.03
A_2	1.05±0.03	1.00±0.02
τ_2 (ps)	5.23±0.28	5.08±0.16

[(a)] Fit to Equation $S(T) = A_0 + \sum_{i=1}^{2} A_i \exp(-T/\tau_i)$.

[(b)] The error is defined as two standard deviations.

VC is generally investigated using transient absorption experiments in which the probe pulse is red-shifted with respect to the peak of the ground state absorption spectrum.[18,28] Such measurements interrogate so-called "hot bands" signifying nonequilibrium population in the ground electronic state. By contrast, the present measurements are conducted in a "one-color" configuration where all pulses possess identical spectra. Nonetheless, information on VC can still be derived because it is the rate-limiting step governing recovery of the equilibrium system. The VC time constants obtained here (and recently in adenine)[46] are fully consistent with studies of related systems employing red-shifted probe pulses.[18]

5.3. B. Photon Echo Signatures of Environmental Motion

The measurement of essentially identical VC time constants, τ_2, at 100K and 300K cannot be predicted *a priori* because temperature has a complex (many-body) influence on nuclear motions in both the solute and solvent. 2DPE spectroscopy, which is useful for studying such fluctuations, can be regarded as a "pump-probe" experiment with dispersed excitation (pump) and detection (probe) frequencies.[31,42,68] When the delay between excitation and detection, T, is short compared to the time scale of solvent motion, correlations between the excitation, ω_τ, and detection (i.e., emission), ω_t, frequencies manifest in a line shape elongated with respect to the diagonal of the 2DPE spectrum, $\omega_\tau = \omega_t$. Correlations between ω_τ and ω_t are lost as the solvent structure reorganizes around the solute, making the spectrum appear "rounder" with increasing T. Thus, a 2DPE spectrum that is elongated with respect to the diagonal, suggests that the solvent structure has not fully randomized on the time scale of the measurement, T. This effect is observed in Section 4.3 B investigating adenine and discussed in Section 2.6.

Figure 5.3 displays 2DPE spectra acquired at 100K and 300K. Here only spectra acquired at T=0.6ps are presented because the 2DPE line shape changes little in T. The amount of correlation between ω_τ and ω_t is characterized by comparing the diagonal, Γ_d, and anti-diagonal, Γ_{ad}, line widths. The line shape is relatively insensitive to T at 300K, whereas it undergoes minor changes between T=0.1ps and T=0.5ps at 100K. It is possible that the (slightly) slower IC time scale at 100K in some way influences the 2DPE peak shape. For example, the dynamics in the line shape may reflect interference between ground state bleach and excited state absorption signal components. Most importantly, the ratios, Γ_{ad}/Γ_d, plotted in Figure 5.3c reveal a greater amount of correlation between ω_τ and ω_t (i.e., smaller ratio) at 100K than at 300K. These data suggest that thermally driven reorganization of the solvent structure around thymine occurs on the picosecond and femtosecond time scales at 100K and 300K, respectively. This finding is perhaps unexpected given the similar VC time constants measured at 100K and 300K (cf., Table 5.1). In comparing these dynamics, it should be noted that the 2DPE line shapes are governed by equilibrium fluctuations of the system because the ground state bleach nonlinearity is probed. Nonetheless, it is reasonable to assume that the nonequilibrium fluctuations associated with VC also slow down significantly at 100K.

5.4. Phenomenological Model for Vibrational Cooling

In this Section, a phenomenological model is used to investigate the influence of solute-solvent interactions on the rate of VC. The model addresses only processes in which vibrational energy is transferred from a mode in the solute to a mode in the solvent with the same frequency; intramolecular vibrational energy redistribution within the

solute is not considered. The system is treated as a single harmonic oscillator, whereas the (harmonic) solvent bath is handled using a correlation function approach commonly employed in optical spectroscopy, which is thoroughly discussed in Chapter 2.[69,70] This level of complexity is sufficient to address: (i) the temperature dependence of the VC rate; (ii) the influence of the solute's mode frequency on VC; (iii) the interplay of the solute-solvent coupling strength and the relaxation rate for thermally driven fluctuations.

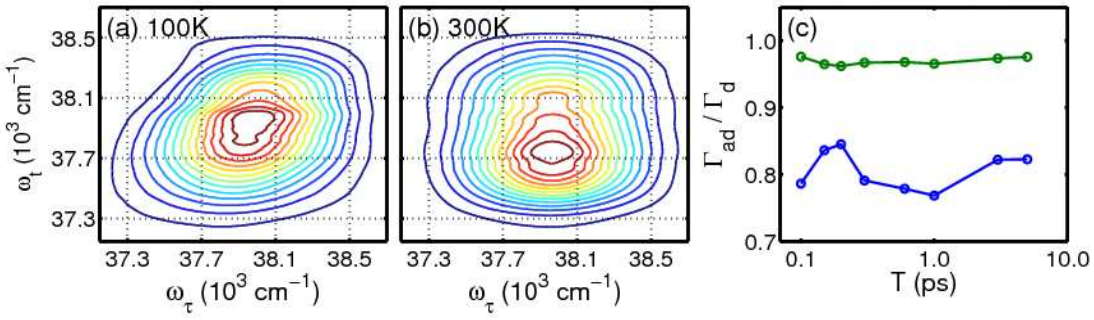

Figure 5.3. Absorptive 2DPE spectra measured at (a) 100K and (b) 300K with T=0.6ps. The electronic polarizability of the solvent prevents the acquisition of signals at T <0.1ps.[46,67] The spectra are plotted on a linear scale with 13 equally spaced contour lines. (c) The ratio in the anti-diagonal and diagonal line width, Γ_{ad}/Γ_d, is plotted with respect to the (logarithmic) pulse delay at 100K (blue) and 300K (green). Additional 2DPE spectra are presented in Appendix 2.[67]

5.4. A. Vibrational Cooling Rate

At second order in perturbation theory, the rate of VC is given by a time correlation function in the solute-solvent interaction operator, $\hat{V}$,

$$K = \frac{1}{\hbar^2}\int_0^\infty dt \left\langle \hat{V}(t)\hat{V}(0)\right\rangle \tag{5.1}$$

where t is the time interval between interactions with $\hat{V}$. The correlation function is expanded in a complete set of harmonic oscillator eigenstates as

$$K = \frac{1}{\hbar^2}\sum_{mn} P_m \int_0^\infty dt \left\langle m\left|\exp\left(i\hat{H}t/\hbar\right)\hat{V}\right|n\right\rangle\left\langle n\left|\exp\left(-i\hat{H}t/\hbar\right)\hat{V}(0)\right|m\right\rangle \tag{5.2}$$

Matrix elements involving the solute-solvent interaction potential can be taken outside the ensemble average, denoted as $\langle\cdots\rangle$, when $\hat{V}$ depends weakly on nuclear motion. The rate is then given by

$$K = \frac{1}{\hbar^2}\sum_{mn} P_m \left|V_{mn}\right|^2 \int_0^\infty dt \exp\left(i\omega_{mn}t\right)\left\langle \exp_+\left[-i\int_0^t dt' U_{mn}\left(t'\right)\right]\right\rangle \tag{5.3}$$

Here $U_{mn}\left(t\right) = Q_m\left(t\right) - Q_n\left(t\right)$ is a solvation operator where $Q_m\left(t\right)$ is a primary Brownian oscillator coordinate coupled to energy level m.[69,70] As shown in Chapter 2 and Reference [70], a cumulant expansion can then be carried out on the time evolution operator

$$\left\langle \exp_+\left[-i\int_0^t dt' U_{mn}\left(t'\right)\right]\right\rangle = 1 - i\int_0^t dt'\left\langle U_{mn}\left(t'\right)\right\rangle + \int_0^t\int_0^{t'} dt'dt''\left\langle U_{mn}\left(t'\right)U_{mn}\left(t''\right)\right\rangle + \cdots \tag{5.4}$$

Under the assumption of Gaussian statistics, only the second order term in the expansion survives, resulting in

$$\int_0^t\int_0^{t'} dt'dt''\left\langle U_{mn}\left(t'\right)U_{mn}\left(t''\right)\right\rangle = \int_0^t\int_0^{t'} dt'dt''\left\langle \left(Q_m\left(t'\right) - Q_n\left(t'\right)\right)\left(Q_m\left(t''\right) - Q_n\left(t''\right)\right)\right\rangle \tag{5.5}$$

By combining Equations (3)-(5), the following expression is obtained

$$K = \frac{1}{\hbar^2}\sum_{mn} P_m \left|V_{mn}\right|^2 \int_0^\infty dt \exp\left[i\omega_{mn}t - g_{mm}\left(t\right) - g_{nn}\left(t\right) + 2g_{mn}\left(t\right)\right] \tag{5.6}$$

where

$$g_{mn}\left(t\right) = \int_0^t\int_0^{t'} dt'dt''\left\langle Q_m\left(t'\right)Q_n\left(t''\right)\right\rangle \tag{5.7}$$

Damping functions, $g_{mn}\left(t\right)$, in which $m \neq n$ are nonzero only if motions of the primary coordinates, $Q_m\left(t\right)$ and $Q_n\left(t\right)$, give rise to correlated fluctuations in the energy levels m and n. Equation (7) is simplified with two assumptions: (i) fluctuations in levels m and

n possess identical statistics, i.e. $g_{mm}(t) = g_{nn}(t)$; (ii) fluctuations in levels m and n are partially correlated such that

$$g(t) = g_{mm}(t) = g_{nn}(t) = 1/2\, g_{mn}(t) \tag{5.8}$$

It should be noted that a general (level-independent) damping function, $g(t)$, is defined in Equation (8). Under these assumptions, the rate constant is given by

$$K = \frac{1}{\hbar^2} \sum_{mn} P_m \left| V_{mn} \right|^2 \Phi\left(\omega_{mn}; T_{Bath}\right) \tag{5.9}$$

where

$$\Phi\left(\omega_{mn}; T_{Bath}\right) = \mathrm{Re} \int_0^\infty dt \exp\left[i\omega_{mn} t - g\left(t; T_{Bath}\right) \right] \tag{5.10}$$

The temperature governing the rate of VC is not well-defined in the present experiments because internal conversion deposits roughly 4eV of vibrational energy in the ground electronic state of the composite solute-solvent system. Initially, the (effective) temperature of the solute is approximately 1200K.[18] In general, the transfer of such a large amount of excess energy from the solute into the solvent causes the temperature of the solvent environment (i.e., bath) to increase substantially.[71,72] Equation (10) states explicitly that the sensitivity of $\Phi\left(\omega_{mn}; T_{Bath}\right)$ to the temperature of the bath, T_{Bath}, enters through a parametric dependence in the damping function, $g\left(t; T_{Bath}\right)$. The form of $g\left(t; T_{Bath}\right)$ employed in this work will be defined in the following Section.

Although Equation (9) is written in a general way, it should be noted that the dominant VC transitions change the number of vibrational quanta by only 1 when the coordinate dependence of $\hat{V}$ is weak and the system is harmonic (cf., appendix A2). Anharmonic oscillators differ in that transitions between states that differ by multiple

vibrational quanta are possible. Such "higher-order" transitions, which parallel a breakdown in selection rules in infrared spectroscopy, have a weak influence on VC in systems with modest anharmonicity. However, for highly anharmonic vibrations, the rate of VC is generally more sensitive to the particular quantum states involved in a transition (compared to a harmonic oscillator) because the energy gaps between successive quantum levels vary with the quantum number (e.g., a Morse oscillator). That is, in an anharmonic system, $\Phi\left(\omega_{mn};T_{Bath}\right)$ would have a maximum in the region of the quantum manifold for which ω_{mn} is resonant with the characteristic frequency of the bath. By contrast, $\Phi\left(\omega_{mn};T_{Bath}\right)$ is independent of the vibrational quantum number because all energy gaps are equal in a harmonic system.

5.4. B. Coupling of the System to Multiple Brownian Oscillator Coordinates

Often, a single overdamped primary Brownian oscillator coordinate provides a sufficient phenomenological description of the fluctuations that drive molecular processes in solution. However, two primary coordinates must be included here to fully account for all relevant classes of solvent motion (e.g., librations, intramolecular modes of solvent). The effects of low-frequency solvent motions on level m are incorporated with a single overdamped Brownian oscillator coordinate for which the odd component of the spectral density is written as[69]

$$C_L\left(\omega\right) = 2\lambda\frac{\omega\Lambda}{\omega^2+\Lambda^2} \tag{5.11}$$

$C_L\left(\omega\right)$ peaks at frequencies smaller than $k_B T_{Bath}$ (k_B is Boltzmann's constant) when the reorganization energy, λ, is much larger than the rate at which fluctuations relax, Λ. Refer to Section 2.2 for a discussion of the spectral density and Figure 2.3 for a physical

interpretation of Λ. $C_L(\omega)$ therefore provides an efficient channel for vibrational energy transfer initiating in low frequency modes of the solute. In this slow modulation regime, the standard deviation of fluctuations in the energy levels of the system can be approximated with $\sqrt{2\lambda k_B T_{Bath}}$.[69] In the opposite limit, when $\Lambda >> \lambda$, $C_L(\omega)$ is spectrally broad with significant amplitude at frequencies greater than $k_B T_{Bath}$. Below it is examined how the interplay between these two parameters, λ and Λ, influences VC kinetics.

The second primary Brownian oscillator coordinate in the model represents higher frequency (librational) modes using the spectral density

$$C_H(\omega) = \frac{S_{avg}\Omega_{avg}^2}{\delta\sqrt{2\pi}} \exp\left[-\frac{(\omega - \Omega_{avg})^2}{2\delta^2}\right] \tag{5.12}$$

where S_{avg} and $S_{avg}\Omega_{avg}$ are respectively the average Huang-Rhys factor and total amount of reorganization energy associated with an inhomogeneous distribution of modes centered at Ω_{avg} with the width δ.

Equation (12) adds a Gaussian line shape to the (delta function) spectral density for an underdamped mode derived in Reference [69]. Alternative methods of treating the higher frequency modes can be envisioned (e.g., Lorentzian distribution), but would not impact the conclusions drawn from the model. The spectral densities are added together, $C(\omega) = C_L(\omega) + C_H(\omega)$, and used to generate the damping function, $g(t;T_{Bath})$, using

$$\begin{aligned} g(t;T_{Bath}) = \frac{1}{2\pi}\int_{-\infty}^{\infty} d\omega \frac{1-\cos(\omega t)}{\omega^2} \coth(\hbar\omega / 2k_B T_{Bath}) C(\omega) + \\ \frac{i}{2\pi}\int_{-\infty}^{\infty} d\omega \frac{\sin(\omega t) - \omega t}{\omega^2} C(\omega) \end{aligned} \tag{5.13}$$

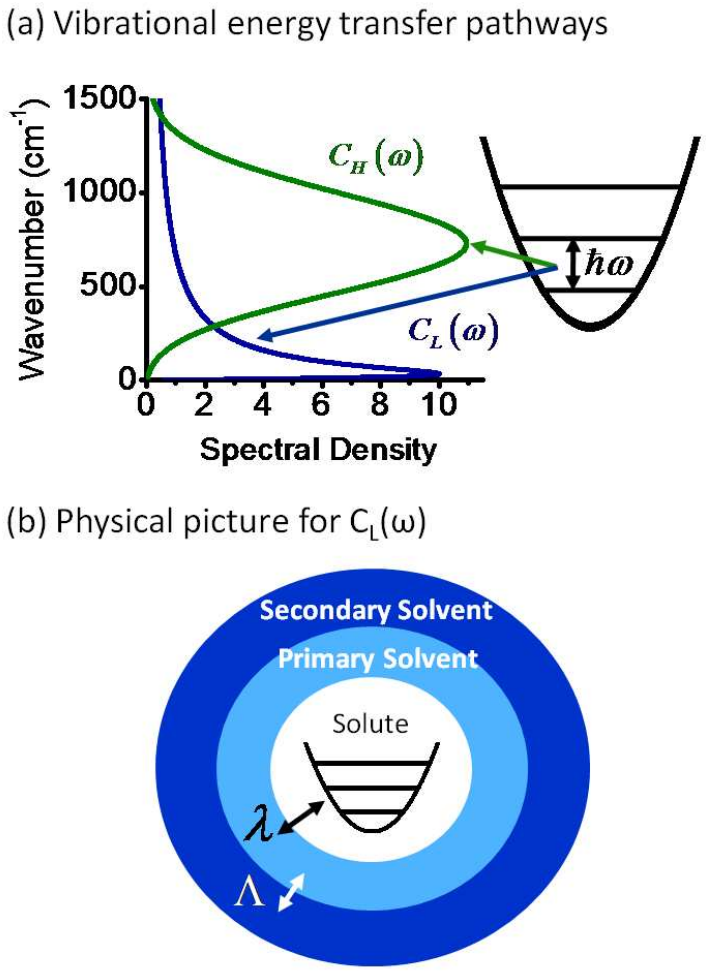

Figure 5.4. (a) Vibrational cooling occurs by way of two relaxation channels associated with the spectral densities, $C_L(\omega)$ and $C_H(\omega)$. (b) The transfer of vibrational energy corresponding to $C_L(\omega)$ is governed by two parameters, λ and Λ. λ is the coupling strength between the solute and the primary solvent shell (i.e., primary Brownian oscillator). Λ is the rate at which fluctuations in the primary solvent shell, and in turn the solute, relax through energy exchange with the secondary solvent shell (i.e., secondary Brownian oscillators). Section 2.2 further discusses the spectral density.

Notably, Equation (13) describes how the temperature of the bath, T_{Bath}, enters the present model for VC. The real part of $g(t;T_{Bath})$, which is primarily governed by the lower frequency ($\omega < k_B T_{Bath}$) part of $C(\omega)$, accounts for the exchange of energy between the solute and solvent. The imaginary part of $g(t;T_{Bath})$ enables (energetically

downhill) VC transitions initiating in high frequency modes of the solute. The key concepts involved in the model are illustrated in Figure 5.4.

5.4. C. Numerical Results

$\Phi(\omega_{mn};T_{Bath})$ is focused on in this Section (rather than Equation (9)) because it carries the key insights into the mechanisms by which temperature influences VC. In Table 5.2, estimates for the parameters of $\Phi(\omega_{mn};T_{Bath})$ are provided. The coupling strength, λ, is chosen for consistency with line widths measured in vibrational spectroscopies (i.e., 10's of cm^{-1}). $C_H(\omega)$ is given a broad width, δ, with a small total reorganization energy, $S_{avg}\Omega_{avg}$, to approximate the spectra of solute-solvent friction computed for water and alcohols. It should be emphasized that the conclusions reached with this model are insensitive to variation of these parameters within a reasonable range. $\Phi(\omega_{mn};T_{Bath})$ is plotted with respect to the transition frequency, ω_{mn}, at T_{Bath}=100K and 300K in Figure 5.5. The coupling strength, λ, is fixed at $10cm^{-1}$ while the time scale of motion in the solvent, Λ^{-1}, is varied from 0.1ps to 10ps. In general agreement with friction spectra derived from molecular dynamics simulations, $\Phi(\omega_{mn};T_{Bath})$ maximizes at $\omega_{mn} < k_B T_{Bath}$ and possesses finite amplitude up to $1000cm^{-1}$.[29,73] At both Λ^{-1}=1ps and 10ps, changing the temperature of the bath from 100K to 300K causes $\Phi(\omega_{mn};T_{Bath})$ to decrease at ω_{mn}<$50cm^{-1}$ and increase at ω_{mn}=50-$300cm^{-1}$. By contrast, $\Phi(\omega_{mn};T_{Bath})$ is relatively unaffected by the temperature change when Λ^{-1}=0.1ps. Figure 5.5 also makes clear that $\Phi(\omega_{mn};T_{Bath})$ is insensitive to the temperature change for all values of Λ^{-1} when ω_{mn}>$300cm^{-1}$. This insensitivity is found because the solvent primarily acts as an

energy accepting reservoir at $\omega > k_B T_{Bath}$ (i.e., it is controlled by imaginary part of $g(t;T_{Bath})$ in Equation (13)). Additional calculations presented in the Supporting Information show that the insights established in Figure 5.5 generalize to a broader range of temperatures.[67]

Table 5.2. Parameters used in rate calculations

Parameter	Value
λ	10 cm^{-1}
Λ	Varied
Ω_{avg}	500 cm^{-1}
δ	700 cm^{-1}
S_{avg}	0.02

Connections between the model and experimental observations are more clearly drawn using

$$\eta(\omega_{mn};T_{VET}) = \frac{\Phi(\omega_{mn};T_{Bath} = T_{VET} + 300\text{K})}{\Phi(\omega_{mn};T_{Bath} = T_{VET} + 100\text{K})} \tag{5.14}$$

In the two experiments under consideration, the temperatures of the solutions are 100K and 300K before the laser pulses arrive at the sample. Subsequent to internal conversion in the solute, vibrational energy is transferred into the surrounding solvent, thereby causing the temperature of the bath to increase. $\eta(\omega_{mn};T_{VET})$ accounts for this vibrational energy transfer induced temperature increase with the parameter, T_{VET}. The most appropriate value of T_{VET} is not well-defined. In the lower limit, T_{VET} =0 in the equilibrium system. The upper limit of T_{VET} must be much less than the initial

temperature of the solute (i.e., 1200K)[18] because the vibrational energy becomes distributed among numerous low frequency intermolecular modes in the bath. For example, molecular dynamics simulations have found that the temperature increase in the environment of a heme protein is less than 10% of the initial non-equilibrium temperature (500-700K) in the heme chromophore.[71] A phenomenological model describing relaxation of p-nitroaniline in aqueous solution similarly predicts a modest (100K) increase in the temperature of the primary solvent shell.[28] Compared to p-nitroaniline in water, a larger temperature increase is expected in thymine because of its higher electronic resonance frequency and the smaller heat capacity of the methanol/water mixture. As a conservative estimate, it is suggested that the physically reasonable range of T_{VET} has an upper limit of 250K (cf., Appendix 2).[67]

In Figure 5.5c, $\eta(\omega_{mn};T_{VET})$ is plotted at various values of Λ^{-1} under equilibrium conditions (T_{VET}=0). These calculations make clear that an increase in the (experimentally controlled) contribution to T_{Bath} gives rise to a rate increase only when the time scale of the bath is slow (i.e., Λ^{-1}>0.1ps). The insensitivity of the rate to temperature calculated at Λ^{-1}=0.1ps parallels the "motional narrowing" effects known in NMR and optical spectroscopies.[69] A full two-dimensional contour plot of $\eta(\omega_{mn};T_{VET})$ is presented in Figure 5.6. It is predicted that $\eta(\omega_{mn};T_{VET})$ is essentially independent of T_{VET} at all ω_{mn} when Λ^{-1}=0.1ps. However, the experimentally controlled temperature increase (from 100K to 300K) gives rise to a rate enhancement at both Λ^{-1}=1ps and 10ps. The mode frequency, ω_{mn}, for which the enhancement occurs increases with T_{VET}, but does not exceed 300cm^{-1} within the physically reasonable range of T_{VET}. In addition,

the magnitude of the enhancement decreases with increasing T_{VET}. Essentially, no enhancement is found at T_{VET} >300K.

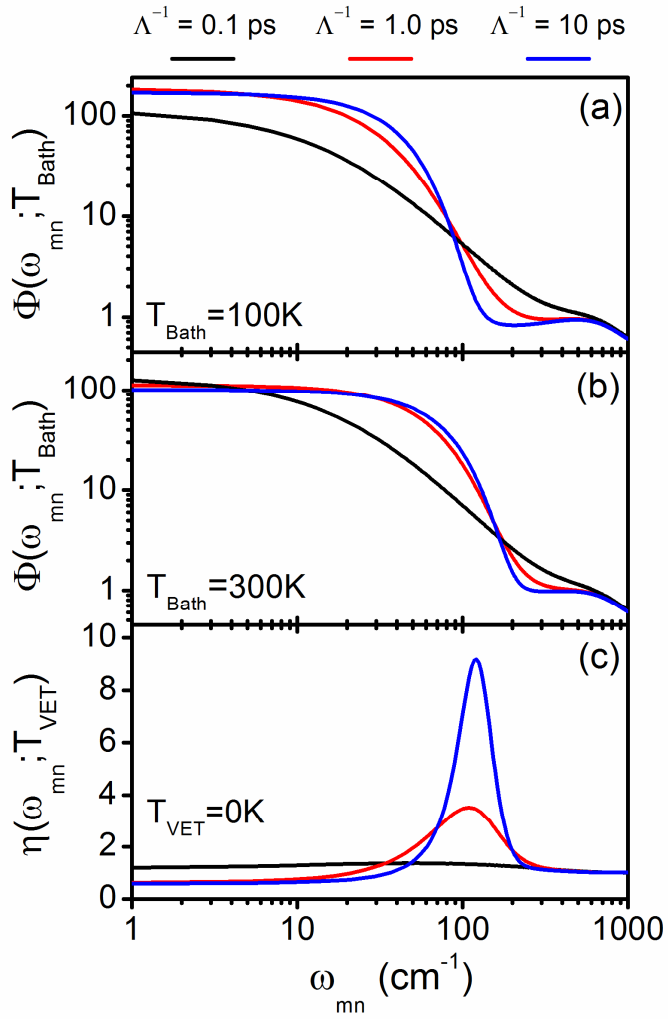

Figure 5.5. (a) $\Phi(\omega_{mn};T_{Bath})$ is computed at (a) T_{Bath} =100K and (b) T_{Bath} =300K with the parameters given in Table 5.2. The time scales of the bath, Λ^{-1}, are specified in the Figure legend. (c) Ratio in $\Phi(\omega_{mn};T_{Bath})$ calculated at 300K and 100K for the equilibrium system (i.e., T_{VET} =0 in Equation (5.14)). A rate enhancement is predicted only when Λ^{-1} exceeds 0.1ps. $\Phi(\omega_{mn};T_{Bath})$ is calculated at higher temperatures of the bath, T_{Bath}, in Appendix 2.[67]

These calculations suggest three possible interpretations of the nearly identical VC rates measured at 100K and 300K. The first possibility is that the time scale of the

solvent, Λ^{-1}, is much greater than 0.1ps and that high frequency (>300cm^{-1}) intramolecular modes of thymine directly transfer vibrational quanta to solvent modes with the same frequencies. This interpretation of the dynamics deserves strong consideration because it is consistent with the isotope effects observed in earlier studies.[19] The second possibility is that the relaxation-induced increase in the temperature of the environment, T_{VET}, reduces the sensitivity of VC to the (experimentally controlled) temperature difference in the equilibrium systems (i.e., 100K versus 300K). Figure 5.6 suggests that such effects likely contribute within the physically reasonable range of T_{VET}. The third possibility is that the time scale of solvent motion is extremely fast (i.e., $\Lambda^{-1} \approx$ 0.1ps even at 100K), thereby making the rate of VC insensitive to temperature regardless of the solute's mode frequency. This third prospect is not consistent with the long-lived correlations between ω_τ and ω_t detected in the 2DPE experiments. 2DPE measurements find slower fluctuations in the *equilibrium* system at 100K because the ground state bleach nonlinearity is probed. Implicit in the rejection of mechanism (iii) is the assumption that the *nonequilibrium* fluctuations associated with VC are also much slower at 100K than they are at 300K. In summary, the observed dynamics are ascribed to a combination of the first two mechanisms. Future work will aim to quantify the relative contributions of these two mechanisms.

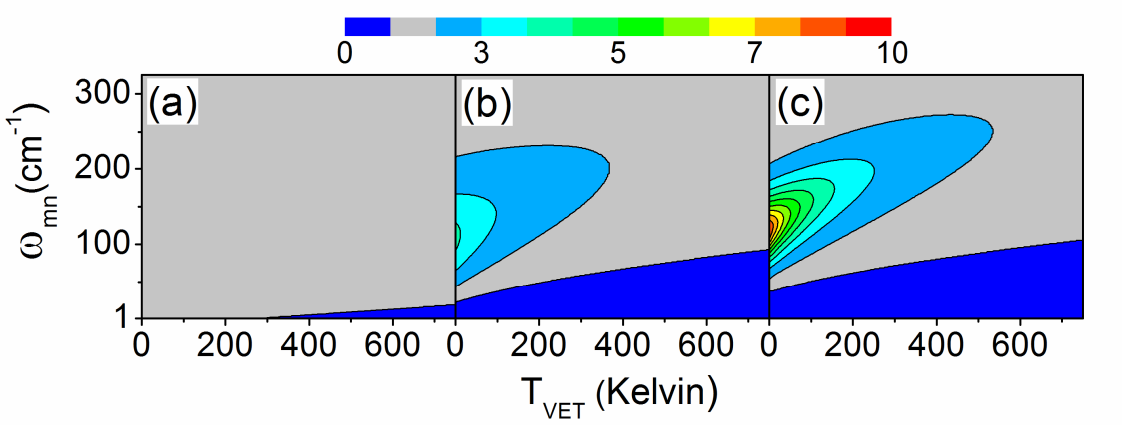

Figure 5.6. $\eta(\omega_{mn};T_{VET})$ is computed at (a) Λ^{-1}=0.1ps, (b) Λ^{-1}=1.0ps, (c) Λ^{-1}=10ps with the parameters given in Table 5.2. These calculations predict that the TG experiments should find a significant enhancement in the rate of vibrational cooling (at 300K versus 100K) provided that: (i) the time scale of the solvent, Λ^{-1}, is much greater 0.1ps; (ii) the VC induced increase in the temperature of the bath, T_{VET}, is less than 300K.

5.5. Conclusion

In conclusion, it is found that thymine undergoes VC at a rate that is insensitive to temperature variation from 100K to 300K in a mixture of methanol and water. A theoretical model suggests three possible explanations for this behavior: (i) the transfer of vibrational energy from the solute to solvent initiates in intramolecular modes of the solute with frequencies >300cm^{-1}; (ii) the relaxation induced increase in the effective temperature of the solvent surrounding the solute reduces the sensitivity of VC to changes in the temperature of the equilibrium system (i.e., 100K versus 300K); (iii) the time scale of nuclear motion in the solvent, Λ^{-1}, approaches 0.1ps even at 100K (i.e., motional narrowing). It is suggested that a combination of mechanisms (i) and (ii) contribute to the present observations. Mechanism (i) must be strongly considered because it is consistent with the known isotope dependence of VC.[19] In addition, the model calculations shown in Figure 5.6 predict that mechanism (ii) plays a role within the physically reasonable temperature range of the bath. The third possibility is rejected on

the grounds that 2DPE spectra acquired at 100K possess long-lived correlations between the excitation, ω_τ, and detection, ω_t, frequencies (cf., Figure 5.3). Overall, this study has obtained new insights into photoinduced relaxation processes in thymine, which will likely generalize to other nucleobases. Essential to the perspective offered here is the recent extension of interferometric TG and 2DPE spectroscopies to the mid-UV spectral range.[46] This chapter represents the first step towards understanding physics with these spectroscopic techniques in the UV.

5.6. References

(1) *Femtochemistry and Femtobiology: Ultrafast Events in Molecular Science*; Martin, M. M.; Hynes, J. T., Eds.; Elsevier: Amsterdam, 2004.

(2) Sundström, V. *Annu. Rev. Phys. Chem.* **2008**, *59*, 53-77.

(3) Middleton, C. T.; de La Harpe, K.; Su, C.; Law, Y. K.; Crespo-Hernández, C. E.; Kohler, B. *Annu. Rev. Phys. Chem.* **2009**, *60*, 217-239.

(4) Hudock, H. R.; Levine, B. G.; Thompson, A. L.; Satzger, H.; Townsend, D.; Gador, N.; Ullrich, S.; Stolow, A.; Martínez, T. J. *J. Phys. Chem. A* **2007**, *111*, 8500-8508.

(5) Kwok, W.-M.; Ma, C.; Phillips, D. L. *J. Am. Chem. Soc.* **2006**, *128*, 11894-11905.

(6) Yarasi, S.; Brost, P.; Loppnow, G. R. *J. Phys. Chem. A* **2007**, *111*, 5130-5135.

(7) Towrie, M.; Doorley, G. W.; George, M. W.; Parker, A. W.; Quinn, S. J.; Kelly, J. M. *Analyst* **2009**, *134*, 1265-1273.

(8) Kohler, B. *J. Phys. Chem. Lett.* **2010**, *1*, 2047-2053.

(9) Asturiol, D.; Lasorne, B.; Robb, M. A.; Blancafort, L. *J. Phys. Chem. A* **2009**, *113*, 10211-10218.

(10) Zgierski, M. Z.; Patchkovskii, S.; Fujiwara, T.; Lim, E. C. *J. Phys. Chem. A* **2005**, *109*, 9384-9387.

(11) Zhang, R. B.; Eriksson, L. A. *J. Phys. Chem. B* **2006**, *110*, 7556-7562.

(12) Kwok, W.-M.; Ma, C.; Phillips, D. L. *J. Am. Chem. Soc.* **2008**, *130*, 5131-5139.

(13) Marguet, S.; Markovitsi, D. *J. Am. Chem. Soc.* **2005**, *127*, 5780-5781.

(14) Liang, J.; Matsika, S. *J. Am. Chem. Soc.* **2011**, *133*, 6799-6808.

(15) Furse, K. E.; Corcelli, S. A. *J. Phys. Chem. Lett.* **2010**, *1*, 1813-1820.

(16) Sage, E. *Photochem. Photobiol.* **1993**, *57*, 163-174.

(17) Pfeifer, G. P.; You, Y.-H.; Besaratinia, A. *Mutat. Res.* **2005**, *571*, 19-31.

(18) Pecourt, J.-M.; Peon, J.; Kohler, B. *J. Am. Chem. Soc.* **2001**, *123*, 10370-10378.

(19) Middleton, C. T.; Cohen, B.; Kohler, B. *J. Phys. Chem. A* **2007**, *111*, 10460-10467.

(20) Nitzan, A.; Silbey, R. J. *J. Chem. Phys.* **1974**, *60*, 4070-4075.

(21) Whitnell, R. M.; Wilson, K. R.; Hynes, J. T. *J. Phys. Chem.* **1990**, *94*, 8625-8628.

(22) Tuckerman, M.; Berne, B. J. *J. Chem. Phys.* **1993**, *98*, 7301-7318.

(23) Owrutsky, J. C.; Raftery, D.; Hochstrasser, R. M. *Annu. Rev. Phys. Chem.* **1994**, *45*, 519-555.

(24) Kenkre, V. M.; Tokmakoff, A.; Fayer, M. D. *J. Chem. Phys.* **1994**, *101*, 10618-10629.

(25) Deng, Y.; Stratt, R. M. *J. Chem. Phys.* **2002**, *117*, 1735-1749.

(26) Ladanyi, B. M.; Stratt, R. M. *J. Chem. Phys.* **1999**, *111*, 2008-2018.

(27) Stratt, R. M.; Maroncelli, M. *J. Phys. Chem.* **1996**, *100*, 12981-12996.

(28) Kovalenko, S. A.; Schanz, R.; Hennig, H.; Ernsting, N. P. *J. Chem. Phys.* **2001**, *115*, 3256-3273.

(29) Lim, M.; Gnanakaran, S.; Hochstrasser, R. M. *J. Chem. Phys.* **1997**, *106*, 3485-3493.

(30) Brixner, T.; Stenger, J.; Vaswani, H. M.; Cho, M.; Blankenship, R. E.; Fleming, G. R. *Nature* **2005**, *434*, 625-628.

(31) Jonas, D. M. *Annu. Rev. Phys. Chem.* **2003**, *54*, 425-463.

(32) Fayer, M. D. *Annu. Rev. Phys. Chem.* **2008**, *60*, 21-38.

(33) Kim, Y. S.; Hochstrasser, R. M. *Proc. Natl. Acad. Sci.* **2005**, *102*, 11185-11190.

(34) Collini, E.; Wong, C. Y.; Wilk, K. E.; Curmi, P. M. G.; Brumer, P.; Scholes, G. D. *Nature* **2010**, *463*, 644-647.

(35) Anna, J. M.; Ross, M. R.; Kubarych, K. J. *J. Phys. Chem. A* **2009**, *113*, 6544-6547.

(36) Panitchayangkoon, G.; Hayes, D.; Fransted, K. A.; Caram, J. R.; Harel, E.; Wen, J.; Blankenship, R. E.; Engel, G. S. *Proc. Natl. Acad. Sci.* **2010**, *107*, 12766-12770.

(37) Myers, J. A.; Lewis, K. L. M.; Fuller, F. D.; Tekavec, P. F.; Yocum, C. F.; Ogilvie, J. P. *J. Phys. Chem. Lett.* **2010**, *1*, 2774-2780.

(38) Bian, H.; Wen, X.; Li, J.; Chen, H.; Han, S.; Sun, X.; Song, J.; Zhuang, W.; Zheng, J. *Proc. Natl. Acad. Sci.* **2011**, *108*, 4737-4742.

(39) Asplund, M. C.; Zanni, M. T.; Hochstrasser, R. M. *Proc. Natl. Acad. Sci.* **2000**, *97*, 8219-8224.

(40) Khalil, M.; Demirdöven, N.; Tokmakoff, A. *J. Phys. Chem. A* **2003**, *107*, 5258-5279.

(41) Hybl, J. D.; Albrecht Ferro, A.; Jonas, D. M. *J. Chem. Phys.* **2001**, *115*, 6606-6622.

(42) Ogilvie, J. P.; Kubarych, K. J. *Adv. At. Mol. Opt. Phys.* **2009**, *57*, 249-321.

(43) Sperling, J.; Nemeth, A.; Hauer, J.; Abramavicius, D.; Mukamel, S.; Kauffmann, H. F.; Milota, F. *J. Phys. Chem. A* **2010**, *114*, 8179-8189.

(44) Tekavec, P. F.; Lott, G. A.; Marcus, A. H. *J. Chem. Phys.* **2007**, *127*, 214307/1-214307/21.

(45) Tian, P.; Keusters, D.; Suzaki, Y.; Warren, W. S. *Science* **2003**, *300*, 1553-1555.

(46) West, B. A.; Womick, J. M.; Moran, A. M. *J. Phys. Chem. A* **2011**, 10.1021/jp204416m.

(47) Tseng, C.-H.; Matsika, S.; Weinacht, T. C. *Opt. Express* **2009**, *17*, 18788-18793.

(48) Selig, U.; Schleussner, C.-F.; Foerster, M.; Langhojer, F.; Nuernberger, P.; Brixner, T. *Opt. Lett.* **2010**, *35*, 4178-4180.

(49) Zimdars, D.; Francis, R. S.; Ferrante, C.; Fayer, M. D. *J. Chem. Phys.* **1997**, *106*, 7498-7511.

(50) Reuther, A.; Iglev, H.; Laenan, R.; Laubereau, A. *Chem. Phys. Lett.* **2000**, *325*, 360-368.

(51) Durfee III, C. G.; Backus, S.; Murnane, M. M.; Kapteyn, H. C. *Opt. Lett.* **1997**, *22*, 1565-1567.

(52) Jailaubekov, A. E.; Bradforth, S. E. *Appl. Phys. Lett.* **2005**, *87*, 021107/1-021107/3.

(53) Eimerl, D.; Davis, L.; Velsko, S.; Graham, E. K.; Zalkin, A. *Journal of Applied Physics* **1987**, *62*, 1968-1983.

(54) Cowan, M. L.; Ogilvie, J. P.; Miller, R. J. D. *Chem. Phys. Lett.* **2004**, *386*, 184-189.

(55) Goodno, G. D.; Dadusc, G.; Miller, R. J. D. *J. Opt. Soc. Am. B* **1998**, *15*, 1791-1794.

(56) Brixner, T.; Mancal, T.; Stiopkin, I. V.; Fleming, G. R. *J. Chem. Phys.* **2004**, *121*, 4221-4236.

(57) Lepetit, L.; Chériaux, G.; Joffre, M. *J. Opt. Soc. Am. B* **1995**, *12*, 2467-2474.

(58) Gallagher, S. M.; Albrecht, A. W.; Hybl, J. D.; Landin, B. L.; Rajaram, B.; Jonas, D. M. *J. Opt. Soc. Am. B* **1998**, *15*, 2338.

(59) Fanciulli, R.; Cerjak, I.; Herek, J. L. *Rev. Sci. Instrum.* **2007**, *78*, 053102/1-053102/5.

(60) Moran, A. M.; Maddox, J. B.; Hong, J. W.; Kim, J.; Nome, R. A.; Bazan, G. C.; Scherer, N. F. *J. Chem. Phys.* **2006**, *124*, 194904:1-15.

(61) Vauthey, E.; Henseler, A. *J. Phys. Chem.* **1995**, *99*, 8652-8660.

(62) Fourkas, J. T.; Fayer, M. D. *Acc. Chem. Res.* **1992**, *25*, 227-233.

(63) Pecourt, J.-M.; Peon, J.; Kohler, B. *J. Am. Chem. Soc.* **2000**, *122*, 9348-9349.

(64) Peon, J.; Zewail, J. *Chem. Phys. Lett.* **2001**, *348*, 255-262.

(65) Onidas, D.; Markovitsi, D.; Marguet, S.; Sharonov, A.; Gustavsson, T. *J. Phys. Chem. B* **2002**, *106*, 11367-11374.

(66) Perun, S.; Sobolewski, A. L.; Domcke, W. *J. Phys. Chem. A* **2006**, *110*, 13238-13244.

(67) *See supplementary material at http://dx.doi.org/10.1063/1.3628451 for additional experimental details, model calculations, and TG signals obtained for adenine and thymidine.*

(68) Mukamel, S. *Annu. Rev. Phys. Chem.* **2000**, *51*, 691-729.

(69) Mukamel, S. *Principles of Nonlinear Optical Spectroscopy*; Oxford University Press: New York, 1995.

(70) Mukamel, S.; Abramavicius, D. *Chem. Rev.* **2004**, *104*, 2073-2098.

(71) Henry, E. R.; Eaton, W. A.; Hochstrasser, R. M. *Proc. Natl. Acad. Sci.* **1986**, *83*, 8982-8986.

(72) Hamm, P.; Ohline, S. M.; Zinth, W. *J. Chem. Phys.* **1997**, *106*, 519-529.

(73) Chorny, I.; Ceiceli, J.; Benjamin, I. *J. Chem. Phys.* **2002**, *116*, 8904-8911.

(74) McHale, J. *Molecular Spectroscopy*; Prentice Hall: Upper Saddle Creek River, NJ, 1999.

(75) Parson, W. W. *Modern Optical Spectroscopy*; Springer-Verlag: Berlin, 2007.

Chapter 6 . Interplay Between Vibrational Energy Transfer and Excited State Deactivation in DNA Components

6.1. Introduction

It is of fundamental interest to understand the principles governing selection of the molecules to which nature entrusts its all-important genetic code. The DNA of organisms exposed to sunlight is subject to a constant cycle of photodamage and repair. When the solar fluence is particularly high, the DNA repair machinery within a cell cannot keep pace with the rate of photodamage and deleterious lesions take hold (e.g., thymine dimers).[1,2] Fortunately, the light-induced production of lesions is relatively rare because DNA has evolved mechanisms for suppressing these undesired chemical reactions. Delineation of photoprotection mechanisms is challenged by the complexity of electronic structure in DNA. Recent studies show that long-lived collective excitations (i.e., excitons or excimers) form in the polymer and even dominate in systems with uniform base sequences.[3,4] By contrast, a significant fraction of the electronic excitations in model systems with realistic base sequence disorder undergo sub-picosecond internal conversion processes similar to those found in the individual bases.[5] Such rapid excited state deactivation holds implications for photoprotection because all slower excited state chemical reactions are necessarily suppressed.

Knowledge of electronic relaxation processes in DNA progresses steadily with experimental capabilities and advances in theoretical methods. Femtosecond transient

---

Reprinted with permission from *J. Phys. Chem. A*, **DOI:** 10.1021/jp306799e (2012)

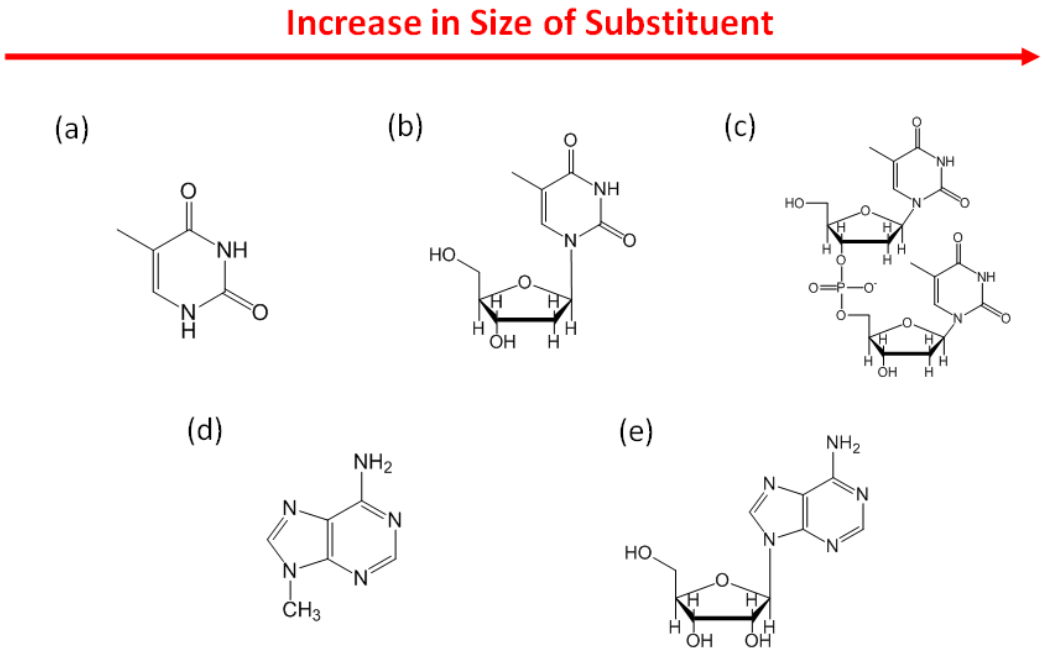

Figure 6.1. Photoinduced relaxation is investigated in the thymine family of systems in the top row: (a) thymine; (b) thymidine; (c) thymine dinucleotide. These molecules are chosen to expose the interplay between internal conversion and vibrational energy transfer between the base and components of the DNA backbone (e.g., deoxyribose ring, neighboring unit). Signal interpretation is aided by comparisons to (d) 9-methyladenine and (e) adenosine.

absorption experiments were first used to uncover the sub-picosecond internal conversion time scales in components of DNA.[6] Various laser spectroscopies have since provided many important insights into the fundamental photophysics at work in these systems.[7-14] Theoretical models have also contributed valuable information about the potential energy landscapes and conical intersections governing excited state dynamics.[15-22] Despite this substantial body of work, there is still much to learn about the mechanisms behind these extraordinary processes. One challenge is to draw connections between experimental studies in solution and the potential energy surfaces generated theoretically. The fundamental problem is that realistic simulations of relaxation processes in solution are computationally expensive because of the large number of degrees of freedom involved.

In addition, information about the excited state potential energy landscapes is not readily obtained in ensemble measurements because population does not accumulate in particular areas of these surfaces. Temperature variation would seem to be a clear way to interrogate energy barriers between the Franck-Condon region of the excited state surface and the conical intersection(s) through which the ground state is repopulated. However, the internal conversion rates in DNA have never been explored over a wide range of temperatures (i.e., down to cryogenic temperatures), partly because of the technical challenges involved.

In this chapter, femtosecond laser spectroscopies are used to examine the dynamics of the short-lived electronic excitations in small components of DNA. The thymine family of systems shown in Figure 6.1 is chosen to expose vibrational energy transfer (VET) channels between the bases, which initially absorb the UV light, and components of the DNA backbone. Comparison of thymine and thymidine isolates the effects of VET between the base and the deoxyribose ring, whereas VET between neighboring units occurs only in the dinucleotide. For this study, it is useful to organize the systems according to the size of the substituent (i.e., the reservoir for excess vibrational quanta), which increases from the nucleobase to the dinucleotide. Implicit in this experimental plan is the assumption of negligible contributions from delocalized electronic excitations in the dinucleotide (i.e., the neighboring unit is simply regarded as an intramolecular heat bath). Linear absorbance and transient absorption anisotropy measurements presented in the Supporting Information are consistent with this view of the dinucleotide's electronic structure. A unique contribution of the present work is the exploration of these relaxation processes at temperatures ranging from 100K to 300K.

Temperature variation is carried out in order to uncover characteristics of the thermal fluctuations that connect the Franck-Condon geometries to the conical intersections (discussed in Chapter 1) leading back to the ground states. For example, the sizes of energy barriers located on the $\pi\pi^*$ potential energy surfaces are readily estimated by conducting measurements over this broad range of temperatures. Examination of the thymine family of systems is aided by comparison to 9-methyladenine and the adenosine whose structures are also shown in Figure 6.1.

This study leverages several recent technical developments in femtosecond laser spectroscopies. Over the past decade, the signal quality of conventional "pump-probe" methods has greatly improved and coherent multidimensional spectroscopies have been implemented at visible and infrared wavelengths.[23-27] Progress towards the UV spectral region is motivated by the numerous biological systems whose lowest frequency electronic resonances are found in this wavelength range (e.g., nucleic acids, amino acids).[12,28,29] To this end, an experimental apparatus was recently constructed that combines a specialized method for generating 25fs laser pulses at 265nm with the sensitivity afforded by diffractive-optic based interferometry. This setup enabled the application of four-wave mixing experiments with unprecedented signal-to-noise ratios in the UV spectral range, demonstrated by experimentation carried out in Chapters 4 and 5.[30,31] Importantly, these extraordinarily sensitive measurements were conducted at fluences for which photo-ionization of both the solutes and solvents were negligible. This is not a trivial point because the efficiencies of these ionization processes grow as the laser pulse duration becomes shorter.[6,30,32] Here these new capabilities are used to

explore relaxation mechanisms in a family of DNA components chosen to draw clear connections between structure and function.

6.2. Basic Physics of Intramolecular Vibrational Energy Transfer

In the DNA components shown in Figure 6.1, ultraviolet light absorption (near 265nm) concentrates an excess amount of energy on the bases because they are the parts of the molecules that are most responsive to the external electromagnetic field. This excess energy flows onto "cooler" parts of the molecule (e.g., the deoxyribose ring, neighboring units) in the form of vibrational quanta. Such intramolecular VET processes influence both the ground and excited state dynamics probed in this work. There exist widely varying perspectives on the factors that control VET (or intramolecular vibrational energy redistribution depending on the choice of basis set) in these systems. In this Section, a simple and intuitive model is outlined to establish a basic physical picture of the process. The experimental results presented below will be discussed in the context of this model.

At second order in perturbation theory, the rate of VET can be written as a time correlation function in the coupling, $\hat{V}$, between the donor levels on the base and the acceptor levels on the substituent

$$K = \frac{1}{\hbar^2}\int_{-\infty}^{\infty} dt \left\langle \hat{V}(t)\hat{V}(0)\right\rangle \qquad (6.1)$$

It should be noted that Equation 6.1 applies generally to all (intramolecular and intermolecular) VET processes in which the inherent approximations hold (e.g., coupling is perturbative, system is near equilibrium).[33-39] When considering dynamics in the ground electronic state, it should be recognized that the base possesses more than 4eV of excess energy immediately following internal conversion. The present model therefore

provides only qualitative insights into the factors controlling vibrational cooling in the ground electronic state. By contrast, it should reasonably describe VET dynamics in the excited electronic state because the amount of excess energy found in the base is much smaller (i.e., the difference between the 4.7eV photon energy and 4.5eV electronic origin).[40]

The rate is next expanded in a basis of vibrational states[41]

$$K = \frac{1}{\hbar^2}\sum_{mn} P_m \int_{-\infty}^{\infty} dt \left\langle m\middle|\exp\left(i\hat{H}t/\hbar\right)\hat{V}\middle|n\right\rangle\left\langle n\middle|\exp\left(-i\hat{H}t/\hbar\right)\hat{V}(0)\middle|m\right\rangle \tag{6.2}$$

where the indices m and n respectively correspond to initial and final states (P_m is the Boltzmann population of level m). Matrix elements involving the perturbation can be taken outside the ensemble average when $\hat{V}$ depends weakly on nuclear motion. The rate can then be written as[41,42]

$$K = \frac{1}{\hbar^2}\sum_{mn} P_m \left|V_{nm}\right|^2 \int_{-\infty}^{\infty} dt \exp\left[-i\left(E_n - E_m\right)t/\hbar\right]\left\langle \exp_+\left[-i\int_0^t dt'\left(Q_m(t') - Q_n(t')\right)\right]\right\rangle \tag{6.3}$$

where $Q_m(t)$ and $Q_n(t)$ are primary Brownian oscillator coordinates coupled to energy levels m and n. Under the assumption of Gaussian statistics, a cumulant expansion yields[41,42]

$$K = \frac{1}{\hbar^2}\sum_{mn} P_m \left|V_{nm}\right|^2 \int_{-\infty}^{\infty} dt \exp\left[-i\left(E_n - E_m\right)t/\hbar - i\lambda_{nm}t/\hbar - g_{mm}(t) - g_{nn}(t)\right] \tag{6.4}$$

where λ_{nm} is the reorganization energy and $g_{mm}(t)$ is a damping function that captures the fluctuation statistics for level m. In writing Equation (4), uncorrelated energy level fluctuations for the initial and final states are assumed (i.e., $g_{mn}(t) = 0$).[41,42]

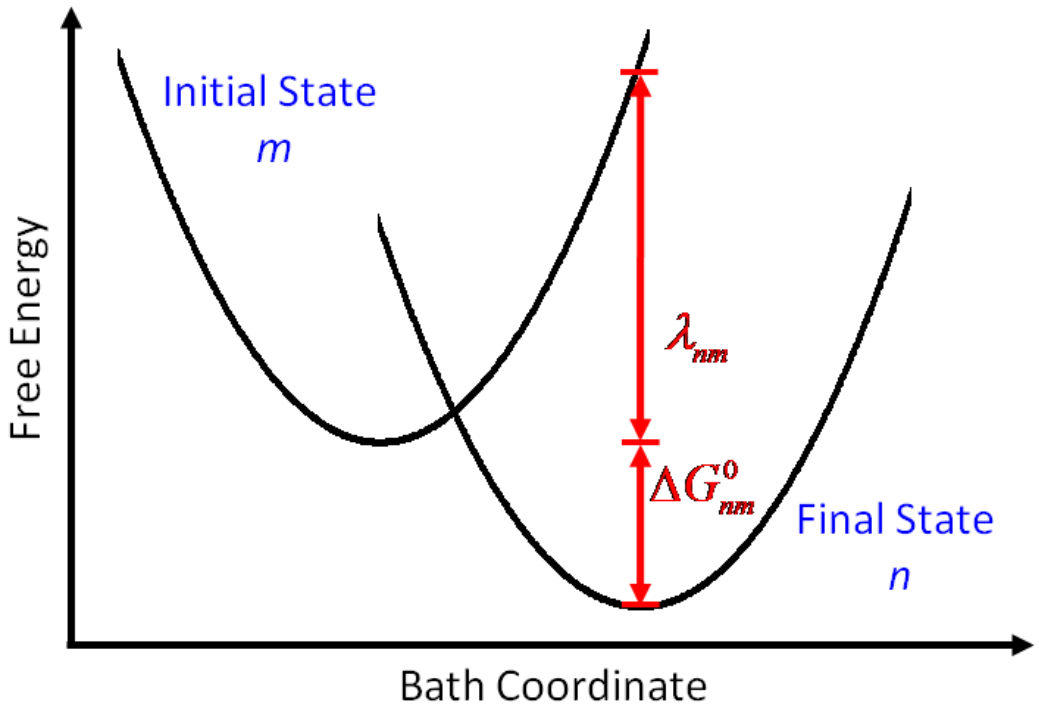

Figure 6.2. Section II presents a phenomenological model for VET. Shown here are free energy surfaces associated with the initial and final states, m and n, in Equation (7). The total VET rate is given by the sum over all relaxation channels, which each possess independent bath coordinates whose displacements and curvatures are governed by the reorganization energy for the transition, λ_{nm}.

The energy level fluctuations in these systems potentially span a broad range of time scales and amplitudes. These effects will be explored with the aid of electronic structure calculations in future work. Here simplifications are introduced to make clear the basic physics at work in the VET process. First, the damping functions are written as[42]

$$g_{mm}(t) = \frac{1}{2\hbar^2}\Delta_{mm}^2 t^2 \tag{6.5}$$

and

$$g_{nn}(t) = \frac{1}{2\hbar^2}\Delta_{nn}^2 t^2 \tag{6.6}$$

by assuming: (i) the motions in the primary Brownian oscillator coordinate are overdamped; (ii) the standard deviations in the energy level fluctuations, Δ_{mm} and Δ_{nn}, are large compared to their relaxation rates. These are essentially the same assumptions that lead to Gaussian spectroscopic line shapes (cf., Equation (8.52) in Reference [42]). By combining Equations (4)-(6) and evaluating the time integral, the rate is expressed as[42,43]

$$K = \frac{\sqrt{\pi}}{\hbar} \sum_{mn} P_m \frac{|V_{nm}|^2}{\sqrt{\lambda_{nm} k_B T}} \exp\left[\frac{-\left(\Delta G^0_{nm} + \lambda_{nm}\right)^2}{4\lambda_{nm} k_B T} \right] \tag{6.7}$$

where the reorganization energy for the transition is

$$\lambda_{nm} = \frac{\Delta^2_{mm} + \Delta^2_{nn}}{2k_B T} \tag{6.8}$$

Equation (8) indicates that, although the donor and acceptor levels are subject to independent fluctuations, a single free energy coordinate for the VET process can still be defined because the damping functions simply add together in the argument of the exponential in Equation (4). The variance in the fluctuations for the reaction coordinate is the sum of the variances for the two primary Brownian oscillator coordinates, $Q_m(t)$ and $Q_n(t)$. Thus, the donor and acceptor free energy wells in Figure 6.2 have the same curvature and the energy gap between the two surfaces is linear in the reaction coordinate. This physical picture suggests convenient parallels to electron transfer theory. Of course, VET and electron transfer processes differ fundamentally in the nature of the coupling between the initial and final states.

In addition to satisfying the approximations outlined above, the present model retains validity only when the coupling between levels, V_{nm}, is small compared to the

reorganization energy for the transition, λ_{nm}. As in Reference [31], it is estimated that the magnitudes of λ_{nm} are probably much less than <10cm^{-1} (based on "typical" vibrational line widths), which places constraints on the particular donor and acceptor coordinates that may be treated perturbatively. In the harmonic approximation, the coupling between the donor and acceptor states is given by

$$\hat{V} = \sum_{\substack{d \in donor \\ a \in acceptor}} \left(\frac{\partial^2 E}{\partial q_d \partial q_a} \right)_0 \hat{q}_d \hat{q}_a \tag{6.9}$$

where q_d and q_a are (local) intramolecular nuclear coordinates associated with the donor and acceptor moieties, respectively. The initial and final states are then naturally described by products of one-dimensional harmonic oscillator eigenvectors

$$\left| m \right\rangle = \prod_{i \in donor} \left| \delta_{i,m} \right\rangle \prod_{j \in acceptor} \left| \alpha_{j,m} \right\rangle \tag{6.10}$$

and

$$\left| n \right\rangle = \prod_{i \in donor} \left| \delta_{i,n} \right\rangle \prod_{j \in acceptor} \left| \alpha_{j,n} \right\rangle \tag{6.11}$$

where i and δ (j and α) represent the nuclear coordinates and vibrational quantum numbers for the donor (acceptor). Combining Equations (9)-(11) gives the following

$$\left\langle n \left| \hat{V} \right| m \right\rangle = \sum_{\substack{d \in donor \\ a \in acceptor}} U_{ad} \left(X_d^+ + X_d^- \right) \left(X_a^+ + X_a^- \right) \prod_{i \neq d} \prod_{j \neq a} \left\langle \delta_{i,n} \middle| \delta_{i,m} \right\rangle \left\langle \alpha_{j,n} \middle| \alpha_{j,m} \right\rangle \tag{6.12}$$

where

$$U_{ad} = \frac{\hbar}{2\sqrt{m_d \omega_d m_a \omega_a}} \left(\frac{\partial^2 E}{\partial q_d \partial q_a} \right)_0 \tag{6.13}$$

$$X_k^+ = \left\langle \xi_{k,n} \middle| \xi_{k,m} + 1 \right\rangle \sqrt{\left(\xi_{k,m} + 1 \right)} \tag{6.14}$$

$$X_k^- = \left\langle \xi_{k,n} \middle| \xi_{k,m} - 1 \right\rangle \sqrt{\xi_{k,m}} \tag{6.15}$$

In X_k^+ and X_k^-, ξ represents a vibrational quantum number and the index k corresponds to either a donor or acceptor coordinate. Equation (12) indicates that transitions will either add or subtract single excitation quanta from vibrations on the donor and acceptor. Moreover, the coupling strength (and transition rate) increases with the vibrational quantum numbers of the donor and acceptor modes. The dependence of the rate on the vibrational quantum number of the donor is particularly important for the ground state dynamics that follow internal conversion because highly excited vibrational states are initially populated.

The key insights provided by the model are summarized as follows. As in electron transfer theory, the rate maximizes when the free energy gap, ΔG_{nm}^0, and reorganization energy, λ_{nm}, possess the same magnitude. Observations are not anticipated to be particularly sensitive to the interplay between these parameters because the reorganization energies are relatively small (roughly estimated at λ_{nm} <10cm^{-1} based on "typical" vibrational spectroscopic line widths), although stronger conclusions should be withheld until molecular dynamics simulations can be conducted. The relationships between the coupling, $\hat{V}$, and the off-diagonal harmonic force constants suggests that the donor and acceptor coordinates must be close in proximity in order to produce an appreciable transition rate. Transitions involving strongly coupled coordinates can even pose a situation in which this perturbative model breaks down (i.e., $V_{nm} > \lambda_{nm}$). For such strong coupling, the VET transition may exhibit adiabatic character wherein the rate becomes sensitive to the time scale of motion on the reaction coordinate (as in electron

transfer adiabaticity).[43-46] It is not clear at present if adiabaticities in the VET transitions are significant. Finally, in the harmonic approximation, large amounts of excess energy are dissipated through a cascade of numerous transitions because in each step the donor sheds only a single quantum of vibrational energy. With such complex pathways taken by the vibrational energy, a mode-specific decomposition of the VET process will be difficult to obtain experimentally, although there may still be hope for experiments employing infrared or UV Raman probes.[13,47-49]

6.3. Experimental Methods

Generation of 25fs, 265nm laser pulses is achieved using a 75 micron diameter hollow-core fiber filled with 800-850 Torr of argon gas.[30,31] Briefly, 800nm and 400nm pulses with 40 μJ energies and 180fs durations are focused into the fiber to generate 25fs, 265nm laser pulses with 500nJ energies. The time-bandwidth product of these pulses ($\approx$ 0.5) is close to the Fourier transform limit for Gaussian pulse envelopes (0.44). It is noted that 25fs UV pulses are generated in this setup despite the 150fs durations of the 400 and 800nm input pulses because the setup is operated at a pressure exceeding that associated with optimal phase matching of the lowest order mode of each laser beam (250 Torr).[50,51] In this way, the UV bandwidth is enhanced at the expense of the pulse energy.

Transient grating (TG) experiments utilize a diffractive optic-based interferometer, which was fully described in earlier publications (and previous chapters).[30,31] In this apparatus, pump and probe pulses are focused onto a diffractive optic, thereby generating a four-pulse laser beam geometry composed of the +/-1 diffraction orders of the incident laser beams. Three of the laser pulses induce the nonlinear polarization and the fourth (attenuated) pulse is used as a reference field for

signal detection by spectral interferometry.[24] In all experiments, the signals are detected using a back-illuminated CCD array (Princeton Instruments PIXIS 100B) mounted on a 0.3 meter spectrograph with a 3600 g/mm grating. Integration times range between 100-400 ms based on the signal intensity. The delay between the pump and probe pulses is scanned 20-40 times as needed to optimize the signal-to-noise ratios.

Time-resolved fluorescence (TRF) experiments are conducted by down-converting the UV fluorescence into the visible wavelength range. Difference frequency mixing of the fluorescence emission with 200fs, 800nm gate pulses is accomplished using a 0.5mm thick Type I BBO crystal. The fluorescence is collected from the sample with a 10cm focal length, 90 degree off-axis parabolic mirror. A second 20cm focal length parabolic mirror is used to focus the emission on the BBO. Signals are detected with a photomultiplier tube (PMT) and processed using a lock-in amplifier referenced to the 1kHz repetition rate of the laser system. Bandpass filters centered at either 510nm or 560nm are used to suppress scattered light in experiments conducted on the adenine and thymine systems, respectively. The transmission spectra of the filters are chosen to match the peaks of the fluorescence emission for the two families of molecules. The peak powers of the incident 265nm, 300fs laser pulses are 5GW/cm^2. Shorter UV pulses are not employed because appreciable solute ionization is induced at greater peak powers.[30] The time resolution of this setup is approximately 500fs.

Thymine, thymidine, 9-methyladenine, and adenosine are purchased from Fischer Scientific. The thymine dinucleotide was purchased from Midland Certified Reagents. All systems are dissolved in an 85:15 mixture of methanol:water because this combination produces a glass with high optical quality at 100K.[30] The solutions are

contained in a 0.5mm thick fused silica cuvette mounted on a low-noise rotating sample holder inside a liquid nitrogen cooled cryostat (Oxford Instruments Optistat-DN).[52] In the TG experiments, each of the three incoming pulses possesses a fluence of 4.65×10^{13} photons/cm^2 and a peak power of 1.4GW/cm^2. By summing the fluences of pulses 1 and 2, it is estimated that approximately 0.4% of the molecules in the focal volume are photoexcited. The use of larger laser fluences must be avoided with 25fs pulses because photoionization of the solute becomes problematic at greater peak powers, discussed and shown in Chapter 4.[30] Finally, it should be noted that the absorptive and dispersive signal components are distinguished using the dispersive thermal grating induced by fast non-radiative relaxation in the base. Further information on this "phasing" procedure is provided in the Supporting Information.

6.4. Results and Discussion

In this Section, the mechanisms governing ground state vibrational cooling are discussed and the deactivation of $\pi\pi^*$ excitations in the thymine family of systems shown in Figure 6.1. The two experimental techniques employed in this work provide complementary information. TG measurements yield the total amount of time needed for a system to recover equilibrium following light absorption. Equilibrium recovery is dominated by ground state dynamics at 300K because the excited state lifetimes are short compared to the time scale of ground state vibrational cooling. By contrast, TG is much more sensitive to excited state relaxation at cryogenic temperatures because the $\pi\pi^*$ lifetimes of these systems increase as the temperature decreases.[53,54] In addition to TG, TRF measurements are employed at 300K to distinguish contributions from ground and excited state processes to the total equilibrium recovery time.

6.4. A. Probing Ground State Vibrational Cooling Dynamics

The time scale of ground state vibrational cooling is derived using TG and TRF experiments conducted at 300K, which are shown in Figure 6.3. The TG measurements primarily reflect ground state bleach nonlinearities and demonstrate that equilibrium recovery occurs within approximately 5 picoseconds. The TRF signals show that the ππ* lifetime is sub-picosecond, thereby confirming that ground state dynamics dominate the TG response at 300K. In these TRF measurements, laser pulses with 300fs durations were used in order to achieve adequate signal strength without appreciable ionization of the solute (i.e., peak power held under 5 GW/cm^2). For this reason, it is possible that these experiments miss some of the shortest decay components found in earlier work on some of these same systems.[55] Nonetheless, the present TRF measurements are useful and well-motivated because the time resolution is sufficient to establish how the ππ* lifetimes vary within this family of molecules in this particular solvent mixture.

The TG and TRF time constants obtained for all systems at 300K are summarized in Figure 6.4. As in work presented on thymine in Chapter 5, the TG signals are fit with sums of 2 exponentials (cf., appendix A3).[30] Short-lived (<300fs) rising exponentials reflect interference between ground state bleach and excited state absorption signal components, whereas picosecond exponential decay times are associated with the overall recovery of equilibrium. The time scale of vibrational cooling in the ground electronic state is estimated by solving coupled differential equations for a two-step kinetic process.

The sequence involves three distinct species: the electronically excited molecule, $S_{\pi\pi^*}$; the vibrationally hot system in the ground electronic state, S^*_{ground}; the equilibrium

system in the ground electronic state, S_{ground}. The (irreversible) relaxation scheme can be written as

$$S_{\pi\pi^*} \xrightarrow{k_{IC}} S^*_{ground} \xrightarrow{k_{VC}} S_{ground} \tag{6.16}$$

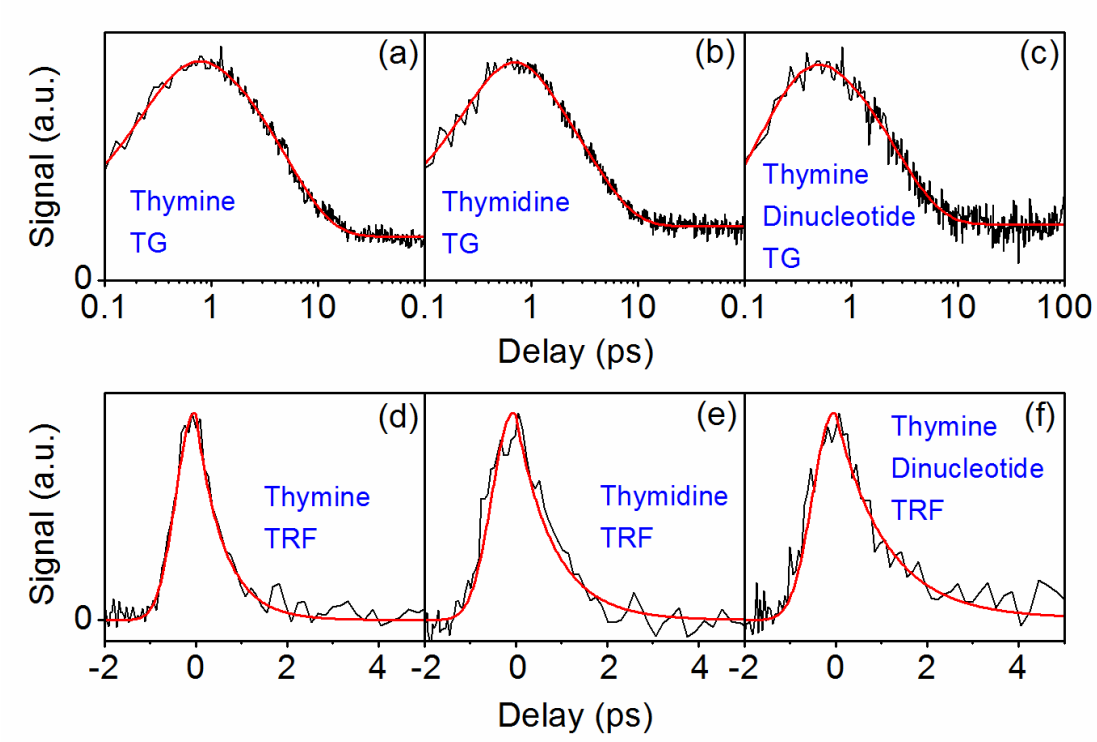

Figure 6.3. TG (top row) and TRF (bottom row) experiments are conducted on the thymine family of systems at 300K. The solutes are dissolved in an 85:15 mixture of methanol:water. The decay of the TG signal reflects equilibrium recovery, whereas TRF provides information specific to the ππ* lifetime. The absorptive part of the TG signal field displayed in panels (a)-(c) corresponds to a "bleach" of the ground state. Fitting parameters are tabulated in Appexdix 3.

where k_{IC} and k_{VC} are rate constants corresponding to internal conversion and vibrational cooling, respectively. The TRF measurements yield k_{IC} directly, whereas the TG experiments detect growth in the population of S_{ground}. The rate constants, k_{VC}, presented in Figure 6.4 are parameterized to generate growth kinetics that reproduce the time constants obtained in the TG experiments.

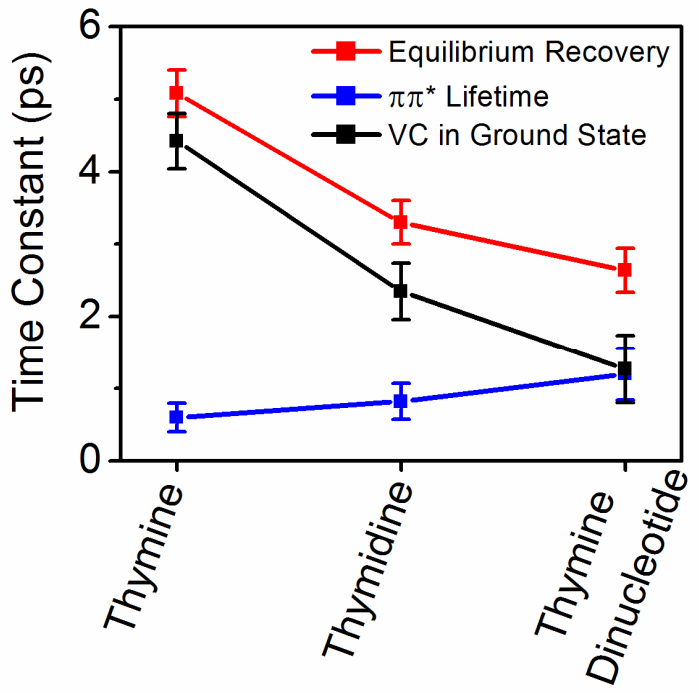

Figure 6.4. TG and TRF measurements conducted at 300K provide time constants associated with equilibrium recovery (red) and the ππ* lifetimes (blue), respectively. The inverse of the vibrational cooling rate in the ground state, k_{VC}^{-1} (black), is estimated using the two-step kinetic scheme defined in Equation (6.16). The error bars correspond to twice the standard errors of the fits.

The data show that the time scale of vibrational cooling speeds up markedly with the sizes of the molecules. Section II defines the aspects of the mechanism responsible for this rate enhancement. First, the density of nuclear states on the acceptor moiety increases with the molecular size. Growth in the density of states is incorporated through the sum over final states (n) in Equation (7) and the sum over acceptor coordinates (a) in Equation (9). While the number of terms in Equation (7) grows with the molecular size, it should also be recognized that the argument of the exponential constrains the number of acceptor states that contribute to depopulation of a particular donor state. The second important factor governing the VET rate is the interaction between donor and acceptor states. The operator in Equation (9) defines the interaction as a sum over the quadratic

force constants associated with coordinates located on the base and substituent. The largest (through-bond) couplings should naturally be found for coordinates on the substituent that are in closest proximity to the base. According to Equation (12), VET should be most rapid immediately following internal conversion because the transfer of vibrational quanta then involves the most highly excited levels in the base. It has been suggested that spatial overlap in the donor and acceptor states is a prerequisite for efficient population flow. This perspective implies a delocalized basis set and should be preferred for the description of intramolecular vibrational energy redistribution processes in which the donor and acceptor coordinates are located on the same moiety.[56-58]

In summary, the rate enhancement displayed in Figure 6.4 primarily reflects an increase in the size of the substituent. The effect of VET onto the deoxyribose ring is exposed by comparing thymine and thymidine, whereas VET onto the adjacent unit is similarly uncovered by comparing thymidine and the dinucleotide. The data do not provide the identities of the dominant donor and acceptor coordinates or the magnitudes of their couplings. However, the sensitivity of the equilibration time to the size of the substituent underscores the importance of the covalent bonding between the base and substituent. The absence of through-bond mechanical couplings in the solute-solvent interaction potential is apparently why solute-to-solvent VET is slower than the intramolecular VET dynamics examined in this mixture of methanol and water.[31] This convenient separation in time scales may not generalize to purely aqueous solutions where the rate of solute-to-solvent VET is accelerated.[47] Most importantly, this set of experiments establishes that the substituent functions as reservoir for excess vibrational

quanta initially located on the photoexcited base. The influence of this reservoir on the excited state dynamics is investigated next.

6.4. B. Coupling Between Internal Conversion and Vibrational Energy Flow

Internal conversion processes initiating in the ππ* electronic states are monitored directly at 300K using TRF measurements. However, a different approach must be taken at lower temperatures because efforts to carry out TRF experiments in a cryostat were thwarted by technical problems (e.g., light scattering, light collection efficiency). Fortunately, as shown in Figure 6.5, high-quality TG signals can still be obtained with the samples inside the cryostat. The increases in the TG time constants found below 300K reflect growth in the ππ* lifetimes at lower temperatures.[53,54] In Chapter 5 the equilibrium recovery rate in thymine was found to be experimentally indistinguishable at 100K and 300K, which indicates that the vibrational cooling rates change negligibly in this temperature range. It was concluded that heating of the primary solvent shell is primarily responsible for this insensitivity of the vibrational cooling time to the equilibrium temperature of the sample.[30] The transfer of vibrational energy to librational modes of the solvent, whose frequencies are greater than k_BT, also plays an important role.[31,59] Here it is assumed that temperature independent vibrational cooling rates persist in thymidine and the dinucleotide because (i) approximately ~4eV of energy is similarly released into the surrounding solvent on the time scale of a few picoseconds and (ii) high frequency VET channels should also operate in this hydrogen-bonding solvent mixture.

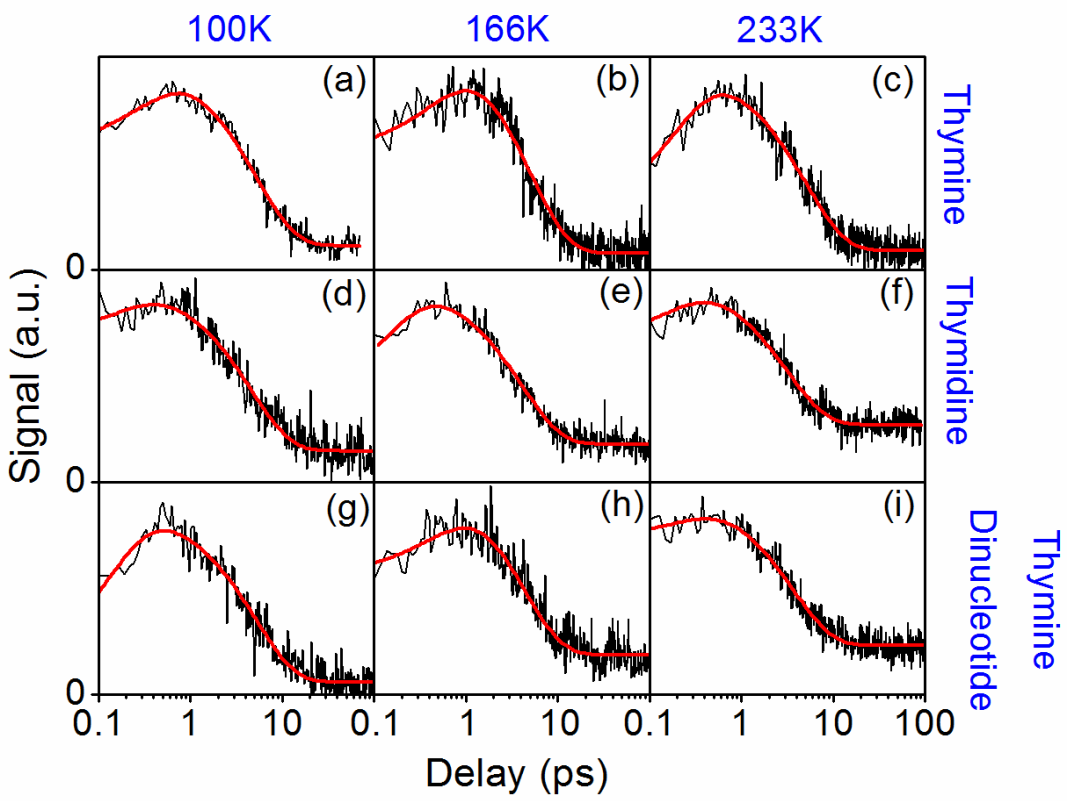

Figure 6.5. The time scale of equilibrium recovery is probed using TG spectroscopy at 100K (left), 166K (middle), and 233K (right). Absorptive parts of the TG signals are displayed for thymine (top), thymidine (middle), and the thymine dinucleotide (bottom). Each transient is fit to a sum of two exponentials (i.e., one rising and one decaying component). Fitting parameters are tabulated in Appendix 3.

The determination of ππ* lifetimes at low temperatures follows a kinetic analysis similar to that described in the previous section. First, k_{VC} is obtained by assuming temperature independent vibrational cooling rates between 100K and 300K. The rate constants, k_{IC}, are then adjusted until the growth in the population of the equilibrium species, S_{ground}, reproduces the time constants found in the TG experiments. The TG time constants obtained at all temperatures are summarized in Figure 6.6. Figure 6.7 presents the ππ* lifetimes extracted from these data. While this approach is indirect, it provides robust physical insight into the effect of temperature on the ππ* lifetimes. The

assumptions are physically reasonable and possible discrepancies are taken into account by setting the uncertainties equal to twice the standard error.

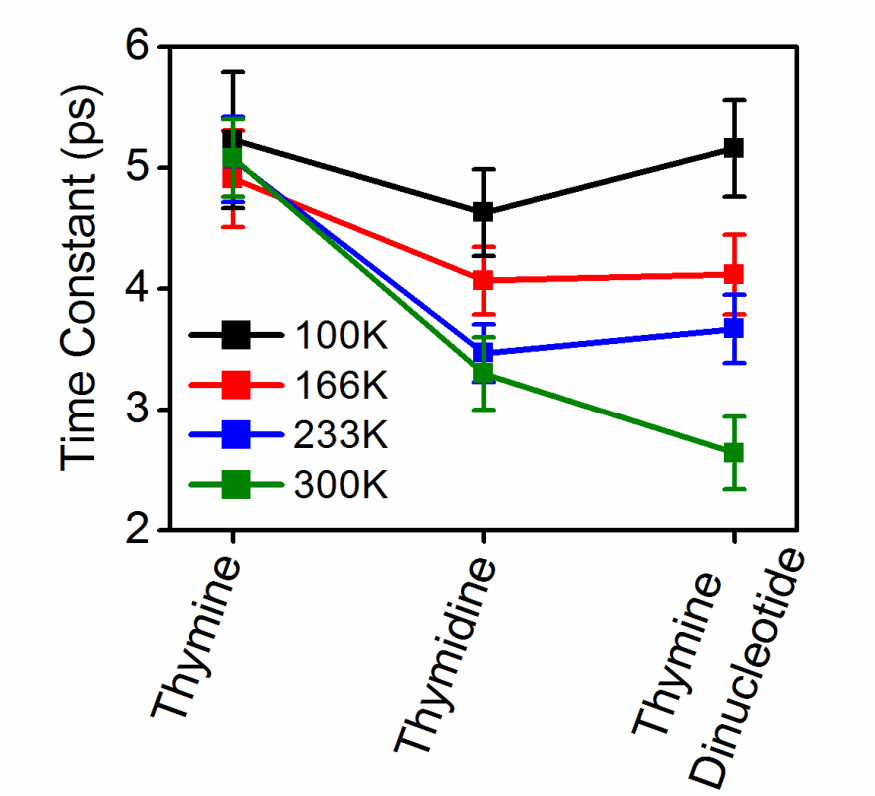

Figure 6.6. Summary of transient grating time constants obtained for all thymine systems at all temperatures. The error bars correspond to twice the standard errors in the fits.

The present study establishes two important trends in the ππ* lifetimes: (i) the ππ* lifetimes of thymidine and the thymine dinucleotide decrease with increasing temperature; (ii) the ππ* lifetimes increase with the sizes of the substituents at all temperatures. The Arrenhius equation, $K = Ae^{-E_a/RT}$, is a sensible starting point for describing the physics behind these two observations. In Figure 6.7, an Arrhenius analysis is carried out on the internal conversion time constants, k_{IC}, at temperatures ranging from 100K to 300K. The fitting parameters summarized in Table 6.1 suggest

that VET onto the substituent influences both the effective energy barrier, E_a, and the frequency factor, A. Next discussed are the physical insights derived from these fitting parameters.

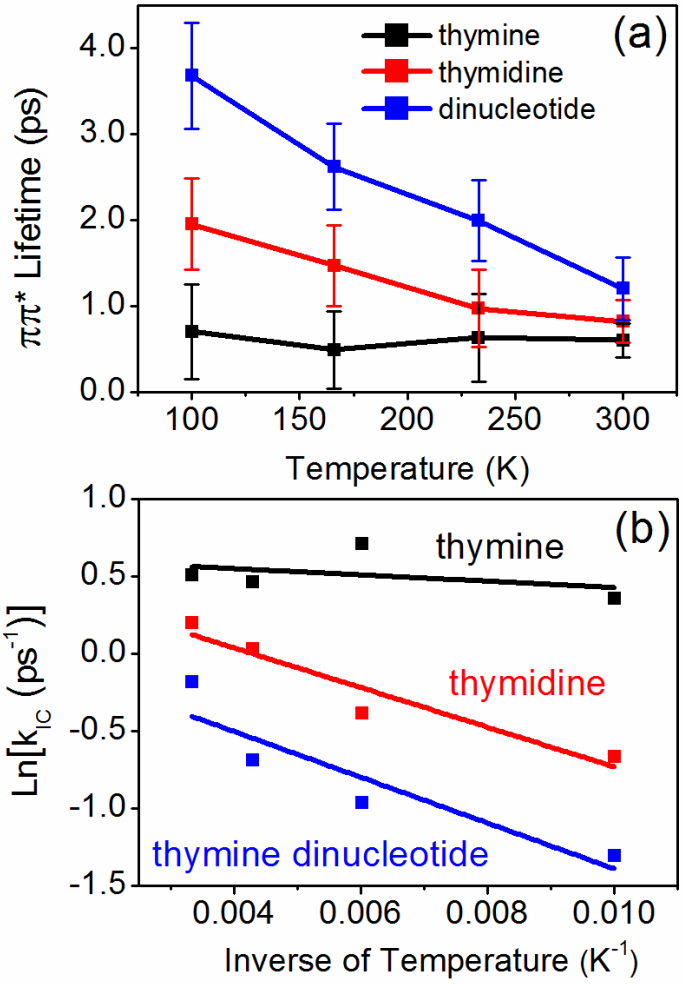

Figure 6.7. (a) ππ* lifetimes obtained for the thymine family of systems at temperatures ranging from 100K to 300K. The lifetimes increase with the size of the substituent at all temperatures. (b) Arrhenius plots for internal conversion rates, k_{IC}. Fitting parameters are given in Table 6.1.

Table 6.1. Arrhenius Fitting Parameters for Figure 6.7

[(a)]Parameter	Thymine	Thymidine	Thymine Dinucleotide
A (meV)	7.8±2.6	7.2±2.2	4.5±1.5
E_a (meV)	1.7±0.6	11.0±2.4	12.8±3.8

(a) Ranges in the parameters represent the standard error

These data are consistent with the presence of an energy barrier between the Franck-Condon region of the ππ* surface and the conical intersection(s) leading back to the ground electronic state. The influence of this barrier on the internal conversion process is illustrated in Figure 6.8 (it is also possible that short-lived nπ* intermediate states are involved but the point is the same). The photoexcited base initially possesses excess vibrational energy because it is excited near the peak of the linear absorption spectrum. This excess energy can be used to surmount the energy barrier on the path to the conical intersection. However, as time progresses, VET from the base onto the substituent causes the wavepacket to sink deeper into the potential energy well, thereby suppressing internal conversion. In this interpretation, the ππ* lifetime of thymine is insensitive to temperature because it is not covalently bonded to an intramolecular heat bath (and solute-to-solvent VET is slower than internal conversion).[31] By contrast, thymidine rapidly loses vibrational energy to the deoxyribose ring and therefore must approach the conical intersection through a thermally activated process. The ππ* lifetime of the dinucleotide is apparently longer than that of the nucleoside because the larger heat bath associated with the neighboring unit allows a greater amount of heat to flow out of the base. The 13meV barrier size indicated by the present data is in

reasonable agreement with the ~50meV barrier recently calculated for isolated thymine.[17] In making this comparison, it should be recognized that the size of the barrier can only be estimated based on the present experiments because internal conversion and intramolecular VET occur on similar time scales.

The Arrhenius frequency factors, A, in Table 6.1 decrease as the sizes of the substituents increase. In transition state theory, A reflects the frequency with which the energy barrier is encountered. The frequency factor is interpreted in terms of the distribution of geometries in the photoexcited ensemble in Figure 6.8. That is, the transfer of vibrational energy to the substituent causes the wavepacket to become narrower in addition to sinking deeper into the potential energy well. Narrowing of the wavepacket reduces the probability for a portion of the ensemble to spread into the region of the barrier, which in turn decreases the probability that the barrier is encountered.

The relaxation scheme shown in Figure 6.8 pertains only to relaxation processes in which ππ* singlet excitations rapidly deactivate and repopulate the ground state. This is not the only relaxation pathway in thymine systems.[47] Some of the relaxation pathways produce long-lived triplet states. The TG signal amplitude at long delay times (T>300ps) is one signature of triplet formation. Although it has not been studied quantitatively, a significant increase in (steady-state) visible luminescence is observed at temperatures below 200K, which is also consistent with triplet formation.

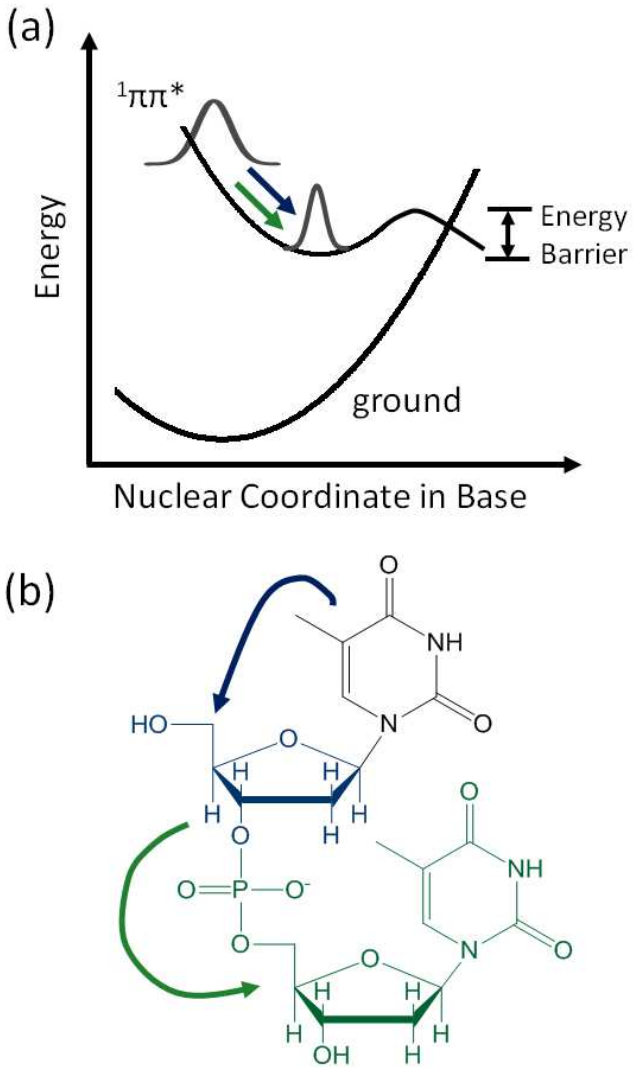

Figure 6.8. (a) Photoexcitation produces a vibrationally "hot" wavepacket which then relaxes through VET onto the substituent. This loss of heat causes the wavepacket to narrow and sink deeper into the potential energy well, thereby suppressing internal conversion. (b) The two VET channels indicated in panel (a) are drawn on the molecular structure of the thymine dinucletide. Vibrational energy first flows onto the deoxyribose ring then onto the adjacent unit.

Such intersystem crossing dynamics, while interesting, are beyond the scope of this study. The present experimental approach is insensitive to intersystem crossing, because TG is used to monitor the return of population to the ground electronic state (i.e., the ground state bleach nonlinearity is probed).[42] Therefore, the time constants shown in Figure 6.4, 6.6, and 6.7 are insensitive to processes resulting in the production of long-

lived excited states. It is suggested that a study of triplet formation should combine (i) time-resolved luminescence measurements in the visible spectral range and (ii) transient absorption experiments in which long-lived excited state absorption nonlinearities are detected.

6.4. C. Effect of Solvent Viscosity on Kinetics

Use of the Arrhenius analysis in Section IVB implicitly neglects the effect of the solvent's viscosity on the probability of barrier crossing. This is generally not a safe assumption. Kramers established long ago that a turnover in the rate of barrier crossing should be found as a function of the friction exerted on the reaction coordiante.[60] In the high friction limit, for example, the rate is smaller than that predicted by transition state theory and scales as the inverse of the viscosity.[37] For practical purposes, the friction is often taken to scale linearly with the viscosity of the bath (i.e., Stokes Law).[61] Now consider that the viscosity of the 85:15 mixture of methanol:water increases from approximately 1.3cP at 300K to 215cP at 166K.[62] In addition, the solvent undergoes an astronomical (orders of magnitude) increase in viscosity when it freezes near 150K. The fact that the measured internal conversion rate varies by only a factor of 3 between 100K and 300K suggests that the viscosity of the solvent couples weakly to the reaction coordinate. Electronic structure calculations indicate that the reaction coordinate for the thymine family of systems primarily involves out-of-plane displacement of the oxygen atom neighboring the methyl group.[63] Results indicate that rigidity in the surrounding solvent does little to suppress this out-of-plane motion.

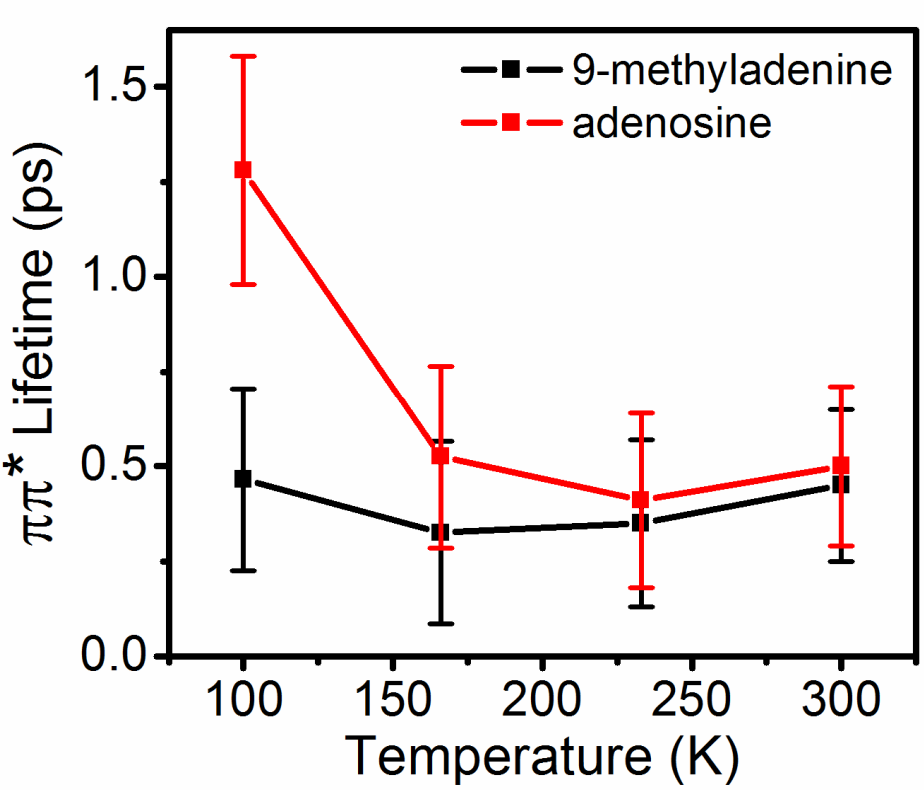

Figure 6.9. Excited state lifetimes of 9-methyladenine (black) and adenosine (red) obtained using a procedure analogous to that applied to the thymine family of systems (cf., Equation (16)). The data show that the lifetime of 9-methyladenine is temperature-independent, whereas that in adenosine increases by a factor of 2.5 in the frozen sample at 100K. This behavior is interpreted as a viscosity dependent effect. The full set of experiments used to generate these time constants is presented in the Supporting Information.

In this Section, 9-methyladenine and adenosine are examind in order to evaluate the hypothesis that viscosity dependent effects do not take hold in the thymine family of systems because of minor out-of-plane distortions in the equilibrium geometry at the conical intersection. The key idea motivating these experiments is that the conical intersection in adenine is accessed through significant ring puckering, which involves relatively large out-of-plane displacements of several heavy atoms.[63] Viscosity dependent effects are postulated to arise in the adenine systems because the reaction coordinate is more likely to couple to the surrounding solvent. Figure 6.9 presents

excited state lifetimes determined for 9-methyladenine and adenosine. All of the data used to generate these time constants are shown in the Supporting Information. Similar to the thymine nucleobase, the lifetime of 9-methyladenine is independent of temperature in the 100K-300K range. By contrast, adenosine exhibits temperature independent dynamics from 166K-300K but possesses a longer lifetime in the frozen sample at 100K. It is quite possible that this is a viscosity dependent effect. However, given the enormous viscosity increase in the frozen sample, it is somewhat surprising that that lifetime increases by only a factor of 2.5. This apparently indicates that the rigid environment does little to suppress out-of-plane motions in the solute. It is also peculiar that the dynamics in 9-methyladnenine are apparently viscosity independent. It may be that the excess vibrational energy present in the base promotes competition with the friction imposed by the environment.

Overall, the dynamics observed in 9-methyladenine and adenosine suggest that a realistic description of the internal conversion processes will probably require a fairly sophisticated model. Nonetheless, the weak sensitivity to viscosity observed in adenosine reinforces the interpretation that the measurements are indeed sensitive to thermally activated barrier crossing dynamics in the thymine family of systems. The key issue is apparently whether or not out-of-plane geometric distortions at the conical intersection are sufficient to displace (couple to) the surrounding solvent molecules. Molecular dynamics simulations will hopefully offer deeper insights into these intermolecular interactions and their effects on internal conversion.

6.5. Concluding Remarks

In summary, femtosecond laser spectroscopies have been conducted over a wide range of temperatures (100K-300K) to investigate ground and excited state relaxation

processes in the thymine family of systems shown in Figure 6.1. Transient grating and time resolved fluorescence experiments were used to establish that the substituent of the base functions as a heat bath to which the base can rapidly transfer excess vibrational quanta (cf., Figure 6.4). An Arrhenius analysis of the ππ* lifetimes in the thymine family of systems then showed that the amount of excess vibrational energy dissipated by the base increases with the size of the substituent (cf., Figure 6.7). This intramolecular heat flow suppresses nuclear motion over the approximate 13meV energy barrier between the Franck-Condon geometry and the conical intersection leading back to the ground electronic state. Figure 6.8 interprets the physics in terms of the position and width of an excited state wavepacket. Interestingly, the solvent viscosity has a negligible effect on the internal conversion rate in the thymine systems, whereas the ππ* lifetime of adenosine increa0ses by a factor of 2.5 when the solution freezes. The sensitivity to the solvent viscosity observed in adenosine may be attributed to relatively large out-of-plane atomic displacements at the geometry of the conical intersection.

The principal finding of this study is that the process illustrated in Figure 6.8 contributes to the measured dynamics. Moreover, data indicate that the transfer of vibrational energy onto the deoxyribose ring couples most significantly to the internal conversion rate, whereas the neighboring unit in the dinucleotide serves as a secondary heat bath. Because internal conversion and VET occur on similar time scales, the size of the barrier on the ππ* surface can only be estimated based on the present experiments. Measurements in which these systems are excited at their electronic origins would be helpful in this regard because a large amount of excess vibrational energy would not be imparted to the base. It should also be emphasized that only the fastest internal

conversion processes are investigated in this work. Thymine is known to possess multiple internal conversion pathways, some of which involve an intermediate nπ* electronic state.[64] The formation of long-lived triplet excitations is another decay pathway that is beyond the scope of the present study.

Future work will consider the implications of VET processes for the electronic structure in natural DNA. Emerging from recent literature is a physical picture in which resonances with fairly localized (2-3 units) Frenkel exciton states first absorb the UV light before transforming into excimers on the 100fs time scale (i.e., exciton self-trapping).[47] Such dynamics are fairly ubiquitous for π-stacked systems with modest intermolecular Coulombic couplings and strong solute-solvent interactions (i.e., large fluctuation amplitudes). For example, dimers in α-perylene have long been known to relax through similar pathways.[65,66] Intermolecular vibronic couplings may play some role in the self-trapping process. Such vibronic excitons, which were originally studied in molecular crystals,[67,68] have now been implicated in light harvesting proteins and molecular aggregates.[69-72] Other research in the Moran laboratory has shown that particularly interesting effects arise when heterogeneity in the site energies is offset by the frequencies of intramolecular vibrational modes.[69] Thus, one possibility is that vibronic excitations underly (short-lived) delocalized states in systems with realistic sequence disorder. In this scenario, both VET and exciton self-trapping will limit the vibronic exciton lifetimes. The present study hopefully contributes to the understanding of intramolecular VET dynamics in the present systems and that this knowledge can be integrated into a comprehensive picture of electronic structure in natural DNA.

6.6. References

(1) Pfeifer, G. P.; You, Y.-H.; Besaratinia, A. *Mutat. Res.* **2005**, *571*, 19-31.

(2) Sage, E. *Photochem. Photobiol.* **1993**, *57*, 163-174.

(3) Markovitsi, D.; Gustavsson, T.; Vayá, I. *J. Phys. Chem. Lett.* **2010**, *1*, 3271-3276.

(4) Kohler, B. *J. Phys. Chem. Lett.* **2010**, *1*, 2047-2053.

(5) de La Harpe, K.; Kohler, B. *J. Phys. Chem. Lett.* **2011**, *2*, 133-138.

(6) Pecourt, J.-M.; Peon, J.; Kohler, B. *J. Am. Chem. Soc.* **2001**, *123*, 10370-10378.

(7) Peon, J.; Zewail, J. *Chem. Phys. Lett.* **2001**, *348*, 255-262.

(8) Onidas, D.; Markovitsi, D.; Marguet, S.; Sharonov, A.; Gustavsson, T. *J. Phys. Chem. B* **2002**, *106*, 11367-11374.

(9) Satzger, H.; Townsend, D.; Zgierski, M. Z.; Patchkovskii, S.; Ullrich, S.; Stolow, A. *Proc. Natl. Acad. Sci.* **2006**, *103*, 10196-10201.

(10) Kwok, W.-M.; Ma, C.; Phillips, D. L. *J. Am. Chem. Soc.* **2006**, *128*, 11894-11905.

(11) Evans, N. L.; Ullrich, S. *J. Phys. Chem. A* **2010**, *114*, 11225-11230.

(12) Tseng, C.-H.; Sándor, P.; Kotur, M.; Weinacht, T. C.; Matsika, S. *J. Phys. Chem. A* **2011**, *116*, 2654-2661.

(13) Towrie, M.; Doorley, G. W.; George, M. W.; Parker, A. W.; Quinn, S. J.; Kelly, J. M. *Analyst* **2009**, *134*, 1265-1273.

(14) Billinghurst, B. E.; Loppnow, G. R. *J. Phys. Chem. A* **2006**, *110*, 2353-2359.

(15) Liang, J.; Matsika, S. *J. Am. Chem. Soc.* **2011**, *133*, 6799-6808.

(16) Oladepo, S. A.; Loppnow, G. R. *J. Phys. Chem. B* **2011**, *115*, 6149-6156.

(17) Hudock, H. R.; Levine, B. G.; Thompson, A. L.; Satzger, H.; Townsend, D.; Gador, N.; Ullrich, S.; Stolow, A.; Martínez, T. J. *J. Phys. Chem. A* **2007**, *111*, 8500-8508.

(18) Furse, K. E.; Corcelli, S. A. *J. Phys. Chem. Lett.* **2010**, *1*, 1813-1820.

(19) Gustavsson, T.; Bányász, A.; Lazzarotto, E.; Markovitsi, D.; Scalmani, G.; Frisch, M. J.; Barone, V.; Improta, R. *J. Am. Chem. Soc.* **2006**, *128*, 607-619.

(20) Asturiol, D.; Lasorne, B.; Worth, G. A.; Robb, M. A.; Blancafort, L. *Phys. Chem. Chem. Phys.* **2010**, *12*, 4949-4958.

(21) Serrano-André, L.; Merchá, M. *J. Photochem. Photobiol. C* **2009**, *10*, 21-32.

(22) Shukla, M. K.; Leszczynski, J. *J. Biomol. Struct. Dynam.* **2007**, *25*, 93-118.

(23) Asplund, M. C.; Zanni, M. T.; Hochstrasser, R. M. *Proc. Natl. Acad. Sci.* **2000**, *97*, 8219-8224.

(24) Lepetit, L.; Chériaux, G.; Joffre, M. *J. Opt. Soc. Am. B* **1995**, *12*, 2467-2474.

(25) Goodno, G. D.; Dadusc, G.; Miller, R. J. D. *J. Opt. Soc. Am. B* **1998**, *15*, 1791-1794.

(26) Jonas, D. M. *Annu. Rev. Phys. Chem.* **2003**, *54*, 425-463.

(27) Brixner, T.; Stenger, J.; Vaswani, H. M.; Cho, M.; Blankenship, R. E.; Fleming, G. R. *Nature* **2005**, *434*, 625-628.

(28) Auböck, G.; Consani, C.; van Mourik, F.; Chergui, M. *Opt. Lett.* **2012**, *37*, 2337-2339.

(29) Selig, U.; Schleussner, C.-F.; Foerster, M.; Langhojer, F.; Nuernberger, P.; Brixner, T. *Opt. Lett.* **2010**, *35*, 4178-4180.

(30) West, B. A.; Womick, J. M.; Moran, A. M. *J. Phys. Chem. A* **2011**, *115*, 8630-8637.

(31) West, B. A.; Womick, J. M.; Moran, A. M. *J. Chem. Phys.* **2011**, *135*, 114505:1-114505:9.

(32) Reuther, A.; Iglev, H.; Laenan, R.; Laubereau, A. *Chem. Phys. Lett.* **2000**, *325*, 360-368.

(33) Owrutsky, J. C.; Raftery, D.; Hochstrasser, R. M. *Annu. Rev. Phys. Chem.* **1994**, *45*, 519-555.

(34) Deng, Y.; Stratt, R. M. *J. Chem. Phys.* **2002**, *117*, 1735-1749.

(35) Uzer, T.; Miller, W. H. *Physics Reports* **1991**, *199*, 73-146.

(36) Nitzan, A.; Silbey, R. J. *J. Chem. Phys.* **1974**, *60*, 4070-4075.

(37) Nitzan, A. *Chemical Dynamics in Condensed Phases*; Oxford University Press: Oxford, 2006.

(38) Kenkre, V. M.; Tokmakoff, A.; Fayer, M. D. *J. Chem. Phys.* **1994**, *101*, 10618-10629.

(39) Gruebele, M.; Wolynes, P. G. *Acc. Chem. Res.* **2004**, *37*, 261-267.

(40) Yarasi, S.; Brost, P.; Loppnow, G. R. *J. Phys. Chem. A* **2007**, *111*, 5130-5135.

(41) Mukamel, S.; Abramavicius, D. *Chem. Rev.* **2004**, *104*, 2073-2098.

(42) Mukamel, S. *Principles of Nonlinear Optical Spectroscopy*; Oxford University Press: New York, 1995.

(43) Sparpaglione, M.; Mukamel, S. *J. Chem. Phys.* **1988**, *88*, 3263-3280.

(44) Sumi, H. *J. Phys. Soc. Jpn.* **1980**, *49*, 1701-1712.

(45) Zusman, L. D. *Chem. Phys.* **1980**, *49*, 295-304.

(46) Sparpaglione, M.; Mukamel, S. *J. Chem. Phys.* **1988**, *88*, 4300-4311.

(47) Middleton, C. T.; de La Harpe, K.; Su, C.; Law, Y. K.; Crespo-Hernández, C. E.; Kohler, B. *Annu. Rev. Phys. Chem.* **2009**, *60*, 217-239.

(48) Rhinehart, J. M.; Challa, J. R.; McCamant, D. W. *J. Phys. Chem. B* **2012**, DOI: 10.1021/jp3020645.

(49) Yoshida, K.; Iwata, K.; Nishiyama, Y.; Kimura, Y.; Hamaguchi, H.-O. *J. Chem. Phys.* **2012**, *136*, 104504:1-104504:1.

(50) Durfee III, C. G.; Backus, S.; Murnane, M. M.; Kapteyn, H. C. *Opt. Lett.* **1997**, *22*, 1565-1567.

(51) Jailaubekov, A. E.; Bradforth, S. E. *Appl. Phys. Lett.* **2005**, *87*, 021107/1-021107/3.

(52) Fanciulli, R.; Cerjak, I.; Herek, J. L. *Rev. Sci. Instrum.* **2007**, *78*, 053102/1-053102/5.

(53) Callis, P. *Annu. Rev. Phys. Chem.* **1983**, *34*, 329-357.

(54) Becker, R. S.; Kogan, G. *Photochem. Photobiol.* **1980**, *31*, 5-13.

(55) Gustavsson, T.; Sharonov, A.; Markovitsi, D. *Chem. Phys. Lett.* **2002**, *351*, 195-200.

(56) Nesbitt, D. J.; Field, R. W. *J. Phys. Chem.* **1996**, *100*, 12735-12756.

(57) Freed, K. F. *Acc. Chem. Res.* **1977**, *11*, 74-80.

(58) Lehmann, K. K.; Scoles, G.; Pate, B. H. *Annu. Rev. Phys. Chem.* **1994**, *45*, 241-274.

(59) Middleton, C. T.; Cohen, B.; Kohler, B. *J. Phys. Chem. A* **2007**, *111*, 10460-10467.

(60) Kramers, H. A. *Physica* **1940**, *7*, 284.

(61) Batchelor, G. K. *An Introduction to Fluid Dynamics*; Cambridge University Press: Cambridge, 1967.

(62) Austin, J. G.; Kurata, F.; Swift, G. W. *NASA Tech. Brief.* **1968**, *68-10274*.

(63) Barbatti, M.; Aquino, A. J. A.; Szymczak, J. J.; Nachtigallová, D.; Hobza, P.; Lischka, H. *Proc. Natl. Acad. Sci.* **2010**, *107*, 21453-21458.

(64) Hare, P. M.; Crespo-Hernández, C. E.; Kohler, B. *Proc. Natl. Acad. Sci.* **2007**, *104*, 435-440.

(65) Nelson, K. A.; Dlott, D. D.; Fayer, M. D. *Chem. Phys. Lett.* **1979**, *64*, 88-93.

(66) Hochstrasser, R. M.; Nyi, C. A. *J. Chem. Phys.* **1980**, *72*, 2591-2600.

(67) Philpott, M. R. *J. Chem. Phys.* **1971**, *55*, 2039-2054.

(68) Philpott, M. R. *J. Chem. Phys.* **1967**, *47*, 4437-4445.

(69) Womick, J. M.; Moran, A. M. *J. Phys. Chem. B* **2011**, *115*, 1347-1356.

(70) Womick, J. M.; Miller, S. A.; Moran, A. M. *J. Chem. Phys.* **2010**, *133*, 024507.

(71) Christensson, N.; Kauffmann, H. F.; Pullerits, T.; Mančal, T. *J. Phys. Chem. B* **2012**, *116*, 7449-7454.

(72) Polyutov, S.; Kühn, O.; Pullerits, T. *Chem. Phys.* **2012**, *394*, 21-28.

Chapter 7 . Nonlinear Optical Signatures of Ultraviolet Light-Induced Ring Opening in α-Terpinene

7.1. Introduction

Among the most elementary processes in organic chemistry are electrocyclic ring opening reactions in which conjugated cycloalkenes are transformed into conjugated polyenes (e.g., cyclohexadiene becomes hexatriene) [1,2]. The stereospecificities of these reactions depend on whether they involve conrotatory or disrotatory twisting around the broken sigma bond. The Woodward-Hoffman rules leverage knowledge of nodes in the π molecular orbitals to predict the particular type of motion involved in the ring opening process [3,4]. While very elegant and powerful, these rules conveniently hide many intricacies of the physics behind these reactions [5]. For example, research conducted on cyclohexadiene (CHD) shows that photoinduced ring opening is preceded by a sequence of sub-100fs internal conversion transitions [5-16]. Details of these excited state dynamics have only recently come into focus in photo-ionization mass spectrometry experiments employing extraordinarily short ultraviolet laser pulses [8].

In this chapter, femtosecond laser spectroscopies are used to investigate the excited state dynamics preceding ring opening in a derivative of CHD, α-terpinene (α-TP), whose structure is shown in Figure 7.1. Similar relaxation processes are expected to follow photoexcitation in CHD and α-TP because the aliphatic substituents weakly perturb the conjugated π molecular orbitals in the ring [6,8]. Given that similar behaviors

---

Reprinted with permission from *New J. Phys.* **15** 025007 (2013)

are anticipated, it is useful to review what is presently known about photoinduced relaxation in CHD [6-9]. Figure 7.2 presents a schematic for the relevant potential energy surfaces. Photoexcitation of the 1B state, which is a HOMO-to-LUMO transition, initiates (mostly) symmetric wavepacket motion towards a conical intersection with an optically forbidden 2A state characterized by a doubly occupied LUMO orbital. The internal conversion process between states 1B and 2A possesses a time constant of 55fs. Subsequent electronic population transfer from state 2A to the ground state occurs in approximately 80fs. Ring opening and out-of-plane symmetry-breaking motions are thought to occur near the conical intersection between the ground state and state 2A. Adiabatic relaxation in the ground electronic state then separates CHD from the hexatriene photoproduct, which forms with quantum efficiencies of 40% in solution [8,17] and 100% in the gas phase [18]. The origin of the different reaction yields observed in the gas phase and solution is presently unknown [7].

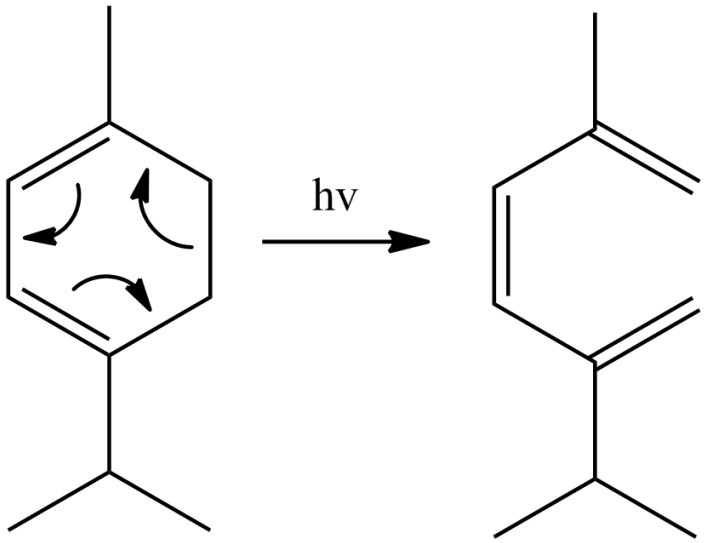

Figure 7.1. Photoinduced ring opening reaction of α-terpinene. This reaction scheme shows only one of the possible isomers generated through ring opening.

The primary goal of this work is to uncover the physics behind analogous internal conversion transitions in α-TP. *To facilitate comparisons with CHD, hereafter the excited states of α-TP will be referred to in the same notation shown in Figure 7.2.* Obviously, α-TP does not possess C_2 symmetry; however, its π molecular orbitals are similar to those in CHD. Notably, the ultrafast transition between the 1B and 2A states has never been directly monitored (in the time domain) for any member of the cyclohexadiene family of molecules in solution because of insufficient time resolution. The direct obtainment of these time constants is a valuable contribution but deeper physical questions will also be addressed. Sub-100fs photoinduced electronic relaxation processes hold a special place in condensed phase dynamics because the environment that surrounds the system generally does not equilibrate on this time scale [19,20]. Here the term "environment" refers to all of the nuclear coordinates in the solute and solvent which are relegated to a heat bath in a reduced quantum mechanical description. Traditional kinetic theories do not apply in the sub-100fs regime because they generally assume that the bath maintains equilibrium throughout the process of interest. In essence, the key issue is that the correlation functions governing non-radiative transitions do not fully decay until a sufficient number of phase-randomizing collisions has occurred. Non-exponential population transfer is one consequence of this coincidence between electronic and nuclear relaxation time scales. Non-exponential internal conversion kinetics are examined in α-TP with the goal of exposing the vibronic couplings from which such non-Markovian dynamics originate. The extraordinary physics associated with vibronic interactions at conical intersections make α-TP an excellent model for photophysical studies [21-23].

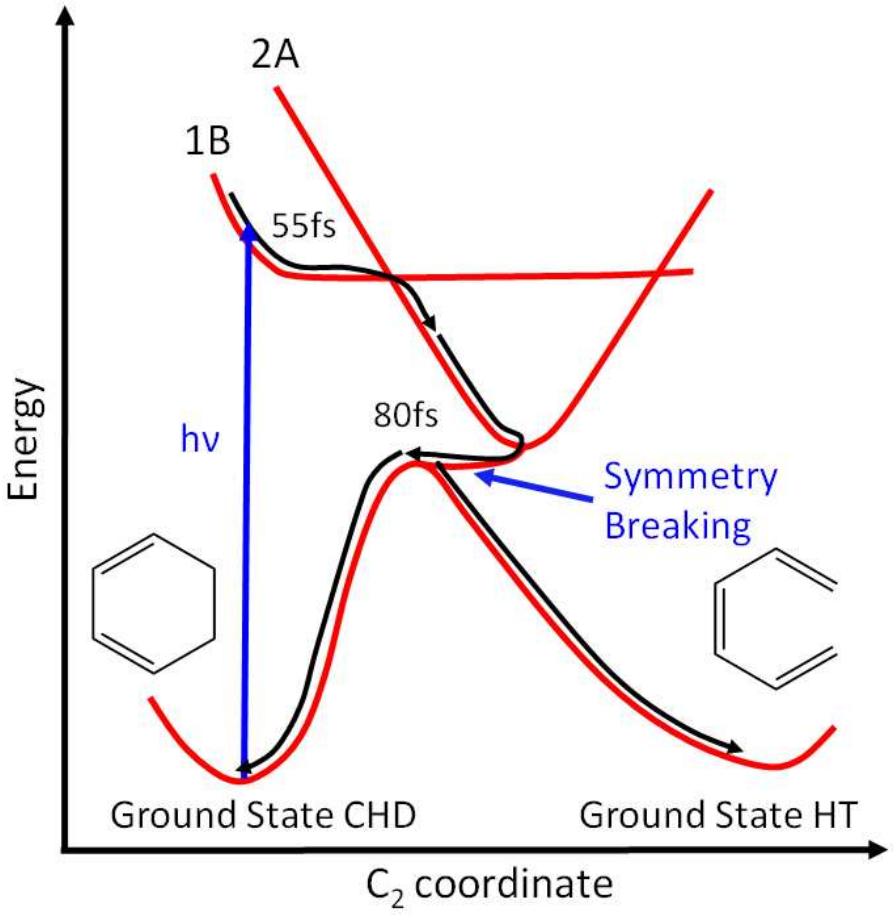

Figure 7.2. Relaxation scheme for cyclohexadiene (CHD). Photoexcitation into the 1B state initiates (mostly) symmetric wavepacket motion towards a conical intersection with state 2A. State 2A transfers population to the ground state within 80fs. Ground state recovery is accompanied by asymmetric nuclear motion. Roughly 40% of the photoexcitations produce hexatriene (HT) in solution (only one of the isomers is shown above). Similar dynamics are thought to mediate the ring opening process in α–terpinene (α-TP). In this work, the electronic states of α-TP are referred to in this same notation to facilitate comparisons with CHD. This figure is adapted from Reference [2] with permission of the American Chemical Society.

Compared to the gas phase, measurements in solution confront the additional problems of dispersion management and undesired nonlinearities in the sample medium. Propagation effects can be minimized by making the sample very thin (100μm or less) [24]. However, it is generally not possible to probe dynamics during the time of laser pulse overlap, because the electronic polarizability of the solvent gives rise to a quasi-

instantaneous "coherence spike" [25-30]. Access to the sub-100fs time scale is afforded only by minimizing the laser pulse durations and, in turn, the width of the coherence spike. Motivated by observations of extremely fast dynamics, the present study makes use of new improvements in the time resolution of the four-wave mixing apparatus. In earlier chapters, the initial implementation of an argon-filled hollow-core waveguide capable of generating 25fs laser pulses is described. The 800cm^{-1} bandwidth was sufficient to carry out two-dimensional photon echo spectrosocopies on components of DNA [29-31]. However, this earlier setup required improvements in two areas. First, the UV bandwidth was limited by the 180fs duration of the 800nm driving pulse derived from a Titanium Sapphire amplifier. Second, UV bandwidths much broader than 800cm^{-1} could not be compressed because of residual third-order dispersion accumulated in a prism compressor. In the chapter, a newly upgraded laser system is employed for 90fs pulse durations at 800nm and use mirrors that impart negative group delay dispersion for UV pulse compression. Now, dynamics at times as short as 40fs following photoexcitation can be observed.

7.2. Experimental Methods

7.2. A. Generation of 20fs laser pulses with cross-modal phase matching in a hollow-core waveguide

It was shown more than a decade ago that broadband UV laser pulses are readily generated in argon-filled hollow-core fibers driven by sub-30fs, 800nm pulses [32-34]. These devices are typically configured to operate with each laser beam in the (lowest order) EH_{11} mode. EH_{11} modes couple well to laser beams with Gaussian spatial profiles at the entrance to the fiber and are subject to less attenuation than higher order modes [35,36]. For these reasons, such auto-modal phase matching (AMP) is generally desirable

because it yields (low-order) UV pulses with the greatest efficiency. Cross-modal phase matching (CMP) describes four-wave mixing processes wherein the three laser beams occupy different modes. CMP has been discussed but never systematically leveraged as a means for optimizing the UV bandwidth. Indeed, AMP should be preferred when extremely short near IR laser pulses are available for pumping an apparatus. Limitations to AMP were explored by Bradforth and co-workers who found that 25fs pulse durations are still attainable with AMP (i.e., all beams in EH_{11}) and 100fs, 800nm driving pulses [37]. In this Section, CMP is shown to be capable of generating 20fs pulse durations despite beginning with 180fs pulses at 800nm. The attainment of extraordinary bandwidths with modest resources suggests that short UV pulses will become readily available.

In the setup, 40μJ pulses at 400nm and 800nm are focused into a hollow-core fiber with a diameter of 75 μm [29,31]. The UV (267nm) pulse energies range between 150nJ and 800nJ depending on the alignment and pressure. Here UV bandwidths achieved are compared before and after a recent upgrade to the laser system in which the pulse duration at 800nm was reduced from 180fs to 90fs by switching from fiber oscillator seed pulses to Ti:Sapphire seed pulses. In Figure 7.3, the UV bandwidths are plotted versus pressure before and after the upgrade. The 800nm beam propagates in the lowest order mode, whereas the 400nm beam is forced to propagate in a higher order mode by slightly misaligning it from the fiber axis. Notably, four well-resolved peaks in the bandwidth are observed below 900 Torr. Corresponding peaks in the pulse energy are evident but are not as pronounced. In these measurements, the bandwidth was first optimized at 850 Torr then the pressure was scanned without modifying the alignment. Thus, measurements conducted before and after the upgrade can be directly compared.

This procedure is probably why the pulse energy and bandwidth do not exhibit identical profiles (i.e., the pulse energy and stability are not re-optimized at each pressure).

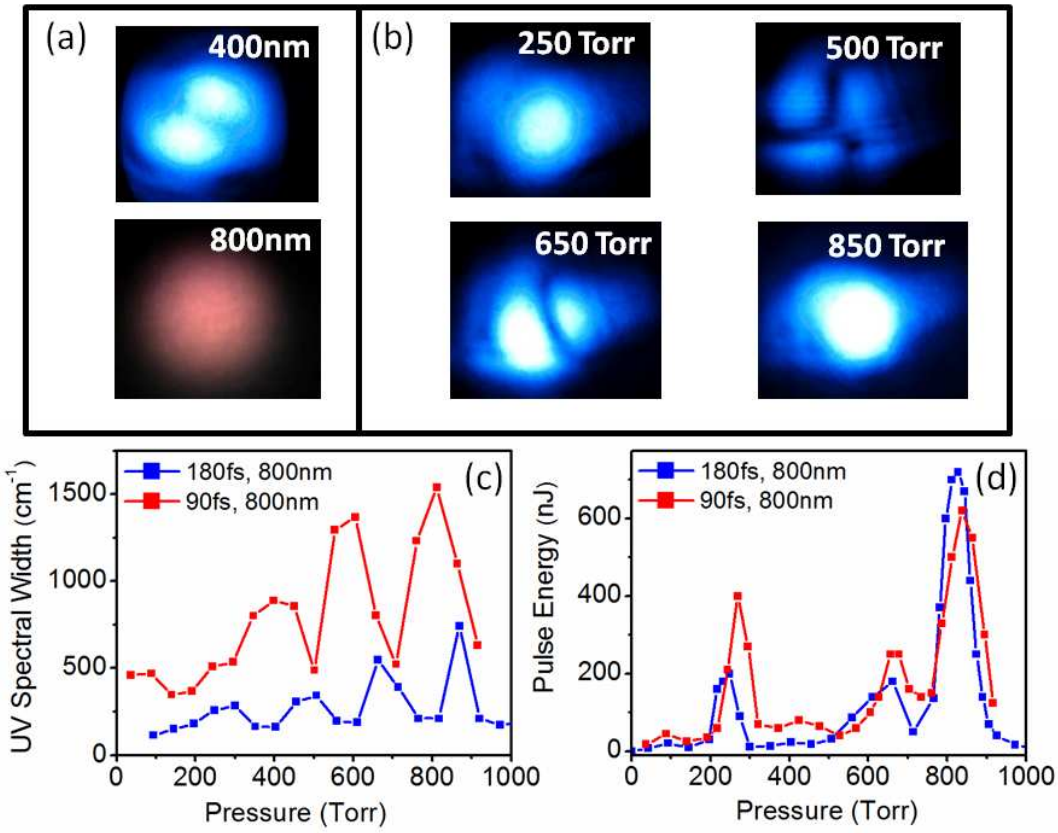

Figure 7.3. (a) Photographs of the 400nm and 800nm beams at the exit of the hollow core fiber at 850 Torr. (b) Photographs of the 267nm laser beam at the fiber exit at four pressures where phase matching is observed. The full-width half-maximum spectral widths (c) and pulse energies (d) at 267nm are plotted with respect to the pressure in the fiber. The blue and red points respectively correspond to measurements conducted with 180fs and 90fs pulses at 800nm.

Nonetheless, the well-resolved peaks in the bandwidth signify the pressures at which phase matching occurs. For this research, it is most important that the EH_{11} UV mode generated at 850 Torr possesses a spectral width that is more than twice as large as that produced with AMP at 250Torr. The broader bandwidth afforded by CMP is attributed to enhanced self-phase modulation at higher pressures.

The particular modes associated with the four nonlinearities observed in Figure 7.3 can be assigned by examining the phase mismatch for the process. The wavevector for light propagation within the fiber is given by [33]

$$k(\lambda, P) = \frac{2\pi n(\lambda, P)}{\lambda}\left[1 - \frac{1}{2}\left(\frac{u_{nm}\lambda}{2\pi a}\right)^2\right] \tag{7.1}$$

where $n(\lambda, P)$ is the refractive index of argon (λ is the wavelength and P is the pressure), a is the fiber radius, and u_{nm} is the modal constant. Phase matched UV generation is achieved under the condition, $\Delta k = 2k_{400} - k_{800} - k_{267}$, where the laser wavelengths are written as subscripts. Table 7.1 summarizes the particular modes associated with each of the four peaks observed in the UV bandwidth. The CMP process

Table 7.1. Summary of phase matching conditions for argon-filled hollow-core fiber

Pressure (Torr) Measured	Pressure (Torr) Calculated	EH Mode at 800nm	EH Mode at 400nm	EH Mode at 267nm
250	253	EH_{11}	EH_{11}	EH_{11}
500	390	EH_{23}	EH_{33}	EH_{23}
650	640	EH_{11}	EH_{11}	EH_{21}
850	790	EH_{31}	EH_{12}	EH_{11}

employed in the experiments is calculated at 790Torr and measured at 800-850 Torr. It is predicted that 800nm and 400nm input beams respectively propagate in EH_{12} and EH_{31} modes, whereas the 267nm UV beam occupies the lowest order EH_{11} mode. The 800nm beam generally appears Gaussian at the exit of the fiber due to the relative attenuation of

higher order modes. However, higher-order 400nm modes are observable at the exit of the fiber under CMP conditions. Propagation of the 400nm pulse in the EH_{31} mode is nominally forbidden for laser beams with (free-space) Gaussian profiles, but this restriction is relaxed when the laser beam is detuned from the fiber axis [35].

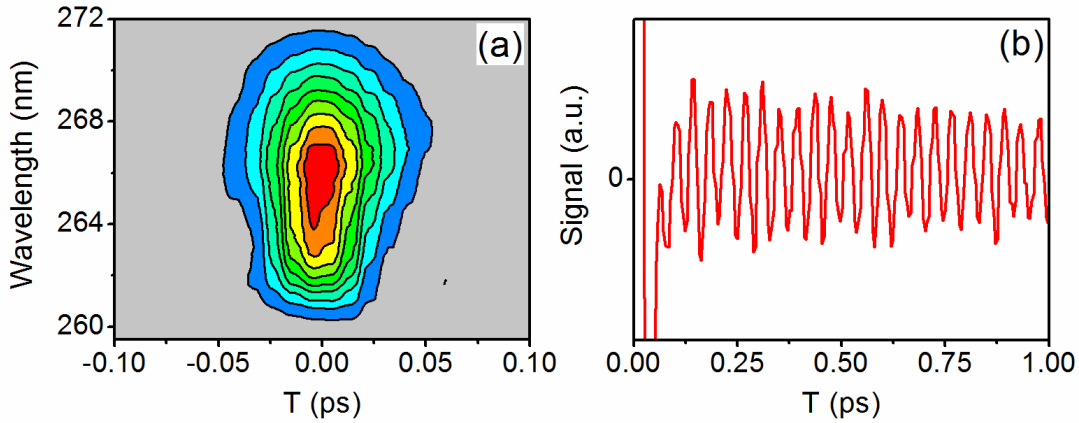

Figure 7.4. (a) Transient grating signal amplitude measured in cyclohexane with 20fs laser pulses at 267nm. (b) The dispersive part of transient grating signal field reveals oscillations with a 42fs period, which correspond to a Raman active vibrational mode of cyclohexane [38].

Of course, the broad UV bandwidth afforded by CMP is useful only if it can be compressed. In this work a dual compressor is utilized, composed of fused silica prisms (85mm separation) and a pair of mirrors that impart negative group delay dispersion (Femtolasers). Prototypes for these mirrors were characterized in earlier work [39]. The chirped mirror compressor is configured for 40 reflections with s-polarized laser beams. Figure 7.4 presents a transient grating FROG spectrogram acquired with cyclohexane wherein a vibrational coherence with a 42fs period is impulsively excited. The laser pulses have time-bandwidth products of approximately 0.45. Analysis suggests that the positive third-order dispersion (TOD) accumulated in the prism compressor is nearly fully compensated for by negative TOD imparted by dielectric mirrors (CVI, TLM1), waveplates, and prism wedges. One drawback associated with CMP at 800-850 Torr is

that multiple modes are more readily produced in the UV. Fortunately, the suppression of multi-mode operation is relatively straightforward because this condition usually gives rise to several distinct peaks in the UV laser spectrum.

7.2. B. Transient grating and photon echo spectroscopies

Transient grating (TG) and two-dimensional photon echo (2DPE) experiments involve a sequence of three laser pulses whose delay times are defined in Figure 7.5. TG measurements use a motorized translation stage to scan T (with τ=0), the interval in which internal conversion and ring opening dynamics occur. 2DPE additionally scans τ from -100fs to +100fs (at various T) by moving fused silica prism wedges in the paths of pulses 1 and 2 [40]. Fourier transformation with respect to τ yields the excitation dimension of the 2DPE spectrum, ω_τ; the emission dimension, ω_t, is obtained by dispersing the signal pulse in the spectrometer. The 2DPE signals of α-TP fully decay by $|\tau|$=40fs because the ππ* resonance possesses a broad line width. The amount of glass associated with a delay of 40fs stretches a 20fs laser pulse at 267nm by less than 0.02fs. Therefore, dispersion associated with displacements of the wedges has a negligible effect on the 2D line shape.

A diffractive optic-based interferometer described in an earlier publication is used to carry out TG and 2DPE experiments [29]. In this setup, the diffractive optic generates a boxcars laser beam geometry in which signals are collected under the phase matching condition, $\mathbf{k}_S = -\mathbf{k}_1 + \mathbf{k}_2 + \mathbf{k}_3$. Three of the laser pulses induce the nonlinear polarization, whereas the fourth (attenuated) pulse is used as a reference field for signal detection by spectral interferometry [41,42]. In all experiments, signals are detected using a back-illuminated CCD array (Princeton Instruments PIXIS 100B) mounted on a 0.3 meter

spectrograph with a 3600 g/mm grating. Integration times range between 100-200ms and are adjusted based on the signal intensity.

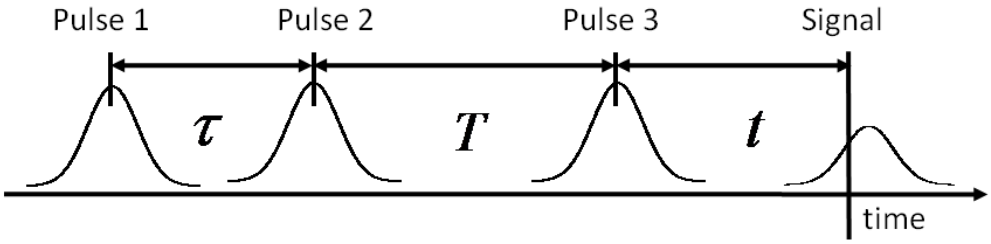

Figure 7.5. Pulse sequence used in TG and 2DPE spectroscopies. Photoexcitation of the system takes place during the experimentally controlled delay, τ; internal conversion and ring opening dynamics occur during the population time, T; the signal is radiated in the emission time, t. TG experiments scan T with τ=0, whereas 2DPE uncovers correlations in the excitation and emission frequencies, ω_τ and ω_t, at various T. All three pulses are centered at 37500cm^{-1} and have 20fs durations. This figure is adapted from Reference [29] with permission of the American Chemical Society.

TG anisotropy measurements are conducted by interleaving sets of 5 scans with parallel and perpendicular pump and probe electric field polarizations. A total of 20 scans are collected for each tensor element. Signal amplitudes for the two tensor elements are also compared at various delay times to ensure that the value of the anisotropy is correct. It is conservatively estimated that this procedure results in an uncertainty of 0.04 in the anisotropy. The polarization condition is varied by rotating a half-waveplate in the path of the "pump" laser beam (i.e., pulses 1 and 2).

Solutions of α-TP are prepared in cylcohexane with optical densities of 0.8 in a 100μm path length. Signal contributions from the solvent are not observed at T>40fs with this optical density. 2DPE spectra are corrected for propagation effects using established procedures [24]. The optical density of the solution has a minor effect on the 2DPE line shapes because the linear absorption coefficient changes little within the laser bandwidth [29]. The sample solution, which has volume of 50mL, flows through a gravity-

fed jet with a 100 micron path length [43]. Use of the jet minimizes dispersion and significantly suppresses scattered light (compared to a cuvette). Absorbance spectra are measured before and after the experiments to confirm the absence of sample degradation. Each of the three incoming laser pulses used in the TG and 2DPE experiments has a fluence of approximately 3.8×10^{13} photons/cm^2 and a peak power of 1.4GW/cm^2. Approximately 0.2% of the molecules are estimated to be photoexcited using the sum of the fluences for pulses 1 and 2. Low pulse energies must be employed because high peak powers, which scale as the inverse of the pulse duration, can readily induce (undesired) ionization of the solute and solvent [29].

7.3. Results and Discussion

7.3. A. Analysis of Linear Absorption Line Shapes

In this Section, line broadening mechanisms are delineated in α-TP by modeling the absorbance spectrum. The absorbance line shape encodes information on solute-solvent interactions, Franck-Condon progressions in the intramolecular modes, and excited state lifetimes. To extract this information, the spectrum is simulated using a framework for the optical response wherein vibronic coupling is incorporated with Brownian oscillator coordinates. Two such modes are sufficient to fit the absorbance spectrum of α-TP. First, consider the fluctuations in the ππ* resonance frequency imposed by thermally driven motions of the solvent and low-frequency intramolecular vibrations. The spectral density associated with this overdamped motion is written as [20]

$$C_{OD}\left(\omega\right)=2\lambda\frac{\omega\Lambda}{\omega^2+\Lambda^2} \tag{7.2}$$

where λ is the reorganization energy and Λ^{-1} is the time scale of the bath. Second, it is known that the C=C stretching mode dominates the higher-frequency intramolecular part of the vibronic response in CHD and its derivatives [15,44]. Contributions from other vibrations, whose couplings are much smaller, cannot be uniquely parameterized based on the absorbance spectrum alone (i.e., resonance Raman data would be needed). Therefore, only the C=C stretching mode is incorporated using the (underdamped) spectral density [20]

$$C_{UD}(\omega) = \frac{1}{2} d^2 \omega_v^2 \left[\delta(\omega - \omega_v) - \delta(\omega + \omega_v) \right] \tag{7.3}$$

where d is the dimensionless displacement and ω_v is the mode frequency. The two components of the spectral density are added together, $C(\omega) = C_{OD}(\omega) + C_{UD}(\omega)$, and the line broadening function is generated with

$$g(t) = \frac{1}{2\pi} \int_{-\infty}^{\infty} d\omega \frac{1 - \cos(\omega t)}{\omega^2} \coth(\beta\hbar\omega/2) C(\omega) + \frac{i}{2\pi} \int_{-\infty}^{\infty} d\omega \frac{\sin(\omega t) - \omega t}{\omega^2} C(\omega \tag{7.4}$$

With $g(t)$ in hand, the linear absorbance line shape is computed using

$$\sigma_A(\omega) = \int_0^{\infty} dt \exp\left[i(\omega - \omega_{\pi\pi^*})t - g(t) - (\gamma t)^b \right] \tag{7.5}$$

where $\omega_{\pi\pi^*}$ is the ππ* electronic transition frequency (i.e., electronic origin), b reflects depopulation of the ππ* state, and b governs the shape of the population decay. The transition dipole is not used as a fitting parameter because the information encoded in the absorbance line shape is of interest (not the magnitude of the extinction coefficient).

Table 7.2. Fitting Parameters for Linear Absorbance Line Shape

Parameter	Non-exponential Lifetime Broadening	Exponential Lifetime Broadening
$\omega_{\pi\pi^*}$	34130 cm^{-1}	34100 cm^{-1}
λ	1500 cm^{-1}	1150 cm^{-1}
Λ^{-1}	100 fs	100 fs
ω_v	1450 cm^{-1}	1450 cm^{-1}
d	1.98	1.98
[(a)] γ^{-1}	50fs	33fs
[(a)] b	4.47	1.00

[(a)] Lifetime broadening parameters, γ and b, are taken directly from the measured anisotropy decay.

Measured and calculated absorbance spectra are shown in Figure 7.6, and the fitting parameters are given in Table 7.2. The Franck-Condon progression associated with the C=C stretching mode is clearly evident despite the fairly broad line width of α-TP. This aspect of the spectrum differs from CHD where the vibronic structure is unresolved because of the extremely short ππ* lifetime [6,15,45]. The absorbance spectrum is fit by constraining the reorganization energy, λ, to be consistent with the value obtained in an earlier resonance Raman intensity analysis for CHD [15]. The frequency and displacement of the C=C stretching mode are then determined based on the vibronic progression in the spectrum. In parameterizing the solvation rate, Λ, the 2DPE measurements presented below are taken into account. They show that a component of the bath relaxes on the 100fs time scale. The linear absorbance spectrum is weakly

affected by the time scale of the bath, Λ^{-1}, when it is greater than 50fs. The low energy tail of the absorbance spectrum is quite sensitive to the population decay parameters, γ and b. The spectrum is fit under the assumptions of both non-exponential ($b \neq 1$) and exponential ($b=1$) dynamics. The lifetime broadening parameters are taken directly from the analysis of transient absorption anisotropy data presented below in order to minimize the number of adjustable degrees of freedom. First, η is set equal to the value determined with a direct fit of the anisotropy ($b=4.47$). The fit is quite reasonable and the lower-frequency side of the calculated spectrum agrees well with the measurement. The spectrum calculated with $b=1.0$ is also in fair agreement, but overestimates the Lorentzian character in the 32000-34000cm^{-1} range.

Notably, these fits focus on the line shape below 38000cm^{-1} because of interference with a higher energy resonance. This portion of the spectrum provides adequate constraints for the parameterization of the model.

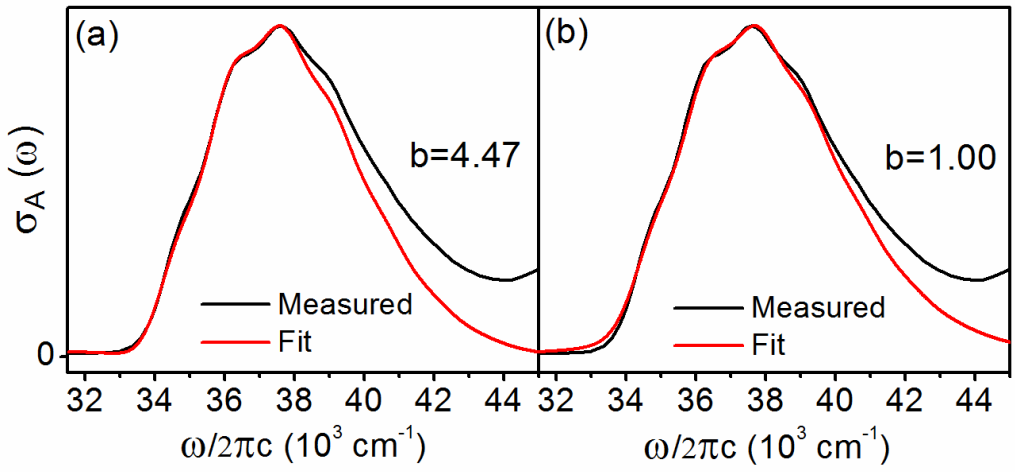

Figure 7.6. Measured (black) and calculated (red) absorbance spectra for α-TP. The data are fit under the assumption of both (a) non-exponential and (b) exponential population decay. Absorbance spectra are computed using Equation (5) and the fitting parameters given in Table 7.2. These fits focus on the absorbance line shape below 38000cm^{-1} because of interference with a higher energy resonance.

Non-exponential population decay should come as no surprise for α-TP and other derivates of CHD because their internal conversion rates are comparable to the fastest nuclear relaxation processes (e.g., solvation and intramolecular vibrational energy redistribution). In the reduced description of quantum mechanics often employed for condensed phases, rate constants are defined as the time integrals of correlation functions involving the operator that couples the initial and final states [19,20,23]. Processes that take place on time scales for which such integrals have not fully converged generally do not exhibit exponential kinetics. Nuclear motions in condensed phases span a broad range of frequencies and time scales, so predictions regarding exponential versus non-exponential kinetic behavior can be difficult to make in some cases. However, the internal conversion transition in α-TP is so fast that it competes even with the sub-100fs dephasing processes that govern the absorbance line shape. It is certain in α-TP that internal conversion takes place on a time scale where the nuclei are still adjusting to the presence of the ππ* excitation.

7.3. B. Probing Internal Conversion Dynamics With Transient Absorption Anisotropies

In this Section, internal conversion dynamics in α-TP are probed using transient absorption signals obtained as the absorptive parts of TG signal fields. The measurements are conducted with both parallel and perpendicular pump and probe electric field polarizations in order to isolate the electronic relaxation process (i.e., suppress contributions from nuclear relaxation). The anisotropy generated using these tensor elements is sensitive to electronic relaxation because the dipoles connecting different pairs of electronic states in a molecule generally have different orientations [46-48].

Sensitivity to the internal conversion process in α-TP derives from excited state absorption (ESA) nonlinearities because the laser spectrum is resonant with only state 1B (i.e., the ππ* electronic state). The key point is that depopulation of the 1B state occurs concomitant with the decay of the component of the optical response associated with ESA. Internal conversion causes the signal field polarization to rotate because ESA possesses contributions from resonances with transition dipole orientations different than the transition dipole connecting the ground state to the 1B excited state.

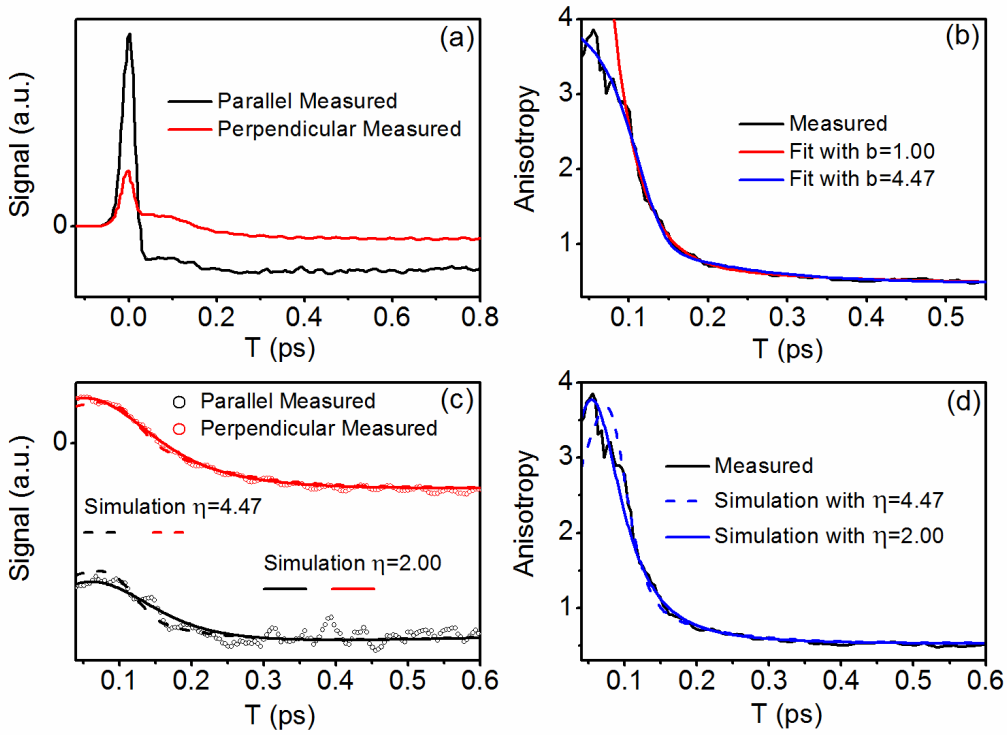

Figure 7.7. (a) Absorptive (real) parts of TG signal fields measured for α-TP with parallel (black) and perpendicular (red) pump and probe polarizations. In this representation, signals with positive and negative signs correspond to a photoinduced absorption and bleach, respectively. (b) The measured anisotropy is fit under the assumption of (red) exponential and (blue) non-exponential relaxation dynamics. Fitting parameters are given in Table 7.3. (c) TG signals acquired with parallel and perpendicular pump and probe polarizations are simulated using Equations (A11) and (A12) with the parameters given in Table 7.4. (d) Measured and calculated anisotropies are compared. The parameter, η, captures the non-exponential shape of the population decay, whereas b possesses small contributions from nuclear dynamics. These data suggest that the depopulation of state 1B follows a Gaussian-like temporal profile.

Transient absorption signals acquired with both parallel, $S_{\parallel}(T)$, and perpendicular, $S_{\perp}(T)$, polarizations are presented in Figure 7.7. $S_{\parallel}(T)$ bleaches instantly following the "coherence spike" at T=0, whereas $S_{\perp}(T)$ changes sign near T =200fs. This sign change is an indication that ESA nonlinearities contribute to the response at short delay times. The anisotropy is first generated with

$$r(T) = \frac{S_{\parallel}(T) - S_{\perp}(T)}{S_{\parallel}(T) + 2S_{\perp}(T)} \tag{7.6}$$

then fit using the following function

$$F(T) = A_0 + A_1 \exp\left[-(T/\tau_1)^b\right] + A_2 \exp(-T/\tau_2) \tag{7.7}$$

$F(T)$ includes both an exponential term and a term in which the exponent, b, enables non-exponential behavior. This phenomenological function is motivated by its ability to distinguish exponential and non-exponential behaviors with a minimum number of parameters.

The anisotropy is fit both with b as a free parameter and with b set equal to 1.0 (see Table 7.3). The full shape of the decay is captured with b=4.47, whereas only the dynamics after T=0.15ps are well-described using b=1.0. For example, note that the fit of the anisotropy with b=1.0 diverges at T=0.10ps. The non-exponential term is assigned to population transfer from state 1B to state 2A. Assignment of the 130fs time constant is not as straightforward. One interpretation is that it reflects the return of population from state 2A to the ground state. In this scenario, the anisotropy derives sensitivity to the depopulation of state 2A through a resonance between state 2A and a

higher energy excited state. A second possibility, considered less likely, is that the anisotropy reflects only the depopulation of state 1B. In this interpretation, the two decay components would correspond to distinct sub-populations prepared by photoexcitation. Simulations of wavepacket dynamics in α-TP, similar to those carried out on CHD [49,50], will be helpful for establishing a detailed microscopic interpretation of the measured dynamics.

Table 7.3. Fitting Parameters for Transient Absorption Anisotropies

[(a)]Parameter	Non-exponential Decay	Exponential Decay
A_0	0.48±0.02	0.47±0.02
A_1	2.27±0.28	36.6±4.9
τ_1 (fs)	120±3	33±2
b	4.47±0.58	1.00±0.00
A_2	1.39±0.46	0.54±0.18
τ_2 (fs)	130±20	189±48

[(a)]Ranges in the fitting parameters correspond to twice the standard error.

The anisotropy is simulated using the model outlined in appendix A4 to further explore the origin of the dynamics in the signal polarization. Decomposing the nonlinear response function into individual terms more directly addresses the temporal profile associated with depopulation of state 1B because the parameter b in Equation (7) may possess contributions from fast nuclear relaxation. The model aims to capture the "true" non-exponential character of the population dynamics with η. As in Equation (7), it is

assumed that the two decay components, τ_1 and τ_2, respectively represent depopulation of the 1B and 2A electronic states. The model also introduces an inertial solvation time constant, τ_{solv}, and a vibrational cooling time, τ_{VC}, associated with the formation of an open-chain photoproduct. In Figure 7.7, the signals are fit with η set equal to both 4.47 and 2.00 in order to evaluate the extent to with the population dynamics differ from the directly measured shape of the anisotropy decay (where b=4.47). The fits are reasonable in both cases but are slightly better with η=2.00 at T<0.15ps, which suggests that the internal conversion process is indeed non-exponential. The model calculations also make clear that the anisotropy decay convolves the depopulation of state 1B with the inertial part of the solvation process. Based on the analysis of the data summarized in Appendix A4, it is conservatively suggested that the true dynamics may range anywhere between η =1.7 and η=3.2. Most importantly, these simulations support the interpretation that state 1B is depopulated in a non-exponential fashion.

7.3. C. Signature of Solvation Dynamics in Photon Echo Line Shapes

The anisotropy measurements presented above are primarily sensitive to electronic relaxation. In this section, 2DPE spectroscopy is used to investigate the nuclear dynamics initiated by photoexcitation. It was established in the first 2D electronic spectroscopy experiments that solvation induces a loss of correlation between the excitation, ω_τ, and detection, ω_t, frequencies [51]. In essence, the 2DPE line shape becomes more circular in appearance as the local solvent geometry loses memory of its initial structure. The present measurements examine similar signatures of solvent reorganization. In addition, the fast internal conversion transitions in α-TP give rise to

vibrational cooling processes in the ground electronic state, which also influence the 2DPE line shapes.

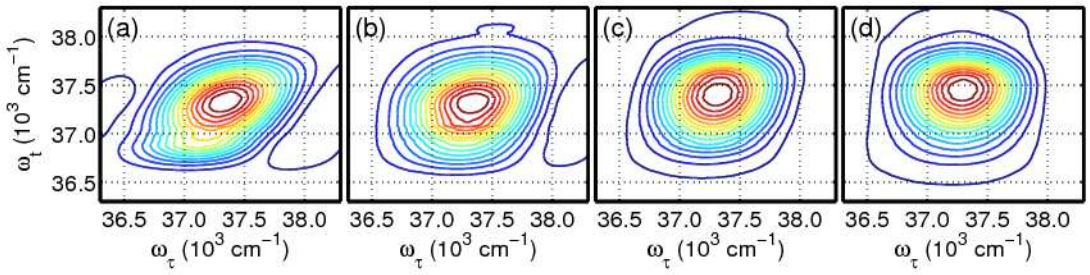

Figure 7.8. (a) Absorptive (real) parts of 2DPE spectra acquired for α-TP at (a) T =100fs; (b) T=125fs; (c) T=225fs; (d) T=500fs. The magic angle polarization condition is employed.

2DPE spectra acquired at delay times ranging from T=100fs-500fs are presented in Figure 7.8. The spectrum at T=100fs possesses an elongated shape signifying correlation between ω_τ and ω_t. Solvation gradually washes out these correlations until the spectrum acquires the fairly circular appearance found at T=500fs. To analyze dynamics in the line shapes, diagonal ($\omega_\tau = \omega_t$) and anti-diagonal ($-\omega_\tau = \omega_t$) slices of the 2D spectra are fit and the ratio of Gaussian widths, Γ_{ad}/Γ_d, with respect to T is plotted and shown in Figure 7.9. A fit to a sum of 2 exponentials reveals processes with 19.8fs and 36.8ps time constants. The robust conclusion to be drawn is that distinct classes of dynamics take place on time scales near 100fs and in the 10's of picoseconds range. The shorter time constant is assigned to reorganization of the solvent and intramolecular vibrational energy redistribution. Because the overall time scales for these processes are generally greater than 20fs, it is suggested that the measurement is primarily sensitive to the departure of the wavepacket from the Franck-Condon geometry. The 36.8ps time constant, which is not well-determined because the range of the fit does not extend beyond T=500fs, most likely represents solute-to-solvent vibrational energy transfer in

the ground electronic state. Evolution in the 2DPE line shapes at T <200fs confirms that internal conversion and nuclear relaxation processes occur simultaneously in α-TP. The non-exponential internal conversion kinetics exhibited by α-TP are a natural consequence of this coincidence in time scales.

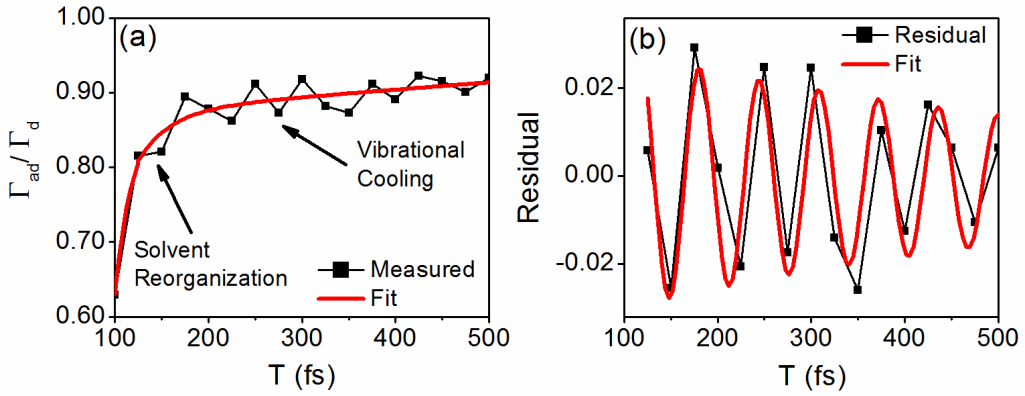

Figure 7.9. (a) Ratio in the anti-diagonal, Γ_{ad}, and diagonal, Γ_d, 2DPE line widths obtained for α-TP with magic angle polarizations. The ratio is fit using $F(T) = A_0 + \sum_{i=1}^{2} A_i \exp(-T/\tau_i)$, where A_0 =1.35, A_1 =-0.45, τ_1 =19.8fs, A_2 =-0.48, and τ_2 =36.8ps. (b) The residual corresponding to panel (a) is fit using $F(T) = A_0 + A_1 \exp(-T/\tau_{damp})\sin[2\pi(T-T_c)/w]$, where A_0 =-0.010, A_1 =0.026, T_C =36.4fs, τ_{damp} =590 fs, and w =63.7fs. The 523cm^{-1} recurrence is assigned to a vibrational mode involving both C=C torsion and HOOP motion on the vinyl group. This suggests that the 523cm^{-1} mode possesses a large excited state potential energy gradient (on the 1B surface) at the equilibrium geometry of the molecule.

Figure 7.9 reveals a coherent quantum beat in the 2DPE line shape. The residual of the fit in panel (a) is fit with a damped sine function. The recurrence in Γ_{ad}/Γ_d corresponds to a vibrational mode with a wavenumber of 523cm^{-1}. Strong vibronic coupling implies that the vibration probably involves motion of the ring (not the substituents) in the vicinity of the ππ* excitation. Thus, the modes of CHD, which are well-characterized, are a natural starting point for making an assignment in α-TP. The C=C torsion (507cm^{-1} in CHD) and hydrogen out-of-plane (HOOP) wagging mode on the

vinyl group (562cm^{-1} in CHD) are the most likely candidates [15]. A computational normal mode analysis conducted on α-TP at the B3LYP/6311G(d) level yields a vibration at 528cm^{-1} with both HOOP and C=C torsion character (the calculation is performed in a dielectric cyclohexane medium using the IEFPCM model) [52]. Therefore, the 523cm^{-1} recurrence in α-TP is assigned to a normal mode composed of both vinyl HOOP and C=C torsion motions.

Detection of the 523cm^{-1} mode indicates that it is associated with a steep potential energy gradient in the 1B state at the equilibrium geometry (i.e., Franck-Condon activity). These recurrences must represent wavepacket motion in the ground electronic state because they persist at delay times, T, that are long compared to the lifetime of the 1B state [20]. Thus, the coherent dynamics displayed in Figure 7.9 have a different origin than those detected in photo-ionization mass spectrometry experiments on CHD where excited state wavepacket motions are interrogated [8]. Finally, it is noted that this quantum beat is not detected in the TG or 2DPE amplitudes. 2DPE electronic spectroscopies applied to other systems have similarly exposed coherent beats in the 2D line shapes [53-55]. The present observation underscores the power of 2DPE spectroscopy for uncovering physics hidden from conventional techniques [51,56-65].

7.4. Concluding Remarks

This investigation of photoinduced relaxation processes in α-TP employs TG and 2DPE spectroscopies with exceptional time resolution in the deep UV spectral region. The finding of non-exponential depopulation of the photoexcited 1B state is the primary contribution of this work. This non-Markovian behavior is concluded to be a natural consequence of the coincidence between electronic and nuclear relaxation time scales in

α-TP. Kinetic models generally assume that equilibrium is established in the bath on a time scale much shorter than that corresponding to non-radiative transitions in the system. This approximation does not hold in α-TP or the parent molecule, CHD, which also possesses a sub-100fs internal conversion transition. α-TP is now believed to be the only system in the CHD family of molecules for which the ultrafast internal conversion process between 1B and 2A has been directly time-resolved in solution.

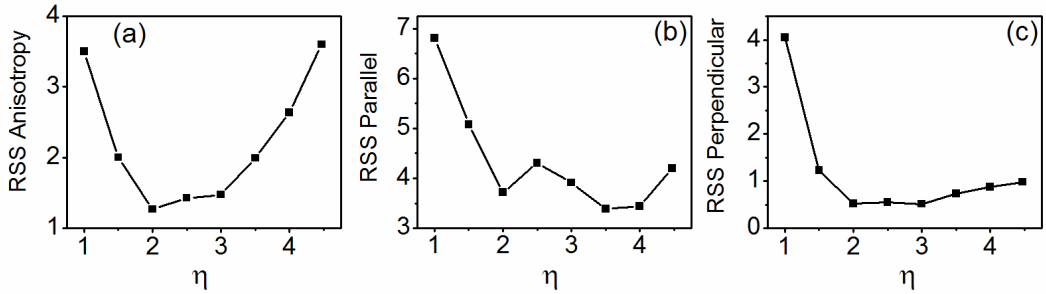

Figure 7.10. Residual sum of squares (RSS) for (a) anisotropy and TG signals acquired with (b) parallel and (c) perpendicular pump and probe electric field polarizations. The RSS in (b) and (c) are divided by 10^8 (i.e., the signal levels are arbitrary). Formulas for the RSS are given in appendix B. It is concluded that the depopulation dynamics of state 1B follow a non-exponential temporal profile in which η ranges from 1.7 to 3.2.

It would not be surprising to find similar non-Markovian population transfer dynamics in CHD and its other derivatives (e.g., α-phellandrene). An often-cited 20fs internal conversion time scale for CHD in solution was determined indirectly using a resonance Raman intensity analysis [15]. This number is not disputed but it is suggested that non-Markovian population decay is more consistent with the linear absorption line shape. As in α-TP, the lower-frequency side of the absorbance spectrum of CHD is primarily sensitive to lifetime broadening. Preliminary model calculations find that the Lorentzian character is greatly overestimated in this region of CHD's absorbance spectrum when a 20fs exponential decay process is assumed. Future work in the

laboratory will directly probe internal conversion dynamics in CHD and its derivatives with the goal of obtaining more detailed knowledge of the excited state dynamics.

The shape of the anisotropy decay in α-TP suggests that the depopulation of state 1B rapidly accelerates within the first 100fs after photoexcitation. That is, the population of state 1B follows a Gaussian-like temporal profile for which the magnitude of the first derivative increases from T=0fs to T=100fs. Data suggest that α-TP is subject to two phases of nuclear motions similar to the symmetric and asymmetric geometry changes that take place in the 1B state of CHD [6]. *In α-TP, it is hypothesized that the excited state wavepacket undergoes several recurrences in the C=C stretching coordinate before displacement along the C=C torsion/vinyl HOOP coordinate finally sets it free from the Franck-Condon region of the 1B potential energy surface. The unconfined wavepacket then transitions from state 1B into state 2A by way of a conical intersection.* In support of this interpretation, the Franck-Condon progression of the C=C stretching mode in the linear absorbance spectrum makes clear that the excited state wavepacket recurs 3-4 times at the Franck-Condon geometry before transitioning into the 2A state (i.e., the period of the C=C stretching mode is 23fs) [66]. In CHD, the photo-initiated wavepacket is known to depart from the 1B state through asymmetric motions. Similarly, based on the observation of a vibrational coherence in the 2DPE data, it is suggested that the wavepacket in α-TP leaves the Franck-Condon geometry in the direction of a normal mode involving both C=C torsion and HOOP motion on the vinyl group. The relatively slow onset of the population transfer process at T=0fs may reflect the suppression of motion along this quasi-out-of-plane coordinate imposed by solvent friction. Theoretical models will be used to establish a more detailed microscopic picture of the dynamics.

Table 7.4. Model Parameters for Transient Absorption Anisotropies

[a]Parameter	η=4.47	η=2.00
$\mu_{K,1B}$	0.90 $\mu_{1A,1B}$	0.90 $\mu_{1A,1B}$
$\mu_{M,2A}$	1.13 $\mu_{1A,1B}$	1.13 $\mu_{1A,1B}$
μ_{PP}	0.60 $\mu_{1A,1B}$	0.60 $\mu_{1A,1B}$
α	55°	60°
β	65°	60°
θ	40°	40°
τ_1	120 fs	120 fs
τ_2	130 fs	130 fs
τ_{solv}	20 fs	20 fs
τ_{VC}	250 fs	270 fs

[a] Model outlined in Appendix A4.

7.5. References

(1) Turro, N. J. *Modern Molecular Photochemistry*; University Science Books: Sausalito, 1991.

(2) Nenov, A.; Kölle, P.; Robb, M. A.; de Vivie-Riedle, R. *J. Org. Chem.* **2010**, *75*, 123-129.

(3) Woodward, R. B.; Hoffmann, R. *Angew. Chem. Int. Ed. Engl.* **1969**, *8*, 781-853.

(4) Van der Lugt, W. T. A. M.; Oosterhoff, L. J. *J. Am. Chem. Soc.* **1969**, *91*, 6042-6049.

(5) Reid, P. J.; Lawless, M. K.; Wickham, S. D.; Mathies, R. A. *J. Phys. Chem.* **1994**, *98*, 5597-5606.

(6) Garavelli, M.; Page, C. S.; Celani, P.; Olivucci, M.; Schmid, W. E.; Trushin, S. A.; Fuss, W. *J. Phys. Chem. A* **2001**, *105*, 4458-4469.

(7) Deb, S.; Weber, P. M. *Annu. Rev. Phys. Chem.* **2011**, *62*, 19-39.

(8) Kosma, K.; Trushin, S. A.; Fuß, W.; Schmid, W. E. *Phys. Chem. Chem. Phys.* **2009**, *11*, 172-181.

(9) Kuthirummal, N.; Rudakov, F. M.; Evans, C. L.; Weber, P. M. *J. Chem. Phys.* **2006**, *125*, 133307.

(10) Fuß, W.; Schikarski, T.; Schmid, W. E.; Trushin, S.; Kompa, K. L. *Chem. Phys. Lett.* **1996**, *262*, 675-682.

(11) Anderson, N. A.; Pullen, S. H.; Walker, L. A.; Shiang, J. J.; Sension, R. J. *J. Phys. Chem. A* **1998**, *102*, 10588-10598.

(12) Pullen, S. H.; Anderson, N. A.; Walker, L. A.; Sension, R. J. *J. Chem. Phys.* **1998**, *108*, 556.

(13) Lochbrunner, S.; Fuss, W.; Schmid, W. E.; Kompa, K. L. *J. Phys. Chem. A* **1998**, *102*, 9334-9344.

(14) Pullen, S. H.; Walker, L. A.; Donovan, B.; Sension, R. J. *Chem. Phys. Lett.* **1995**, *242*, 415-420.

(15) Trulson, M. O.; Dollinger, G. D.; Mathies, R. A. *J. Chem. Phys.* **1989**, *90*, 4274-4281.

(16) Kim, J.; Tao, H.; White, J. L.; Petrovic, V. S.; Martinez, T. J.; Bucksbaum, P. H. *J. Phys. Chem. A* **2012**, *116*, 2758-2763.

(17) Minaard, N. G.; Havinga, E. *Recl. Trav.Chim. Pays. Bas.* **1973**, *92*, 1315-1320.

(18) Rudakov, F.; Weber, P. M. *Chem. Phys. Lett.* **2009**, *470*, 187-190.

(19) Nitzan, A. *Chemical Dynamics in Condensed Phases*; Oxford University Press: Oxford, 2006.

(20) Mukamel, S. *Principles of Nonlinear Optical Spectroscopy*; Oxford University Press: New York, 1995.

(21) Worth, G. A.; Cederbaum, L. S. *Annu. Rev. Phys. Chem.* **2004**, *55*, 127-158.

(22) *Conical Intersections: Theory, Computation and Experiment*; Domcke, W.; Yarkony, D.; Köppel, H., Eds.; World Scientific: Singapore, 2011.

(23) Farrow, D. A.; Qian, W.; Smith, E. R.; Ferro, A. A.; Jonas, D. M. *J. Chem. Phys.* **2008**, *128*, 144510.

(24) Yetzbacher, M. K.; Belabas, N.; Kitney, K. A.; Jonas, D. M. *J. Chem. Phys.* **2007**, *126*, 044511.

(25) Zimdars, D.; Francis, R. S.; Ferrante, C.; Fayer, M. D. *J. Chem. Phys.* **1997**, *106*, 7498-7511.

(26) Reuther, A.; Iglev, H.; Laenen, R.; Laubereau, A. *Chem. Phys. Lett.* **2000**, *325*, 360-368.

(27) Selig, U.; Schleussner, C.-F.; Foerster, M.; Langhojer, F.; Nuernberger, P.; Brixner, T. *Opt. Lett.* **2010**, *35*, 4178-4180.

(28) Tseng, C.-H.; Matsika, S.; Weinacht, T. C. *Opt. Express* **2009**, *17*, 18788-18793.

(29) West, B. A.; Womick, J. M.; Moran, A. M. *J. Phys. Chem. A* **2011**, *115*, 8630-8637.

(30) West, B. A.; Moran, A. M. *J. Phys. Chem. Lett.* **2012**, *3*, 2575-2581.

(31) West, B. A.; Womick, J. M.; Moran, A. M. *J. Chem. Phys.* **2011**, *135*, 114505.

(32) Durfee, C. G.; Backus, S.; Murnane, M. M.; Kapteyn, H. C. *Opt. Lett.* **1997**, *22*, 1565-1567.

(33) Durfee, C. G.; Misoguti, L.; Backus, S.; Kapteyn, H. C.; Murnane, M. M. *J. Opt. Soc. Am. B* **2002**, *19*, 822-831.

(34) Durfee, C. G.; Backus, S.; Kapteyn, H. C.; Murnane, M. M. *Opt. Lett.* **1999**, *24*, 697-699.

(35) Nubling, R. K.; Harrington, J. A. *Opt. Eng.* **1998**, *37*, 2454-2458.

(36) Saito, M.; Sato, S.-Y.; Miyagi, M. *J. Opt. Soc. Am. A* **1993**, *10*, 277-282.

(37) Jailaubekov, A. E.; Bradforth, S. E. *Appl. Phys. Lett.* **2005**, *87*, 021107/1-021107/3.

(38) Wiberg, K.; Shrake, A. *Spectrochim. Acta. Part A* **1973**, *29*, 583-594.

(39) Rivera, C. A.; Bradforth, S. E.; Tempea, G. *Optics Express* **2010**, *18*, 18615-18624.

(40) Brixner, T.; Mancal, T.; Stiopkin, I. V.; Fleming, G. R. *J. Chem. Phys.* **2004**, *121*, 4221-4236.

(41) Lepetit, L.; Chériaux, G.; Joffre, M. *J. Opt. Soc. Am. B* **1995**, *12*, 2467-2474.

(42) Gallagher, S. M.; Albrecht, A. W.; Hybl, J. D.; Landin, B. L.; Rajaram, B.; Jonas, D. M. *J. Opt. Soc. Am. B* **1998**, *15*, 2338-2345.

(43) Tauber, M. J.; Mathies, R. A.; Chen, X.; Bradforth, S. E. *Rev. Sci. Instrum.* **2003**, *74*, 4958-4960.

(44) Reid, P. J.; Doig, S. J.; Mathies, R. A. *J. Phys. Chem.* **1990**, *94*, 8396-8399.

(45) Merchán, M.; Serrano-Andrés, L.; Slater, L. S.; Roos, B. O.; McDiarmid, R.; Xing, X. *J. Phys. Chem. A* **1999**, *103*, 5468-5476.

(46) Fleming, G. R. *Chemical Applications of Ultrafast Spectroscopy*; Oxford University Press: New York, 1986.

(47) Wynne, K.; Hochstrasser, R. M. *Chem. Phys.* **1993**, *171*, 179-188.

(48) Qian, W.; Jonas, D. M. *J. Chem. Phys.* **2003**, *119*, 1611.

(49) Tamura, H.; Nanbu, S.; Ishida, T.; Nakamura, H. *J. Chem. Phys.* **2006**, *124*, 084313.

(50) Hofmann, A.; de Vivie-Riedle, R. *J. Chem. Phys.* **2000**, *112*, 5054-5059.

(51) Jonas, D. M. *Annu. Rev. Phys. Chem.* **2003**, *54*, 425-463.

(52) Frisch, M. J.; Trucks, G. W.; Schlegel, H. B.; Scuseria, G. E.; Robb, M. A.; Cheeseman, J. R.; Scalmani, G.; Barone, V.; Mennucci, B.; Petersson, G. A.; Nakatsuji, H. *Gaussian 09, Revision C.01* **2009**.

(53) Collini, E.; Scholes, G. D. *Science* **2009**, *323*, 369-373.

(54) Engel, G. S.; Calhoun, T. R.; Read, E. L.; Ahn, T. K.; Mancal, T.; Cheng, Y. C.; Blankenship, R. E.; Fleming, G. R. *Nature* **2007**, *446*, 782-786.

(55) Christensson, N.; Milota, F.; Hauer, J.; Sperling, J.; Bixner, O.; Nemeth, A.; Kauffmann, H. F. *J. Phys. Chem. B* **2011**, *115*, 5383-5391.

(56) Karaiskaj, D.; Bristow, A. D.; Yang, L.; Dai, X.; Mirin, R. P.; Mukamel, S.; Cundiff, S. T. *Phys. Rev. Lett* **2010**, *104*, 117401/1-117401/4.

(57) Cho, M. *Chem. Rev.* **2008**, *108*, 1331-1418.

(58) Pakoulev, A. V.; Block, S. B.; Yurs, L. A.; Mathew, N. A.; Kornau, K. M.; Wright, J. C. *J. Phys. Chem. Lett.* **2010**, *1*, 822-828.

(59) Ogilvie, J. P.; Kubarych, K. J. *Adv. At. Mol. Opt. Phys.* **2009**, *57*, 249-321.

(60) Turner, D. B.; Nelson, K. A. *Nature* **2010**, *466*, 1089-1092.

(61) Lott, G. A.; Perdomo-Ortiz, A.; Utterback, J. K.; Widom, J. R.; Aspuru-Guzik, A.; Marcus, A. H. *Proc. Natl. Acad. Sci.* **2011**, *108*, 16521-16526.

(62) Hamm, P.; Zanni, M. T. *Concepts and Methods of 2D Infrared Spectroscopy*; Cambridge University Press: Cambridge, 2011.

(63) Richards, G. H.; Wilk, K. E.; Curmi, P. M. G.; Quiney, H. M.; Davis, J. A. *J. Phys. Chem. Lett.* **2012**, *3*, 272-277.

(64) Caram, J. R.; Lewis, N. H. C.; Fidler, A. F.; Engel, G. S. *J. Chem. Phys.* **2012**, *136*, 104505.

(65) Tseng, C.-H.; Sándor, P.; Kotur, M.; Weinacht, T. C.; Matsika, S. *J. Phys. Chem. A* **2012**, *116*, 2654-2661.

(66) Heller, E. J. *Acc. Chem. Res.* **1981**, *14*, 368-375.

Chapter 8 . Toward Two-Dimensional Photon Echo Spectroscopy with 200nm Laser Pulses

8.1. Introduction

Two-dimensional photon echo (2DPE) spectroscopy has emerged in the past decade as a powerful tool for uncovering a wide variety of phenomena in condensed phases [1-3]. Experiments carried out in the visible and infrared spectral ranges have transformed the understanding of processes ranging from electronic energy transfer to bond making and breaking in liquids [4-10]. Knowledge of photo-induced dynamics in small molecules and biological systems motivates applications of 2DPE in the 200-300 nm wavelength range [11,12]. However, measurements conducted in the deep UV are challenged by dispersion management and the suppression of undesired photo-ionization processes. 2DPE experiments reported near 267 nm (i.e., the third harmonic of a Ti:Sapphire laser) are at the present technical frontier [13-18]. Further progress into the deep UV must contend with experimental difficulties that grow steeply as the wavelength becomes shorter.

In this chapter, the development of transient grating (TG) and 2DPE experiments is described employing 200 nm laser pulses. This work leverages the recent construction of a four-wave mixing spectrometer operational near 267 nm [16]. Several technical issues relevant to the present study were addressed using this apparatus. Here, 60 fs, 200 nm laser pulses generated through filamentation of laser beams in both air and argon are

---

Reprinted with permission from *Optics Express*, **21**, 2118-2125. (2013)

characterized. The 200 nm light intensities, bandwidths, and pulse durations are compared in the two gases. It is shown that TG and 2DPE experiments are readily carried out at 200 nm with a (passively phase-stabilized) diffractive optic-based four-wave mixing interferometer [19]. These proof-of-principle experiments, which examine the DNA nucleoside adenosine, are performed in a two-color configuration, where 200 nm light is used to probe the dynamics initiated by a pair of 267 nm laser pulses.

8.2. Generation and compression of 200 nm laser pulses

One of the primary challenges facing nonlinear spectroscopies at 200 nm is the attainment of sufficiently short laser pulses. Motivations for using gases as nonlinear media in deep UV laser pulse generation have been discussed in earlier chapters and in published work[20-23]. Nonetheless, it is useful to briefly consider why nonlinear optical crystals such as BBO are not well-suited for the applications. For example, the phase matching bandwidth associated with 200 nm sum-frequency generation in a 30 μm thick BBO crystal is approximately 240 cm^{-1} with incident 800 nm and 267 nm laser pulses [24]. A 30 μm thick BBO is chosen for illustration because this would result in the greatest conversion efficiency for the 90 fs, 800 nm pulses available in the laboratory. The key issue is that the bandwidth of the 200 nm pulse does not exceed the bandwidths of the incident pulses. By contrast, it has been demonstrated that bandwidths exceeding 1500 cm^{-1} can be produced at 200 nm in gaseous media [22,23]. Moreover, as will be shown below, the bandwidth achieved at 200 nm is actually greater than the bandwidths of the incident laser pulses because of self-phase modulation in the gas. The bandwidth obtained at 200 nm is more than two times larger than the bandwidth of the 800 nm fundamental pulse produced by the laser system.

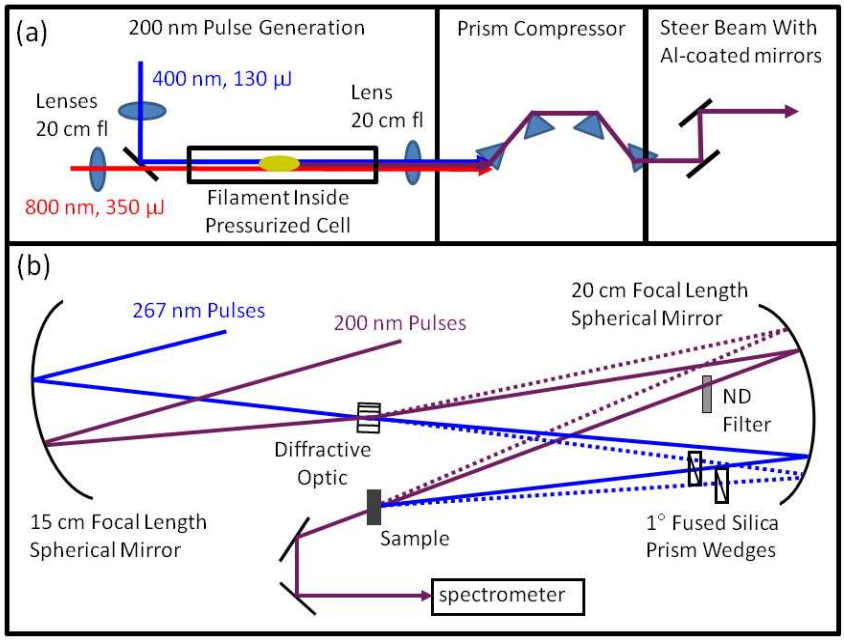

Figure 8.1. (a) Setup used for 200 nm pulse generation and compression. (b) Diffractive optic-based interferometer used for TG and 2DPE measurements. The 200 nm laser pulse probes the holographic grating induced in the sample by the pair of 20 fs, 267 nm pulses.

In earlier work, efficient generation of 200 nm light was achieved by confining the nonlinearity to a hollow-core waveguide filled with argon [20,21]. Initial attempts utilized this approach, but high-quality laser beams with the requisite pulse energies (>50 nJ) could not be obtained without damaging the waveguide. Therefore, filamentation is used in a pressurized cell to produce 200 nm laser pulses with energies exceeding 100 nJ. The experimental apparatus used for pulse generation and characterization is depicted in Figure 8.1. In this setup, 800 nm and 400 nm laser pulses with 90-100 fs durations are focused into a 30 cm long gas cell, which is filled with either air or argon. The focal lengths and incoming pulse energies, which are given in the figure, are chosen based on the conversion efficiency and beam quality at 200 nm. Within the filament, 200 nm light is generated through a cascade of four-wave mixing processes [22,23]. To begin, the third-

harmonic is produced by way of the nonlinearity, $k_{267} = 2k_{400} - k_{800}$, where the subscripts denote the laser wavelengths. The 267 nm pulse then feeds a second process, $k_{200} = 2k_{267} - k_{400}$, that yields 200 nm light.

The 200 nm laser beam is collimated, sent through a prism compressor, then undergoes only two reflections on aluminum-coated mirrors before it enters the diffractive optic-based interferometer shown in Figure 8.1(b). This interferometer, which was designed for operation near 267 nm [15,16], is quite lossy at 200 nm. The pulse energy at the sample position is only 2 nJ (98% loss in interferometer). For this reason, one-color, 200 nm four-wave mixing experiments are not presently possible. Still, TG signals are readily detected when a pair of 20 fs, 267 nm laser pulses is used for optical gating. These 267 nm laser pulses are derived from a hollow-core fiber setup described elsewhere [15].

The 200 nm output of the filamentation process is summarized in Figure 8.2. Similar laser spectra are generated in argon and air; however, the pulse energy is 30% larger in argon than it is in air near 760 Torr. The spectral widths increase slightly with pressure between 380 Torr and 1140 Torr. A spectral width of roughly 500 cm^{-1} is measured at 760 Torr, which corresponds to a Fourier transform-limited electric field duration of 42 fs. Notably, this 500 cm^{-1} spectral width is more than two times larger than the widths of the incident 800 nm and 400 nm laser pulses. As mentioned above, one of the primary advantages of using gaseous nonlinear media is that self-phase modulation enables the production of 200 nm pulses that are significantly shorter than those used to drive the nonlinearity.

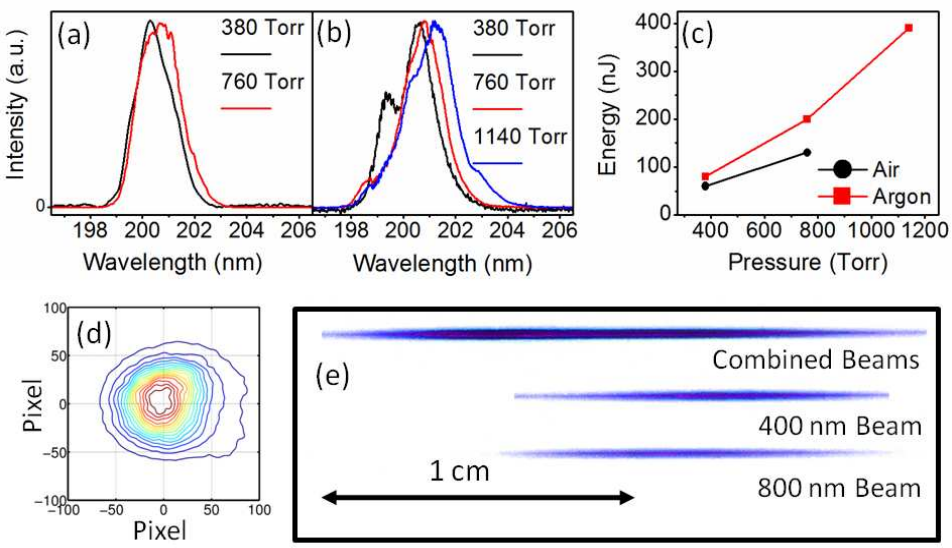

Figure 8.2. (a) Spectra of 200 nm light generated in air and (b) argon at the pressures indicated in the figure legends. (c) Pulse energies measured at 200 nm in air and argon. (d) Spatial profile of 200 nm laser beam derived by processing a photograph with the image utility in Matlab. (e) Photographs of filaments generated with individual 800 nm and 400 nm laser beams are shown below the filament obtained when both beams are overlapped. These filaments were produced in air at atmospheric pressure.

The spatial quality of the laser beam is quite good, although it is slightly elliptical (see Figure 8.2(d)). The width is roughly 7% greater in the vertical dimension than it is in the horizontal dimension. At the exit of the prism compressor, the beam is roughly 1 mm in diameter and it diverges negligibly on the remainder of its 1 meter path to the diffractive optic. Note also that the spatial quality degrades considerably at argon pressures above 1000 Torr. Figure 8.2(e) shows that the filament produced by the overlapped beams is displaced by roughly 5 mm with respect to those generated by the individual beams. The combined filament is also nearly twice as large as those corresponding to the individual beams. Filaments produced by individual laser beams are known to behave similarly with variation in the light intensity [25].

TG spectrograms obtained with three different prism compressor configurations are compared in Figure 8.3. The interval, T, is the delay between the time-coincident 267 nm pulse-pair (i.e., the gate pulses) and the 200 nm pulse. The prism compressor compensates for the ~1160 fs^2 group delay dispersion accumulated in the exit window of the pressurized cell (3 mm CaF_2) and the diffractive optic (1 mm fused silica). In each measurement, the prisms are inserted to minimize the amount of second-order dispersion at 200 nm, whereas the amount of third-order dispersion increases with the prism separation. Third-order dispersion dominates the phase with fused silica prisms separated by 10 cm. Some improvement is observed with a fused silica prism separation of 6.3 cm, but higher-order dispersion is still apparent in the spectrogram. The best result is obtained with CaF_2 prisms, which impart less third-order dispersion than fused silica prisms near 200 nm. While these measurements are useful for evaluating the sensitivity of the pulse width to the type of glass and prism separation, an accurate determination of the pulse duration requires use of a thinner medium. The spectrograms in the top row of Figure 8.3 are temporally broadened by group velocity mismatch (GVM) between the 267 nm and 200 nm pulses, which walk off by approximately 108 fs in the estimated path length of 100 μm.

TG spectrograms measured with 200 nm pulses generated in air and argon are compared in the bottom row of Figure 8.3. In these data, a 50 μm thick BBO is used as the nonlinear medium to suppress effects of GVM. The 267 nm and 200 nm pulses walk off by approximately 43 fs when the electric field polarizations are aligned to the ordinary axis of the crystal. Numerical simulations estimate that the wavelength-integrated temporal width of each spectrogram is broadened by a factor of 1.25 compared

to a hypothetical medium with no GVM. The spectral bandwidth measured in argon is slightly larger (see Figure 8.1); however, the pulses (apparently) cannot be compressed to shorter durations because of higher-order dispersion. As shown in Figure 8.3(f), the pulse durations range from 56-63 fs depending on the pressure and the gas. The time-bandwidth products are near 0.65 if Gaussian pulse envelopes are assumed. Of course, the quality of the compression can be improved by using both gratings and prisms in the compressor [26]. This will be possible if the optics are upgraded for 200 nm light. The present amount of loss in the interferometer prevents the introduction of gratings in the compression scheme.

8.3. Transient grating and photon echo spectroscopies

TG and 2DPE spectroscopies are demonstrated in this section using the experimental setup shown in Figure 8.1. For these measurements, signal detection by spectral interferometry is accomplished using the second 200 nm laser beam produced at the diffractive optic as a reference field [19]. The sample consists of a 100 μm thick jet of adenosine in aqueous solution (OD=0.5) [27]. Adenosine is chosen as a model system because its response to photo-excitation at 267 nm has been characterized in previous work [28]. The present experiments are conducted in a two-color configuration in which light absorption at 267 nm precedes emission at 200 nm. Figure 8.4 shows that the two laser pulses are resonant with separate electronic states. These electronic resonances are primarily localized on the base (not the deoxyribose ring), and thus are also found in the adenine nucleobase.

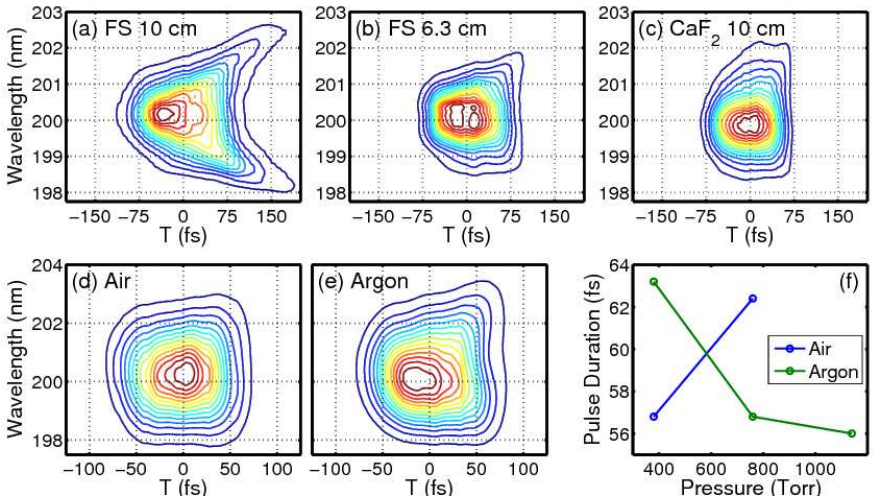

Figure 8.3. (Top Row) TG spectrograms acquired with 20 fs, 267 nm gate pulses in a 250 μm thick fused silica window. Fused silica prisms are separated by (a) 10 cm and (b) 6.3 cm. (c) Calcium fluoride prisms are separated by 10 cm. These 200 nm pulses are generated in air at atmospheric pressure. (Bottom Row) TG spectrograms acquired with 20 fs, 267 nm gate pulses in a 50 μm thick BBO crystal. (d) Measurements conducted with 200 nm pulses generated in (d) air and (e) argon. (f) Pulse durations at 200 nm derived from wavelength-integrated TG signals obtained with a 50 μm thick BBO crystal.

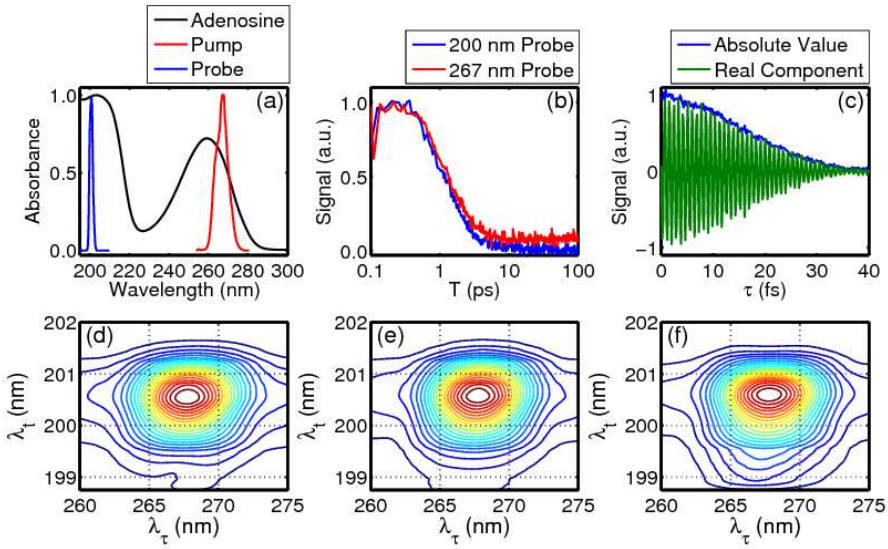

Figure 8.4. Experiments conducted on adenosine in aqueous solution at pH=7. (a) Spectra of laser pulses overlaid on absorbance spectrum of adenosine. (b) Real (absorptive) parts of TG signals acquired with 267 nm pump pulses and either 267 nm (red) or 200 nm (blue) probe pulses. (c) Signal detected at 200 nm plotted with respect to the coherence time, τ. Absolute value of rephasing 2DPE signals acquired at (d) T =250 fs, (e) T =500 fs, and (f) T =1000 fs.

In adenosine, internal conversion between the photo-excited ππ* state and the ground state takes place in less than 500 fs [28]. Several picoseconds are then required for the solute, which is in a "hot" ground state following internal conversion, to transfer more than 4 eV of excess vibrational energy into the surrounding solvent. It has been shown that vibrational cooling governs the decay of the ground state bleach nonlinearity near 267 nm [28]. Because the resonance at 200 nm shares a common ground state, its bleach recovery should report on essentially the same dynamics observed at 267 nm. This prediction is tested by comparing measurements that utilize 267 nm and 200 nm probe pulses in Figure 8.4(b). The similarity in the two transients suggests that the desired nonlinearity is detected (i.e., photo-ionization processes do not dominate the signal), which is consistent with the relatively low 0.3 GW/cm^2 peak power of the 200 nm pulse [15]. The comparable signal qualities found with 267 nm and 200 nm probe pulses indicate similar amounts of noise in the signal phase; the real (absorptive) signal component is plotted, not the absolute value.

2DPE signals are acquired by scanning the delay between the two 267 nm pulses, τ, with sub-cycle steps of 0.16 fs. The signal detected at 200 nm with T=250 fs, which is displayed in Figure 8.4(c), reflects the waveform associated with absorption of 267 nm light. The signal oscillates at the period of the ππ* resonance (~0.9 fs), whereas macroscopic dephasing controls the shape of the decay envelope. The signal is Fourier transformed at each detection wavelength, λ_t (i.e., pixel on CCD detector), to obtain the 2DPE spectra shown in the bottom row of Figure 8.4. These spectra represent the absolute value of the 2DPE rephasing pulse sequence.

In essence, 2DPE spectra correlate absorption and emission frequencies as a function of the delay between these two events, T. The signals reported here reflect correlations between two different electronic resonances. That is, the solute evolves in coherences between different pairs of electronic states during the delays, τ and t. Correlations in τ and t can generally be exposed when the laser bandwidth is greater than the homogeneous line widths of the electronic resonances in the solute [29]. It is not necessary for the bandwidth to exceed the total absorbance line width, which is generally dominated by macroscopic (inhomogeneous) dephasing in a room temperature liquid. Thus, the present 500 cm^{-1} bandwidth at 200 nm should be sufficient for resolving some dephasing processes in aqueous solutions. Solutes in non-polar solvents may also be well-suited for measurements at 200 nm because their line widths are generally narrower.

A preliminary inspection of the 2DPE signals in Figure 8.4 suggests that the line shape changes fairly little with T, which is consistent with earlier 267 nm, one-color experiments at ambient temperatures [15-17]. Notably, these spectra are measured at delay times, T, for which the three incoming laser pulses are not overlapped in the sample; 2DPE spectra cannot be reliably measured during pulse overlap because the quasi-instantaneous, off-resonant response of the solution dominates the signal [15,16]. One prominent change observed in the 2DPE spectra with increasing T is an increase in the signal amplitude at λ_t<199.5 nm. These dynamics are tentatively assigned to solute-to-solvent vibrational energy transfer because of the agreement in time scales [28]. Previous studies of vibrational cooling in DNA nucleosides and other systems suggest that the "hot" ground state wavepacket gives rise to a signal component that shifts towards

shorter wavelengths with increasing T [28,30]. This spectroscopic signature of vibrational cooling is consistent with the data.

8.4. Conclusions

The development of TG and 2DPE experiments employing 200 nm laser pulses is motivated by studies of elementary relaxation processes in small molecules and biological systems. In this work, pulse durations near 60 fs have been achieved at 200 nm using filaments produced in both air and argon. Time-resolved spectroscopies in solution involving shorter 200 nm laser pulses have never been reported. As discussed in related work at 267 nm, diffractive optics are useful in these applications because they facilitate sensitive interferometeric signal detection and, in turn, the use of low laser fluence [14,16,31]. The experimental setup is already capable of conducting high-quality TG experiments with sub-100 fs time resolution. Thus, studies of a wide range of photochemical processes in small molecules are now possible.

For 2DPE spectroscopies at 200 nm, it will be important to increase the laser bandwidth and implement more robust methods of dispersion management. A previous study shows that broader bandwidths can be obtained with shorter incoming 800 nm and 400 nm laser pulses [22]. It is envisioned that compression to the desired 10-20 fs pulse durations will be possible with greater laser fluences because a compressor based on both gratings and prisms can then be employed [26]. In this setup, the available laser fluence can be increased by a factor of 15 if the present aluminum-coated mirrors are replaced with dielectric-coated mirrors. If necessary, it is also possible to increase the amount of laser power used to generate the 200 nm pulses.

8.5. References

(1) Jonas, D. M. *Annu. Rev. Phys. Chem.* **2003**, *54*, 425-463.

(2) Ogilvie, J. P.; Kubarych, K. J. *Adv. At. Mol. Opt. Phys.* **2009**, *57*, 249-321.

(3) Hamm, P.; Zanni, M. T. *Concepts and Methods of 2D Infrared Spectroscopy*; Cambridge University Press: Cambridge, 2011.

(4) Engel, G. S.; Calhoun, T. R.; Read, E. L.; Ahn, T. K.; Mancal, T.; Cheng, Y. C.; Blankenship, R. E.; Fleming, G. R. *Nature* **2007**, *446*, 782-786.

(5) Fayer, M. D. *Annu. Rev. Phys. Chem.* **2009**, *60*, 21-38.

(6) Collini, E.; Wong, C. Y.; Wilk, K. E.; Curmi, P. M. G.; Brumer, P.; Scholes, G. D. *Nature* **2010**, *463*, 644-647.

(7) Nicodemus, R. A.; Ramasesha, K.; Roberts, S. T.; Tokmakoff, A. *J. Phys. Chem. Lett.* **2010**, *1*, 1068-1072.

(8) Sperling, J.; Nemeth, A.; Hauer, J.; Abramavicius, D.; Mukamel, S.; Kauffmann, H. F.; Milota, F. *J. Phys. Chem. A* **2010**, *114*, 8179-8189.

(9) Panitchayangkoon, G.; Hayes, D.; Fransted, K. A.; Caram, J. R.; Harel, E.; Wen, J.; Blankenship, R. E.; Engel, G. S. *Proc. Natl. Acad. Sci.* **2010**, *107*, 12766-12770.

(10) Lott, G. A.; Perdomo-Ortiz, A.; Utterback, J. K.; Widom, J. R.; Aspuru-Guzik, A.; Marcus, A. H. *Proc. Natl. Acad. Sci.* **2011**, *108*, 16521-16526.

(11) Abramavicius, D.; Jiang, J.; Bulheller, B. M.; Hirst, J. D.; Mukamel, S. *J. Am. Chem. Soc.* **2010**, *132*, 7769-7775.

(12) Cannizzo, A. *Phys. Chem. Chem. Phys.* **2012**, *14*, 11205-11223.

(13) Tseng, C.-H.; Matsika, S.; Weinacht, T. C. *Opt. Express* **2009**, *17*, 18788-18793.

(14) Selig, U.; Schleussner, C.-F.; Foerster, M.; Langhojer, F.; Nuernberger, P.; Brixner, T. *Opt. Lett.* **2010**, *35*, 4178-4180.

(15) West, B. A.; Womick, J. M.; Moran, A. M. *J. Phys. Chem. A* **2011**, *115*, 8630-8637.

(16) West, B. A.; Moran, A. M. *J. Phys. Chem. Lett.* **2012**, *3*, 2575-2581.

(17) Tseng, C.-H.; Sándor, P.; Kotur, M.; Weinacht, T. C.; Matsika, S. *J. Phys. Chem. A* **2012**, *116*, 2654-2661.

(18) Auböck, G.; Consani, C.; van Mourik, F.; Chergui, M. *Opt. Lett.* **2012**, *37*, 2337-2339.

(19) Goodno, G. D.; Dadusc, G.; Miller, R. J. D. *J. Opt. Soc. Am. B* **1998**, *15*, 1791-1794.

(20) Durfee, C. G.; Misoguti, L.; Backus, S.; Kapteyn, H. C.; Murnane, M. M. *J. Opt. Soc. Am. B* **2002**, *19*, 822-831.

(21) Jailaubekov, A. E.; Bradforth, S. E. *Appl. Phys. Lett.* **2005**, *87*, 021107.

(22) Fuji, T.; Horio, T.; Suzuki, T. *Opt. Lett.* **2007**, *32*, 2481-2483.

(23) Fuji, T.; Suzuki, T.; Serebryannikov, E. E.; Zheltikov, A. *Phys. Rev. A* **2009**, *80*, 063822.

(24) Smith, A. V.; AS-Photonics: Albuquerque, NM, http://www.as-photonics.com/snlo.

(25) Aközbek, N.; Becker, A.; Chin, S. L. *Laser Phys.* **2005**, *15*, 607-615.

(26) Fork, R. L.; Cruz, C. H. B.; Becker, P. C.; Shank, C. V. *Opt. Lett.* **1987**, *12*, 483-485.

(27) Tauber, M. J.; Mathies, R. A.; Chen, X.; Bradforth, S. E. *Rev. Sci. Instrum.* **2003**, *74*, 4958-4960.

(28) Pecourt, J.-M. L.; Peon, J.; Kohler, B. *J. Am. Chem. Soc.* **2001**, *123*, 10370-10378.

(29) Mukamel, S. *Principles of Nonlinear Optical Spectroscopy*; Oxford University Press: New York, 1995.

(30) Kovalenko, S. A.; Schanz, R.; Hennig, H.; Ernsting, N. P. *J. Chem. Phys.* **2001**, *115*, 3256-3273.

(31) West, B. A.; Womick, J. M.; Moran, A. M. *J. Chem. Phys.* **2011**, *135*, 114505:1-114505:9.

Chapter 9 . Concluding Remarks

Numerous processes in nature and technology depend intimately on the dynamics of excited electronic states in molecules. Examples include photosynthesis, DNA photoprotection, and power conversion in photovoltaic cells. The energy imparted by photon absorption can drive chemical reactions which store the energy in chemical bonds, initiate chemical reactions, or dissipate the energy as heat in vibrational motions. Non-radiative relaxation processes span a broad range of time scales in different systems. On the femtosecond time scale, these processes compete with even the fastest molecular motions. Conical intersections, which were discussed in Section 1.2, promote extremely fast internal conversion transitions between electronic states. Conical intersection are ubiquitous in natural systems; they provide photo stability to DNA[1,2] as well as drive crucial reactions for human life such as the creation of Vitamin D in the skin[3]. Understanding physics surrounding conical intersection dynamics requires sensitive spectroscopic techniques with cutting edge time resolution.[4,5]

The past decade has seen tremendous growth in optical analogues of NMR spectroscopy. In particular, two-dimensional (2D) spectroscopy, which employs a spin echo-like pulse sequence, has yielded transformative insights into processes ranging from energy transfer in photosynthesis to bond making and breaking in liquids. The success of these experiments has inspired predictions that they will one day be extended to the X-ray regime of the electromagnetic spectrum.[6] However, at the time that the research in

this thesis was initiated, the visible wavelength regime represented the high frequency limit at which experiments had been conducted.[7] By combining 2D spectroscopy techniques with specialized deep UV laser pulse generation techniques, this dissertation presented experiments conducted in the ultraviolet regime with the best time resolution and signal-to-noise ratios to date. Technical challenges including suppressing sample photoionization, generating ample laser bandwidths, and dispersion management all had to be overcome. These were discussed in detail in the previous chapters.

Adenine nucleobases were interrogated at room temperature in the first applications described in Chapter 4. These proof-of-principle experiments established the viability of the technique at 267nm and set the stage for the measurements at cryogenic temperatures presented in Chapter 5. Here, it was found that the thymine nucleobase transfers vibrational energy into the solvent at a rate at is insensitive to the temperature of the equilibrium system. Additional measurements showed that this is a ubiquitous property of the nucleobases. In Chapter 6, the lessons learned from these studies were then applied to understand the interplay of excited state deactivation and intramolecular vibrational energy transfer in a family of molecules chosen to uncover the impact of bonding to the DNA backbone. This study was motivated by previous work which found that a majority of excitations in a model double helix with a realistic base sequence returned to their ground state with the same dynamics as an isolated nucleobase.[8]

Chapter 7 presented a study of ring opening reactions in which alpha-terpinine was investigated using a newly upgraded experimental setup which was discussed in Chapter 3 and also in Chapter 7. Here, dynamics on the sub-100fs time scale were

uncovered for the first time in solution. It was found that, upon photo-excitation, specific vibrational modes in the ring opening systems are set in coherent motion. Displacement along these same Franck-Condon active coordinates is associated with passage through the conical intersections involving out of plane twisting motion of the carbon double bonds (Figure 9.1). These vibrational motions manifest as weak oscillations in the experimental data in both alpha-terpinine and CHD , thereby underscoring the value of the extremely sensitive interferometric detection employed in this work.

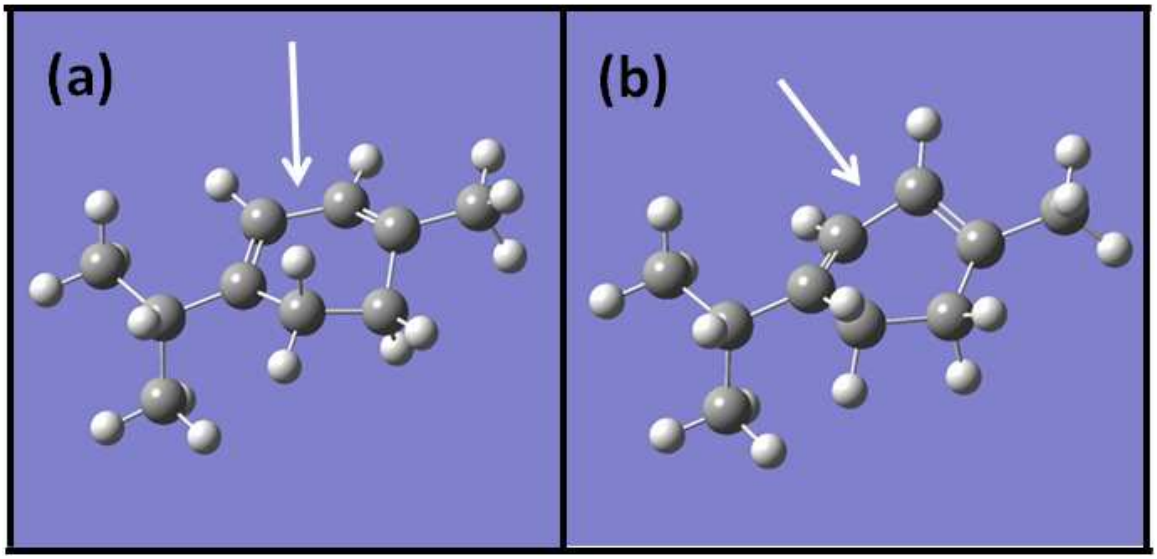

Figure 9.1. Gaussian simulation of the vibrational mode set in motion by UV photon excitation. Shown are the two turning points of the oscillation. Note the strong displacement about twisting of the carbon double bonds comparing (a) to (b). This is the coordinate thought to be most important for passage through the conical intersection in these ring opening systems.

Results obtained for the ring-opening systems hold implications for the coherent control approaches discussed in Section 1.5. Twisting of the carbon double bonds is an important parameter in the conical intersection of states 1B/2A and state 2A/ground (Figure 9.1). The trajectory of the wavepacket at the excited/ground state conical

intersection primarily determines the outcome of the photochemical reaction. If coherence along this displaced mode is maintained through the sequence of internal conversion transitions, then one could potentially control the outcome of the reaction by altering the force field at the Frank-Condon geometry. This idea is illustrated in Figure 9.2. Experiments and models are now under development to test this hypothesis. Such a discovery would have profound impact in the field of quantum control.

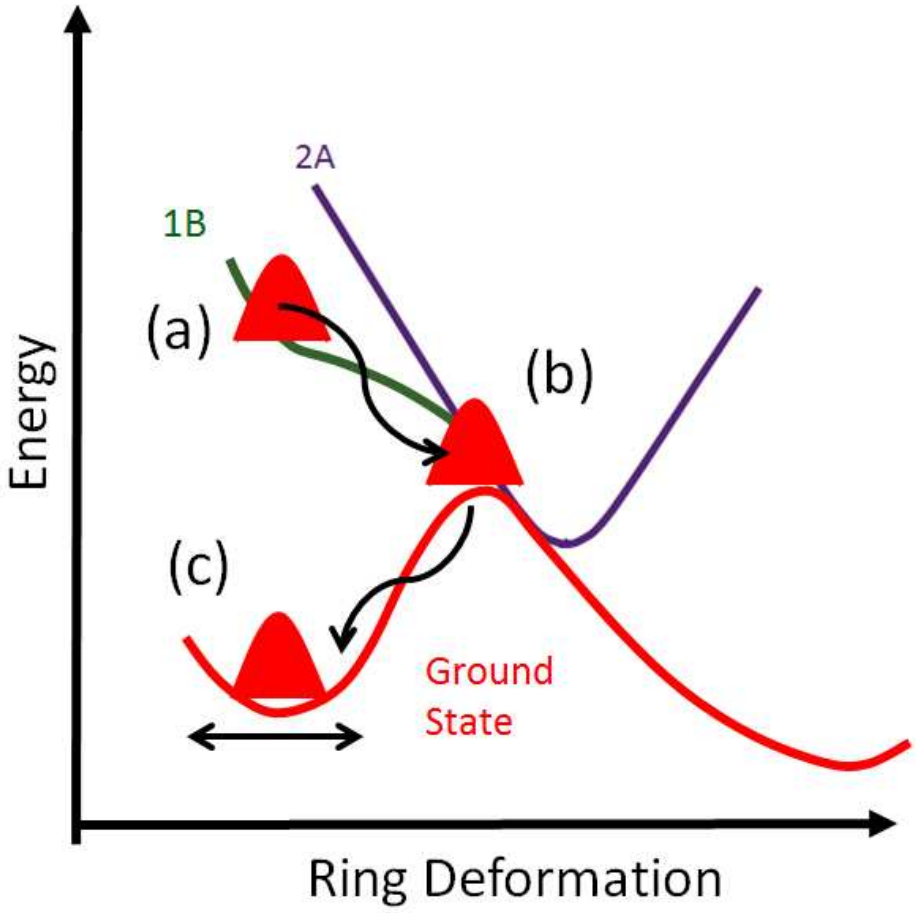

Figure 9.2. (a) Photo excitation places the wavepacket of the ring opening molecules on excited state 1B, setting in motion twisting about carbon double bonds. (b) Transitions between energy states occur impulsively compared to period of wavepacket oscillation. (c) Once the wavepacket returns to the ground state, coherent motion about the ring deformation/twisting motion persists.

As mentioned in the opening chapter, the end goal of extending these spectroscopies to shorter wavelength is attaining the ability to perturb molecules by photo-ionizing core electrons and subsequently monitoring their relaxation, thereby observing the timescale of electron motion. There is a group of researchers in the attosecond physics field who are interested in observing these phenomena.[9] Motions of valence electrons have been predicted to occur on the femtosecond time scale;[10] however current research has focused efforts on producing X-ray laser pulses to achieve this goal. In this regime, the techniques leveraged in the visible and UV to control laser pulses for time resolved measurements are ineffective and new strategies are necessary.

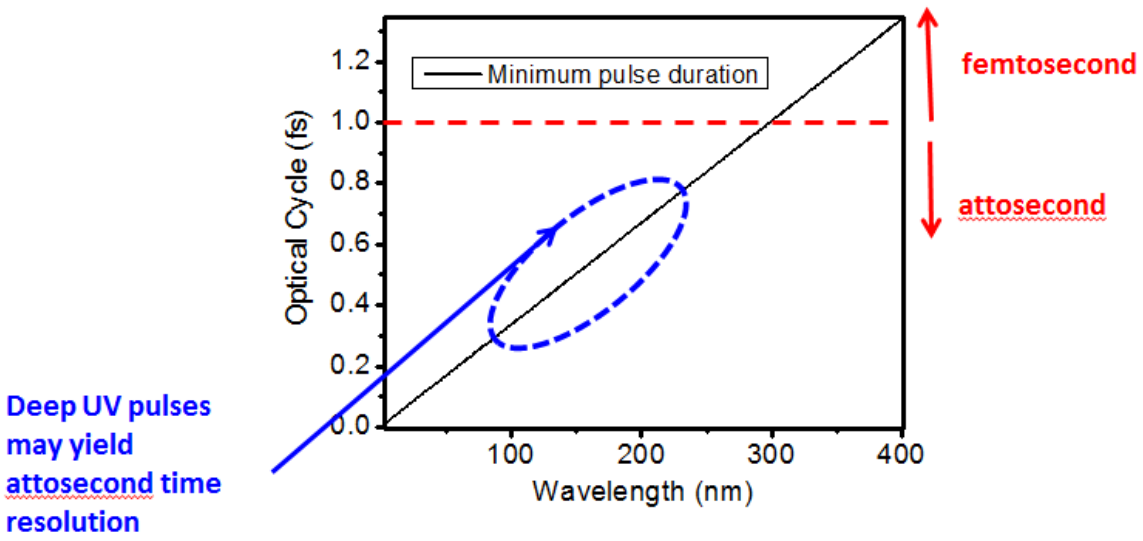

Figure 9.3. The optical cycle as a function of the laser pulse wavelength represents the shortest pulses that can be obtained. Attosecond laser pulses could potentially be achieved in the 100-200nm range where current techniques could be used.

In principle, one need not go to the X-ray regime to produce an attosecond laser pulse because the time duration of a laser pulse is ultimately limited by the duration of the optical cycle of the electric field. For a 267nm laser pulse this is 0.9fs. It is noted that adequate time resolution to excite and probe electron wavepacket motion in a

molecule could be achieved with laser pulses in the 100-200 nm (XUV) range as shown in Figure 9.3. In this regime, techniques employed to generate pulses at 200nm and 267nm can potentially be applied to yield ultrashort laser pulses with the sub-fs durations. The two-color filamentation approach demonstrated in Chapter 8 represents a step towards this goal. It is envisioned that the technical contributions presented in this dissertation will be leveraged to carry out the first attosecond studies of valence electronic wavepackets in molecules.

9.1 References

(1) Kohler, B. *The Journal of Physical Chemistry Letters* **2010**, *1*, 2047-2053.

(2) Middleton, C. T.; de La Harpe, K.; Su, C.; Law, Y. K.; Crespo-Hernández, C. E.; Kohler, B. *Annu. Rev. Phys. Chem.* **2009**, *60*, 217-239.

(3) Tang, K.-C.; Rury, A.; Orozco, M. B.; Egendorf, J.; Spears, K. G.; Sension, R. J. *The Journal of Chemical Physics*, *134*, 104503-13.

(4) Deb, S.; Weber, P. M. *Annu. Rev. Phys. Chem.* **2011**, *62*, 19-39.

(5) Arruda, B.; Smith, B.; Spears, K.; Sension, R. *Faraday Discussions* **2012**, *12*.

(6) Mukamel, S.; Abramavicius, D.; Yang, L.; Zhuang, W.; Schweigert, I. V.; Voronine, D. V. *Acc. Chem. Res.* **2009**, *42*, 553-562.

(7) Ogilvie, J. P.; Kubarych, K. J. *Adv. At. Mol. Opt. Phys.* **2009**, *57*, 249-321.

(8) de La Harpe, K.; Kohler, B. *The Journal of Physical Chemistry Letters* **2011**, *2*, 133-138.

(9) Corkum, P. B. K., F. *Nature Physics* **2007**, *3*, 381-387.

(10) Remacle, F.; Levine, R. D. *Proceedings of the National Academy of Sciences of the United States of America* **2006**, *103*, 6793-6798.

Appendix 1 . Supporting Information for Chapter 4: "Probing Ultrafast Dynamics in Adenine With Mid-UV Four-Wave Mixing Spectroscopies"

A1.1. Influence of Peak Power on TG Signal Profiles

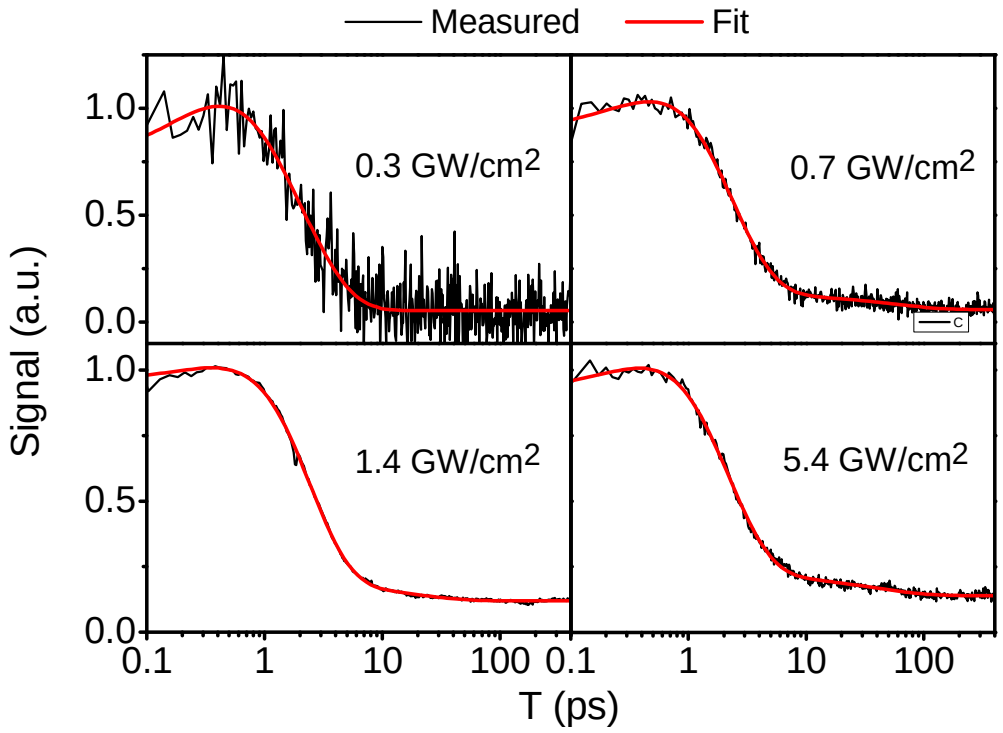

Figure A1.1. Real (absorptive) part of TG signals measured for adenine at the peak powers indicated in the respective panels. Fitting parameters are given in Table 1 of the main paper. The fluence is 4.65×10^{13} photons/cm^2 at 1.4GW/cm^2, which results in excitation of 0.4% of the molecules in the focal volume.

A1.2. Optical Densities and the Correction of Propagation Effects

The photon echo spectra reported in this work are corrected for propagation effects using the theory developed by Jonas and co-workers.[1,2] The key equations are summarized in this Appendix. The quantity measured in diffractive optic-based experiment, where the reference field propagates through the sample, is defined as $\hat{S}^{-}_{2D}(\omega_t,\omega_\tau;T)$ in Reference [2]. Propagation effects on the two-dimensional photon echo spectrum are corrected using

$$\hat{S}_{2D}^{++}(\omega_t,\omega_\tau;T) \approx \frac{\hat{S}_{2D}^{-}(\omega_t,\omega_\tau;T)}{\left|\hat{\varepsilon}_d^0(\omega_t)\right|} \frac{2\omega_\tau \kappa(\omega_\tau) l/c}{1-\exp\left[-2\omega_\tau \kappa(\omega_\tau) l/c\right]} \exp\left[2\omega_t \kappa(\omega_t) l/c\right] \tag{A1.1}$$

Where

$$l = \frac{L}{\sqrt{1-\sin^2\alpha-\sin^2\beta}} \tag{A1.2}$$

$$\kappa(\omega) = \frac{\ln(10)}{4\pi}\frac{\lambda}{L}\mathrm{OD}(\omega) \tag{A1.3}$$

Equations (21), (24), and (25) in Reference [2] have been combined to obtain Equation (A1.1). Here α and β are the half angles between the beams are (2.25°) and $\mathrm{OD}(\omega)$ is the frequency dependent optical density of the sample.

ODs >0.5 are needed to obtain acceptable signal to noise ratios in the experiments, which employ a sample cell with a 0.5mm path length. Signal detection in the setup is additionally challenged by the low UV quantum efficiency of the CCD and the lack of a UV anti-reflection coating in front of the array. Compared to systems in which the absorbance spectra possess features narrow than the laser bandwidth (e.g., molecular aggregates),[3] the use of large ODs is less problematic for adenine because the absorbance changes little (<20%) within the bandwidth of the laser spectrum (cf., Figure 4.1b). Therefore, the laser pulse maintains its spectrum as it propagates in the solution. Figure A1.2 shows that $\hat{S}_{2D}^{-}(\omega_t,\omega_\tau;T)/\left|\hat{\varepsilon}_d^0(\omega_t)\right|$ and $\hat{S}_{2D}^{++}(\omega_t,\omega_\tau;T)$ are nearly indistinguishable up to ODs of 1.0. Signals measured with OD=0.5 and OD=0.75 possess essentially the same line shapes, whereas the appearance of the spectrum undergoes noticeable changes at OD=1.0. OD dependent effects on photon echo line shapes exceeding 10% of the maximum signal strength are not observed when the OD $\leq$ 0.75.

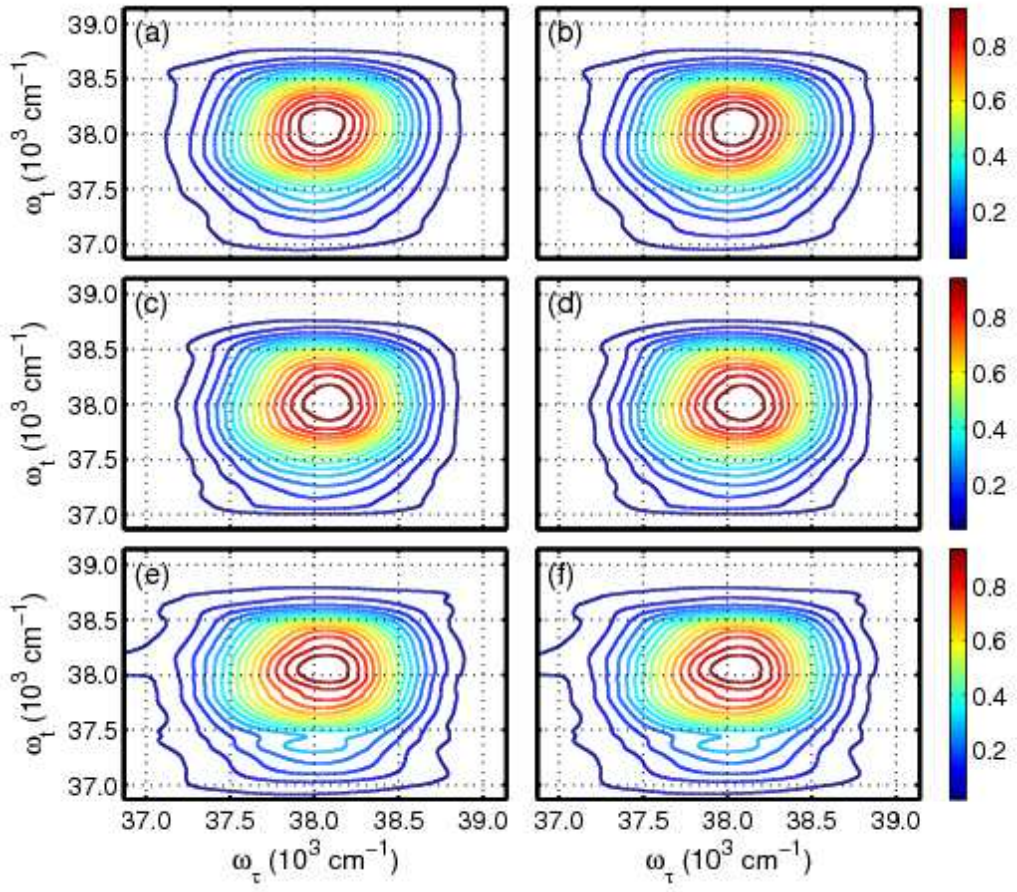

Figure A1.2. Real part of photon echo spectra measured for adenine in a 0.5mm cuvette at T =0.5ps with optical densities (OD) of: (a)-(b) 0.5; (c)-(d) 0.75; (e)-(f) 1.0. Directly measured spectra, $\hat{S}^{-}_{2D}(\omega_t,\omega_\tau;T)/\left|\hat{\varepsilon}^{0}_{d}(\omega_t)\right|$, are presented in the left column. Spectra in the right column, $\hat{S}^{++}_{2D}(\omega_t,\omega_\tau;T)$, are corrected for propagating effects using Equation (S3). ODs >0.5 must be employed to obtain adequate signal strength. As seen in panels (e) and (f), distortions in the spectra are found at ODs near 1.0. Photon echo experiments are therefore performed with ODs<0.75. Application of Equation (S3) has little effect on the spectra because the absorption line widths are broad compared to the laser pulse width (cf., Figure 4.1b).

A1.3. References

(1) Belabas, N.; Jonas, D. M. *J. Opt. Soc. Am. B* **2005**, *22*, 655-674.

(2) Yetzbacher, M. K.; Belabas, N.; Kitney, K. A.; Jonas, D. M. *J. Chem. Phys.* **2007**, *126*, 044511/1-044511/19.

(3) Womick, J. M.; Miller, S. A.; Moran, A. M. *J. Phys. Chem. A* **2009**, *113*, 6587-6598.

Appendix 2 . Supplemental Information for Chapter 4: "Influence of Temperature on Thymine-to-Solvent Vibrational Energy Transfer"

A2.1. Photon Echo Spectra

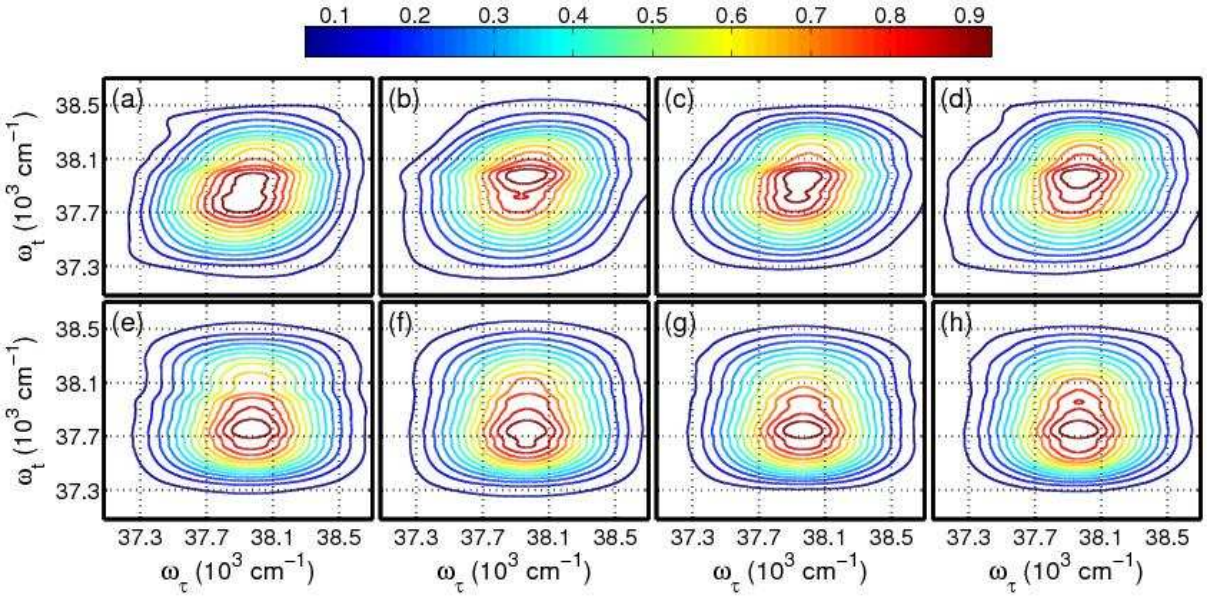

Figure A2.1. Absorptive parts of photon echo spectra acquired at the following delay times: (a),(e) T =0.15ps; (b),(f) T =0.20ps; (c),(g) T =0.60ps; (d),(h) T =3.00ps. Spectra shown in the top and bottom rows correspond to measurements conducted at 100K and 300K, respectively. The amplitude of each spectrum is normalized to 1. The response of the solvent medium prevents the measurement of spectra at T <0.1ps (cf., Figure A2.3).

A2.2. Relaxation Kinetics in Adenine

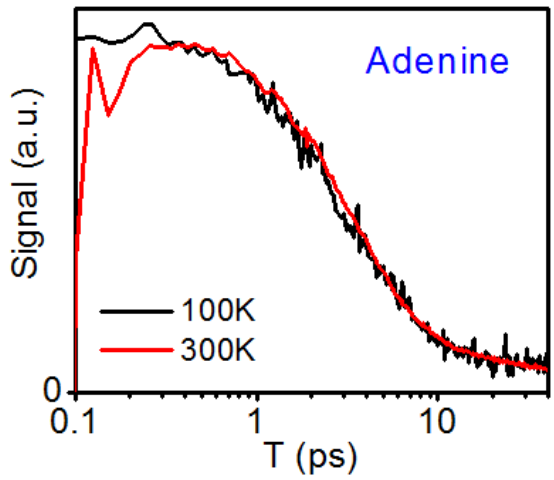

Figure A2.2. Absorptive part of transient grating signal field measured for adenine at 100K (black) and 300K (red). The experiments are conducted with 25fs, 38000cm^{-1} laser pulses under the magic angle polarization condition. These data suggest that the rate of vibrational cooling may be insensitive to temperature for a wide variety of hydrogen bonding solutes and solvents.

A2.3. Model Calculations

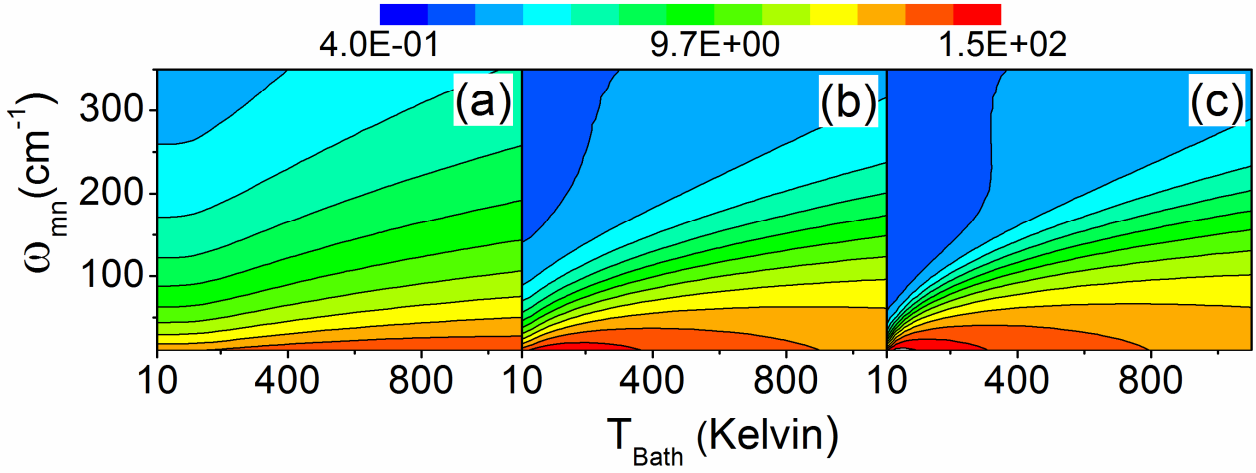

Figure A2.3. $\Phi(\omega_{mn};T_{Bath})$ is computed at (a) Λ^{-1}=0.1ps, (b) Λ^{-1}=1.0ps, (c) Λ^{-1}=10ps. with the parameters are given in Table 2 of the main paper. $\Phi(\omega_{mn};T_{Bath})$ is plotted on a logarithmic scale (base 10) in all three panels.

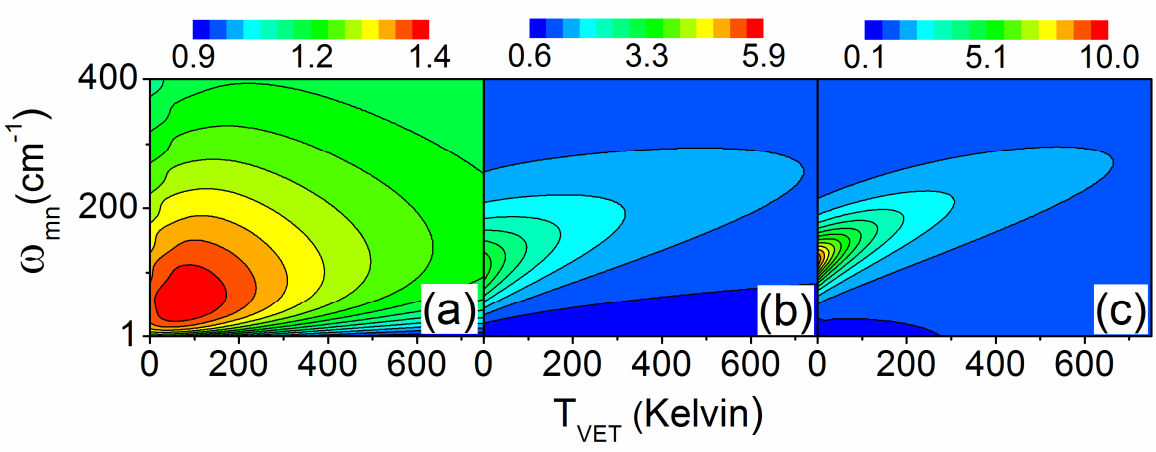

Figure A2.4. $\eta(\omega_{mn};T_{VET})$ is computed at (a) Λ^{-1}=0.1ps, (b) Λ^{-1}=1.0ps, (c) Λ^{-1}=10ps with the parameters given in Table 2 of the main paper. These calculations predict that the TG experiments should find a significant enhancement in the rate of vibrational cooling (at 300K versus 100K) provided that: (i) the time scale of the solvent, Λ^{-1}, is much greater 0.1ps; (ii) the VC induced increase in the temperature of the bath, T_{VET}, is less than 300K. These same calculations are plotted on a common linear scale in Figure 5.7.

A2.4. Estimating the Physically Reasonable Range of T_{VET}

This Section discusses the physically reasonable range of the temperature increase in the solvent environment (i.e., bath) caused by VC in thymine, T_{VET}. First, it is suggested that it is useful to consider thymine in the context of Ernsting's careful and thorough study of relaxation dynamics in p-nitroaniline (PNA) because of the similar molecular structures and relaxation time scales found in these two systems.[1] Using a phenomenological model, it was estimated that VC of PNA in aqueous solution caused the temperature of the bath to increase by 100K within the first 1-2ps after excitation.[1] Thymine releases a larger amount of energy (~4eV) into the solvent environment than does PNA (~3eV) because of its higher electronic resonance frequency. The smaller heat capacity of the methanol/water mixture (~15 meV nm^{-3} K^{-1} at 25°C) should also be taken into account (the heat capacity of water is ~26 meV nm^{-3} K^{-1} at 25°C). Multiplying the

temperature increase of 100K found in PNA by products of ratios in these two quantities (i.e., 4/3 × 26/15) yields a temperature increase of 230K corresponding to the environment of thymine.

It is also useful to consider the volume of the solvent associated with particular temperature increases. Assuming that thymine releases 4eV into the surrounding methanol/water mixture, a temperature increase of 100K is computed for a volume of 2.66nm^3 (i.e., sphere with radius of 0.86nm) using the heat capacity of the solution (~15 meV nm^{-3} K^{-1} at 25°C). Using the same procedure, temperature increases of 200K and 300K are associated with volumes of 1.4nm^3 and 0.9nm^3 (i.e., spheres with radii of 0.69nm and 0.6nm). Temperature increases, $T_{VET} \geq 200$K, appear physically unreasonable given the small "effective" volume of the environment that must be assumed. In this work, it is suggested the conservative upper limit of T_{VET} =250K and examine the full reasonable range of this parameter.

A2.5. Coordinate Dependence of the Solute-Solvent Interaction Operator

Weak coordinate dependence of the solute-solvent interaction operator, $\hat{V}$, was invoked in writing Equation (3) in Chapter 4. Here the implications of this weak coordinate dependence are examined more closely. The matrix element is expanded in a Taylor series

$$V_{mn} = \left\langle m \middle| V_{el}\left(R_0\right) + \left(\frac{dV_{el}}{dR}\right)_0 R + \cdots \middle| n \right\rangle \qquad \text{(A2.1)}$$

where V_{el} denotes implicit integration over electronic degrees of freedom and R is the harmonic oscillator coordinate of the solute. The leading non-zero term is linear in R because all matrix elements involving the first (constant) term, $V_{el}\left(R_0\right)$, vanish when

$m \neq n$. Under the assumption of weak coordinate dependence, truncation of the expansion at the term linear in R leads to a restriction wherein the number of vibrational quanta in the harmonic oscillator can change only by 1 in the VC transition. This restriction parallels selection rules known in infrared vibrational spectroscopy.[2,3]

A2.6. References

(1) Kovalenko, S. A.; Schanz, R.; Hennig, H.; Ernsting, N. P. *J. Chem. Phys.* **2001**, *115*, 3256-3273.

(2) McHale, J. *Molecular Spectroscopy*; Prentice Hall: Upper Saddle Creek River, NJ, 1999.

(3) Parson, W. W. *Modern Optical Spectroscopy*; Springer-Verlag: Berlin, 2007.

Appendix 3 . Supporting Information for Chapter 6: "Interplay Between Vibrational Energy Transfer and Excited State Deactivation in DNA Components"

A3.1. Fitting Parameters for Transient Grating and Fluorescence-Downconversion Signals in the Thymine Family of Systems

This Section presents all fitting parameters for transient grating (TG) and time-resolved fluorescence down-conversion (TRF) signals obtained in the thymine family of systems. Signals and fits are shown in the main text.

Table A3.1. TG Fitting Parameters at 100K

[(a),(b)]Parameter	Thymine	Thymidine	Thymine Dinucleotide
A_0	0.12±0.03	0.25±0.04	0.07±0.02
A_1	-0.96±0.08	-1.07±0.10	-0.93±0.12
τ_1 (ps)	0.25±0.03	0.23±0.03	0.15±0.03
A_2	1.00±0.08	1.00±0.09	1.00±0.10
τ_2 (ps)	5.23±0.4	4.63±0.36	5.16±0.40

[(a)]Fit to Equation $S(T) = A_0 + \sum_{i=1}^{2} A_i \exp(-T/\tau_i)$.

[(b)]Ranges in the parameters correspond to twice the standard errors.

Table A3.2. TG Fitting Parameters at 166K

[a],[b]Parameter	Thymine	Thymidine	Thymine Dinucleotide
A_0	0.07±0.01	0.23±0.02	0.21±0.05
A_1	-0.55±0.05	-0.74±0.10	-0.57±0.07
τ_1 (ps)	0.56±0.09	0.15±0.03	0.60±0.16
A_2	1.00±0.08	1.00±0.04	1.00±0.09
τ_2 (ps)	4.91±0.40	4.07±0.28	4.12±0.33

[a]Fit to Equation $S(T) = A_0 + \sum_{i=1}^{2} A_i \exp(-T/\tau_i)$.

[b]Ranges in the parameters correspond to twice the standard errors.

Table A3.3. TG Fitting Parameters at 233K

[a],[b]Parameter	Thymine	Thymidine	Thymine Dinucleotide
A_0	0.10±0.01	0.37±0.01	0.32±0.02
A_1	-0.82±0.20	-0.71±0.14	-0.31±0.08
τ_1 (ps)	0.20±0.07	0.22±0.05	0.26±0.10
A_2	1.00±0.04	1.00±0.05	1.00±0.06
τ_2 (ps)	5.07±0.35	3.47±0.24	3.67±0.28

[a]Fit to Equation $S(T) = A_0 + \sum_{i=1}^{2} A_i \exp(-T/\tau_i)$.

[b]Ranges in the parameters correspond to twice the standard errors.

Table A3.4. TG Fitting Parameters at 300K

[a],[b]Parameter	Thymine	Thymidine	Thymine Dinucleotide
A_0	0.20±0.03	0.25±0.03	0.27±0.04
A_1	-0.96±0.08	-1.07±0.07	-1.29±0.15
τ_1 (ps)	0.25±0.03	0.23±0.03	0.15±0.02
A_2	1.00±0.07	1.00±0.06	1.00±0.09
τ_2 (ps)	5.08±0.32	3.3±0.3	2.64±0.3

[a]Fit to Equation $S(T) = A_0 + \sum_{i=1}^{2} A_i \exp(-T/\tau_i)$.

[b]Ranges in the parameters correspond to twice the standard errors.

Table A3.5. TRF Fitting Parameters at 300K

[a]Parameter	Thymine	Thymidine	Thymine Dinucleotide
A_0	----------	----------	----------
A_1	1.00±0.03	1.00±0.04	1.00±0.04
τ_1 (ps)	0.60±0.20	0.82±0.25	1.20±0.36

[a]Ranges in the parameters correspond to twice the standard errors.

A3.2. Ruling Out Contributions from Delocalized Electronic Excitations in the Thymine Dinucleotide

The analysis assumes that the electronic structures of the two individual bases in the thymine dinucleotide are negligibly perturbed by the linkage. The measurements in this section support this view of the electronic structure. First, Figure A3.3a shows that the absorbance spectra of thymine, thymidine, and the thymine dinucleotide are fairly

similar. Moreover, the spectra for thymidine and the dinucleotide are nearly indistinguishable. Differences in the spectra for these three systems are ascribed to the effects that the substituents have on the local solvent environments. There is no sign of Frenkel exciton electronic structure in the dinucleotide (e.g., no Davydov splitting).

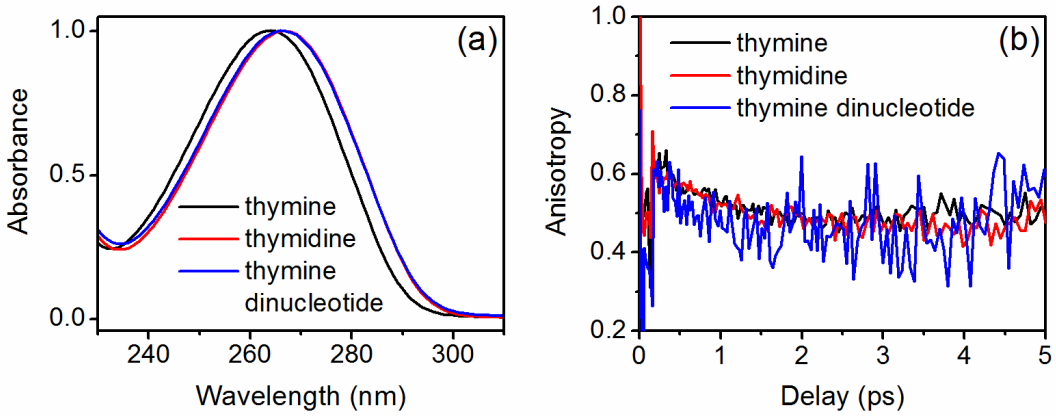

Figure A3.1. (a) Linear absorbance spectra of thymine (black), thymidine (red), and the thymidine dinucleotide (blue) in an 85:15 mixture of methanol:water. (b) Transient absorption anisotropies of the three systems measured with 25fs laser pulses centered at 265nm. These measurements suggest that the ππ* excitations of the thymidine dinucleotide are localized to the individual units.

The transient absorption anisotropy measurements shown in Figure A3.3b impose strong constraints on the view of excited state electronic structure. The initial values of the anisotropies are experimentally indistinguishable in the three systems, which suggests strong similarities in the nature of the electronic states involved in the optical response. The fact that the initial value of the anisotropy exceeds 0.4 (i.e., the expectation for a two-level system) indicates that excited state absorption nonlinearities contribute to the signals. Moreover, it is suggested that the anisotropy changes little in the first 5 ps after excitation because long-lived excited states (possibly ^{1}nπ* or ^{3}ππ* states) are formed in addition to the short-lived excitations that are the primary emphasis of this work. The presence of multiple relaxation channels in thymine was established in earlier work.[1] For

illustration, consider a four-level system in Figure A4.4 (i.e., the minimum number of levels needed to explain the optical response). The initial value of the anisotropy depends on the two transition dipole magnitudes, μ_{ca} and μ_{db}, and the angle between the two dipoles, $\theta_{ca,db}$. Here μ_{ca} connects the ground state to the ππ* state, whereas μ_{db} connects a long-lived dark state (dark in the linear absorbance), perhaps the ^{1}nπ* or ^{3}ππ* states, to a higher lying excited state. The following equations incorporate only the ground state bleach and excited state absorption nonlinearities. The excited state emission response can be neglected at 265nm after 100-200fs because nuclear relaxation shifts this nonlinearity of the spectral region to which the experiment is sensitive. The signal components associated with parallel and perpendicular pump and probe polarizations are given by[2]

$$S_{\parallel} = \frac{1}{15}\left\{6\mu_{ca}^4 - \left[2 + 4\cos^2\left(\theta_{ca,db}\right)\right]\mu_{ca}^2\mu_{db}^2\right\} \tag{A3.1}$$

$$S_{\perp} = \frac{1}{30}\left\{4\mu_{ca}^4 - \left[8 - 4\cos^2\left(\theta_{ca,db}\right)\right]\mu_{ca}^2\mu_{db}^2\right\} \tag{A3.2}$$

The anisotropy is computed using

$$r = \frac{S_{\parallel} - S_{\perp}}{S_{\parallel} + 2S_{\perp}} \tag{A3.3}$$

The key is that delocalized electronic structure in the dinucleotide would give rise to additional terms in the optical response. Such “cross terms” in the ground state bleach nonlinearity of excitonic systems have been discussed elsewhere.[3] The fact that the anisotropies of these systems are experimentally indistinguishable suggests that the dinucleotide does not possess signal components characteristic of delocalized electronic states. Electronic energy transfer between states localized on the two bases in the

dinucleotide is similarly ruled out because this would also cause its anisotropy to differ from those measured in the other two systems.

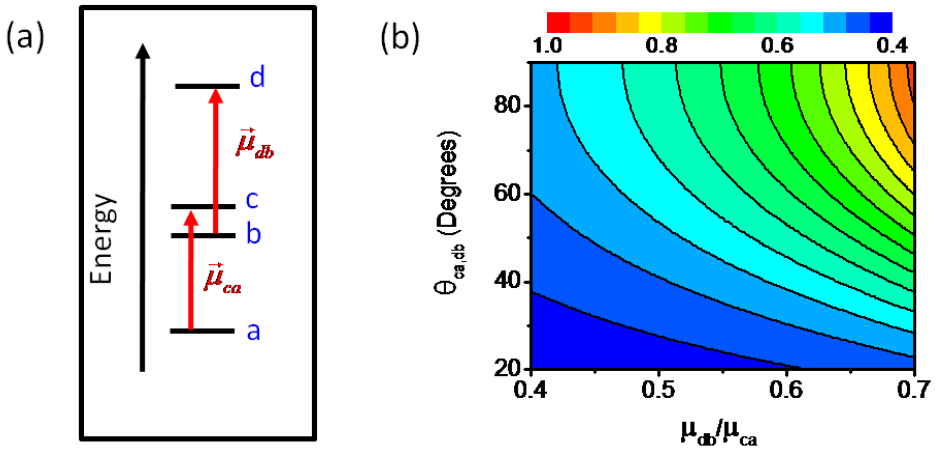

Figure A3.2. Anisotropy computed using Equations (S1)-(S3). This calculation shows that the anisotropies shown in Figure A4.3 can be understood in terms of a simple four-level model with ground state bleach and excited state absorption nonlinearities. Exciton delocalization and energy transfer is ruled out in the dinucleotide because they would lead to additional terms in the optical response function.

A3.3. Examination of 9-methyladenine and adenosine

Dynamics observed in the thymine family of systems appear weakly correlated with the viscosity of the solvent. It is suggested that this absence of correlation reflects negligible coupling between the reaction coordinate and the solvent bath. To explore the generality of this behavior an analogous set of experiments has been conducted on two adenine systems because the geometry of the conical intersection involves significant displacements in many of the heavy atoms (i.e., puckering of the rings).[4] The signals and fits are presented in this section. Excited state lifetimes extracted from these data are shown in Figure 6.9.

As in the thymine family of systems, the vibrational cooling rate for 9-methyladenine and adenosine is taken to be independent of the sample temperature. This

assumption is supported by the insensitivity of the TG time constants for 9-methyladenine to temperature in the 100K to 300K range; this same behavior is exhibited by thymine.[5] With this assumption in hand, the lifetimes can be determined at 100K-233K range using the same kinetic scheme applied to the thymine systems (cf., Equation 16 in main paper).

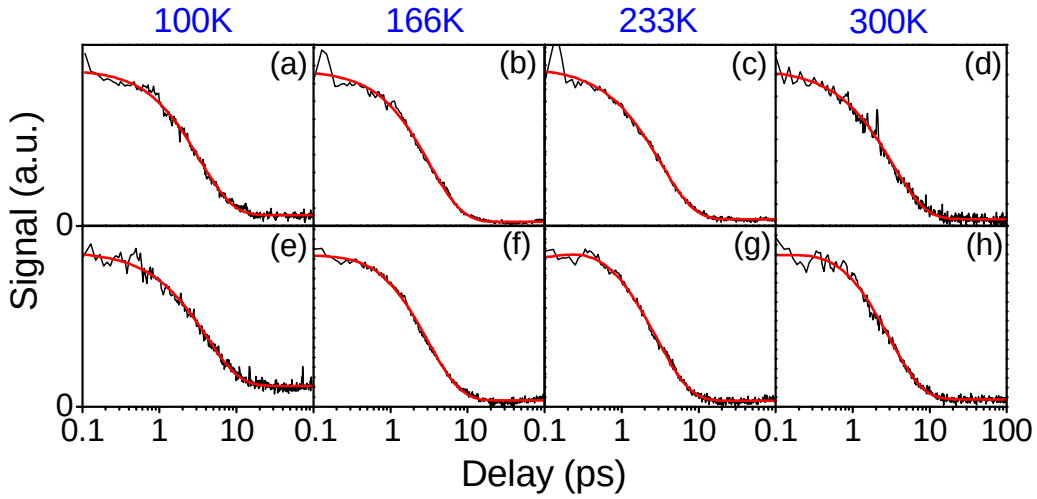

Figure A3.3. TG signals (black) and fits (red) obtained for 9-methyladenine (top row) and adenosine (bottom row). Temperatures are shown above the respective panels.

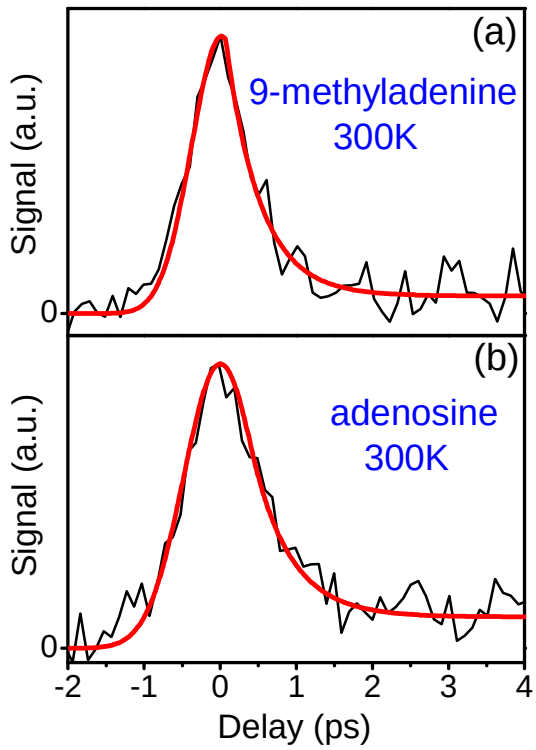

Figure A3.4. TRF signals obtained for (a) 9-methyladenine and (b) adenosine at 300K.

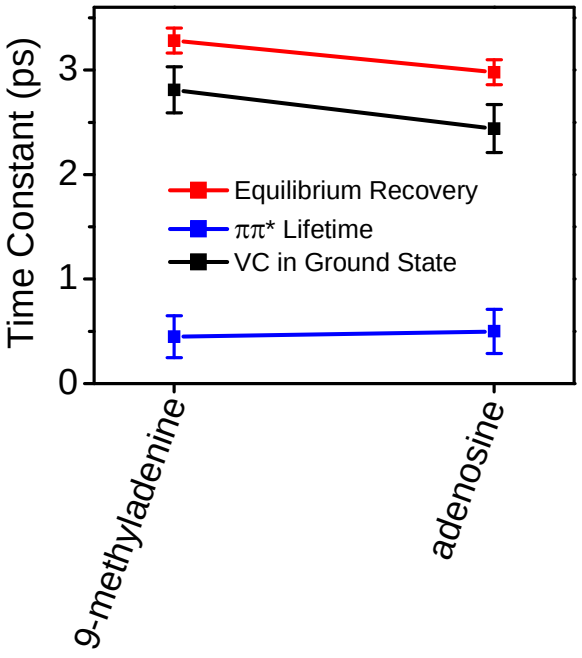

Figure A3.5. Summary of time constants obtained at 300K for 9-methyladenine and adenosine. This figure is analogous to Figure 6.4, which presents data for the thymine systems, in the main paper.

Table A3.6. TG Fitting Parameters for Adenine Systems at 100K

[(a),(b)]Parameter	9-Methyladenine	Adenosine
A_0	0.07±0.02	0.16±0.01
A_1	-0.04±0.02	1.00±0.02
τ_1 (ps)	0.32±0.20	4.05±0.05
A_2	1.00±0.05	----------
τ_2 (ps)	3.31±0.10	----------

[(a)]Fit to Equation $S(T) = A_0 + \sum_{i=1}^{2} A_i \exp(-T/\tau_i)$.

[(b)]Ranges in the parameters correspond to twice the standard errors.

Table A3.7. TG Fitting Parameters for Adenine Systems at 167K

[(a),(b)]Parameter	9-Methyladenine	Adenosine
A_0	0.03±0.01	0.04±0.002
A_1	-0.06±0.03	-0.11±0.03
τ_1 (ps)	0.51±0.28	0.33±0.18
A_2	1.00±0.04	1.00±0.03
τ_2 (ps)	3.14±0.10	3.01±0.72

[(a)]Fit to Equation $S(T) = A_0 + \sum_{i=1}^{2} A_i \exp(-T/\tau_i)$.

[(b)]Ranges in the parameters correspond to twice the standard errors.

Table A3.8. TG Fitting Parameters for Adenine Systems at 233K

[a],[b]Parameter	9-Methyladenine	Adenosine
A_0	0.04±0.002	0.04±0.003
A_1	1.00±0.05	-0.21±0.06
τ_1 (ps)	3.23±0.05	0.18±0.07
A_2	----------	1.00±0.04
τ_2 (ps)	----------	2.87±0.05

[a]Fit to Equation $S(T) = A_0 + \sum_{i=1}^{2} A_i \exp(-T/\tau_i)$.

[b]Ranges in the parameters correspond to twice the standard errors.

Table A3.9. TG Fitting Parameters for Adenine Systems at 300K

[a],[b]Parameter	9-Methyladenine	Adenosine
A_0	3.15±0.29	0.05±0.003
A_1	69.5±0.86	-0.15±0.05
τ_1 (ps)	3.28±0.08	0.28±0.14
A_2	----------	1.00±0.03
τ_2 (ps)	----------	2.98±0.08

[a]Fit to Equation $S(T) = A_0 + \sum_{i=1}^{2} A_i \exp(-T/\tau_i)$.

[b]Ranges in the parameters correspond to twice the standard errors.

Table A3.10. TRF Fitting Parameters for Adenine Systems at 300K

[(a)]Parameter	9-Methyladenine	Adenosine
A_0	----------	0.26±0.03
A_1	1.00±0.03	1.00±0.05
τ_1 (ps)	0.45±0.15	0.50±0.15

[(a)]Ranges in the parameters correspond to twice the standard errors.

A3.4. Phasing of Transient Grating Signals With Dispersive Thermal Grating

Spectral interferometry is used for the detection of transient grating signals in this work.[6] With this technique, the signal phase must be calibrated by using a reference measurement, a procedure often referred to among specialists as "phasing".[7] Signal phases can be determined by comparing heterodyne-detected signals to pump-probe spectra, although it is found that this is not necessarily a strong constraint in systems with broad line widths. If a flow system is used, another option is to exchange the solution for the transparent solvent (the interference fringes shift between samples). The samples studied here are held in a cryostat so comparison to the solvent is not feasible. In addition, pump-probe signals are below the detection threshold because of the low laser fluences employed. Therefore, the dispersive thermal grating is used, which is caused by fast non-radiative ground state recovery in the solute, to calibrate the signal phase. This method is ideal for the DNA components because the thermal grating is associated with a large signal amplitude and phasing is accomplished without exchanging the sample for a reference. In essence, the thermal grating is an internal standard for the signal phase. As in alternative phasing approaches, a single parameter is used to set the phase for all delay times.

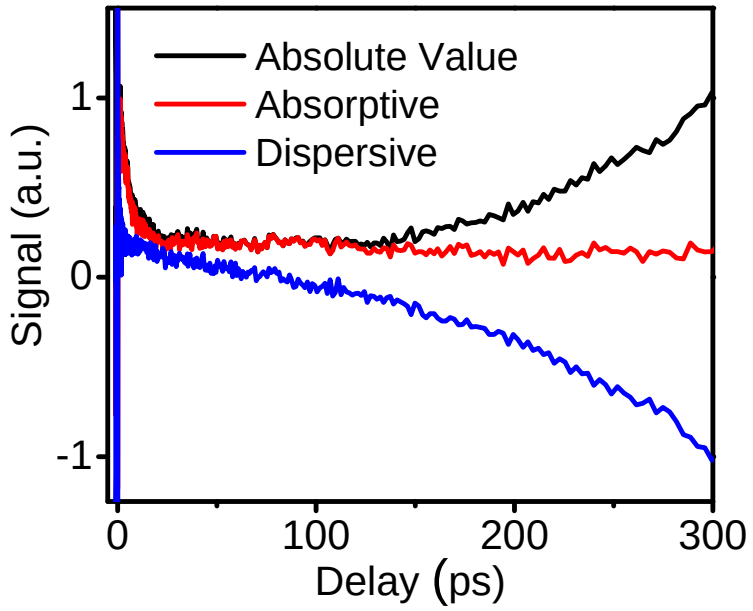

Figure A3.6. Transient grating signals measured for thymine in an 85:15 mixture of methanol:water. The signal rises on the 100's of ps time scale because of a thermal grating caused by fast non-radiative ground state recovery in thymine.

A3.5. References

(1) Hare, P. M.; Crespo-Hernández, C. E.; Kohler, B. *Proc. Natl. Acad. Sci.* **2007**, *104*, 435-440.

(2) Dreyer, J.; Moran, A. M.; Mukamel, S. *Bull. Korean Chem. Soc.* **2003**, *24*, 1091-1096.

(3) Womick, J. M.; Moran, A. M. *J. Phys. Chem. B* **2009**, *113*, 15771-15782.

(4) Barbatti, M.; Aquino, A. J. A.; Szymczak, J. J.; Nachtigallová, D.; Hobza, P.; Lischka, H. *Proc. Natl. Acad. Sci.* **2010**, *107*, 21453-21458.

(5) West, B. A.; Womick, J. M.; Moran, A. M. *J. Chem. Phys.* **2011**, *135*, 114505:1-114505:9.

(6) Lepetit, L.; Chériaux, G.; Joffre, M. *J. Opt. Soc. Am. B* **1995**, *12*, 2467-2474.

(7) Jonas, D. M. *Annu. Rev. Phys. Chem.* **2003**, *54*, 425-463.

Appendix 4 . Supporting Information for Chapter 7: "Nonlinear Optical Signal of Ultraviolet Light Induced Ring Opening in α –Terpinine

A4.1 Model for the Transient Absorption Anisotropy

In this appendix, a phenomenological model for the optical response is outlined in order to derive further insights from the absorptive TG signals shown in Figure 7.7. The optical response is generally partitioned into three components: the ground state bleach (GSB), excited state emission (ESE), and excited state absorption (ESA) [1]. The GSB and ESE nonlinearities are fully described in terms of the 1A (ground), 2A, and 1B electronic states in α-TP, where this notation is adapted from analogous states in CHD (see Figure 7.2). The ESA signal components involve additional excited states that enter the response only by introducing additional resonances; these higher energy states are never populated in the four wave mixing process.

Expressions for the GSB signal components are easily generated because the laser spectrum is resonant only with the 1B state (the ππ* state). The parallel and perpendicular tensor components are given by

$$S_{\parallel}^{GSB} = \frac{2}{5}\mu_{1B,1A}^{4} \tag{A4.1}$$

$$S_{\perp}^{GSB} = \frac{2}{15}\mu_{1B,1A}^{4} \tag{A4.2}$$

where $\mu_{1B,1A}$ is the magnitude of the transition dipole connecting the 1A ground state to the 1B excited state. The coefficients of $S_{\parallel}^{GSB}$ and $S_{\perp}^{GSB}$ represent orientational averages for the isotropic system [2,3]. The ESE response involves the same four transition dipoles present in the GSB nonlinearity but additionally decays as state 1B transfers population to state 2A. The model must also account for Stokes shifting of the ESE response out of the 36700cm^{-1}-37900cm^{-1} spectral window defined by the probe pulse. The

reorganization energy determined from fitting the absorbance line shape in Section IIIA suggests that the Stokes shift is in the 2300cm^{-1}- 3000cm^{-1} range (i.e., the reorganization energy is approximately half of the Stokes shift) [1], so the measurements lose sensitivity to the ESE nonlinearity during the inertial part of the solvation process. The parallel and perpendicular ESE tensor components are written as

$$S_{\parallel}^{ESE}(T) = \frac{2}{5}\mu_{1B,1A}^{4}\exp\left[-(T/\tau_1)^{\eta} - (T/\tau_{solv})^{2}\right] \tag{A4.3}$$

$$S_{\perp}^{ESE}(T) = \frac{2}{15}\mu_{1B,1A}^{4}\exp\left[-(T/\tau_1)^{\eta} - (T/\tau_{solv})^{2}\right] \tag{A4.4}$$

where τ_{solv} represents the (Gaussian) inertial solvation dynamics. Notably, τ_{solv} is not the total solvation time scale, rather it represents the (shorter) amount of time needed for the excited state wavepacket to depart from the Franck-Condon geometry. The parameter, η, more directly addresses the depopulation of state 1B than does b in Equation (7), because time-coincident electronic and nuclear relaxation processes are disentangled in the present model.

Three ESA signal components are needed to fully capture the decay profile of the anisotropy. First, the ESA nonlinearity that decays concomitant with depopulation of state 1B is given by

$${}^{1B}S_{\parallel}^{ESA}(T) = \frac{2}{15}\mu_{1B,1A}^{2}\mu_{K,1B}^{2}\left[1+2\cos^{2}(\alpha)\right]\exp\left[-(T/\tau_1)^{\eta}\right] \tag{A4.5}$$

$${}^{1B}S_{\perp}^{ESA}(T) = \frac{2}{15}\mu_{1B,1A}^{2}\mu_{K,1B}^{2}\left[2-\cos^{2}(\alpha)\right]\exp\left[-(T/\tau_1)^{\eta}\right] \tag{A4.6}$$

where $\mu_{K,1B}$ is the magnitude of a transition dipole connecting state 1B to the higher energy state K, and α is the angle between the $\mu_{1B,1A}$ and $\mu_{K,1B}$ transition dipoles. Population transfer to the excited state 2A gives rise to a similar ESA nonlinearity

$${}^{2A}S_{\parallel}^{ESA}(T) = \frac{2}{15}\mu_{1B,1A}^{2}\mu_{M,2A}^{2}\left[1+2\cos^{2}(\beta)\right]\left\{\exp(-T/\tau_2) - \exp\left[-(T/\tau_1)^{\eta} - T/\tau_2\right]\right\} \tag{A4.7}$$

$$ {}^{2A}S_{\perp}^{ESA}(T) = \frac{2}{15}\mu_{1B,1A}^{2}\mu_{M,2A}^{2}\left[2-\cos^{2}(\beta)\right]\left\{\exp(-T/\tau_{2})-\exp\left[-(T/\tau_{1})^{\eta}-T/\tau_{2}\right]\right\} \quad \text{(A4.8)} $$

These sums of exponentials ensure that ${}^{2A}S_{\parallel}^{ESA}(T)$ and ${}^{2A}S_{\perp}^{ESA}(T)$ grow when state 2A accepts population from state 1B and decay when state 2A is depopulated. As in the ESA component associated with state 1B, $\mu_{M,2A}$ is the magnitude of a transition dipole connecting state 2A to state M, and β is the angle between the $\mu_{1B,1A}$ and $\mu_{M,2A}$ transition dipoles. A third ESA signal component is required to obtain an anisotropy that is greater than 0.4 at long delay times. It is postulated that the TG measurement is sensitive to the formation of an open-chain photoproduct that (like the regenerated α-TP) undergoes vibrational cooling following ground state recovery. This ESA signal component is written as

$$ {}^{PP}S_{\parallel}^{ESA}(T) = \frac{2}{15}\mu_{1B,1A}^{2}\mu_{PP}^{2}\left[1+2\cos^{2}(\theta)\right]\left[1-\exp(-T/\tau_{vc})\right] \quad \text{(A4.9)} $$

$$ {}^{PP}S_{\perp}^{ESA}(T) = \frac{2}{15}\mu_{1B,1A}^{2}\mu_{PP}^{2}\left[2-\cos^{2}(\theta)\right]\left[1-\exp(-T/\tau_{vc})\right] \quad \text{(A4.10} $$

The identity of the photoproduct has not been determined, so the transition dipole magnitude, μ_{PP}, is written in a general way. The angle between the $\mu_{1B,1A}$ and μ_{PP} transition dipoles is denoted as θ. ${}^{PP}S_{\parallel}^{ESA}(T)$ and ${}^{PP}S_{\perp}^{ESA}(T)$ are taken to depend only on the time constant, τ_{vc}, under the assumption that vibrational cooling is slow compared to the internal conversion process. The main conclusions of this work are insensitive to inclusion of ${}^{PP}S_{\parallel}^{ESA}(T)$ and ${}^{PP}S_{\perp}^{ESA}(T)$ because vibrational cooling is slow compared to internal conversion between 1B and 2A.

Finally, the total parallel and perpendicular signals are obtained by summing the individual components.

$$ S_{\parallel}^{Total}(T) = -S_{\parallel}^{GSB} - S_{\parallel}^{ESE}(T) + {}^{1B}S_{\parallel}^{ESA}(T) + {}^{2A}S_{\parallel}^{ESA}(T) + {}^{PP}S_{\parallel}^{ESA}(T) \quad \text{(A4.11} $$

$$S_{\perp}^{Total}(T) = -S_{\perp}^{GSB} - S_{\perp}^{ESE}(T) + {}^{1B}S_{\perp}^{ESA}(T) + {}^{2A}S_{\perp}^{ESA}(T) + {}^{PP}S_{\perp}^{ESA}(T) \quad \text{(A4.12}$$

$S_{\parallel}^{Total}(T)$ and $S_{\perp}^{Total}(T)$ take into account the sign convention used in the transient absorption signals presented in Figure 7.7 (i.e., the bleach has a negative sign). With $S_{\parallel}^{Total}(T)$ and $S_{\perp}^{Total}(T)$ in hand, the anisotropy can be computed using Equation (6).

A4.2. Evaluation of Constraints in Model Calculations

In order to evaluate the sensitivity of the model calculations to the value of η, an error analysis is carried out for both the anisotropy and the individual tensor elements. The residuals sum of squares is defined as

$$RSS = \sum_{j} \left(X_{measured}(T_j) - X_{calculated}(T_j) \right)^2 \quad \text{(A4.13}$$

where the quantities $X_{measured}(T_j)$ and $X_{calculated}(T_j)$ correspond to $r(T_j)$, $S_{\parallel}(T_j)$, and $S_{\perp}(T_j)$. The delay points, T_j, range from 40fs-600fs. The RSS determined with the measurements and the model presented in appendix A are displayed in Figure 7.10. Example fits are presented in the bottom row of Figure 7.7. The fitting procedure first sets η equal to the indicated value, then minimizes the RSS values by varying the other parameters. Fitting the anisotropy together with the two tensor components imposes powerful constraints on the parameters. There is only a small region in parameter space for which reasonable fits are obtained at T <0.2ps. The angles, α and β, are between 55°-65°; τ_{solv} is 15fs-20fs; the transition dipole magnitudes vary by less than 4% from the values given for η=2.0 in Table 7.4. Conservatively, this analysis suggests that the depopulation dynamics of state 1B follow a non-exponential temporal profile in which η ranges from 1.7 to 3.2.

A4.3. References

(1) Mukamel, S. *Principles of Nonlinear Optical Spectroscopy*; Oxford University Press: New York, 1995.

(2) Hochstrasser, R. M. *Chem. Phys.* **2001**, *266*, 273-284.

(3) Dreyer, J.; Moran, A. M.; Mukamel, S. *Bull. Korean Chem. Soc.* **2003**, *24*, 1091-1096.